

THORETICAL AND EXPERIMENTAL INVESTIGATION OF THE PLASMONIC  
PROPERTIES OF NOBLE METAL NANOPARTICLES

A Dissertation  
Presented to  
The Academic Faculty

By

Rachel Deanne Near

In Partial Fulfillment  
Of the Requirements for the Degree  
Doctor of Philosophy in the School of Chemistry and Biochemistry

Georgia Institute of Technology

August 2013

Copyright © Rachel Deanne Near 2013

THORETICAL AND EXPERIMENTAL INVESTIGATION OF THE PLASMONIC  
PROPERTIES OF NOBLE METAL NANOPARTICLES

Approved by:

Dr. Mostafa A. El-Sayed  
Advisor  
School of Chemistry and Biochemistry  
*Georgia Institute of Technology*

Dr. Thomas Orlando  
School of Chemistry and Biochemistry  
*Georgia Institute of Technology*

Dr. David Sherrill  
School of Chemistry and Biochemistry  
*Georgia Institute of Technology*

Dr. Ken Brown  
School of Chemistry and Biochemistry  
*Georgia Institute of Technology*

Dr. Vladimir Tsukruk  
School of Material Science and  
Engineering  
*Georgia Institute of Technology*

Date Approved  
June 24th, 2013



*For my family*

## ACKNOWLEDGEMENTS

I must thank Dr. Mostafa El-Sayed for his support, guidance and funding not only during my five years at Georgia Tech as a graduate student, but for the two summers I spent in his lab as an undergraduate. I credit Dr. El-Sayed with sparking my passion for the area of study that would become the focus of my graduate studies. His passion for science is truly infectious and I am one of the many who have benefited from it.

I would also like to thank my committee members Drs. Thomas Orlando, David Sherrill, Kenneth Brown and Vladimir Tsukruk for their help guiding me through this work and helping me grow as a scientist. I have had the honor to collaborate with many other scientists, all of whom have contributed to my knowledge and to this thesis. Thank you to Erik Dreaden, Chris Tabor, Augustine Urbas, Ruth Pacter, Chun-Wan Yen, Steven Hayden, Adam Poncheri, Brian Snyder, Meg Mackey, Lauren Austin, Susie Eustis, and Fiona O'Connell. Thank you also to the wonderful cleanroom staff, especially Devin Brown and Nicole Devlin. Without the support staff, I'm fairly certain our building would fall apart, so many thanks indeed to Mike Riley, Carol Dawkins, Erica Jones and Paul Ficklin-Alred.

As I have had the pleasure of working in the same lab as both an undergraduate and graduate student, the number of people who have had a significant impact on my work is vast. In particular, Dr. Susie Eustis was my mentor during my first research experiences in Dr. El-Sayed's lab. I owe her many thanks for all I learned that summer. My choice to

continue research with this group had much to do with the enjoyable and enlightening experience I had with her. I also owe thanks to Dr. Chris Tabor for the wonderful mentorship wherein I learned most of the techniques that were used as the foundation of this thesis. I have much appreciated his continued mentorship even after his graduation. Steven Hayden has been an invaluable addition to my personal and scientific life. He has often believed in me when even I have failed to do so, for which I do not know if I can ever repay him. There is a long list of others who have all helped contribute to this thesis in some way. Thank you to Meg Mackey, Justin Bordley, Erik Dreaden, Daniel O'Neil, Li Chu, Bin Kang, Chun-Wan Yen, Lauren Austin, Adam Poncheri, and Brian Snyder.

The constant and unwavering support from my family throughout this process has been essential. I have always attributed my scientific tendencies to my mother, Debbie Givens. She has served as a wonderful role model of a strong scientific woman my entire life. Her constant support and guidance have been crucial. My sister, Michelle, has always been there to remind me that enjoying life is more important than anything. Without the support from my husband, Jonathan Near, I do not know if I would have made it here. Thank you for being my rock.

## TABLE OF CONTENTS

Dedication.....	iii
Acknowledgements.....	iv
List of Tables.....	ix
List of Figures.....	x
List of Abbreviations and Symbols.....	xxix
Summary.....	xxxii
I. Introduction to Metallic Nanoparticles.....	1
1.1 Plasmonic Responses in Metallic Films and Nanoparticles.....	1
1.2 Radiative Applications of Noble Metal Nanoparticles.....	5
1.3 Near-field Coupling between Plasmonic Nanoparticles.....	8
1.4 References.....	12
II. Fabrication and Instrumentation.....	17
2.1 Electron Beam Lithography Fabrication.....	17
2.2 Electron and Surface Probe Microscopes: SEM.....	22
2.3 Spectroscopic Measurements.....	22
2.4 Theoretical Modeling: Discrete Dipole Approximation.....	23
2.5 References.....	26
III. Think to Thick, Short to Long: Energetic Properties of Gold Nanorods by Theoretical Modeling.....	28
3.1 Summary.....	28
3.2 Introduction.....	28
3.3 Methods.....	30
3.4 Results and Discussion.....	30
3.4.1 Intensity of the longitudinal plasmon band.....	33
3.4.2 Energy of the longitudinal plasmon resonance.....	33
3.5 Conclusions.....	35
3.6 References.....	37

IV. Rapid and Efficient Prediction of Optical Extinction Coefficients for Gold Nanospheres and Gold Nanorods.....	40
4.1 Summary.....	40
4.2 Introduction.....	41
4.3 Methods.....	42
4.3.1 Reagents.....	42
4.3.2 Synthesis of gold nanorods.....	43
4.3.3 Thermal reshaping of gold nanorods.....	44
4.3.4 Characterization of gold nanoparticles.....	44
4.3.5 Theoretical methods.....	46
4.4 Results and Discussion.....	47
4.4.1 Modeling the optical properties of gold nanospheres.....	47
4.4.2 Thermal treatment of gold nanorods.....	53
4.4.3 Modeling the optical properties of gold nanorods.....	58
4.5 Conclusions.....	65
4.6 References.....	67
V. Extinction vs. Absorption: Which is the Indicator of Plasmonic field strength for Silver Nanocubes?.....	69
5.1 Summary.....	69
5.2 Introduction.....	70
5.3 Methods.....	72
5.4 Results and Discussion.....	72
5.4.1 40 nm Silver Nanosphere.....	72
5.4.2 40 nm Silver Nanocube.....	77
5.4.3 60 nm Silver Nanocube.....	84
5.4.4 86 nm Silver Nanocube.....	90
5.4.4.1 Higher Order Modes.....	92
5.4.4.2 Quadrupole and Dipole Modes.....	95
5.5 Conclusions.....	100
5.6 References.....	103
VI. Pronounced Effects of Anisotropy on Plasmonic Properties of Nanorings fabricated by Electron beam Lithography.....	106
6.1 Summary.....	106
6.2 Introduction.....	106
6.3 Methods.....	110
6.4 Results and Discussion.....	112
6.5 Conclusions.....	131
6.6 References.....	133

VII. Hollow Gold Nanorectangles: The Roles of Polarization, Substrate and Orientation.....	138
7.1 Summary.....	138
7.2 Introduction.....	139
7.3 Methods.....	142
7.4 Results and Discussion.....	144
7.4.1 Long Orientation.....	144
7.4.2 Tall Orientation.....	167
7.5 Conclusions.....	187
7.6 References.....	189
Appendix A - Discrete Dipole Approximation Methodology.....	192
A.1 Summary.....	192
A.2 Introduction.....	192
A.2.1 Computer Cluster.....	193
A.3 Two types of calculations and the required files.....	194
A.4 Parameter file.....	197
A.5 Shape file.....	202
A.5.1 Shape generator and making a single solid particle.....	205
A.5.2 Single hollow particle.....	212
A.5.3 Multiple particles.....	214
A.5.4 ImajeJ Method.....	216
A.5.5 Particle on a substrate.....	217
A.5.6 From scratch.....	219
A.6 Dielectric file.....	219
A.7 a_0.f and a.pbs.....	223
A.8 Spectra calculations.....	228
A.8.1 Running the spectra calculations.....	228
A.8.2 Data processing.....	231
A.9 Field calculations.....	232
A.9.1 Running the field calculations.....	233
A.9.2 Data Processing.....	237
A.9.3 Three dimensional composite plots.....	251
A.10 Trouble shooting.....	263
A. 11 References.....	264
Vita.....	265

## LIST OF TABLES

Table 3-1.....	32
Constants corresponding to the fits provided in Figure III-1.	
Table 5-1.....	92
Summary of field plot data at different wavelength for 86 nm AgNC. "Extinction", "absorption" and "scattering" refer to the value for those spectra at the wavelength of interest. "Max field" is the largest field enhancement value observed for any slice of the particle.	

## LIST OF FIGURES

Figure 1-1 .....	3
<p>A) Surface plasmon polariton (SPP) propagates along a thin metal film at the metal / dielectric interface in response to electric field stimulus. The “skin depth”, the distance the field penetrates into the material, is different for the metal and the dielectric. B.) Localized Surface Plasmon Resonance (LSPR) in a metallic nanoparticle where the size of the particle is much smaller than the wavelength of light</p>	
Figure 1-2 .....	8
<p>Electric field contours for A) Ag sphere of radius 30 nm. Maximum field enhancement is 50x initial intensity. B) Ag prism with edge length of 60 nm. Maximum field enhancement is 3500x initial intensity C) Dimer of 36 nm Ag spheres separated by 2 nm. Maximum enhancement 11,000 x the initial intensity. D) Tip-to-tip dimer of Ag prisms separated by 2 nm. Maximum enhancement is 53,000x initial intensity. The wavelengths in each panel are the resonant wavelengths for that particular system.</p>	
Figure 2-1 .....	19
<p>Diagram of proximity effect adapted from SPIE Handbook of Microlithography. a) Monte Carlo simulation of the back and forward scattering caused by the substrate-electron interactions as the electron beam exposes a thin PMMA resist layer (shown in blue) that is supported on a silicon wafer (shown in yellow) with an acceleration voltage of 20kV. b) The same simulation as in (a) with the assumption that the substrate is only 50 nm thick at the spot of exposure (shown in pink), as is the case with the Si<sub>3</sub>N<sub>4</sub> substrates used in this work.</p>	
Figure 2-2.....	20
<p>General electron beam lithography fabrication process. 1) Spin-coating of a thin layer (~100nm) of an electron sensitive resist (PMMA) onto a conductive substrate (typically silicon). 2) Exposure of the PMMA resist with a focused beam of electrons. 3) Development of the sample (removal of exposed areas of PMMA). 4) Evaporation of metal onto the substrate and into the exposed areas of the PMMA resist. 5) Removal of all polymer resist to leaving only the fabricated structures.</p>	
Figure 2-3 .....	22
<p>Schematic of the Si<sub>3</sub>N<sub>4</sub>/Si substrates used in the EBL fabrications. The Si<sub>3</sub>N<sub>4</sub> windows are shown as white rectangles and the surrounding Si substrate is shown in grey.</p>	



Figure 3-1 .....	32
DDA extinction spectra for AuNRs in water of varying diameter and AR grouped by (A) diameter and (B) AR, as indicated by color. Extinction intensity trends (C) cubically by diameter and (D) linearly by AR, emphasizing the role of cubic volume. The change in the longitudinal plasmon wavelength is (E) linear by diameter, indicating a dependence on anisotropy, and (F) exponential by AR from electromagnetic retardation effects in large nanoparticles.	
Figure 3-2 .....	34
(A) The position of the longitudinal plasmon wavelength is linear by AR, indicating a dependence on anisotropy. (B) The change in the longitudinal wavelength is exponential by length from electromagnetic retardation effects in large nanoparticles.	
Figure 4-1 .....	48
DDA extinction spectra for AuNS of varying diameter (indicated in legend) The extinction increases as the size of the AuNS increases with very little change in peak position.	
Figure 4-2 .....	50
Empirical formula relating the volume of the AuNS to the volume of the system in DDA. The data fit well ( $R^2 = 0.999$ ) to an allometric formula, $y = a \cdot x^b$ .	
Figure 4-3 .....	51
Fit of predicted extinction coefficients (PEC) against AuNS volume (blue line) with experimental extinction coefficients (EEC) from literature (colored spheres). All the experimental data points fall on the relation derived theoretically, indicating a good agreement.	
Figure 4-4 .....	52
DDA extinction spectrum for a 40 nm AuNS in water.	
Figure 4-5 .....	54
TEM micrograph of AuNRs $54.3 \pm 3.4 \times 15.1 \pm 1.0$ nm capped with CTAB. The longitudinal plasmon band appears ca. 800 nm.	
Figure 4-6 .....	55
TEM micrographs with overlaid, corresponding optical extinction spectra showing the progression from gold nanorods (top) to gold nanospheres (bottom) over time with heat.	

Figure 4-7 .....	56
Length and width of gold nanorods over time. These nanorods become shorter and fatter as they thermally melt, finally producing nanospheres.	
Figure 4-8 .....	57
Experimental extinction spectra showing thermal transition from gold nanorods to gold nanospheres. The longitudinal plasmon resonance blue-shifts while the transverse plasmon resonance red-shifts.	
Figure 4-9 .....	58
Experimental extinction coefficients by longitudinal plasmon resonance wavelength obtained via ICP-MS.	
Figure 4-10 .....	59
DDA extinction spectra for AuNR of varying dimensions (indicated in legend). The extinction intensity and peak position depend on both dimensions of the AuNR even though light is polarized along the length of the AuNR to isolate only the longitudinal mode.	
Figure 4-11 .....	61
Empirical formula relating the volume of the AuNR to the system volume in DDA. The data fit well ( $R^2 = 0.995$ ) to an exponential formula, $y = y_0 + A \cdot \exp[(x-x_0)/t]$ .	
Figure 4-12 .....	62
Fit of predicted extinction coefficients (PEC) against AuNR volume (blue line) with experimental extinction coefficients (EEC, orange spheres). All the experimental data points fall on the relation derived theoretically, indicating a good agreement.	
Figure 4-13 .....	63
DDA extinction spectrum for the longitudinal mode of a 30x10 AuNR in water.	
Figure 4-14 .....	64
Theoretical extinction spectra of 10 nm diameter AuNR of indicated aspect ratio (AR). Extinction intensity increases with increasing AR; resonant wavelength red-shifts strongly with increasing AR (top right panel). The predicted extinction coefficients increase with increasing aspect ratio (bottom right panel).	

Figure 5-1 .....	74
<p>a) DDA extinction (black), absorption (red) and scattering (green) spectra for a 40 nm AgNS in water. b) Comparison of spectral value trends with field enhancement trends for the dipole mode of a 40 nm AgNS. It can be seen that the maximum in field strength corresponds to the maximum spectral values.</p>	
Figure 5-2 .....	75
<p>Three-dimensional representation for the electric field enhancement of a 40 nm AgNS when excited with a wavelength of 393 nm. The field location and field vector orientations indicate that this is the dipole mode.</p>	
Figure 5-3 .....	75
<p>Representative field vector plot (middle slice of a 40 nm AgNS at 393 nm). As shown, a plus sign will indicate when all the vectors are pointing towards an area, and a minus sign indicate when all the vectors are pointing away from an area.</p>	
Figure 5-4 .....	76
<p>Three-dimensional representation for the electric field enhancement of a 40 nm AgNS when excited with a wavelength of 388 nm.</p>	
Figure 5-5 .....	77
<p>Three-dimensional representation for the electric field enhancement of a 40 nm AgNS when excited with a wavelength of 398 nm.</p>	
Figure 5-6 .....	79
<p>a) DDA extinction (black), absorption (red) and scattering (green) spectra for a AgNC in water with a 40 nm edge length. Higher order modes are present, but the modes are well separated. Absorption dominates scattering. b) Comparison of spectral value trends with field enhancement trends for the dipole mode of a 40 nm AgNC. The maximum field strength occurs at the spectral maxima, which all coincide. c) Comparison of spectral value trends with field enhancement trends for the quadrupole mode of a 40 nm AgNC. The maximum field strength occurs at the spectral maxima, which all coincide.</p>	
Figure 5-7 .....	80
<p>Three-dimensional representation for the electric field enhancement of a 40 nm AgNC when excited with a wavelength of 475 nm. The field locations and field vector orientations indicate that this is the dipole mode.</p>	
Figure 5-8 .....	81
<p>Three-dimensional representation for the electric field enhancement of a 40 nm AgNC when excited with a wavelength of 482 nm.</p>	

Figure 5-9 .....	81
Three-dimensional representation for the electric field enhancement of a 40 nm AgNC when excited with a wavelength of 487 nm.	
Figure 5-10 .....	82
Three-dimensional representation for the electric field enhancement of a 40 nm AgNC when excited with a wavelength of 435 nm. The field location and field vector orientations indicate that this is the quadrupole mode.	
Figure 5-11 .....	83
Three-dimensional representation for the electric field enhancement of a 40 nm AgNC when excited with a wavelength of 440 nm.	
Figure 5-12 .....	84
Three-dimensional representation for the electric field enhancement of a 40 nm AgNC when excited with a wavelength of 445 nm.	
Figure 5-13 .....	85
a) DDA extinction (black), absorption (red) and scattering (green) spectra for a AgNC in water with a 60 nm edge length. Higher order modes are present, but the modes are well separated. Scattering dominates absorption. b) Comparison of spectral value trends with field enhancement trends for the dipole mode of a 60 nm AgNC. The maximum field strength trends with the absorption, not the scattering or extinction. c) Comparison of spectral value trends with field enhancement trends for the quadrupole mode of a 60 nm AgNC. The maximum field strength trends with the absorption, not the scattering or extinction.	
Figure 5-14 .....	86
Three-dimensional representation for the electric field enhancement of a 60 nm AgNC when excited with a wavelength of 433 nm. The field location and field vector orientations indicate that this is the quadrupole mode.	
Figure 5-15 .....	87
Three-dimensional representation for the electric field enhancement of a 60 nm AgNC when excited with a wavelength of 441 nm.	
Figure 5-16 .....	87
Three-dimensional representation for the electric field enhancement of a 60 nm AgNC when excited with a wavelength of 443 nm.	

Figure 5-17 .....	88
Three-dimensional representation for the electric field enhancement of a 60 nm AgNC when excited with a wavelength of 492 nm. The field location and field vector orientation indicate that this is the dipole mode.	
Figure 5-18 .....	89
Three-dimensional representation for the electric field enhancement of a 60 nm AgNC when excited with a wavelength of 495 nm.	
Figure 5-19 .....	89
Three-dimensional representation for the electric field enhancement of a 60 nm AgNC when excited with a wavelength of 505 nm.	
Figure 5-20 .....	91
a) DDA extinction (black), absorption (red) and scattering (green) spectra for a AgNC in water with an 86 nm edge length. Higher order modes are present and there is considerable overlap between the modes. Scattering dominates absorption. b) Comparison of spectral value trends with field enhancement trends for the quadrupole mode of an 86 nm AgNC. The maximum field strength trends with the absorption, not the scattering or extinction.	
Figure 5-21 .....	93
Three-dimensional representation for the electric field enhancement of an 86 nm AgNC when excited with a wavelength of 377.5 nm. The field locations and field vector orientations indicate that this is a higher order multipole mode.	
Figure 5-22 .....	93
Three-dimensional representation for the electric field enhancement of an 86 nm AgNC when excited with a wavelength of 405 nm. The field locations and field vector orientations indicate that this is a higher order multipole mode.	
Figure 5-23 .....	94
Three-dimensional representation for the electric field enhancement of an 86 nm AgNC when excited with a wavelength of 417 nm. The field locations and field vector orientations indicate that this is a higher order multipole mode.	
Figure 5-24 .....	94
Three-dimensional representation for the electric field enhancement of an 86 nm AgNC when excited with a wavelength of 440 nm. The field locations and field vector orientations indicate that this is a higher order multipole mode.	

Figure 5-25 .....	95
Three-dimensional representation for the electric field enhancement of an 86 nm AgNC when excited with a wavelength of 443 nm. The field locations and field vector orientations indicate that this is the quadrupole mode.	
Figure 5-26 .....	96
Three-dimensional representation for the electric field enhancement of an 86 nm AgNC when excited with a wavelength of 447 nm.	
Figure 5-27 .....	96
Three-dimensional representation for the electric field enhancement of an 86 nm AgNC when excited with a wavelength of 454 nm.	
Figure 5-28 .....	97
Three-dimensional representation for the electric field enhancement of an 86 nm AgNC when excited with a wavelength of 462 nm.	
Figure 5-29 .....	98
Three-dimensional representation for the electric field enhancement of an 86 nm AgNC when excited with a wavelength of 470.5 nm. The field locations and field vector orientations indicate that this is a hybrid between the quadrupole and dipole modes.	
Figure 5-30 .....	98
Three-dimensional representation for the electric field enhancement of an 86 nm AgNC when excited with a wavelength of 487 nm.	
Figure 5-31 .....	99
Three-dimensional representation for the electric field enhancement of an 86 nm AgNC when excited with a wavelength of 523 nm. The field locations and field vector orientations indicate that this is the dipole mode.	
Figure 6-1 .....	113
Selected SEM images of nanoring dimers fabricated by EBL. The average dimensions of the rings are $127.6 \pm 2.5$ nm and $57.8 \pm 2.3$ nm for the outer and inner diameters, respectively. The interparticle separations are 0, $17.8 \pm 3.4$ , $37.5 \pm 2.9$ , $53.8 \pm 1.7$ , $68.3 \pm 3.4$ , and $239.2 \pm 3.7$ nm for A-F respectively. The scale bars in A-F are all 300 nm. The insets in B and F are highly magnified images of one dimer. The scale bars in the insets are both 30 nm.	
Figure 6-2 .....	115
Initial DDA results for a ring dimer with an interparticle separation of 240 nm, simulating an isolated structure. The position of the peaks is practically the same for the two different polarization conditions.	

Figure 6-3 .....	116
<p>Normalized experimental extinction spectra for nanoring dimers with a range of interparticle separations irradiated with unpolarized light. Two distinct bands are observed, one appearing around 1000 nm, whose position does not appreciably change with interparticle separation, and one appearing between 1100 and 1200 nm, whose position red shifts significantly as the interparticle separation is decreased.</p>	
Figure 6-4 .....	117
<p>Fractional shift of the wavelength (<math>\Delta\lambda/\lambda_0</math>) plotted against the interparticle separation scaled by the outer diameter (<math>s/D</math>) for the peak at 1000 nm (black) and the peak at 1100 nm (red). The solid line of the same color as the corresponding data set shows the exponential fit of each plot.</p>	
Figure 6-5 .....	119
<p>Normalized experimental extinction spectra for nanoring dimers of varying interparticle separations with polarization parallel and to the interparticle axis (as indicated in inset). Only one extinction band is observed. As the interparticle separation decreases, the extinction band red shifts.</p>	
Figure 6-6 .....	120
<p>The fractional shift of the band isolated under parallel polarization plotted against the interparticle separation scaled by the outer diameter. The data fits well (<math>R^2 = 0.91</math>) to the exponential model.</p>	
Figure 6-7 .....	121
<p>Normalized experimental extinction spectra for nanoring dimers of varying interparticle separations with polarization perpendicular to the interparticle axis (as indicated in inset). Only one extinction band is observed. As the interparticle separation decreases, the extinction band blue shifts.</p>	
Figure 6-8 .....	122
<p>The fractional shift of the band isolated under perpendicular polarization plotted against the interparticle separation scaled by the outer diameter. The data fits well (<math>R^2 = 0.93</math>) to the exponential model.</p>	
Figure 6-9 .....	124
<p>a) SEM image of nanoring dimers with interparticle separation is <math>17.8 \pm 3.4</math> nm. The scale bar is 300 nm. b) High resolution SEM image of a single nanoring demonstrating the particle anisotropy. The scale bar is 30 nm.</p>	

Figure 6-10 .....	127
DDA-simulated extinction spectra (in air) of ten single nanorings calculated using the SEM based shape files with light polarized a) parallel and b) perpendicular to the interparticle axis (as indicated in insets).	
Figure 6-11 .....	128
FDTD calculated spectra for a perfect nanoring dimer (black), and an SEM based nanoring dimer (red), both representing the sample with the smallest interparticle separation ( $17.8 \pm 3.4$ nm). All spectra are done in vacuum with no substrate present.	
Figure 6-12 .....	130
FDTD extinction spectra for nanoring dimers of varying interparticle separations with polarization parallel to the interparticle axis. Introduction of the substrate induces a Fano lineshape in the model for the dimer with an interparticle separation of 22.0 nm. Furthermore, use of the SEM-based dimer in the calculations has increased the Fano lineshape and most closely resembles the corresponding experimental spectra.	
Figure 7-1 .....	145
Selected SEM images of gold hollow rectangle pairs fabricated via EBL on $\text{Si}_3\text{N}_4$ membranes. The particles have outer dimensions of $197 \pm 4$ by $134 \pm 6$ nm and inner dimensions of $109 \pm 5$ by $53 \pm 3$ nm. The interparticle separations are a) $27 \pm 2$ nm, b) $71 \pm 2$ nm, c) $191 \pm 3$ nm, and d) $596 \pm 8$ nm. The scale bars are 300 nm.	
Figure 7-2 .....	146
DDA in air for isolated particle with light polarized parallel (black) and perpendicular (red) to the long axis of the particle. For parallel polarization, only one peak is present at 936 nm. For perpendicular polarization, one major peak is present at 844 nm and one minor peak is present at 574 nm.	
Figure 7-3 .....	148
Composite field plot for isolated particle in air with parallel polarization at 936 nm. The field is located at the corners of the particle in each slice. The field vectors are pointing away from the right of the particle and towards the left in each slice. The field location and orientation indicates this is the dipole mode.	
Figure 7-4 .....	148
Representative field vector plot (top slice of a hollow rectangle) for an isolated hollow rectangle in air with parallel polarization at $\lambda = 936$ nm. As shown, a plus sign will indicate when all the vectors are pointing towards an area, and a minus sign indicate when all the vectors are pointing away from an area.	



Figure 7-5 .....	150
Composite field plots for isolated particle in air with perpendicular polarization at 844 nm (main peak). The field is located at the corners of the particle in each slice. The field vectors are pointing away from the back of the particle and towards the front in each slice. The field location and orientation indicates this is the dipole mode.	
Figure 7-6 .....	150
Representative field vector plot (top slice of a hollow rectangle) for an isolated hollow rectangle in air with perpendicular polarization at $\lambda = 844$ nm. As shown, a plus sign will indicate when all the vectors are pointing towards an area, and a minus sign indicate when all the vectors are pointing away from an area.	
Figure 7-7 .....	151
Composite field plots for isolated particle in air with perpendicular polarization at 574 nm (minor peak). The field is located at the outer corners and the interior long sides of the particle in each slice. The field vectors alternate orientation along the sides and corners. The field location and orientation indicates this is the quadrupole mode.	
Figure 7-8 .....	151
Representative field vector plot (top slice of a hollow rectangle) for an isolated hollow rectangle in air with perpendicular polarization at $\lambda = 574$ nm. As shown, a plus sign will indicate when all the vectors are pointing towards an area, and a minus sign indicate when all the vectors are pointing away from an area.	
Figure 7-9 .....	153
DDA extinction spectra for hollow gold nanorectangles with long orientation in air ( i.e. no substrate) and light polarized a) parallel and b) perpendicular to the interparticle axis (as indicated in the insets). The interparticle separations are indicated in the legend. The spectra show the expected red shift and blue shift for parallel and perpendicular polarization, respectively.	
Figure 7-10 .....	155
Experimental extinction spectra for hollow gold nanorectangles with long orientation and polarization a) parallel and b) perpendicular (as indicated in the insets) to the interparticle axis. The interparticle separations are indicated in the legend. There are two distinct peaks present for the parallel polarization, which red shift and change in intensity as the interparticle separation decreases. For the perpendicular polarization the expected blue shift is seen as the interparticle separation decreases.	

Figure 7-11 .....	156
<p>Ten raw experimental extinction spectra for hollow gold nanorectangles with an interparticle separation of <math>27 \pm 2</math> nm long orientation and polarization parallel to the interparticle axis. The spectra are very similar to one another, indicating good uniformity across the entire sample. The main peak position occurs at 1496 nm with a relative standard deviation of only 0.5%.</p>	
Figure 7-12 .....	158
<p>DDA extinction spectra for hollow gold nanorectangles with long orientation on a substrate light polarized a) parallel and b) perpendicular to the interparticle axis (indicated in the insets). The interparticle separations are indicated in the legend.</p>	
Figure 7-13 .....	161
<p>Field enhancement values at the resonant wavelength for the dipole mode of the particles in air with light polarized parallel to the interparticle axis. The interparticle separations are indicated in the legend. For all cases, the field enhancement is greatest at the top and bottom of the particles, and reaches a minimum in the middle.</p>	
Figure 7-14 .....	161
<p>Composite field plot for isolated particle on a substrate with parallel polarization at 1220 nm. The field is located at the corners of the particle in each slice. The field vectors are pointing away from the right of the particle and towards the left in each slice. The field location and orientation indicates this is the dipole mode.</p>	
Figure 7-15 .....	162
<p>Composite field plot for isolated particle on a substrate with parallel polarization at 1340 nm. The field is located at the corners of the particle in each slice. The field vectors are pointing away from the right of the particle and towards the left in each slice. The field location and orientation indicates this is the dipole mode.</p>	
Figure 7-16 .....	162
<p>Field enhancement values for the particle pair with an interparticle separation of <math>596 \pm 8</math> nm on a substrate with light polarized parallel to the interparticle axis at several wavelengths (as indicated in the legend). For the wavelengths to the blue of 1300 nm, the field is most intense in the middle z slice of the particle. Meanwhile, for wavelengths to the red of 1300 nm, the field is most intense at the bottom z slice of the particle.</p>	

Figure 7-17 .....	163
Diagram illustrating substrate effect for a single particle under parallel polarization. a) In air, the field is symmetric and most intense at the top and bottom of the particle. b) In the presence of the substrate, the field at the bottom of the particle interacts with the substrate and leads to the two peaks observed experimentally.	
Figure 7-18 .....	164
Composite field plot for particle pair with an interparticle separation of $27\pm 2$ nm on a substrate with perpendicular polarization at 680 nm. The field is located at the corners and sides of the particle in each slice. The field vectors are pointing away from the front corners and middle of the back side and towards the back corners and middle of the front side. The field location and orientation indicates this is the quadrupole mode. The field is most intense at the bottom slice of the particle.	
Figure 7-19 .....	164
Composite field plot for particle pair with an interparticle separation of $27\pm 2$ nm on a substrate with perpendicular polarization at 1110 nm. The field is located at the corners of the particle in each slice. The field vectors are pointing away from the back of the particle and towards the front in each slice. The field location and orientation indicates this is the dipole mode. The field is most intense at the bottom slice of the particle.	
Figure 7-20 .....	165
Composite field plot for particle pair with an interparticle separation of $27\pm 2$ nm on a substrate with perpendicular polarization at 1420 nm. The field is located at the corners of the particle in each slice. The field vectors are pointing away from the back of the particle and towards the front in each slice. The field location and orientation indicates this is the dipole mode. The field is most intense at the middle slice of the particle.	
Figure 7-21 .....	166
a) Fractional shift of calculated dipolar plasmon peak. The data fits the expected exponential decay well ( $R^2 = 0.93$ ). b) Fractional shift of experimental dipolar plasmon peak. The data fits the expected exponential decay well ( $R^2 = 0.95$ ).	
Figure 7-22 .....	168
Selected SEM images of gold hollow rectangle pairs fabricated via EBL on $\text{Si}_3\text{N}_4$ membranes. The particles have outer dimensions of $140\pm 6$ by $197\pm 4$ nm and inner dimensions of $53\pm 4$ by $106\pm 5$ nm. The interparticle separations are a) $25\pm 2$ nm, b) $73\pm 3$ nm, c) $189\pm 7$ nm, and d) $284\pm 8$ nm. The scale bars are 300 nm.	

Figure 7-23 .....	169
DDA in air for isolated particle with light polarized parallel (black) and perpendicular (red) to the short axis of the particle. For parallel polarization, one major peak is present at 855 nm and one minor peak is present at 570. For perpendicular polarization, only one peak is present at 920 nm.	
Figure 7-24 .....	170
Composite field plots for isolated particle in air with parallel polarization at 855 nm (main peak). The field is located at the corners of the particle in each slice. The field vectors are pointing away from the right of the particle and towards the left in each slice. The field location and orientation indicates this is the dipole mode.	
Figure 7-25 .....	170
Representative field vector plot (top slice of a hollow rectangle) for an isolated hollow rectangle in air with parallel polarization at $\lambda = 855$ nm. As shown, a plus sign will indicate when all the vectors are pointing towards an area, and a minus sign indicate when all the vectors are pointing away from an area.	
Figure 7-26 .....	172
Composite field plots for isolated particle in air with parallel polarization at 570 nm (minor peak). The field is located at the outer corners and the interior long sides of the particle in each slice. The field vectors alternate orientation along the sides and corners. The field location and orientation indicates this is the quadrupole mode.	
Figure 7-27 .....	172
Representative field vector plot (top slice of a hollow rectangle) for an isolated hollow rectangle in air with parallel polarization at $\lambda = 570$ nm. As shown, a plus sign will indicate when all the vectors are pointing towards an area, and a minus sign indicate when all the vectors are pointing away from an area.	
Figure 7-28 .....	174
Composite field plots for isolated particle in air with perpendicular polarization at 920 nm. The field is located at the corners of the particle in each slice. The field vectors are pointing away from the back of the particle and towards the front in each slice. The field location and orientation indicates this is the dipole mode.	

Figure 7-29 .....	174
<p>Representative field vector plot (top slice of a hollow rectangle) for an isolated hollow rectangle in air with perpendicular polarization at <math>\lambda = 920</math> nm. As shown, a plus sign will indicate when all the vectors are pointing towards an area, and a minus sign indicate when all the vectors are pointing away from an area.</p>	
Figure 7-30 .....	176
<p>DDA extinction spectra for hollow gold nanorectangles in air (i.e. no substrate) with light polarized a) parallel and b) perpendicular to the interparticle axis (as indicated in the insets). The interparticle separations are indicated in the legend. As the interparticle separation decreases, we observe the expected red shift for parallel polarization and the expected slight blue shift for perpendicular polarization.</p>	
Figure 7-31 .....	178
<p>Experimental extinction spectra for hollow gold nanorectangles with light polarized a) parallel and b) perpendicular to the interparticle axis (as indicated in the insets). The interparticle separations are indicated in the legend.</p>	
Figure 7-32 .....	180
<p>DDA extinction spectra for hollow gold nanorectangles on a substrate with polarization a) parallel and b) perpendicular to the interparticle axis (as indicated in the insets). The interparticle separations are indicated in the legend.</p>	
Figure 7-33 .....	181
<p>Composite field plot for particle on a substrate with an interparticle separation of <math>284 \pm 8</math> nm with parallel polarization at 710 nm (minor peak). The field is located at the outer corners and the interior long sides of the particle in each slice. The field vectors alternate orientation along the sides and corners. The field location and orientation indicates this is the quadrupole mode.</p>	
Figure 7-34 .....	181
<p>Composite field plot for particle on a substrate with an interparticle separation of <math>284 \pm 8</math> nm with perpendicular polarization at 920 nm. The field is located at the corners of the particle in each slice. The field vectors are pointing away from the back of the particle and towards the front in each slice. The field location and orientation indicates this is the dipole mode.</p>	

Figure 7-35 .....	182
Field enhancement values at the resonant wavelength for the dipole mode of the particles in air with light polarized parallel to the interparticle axis. The interparticle separations are indicated in the legend. For all cases, the field enhancement is greatest at the top and bottom of the particles, and reaches a minimum in the middle.	
Figure 7-36 .....	184
Composite field plot for isolated particle on a substrate with parallel polarization at 1190 nm. The field is located at the corners of the particle in each slice. The field vectors are pointing away from the right of the particle and towards the left in each slice. The field location and orientation indicates this is the dipole mode.	
Figure 7-37 .....	185
Composite field plot for isolated particle on a substrate with parallel polarization at 1350 nm. The field is located at the corners of the particle in each slice. The field vectors are pointing away from the right of the particle and towards the left in each slice. The field location and orientation indicates this is the dipole mode.	
Figure 7-38 .....	186
Field enhancement values for the particle pair with an interparticle separation of $284 \pm 8$ nm on a substrate with light polarized parallel to the interparticle axis at several wavelengths (as indicated in the legend). a) For the wavelengths to the blue of 1240 nm, the field is most intense at the bottom z slice of the particle. b) Meanwhile, for wavelengths to the red of 1240 nm, the field is most intense at the middle z slice of the particle.	
Figure A - 1.....	196
An example of the ddscat.pbs file.	
Figure A - 2.....	198
The ddscat.par or parameter file	
Figure A - 3.....	203
Example of a correct shape.dat file.	
Figure A - 4.....	207
Setting the columns to xyz xyz.	
Figure A - 5.....	208
Creating a 3D scatter plot.	
Figure A - 6.....	209
How to disable speed mode.	

Figure A - 7.....	210
ASCII export options.	
Figure A - 8.....	211
Incorrect shape file headings after exporting from Origin.	
Figure A - 9.....	213
Renumbering the index column with row numbers.	
Figure A - 10.....	221
Dielectric file, diel.tab, for gold in air.	
Figure A - 11.....	222
Dielectric file, diel.tab, for gold in water.	
Figure A - 12.....	224
Changing the final plot/matrix size in the a_0.f file	
Figure A - 13.....	226
Choosing slice number in the a_0.f file.	
Figure A - 14.....	227
The a.pbs file.	
Figure A - 15.....	228
Folder containing the files needed for a spectral calculation.	
Figure A - 16.....	229
The command for submitting the ddscat.pbs calculation.	
Figure A - 17.....	230
Output from the spectra calculations.	
Figure A - 18.....	232
The qtable file data.	
Figure A - 19.....	233
Folder containing the files for a field calculation.	
Figure A - 20.....	235
The ddscat.par file for a field calculation.	
Figure A - 21.....	236
Output for the modified ddscat code.	

Figure A - 22.....	237
Output for the field calculation.	
Figure A - 23.....	238
Delete the last four columns of the field data.	
Figure A - 24.....	239
Convert the data to a matrix.	
Figure A - 25.....	240
Choosing to set the matrix dimensions.	
Figure A - 26.....	240
Setting the matrix dimensions.	
Figure A - 27.....	242
Generating a contour plot.	
Figure A - 28.....	242
Editing the plot details.	
Figure A - 29.....	243
Changing the color map scale.	
Figure A - 30.....	243
Changing the color fill.	
Figure A - 31.....	244
Exiting speed mode.	
Figure A - 32.....	245
The fort.32 file data.	
Figure A - 33.....	246
Inserting columns into the fort.32 data.	
Figure A - 34.....	247
Setting the values for column c.	
Figure A - 35.....	248
Setting the values for column d.	
Figure A - 36.....	249
Setting the fort.32 columns to xy xy.	



Figure A - 37.....	250
Creating the vector plot.	
Figure A - 38.....	251
The three matrices.	
Figure A - 39.....	252
Creating the color map plot.	
Figure A - 40.....	252
The initial 3D color map plot.	
Figure A - 41.....	253
Setting the color map scale.	
Figure A - 42.....	254
Changing the grids.	
Figure A - 43.....	254
Selecting only bottom contour to color fill.	
Figure A - 44.....	255
Deselecting speed mode.	
Figure A - 45.....	256
Setting the plot to orthographic display mode.	
Figure A - 46.....	256
Setting the planes to not be colored.	
Figure A - 47.....	258
Hiding the z axis.	
Figure A - 48.....	258
Hiding the yz and xz planes.	
Figure A - 49.....	259
Hiding the major axis labels.	
Figure A - 50.....	259
Final figures to combine into the 3D composite.	
Figure A - 51.....	260
Merging the graphs.	

Figure A - 52.....	260
Keeping the old graphs.	
Figure A - 53.....	261
Setting the merged graph to be 1 row and column.	
Figure A - 54.....	261
The initial merged plot.	
Figure A - 55.....	262
The final merged plot.	

## LIST OF ABBREVIATIONS AND SYMBOLS

$\alpha$	dipole polarizability
$\epsilon$	dielectric permittivity
$\gamma$	shape factor
$\lambda$	wavelength
s	interparticle separation
Å	angstrom
D	particle diameter
V	Volume
au	arbitrary units
cm	centimeter
$\Delta\lambda$	shift or change in wavelength
kV	kilovolts
nA	nanoAmperes
nm	nanometers
$\mu\text{C}$	microCoulombs
$\mu\text{m}$	micrometers or microns
R/s	ramps per second
DDA	Discrete Dipole Approximation
EBL	Electron Beam Lithography
FDTD	Finite-Difference Time-Domain

IPA	Isopropyl Alcohol
LSPR	Localized Surface Plasmon Resonance
MIBK	methyl isobutyl ketone
NIR	Near Infrared
PMMA	poly methyl methacrylate
RIU	Refractive index units
RPM	rotations per minute
RSD	Relative Standard Deviation
SEM	Scanning electron microscope
SERS	Surface Enhanced Raman Scattering
SPP	Surface Plasmon Polaritons
UV	Ultraviolet
Au	Gold
Ag	Silver
Cu	Copper
Cr	Chrome
Si	Silicon
Si <sub>3</sub> N <sub>4</sub>	silicon nitride
AgNC	Silver nanocube
AgNS	Silver nanosphere
AuNS	Gold nanosphere
AuNR	Gold Nanorod

## SUMMARY

Noble metal nanoparticles are of great interest due to their tunable optical and radiative properties. The specific wavelength of light at which the localized surface plasmon resonance occurs is dependent upon the shape, size and composition of the particle as well as the dielectric constant of the host medium. Thus, the optical properties of noble metal nanoparticles can be systematically tuned by altering these specific parameters. The purpose of this thesis is to investigate some of these properties related to metallic nanoparticles. The first several chapters focus on theoretical modeling to predict and explain various plasmonic properties of gold and silver nanoparticles while the later chapters focus on more accurately combining experimental and theoretical methods to explain the plasmonic properties of hollow gold nanoparticles of various shapes.

Chapter I serves as an introduction to metallic nanoparticles and their optical properties, including a discussion of plasmonics. Chapter II discusses the various methods for fabrication, characterization and theoretical modeling that will be used throughout the various other chapters of this thesis.

Chapters III-V are focused on elucidating fundamental plasmonic properties of various systems using theoretical methods. Chapter III is a fundamental investigation into the plasmonic properties of gold nanorods. In this investigation, equations are formulated to explain the relations between the dimensions of the gold nanorods and the longitudinal

plasmon peak position and intensity are explored. In Chapter IV, a method is developed by which it is possible to predict the experimental extinction coefficient of gold nanospheres and gold nanorods based purely upon their theoretical spectra. In Chapter V a three-dimensional modeling technique is developed that is then used assign various peaks to different plasmon modes as well as to probe the relation between peak intensity and electromagnetic field enhancement for the various modes.

Chapters VI and VII focus on fabricating new types of hollow nanostructures with electron beam lithography and then developing methods to more accurately combine these results with theoretical methods. In Chapter VI a sample of nanoring dimers is fabricated and discussed. It is found that anisotropy in the particle shape has pronounced effects on the optical properties of the system. Furthermore, it was found that a new technique for preparing the files that define shape in the theoretical modeling was needed to achieve agreement with the experimental results. The ideas gleaned from Chapter VI on the rings are then extended in Chapter VII to two samples of hollow rectangle dimers. The techniques developed for modeling the rings are applied to the rectangles by which the effects from substrate, polarization and particle orientation are assessed.

Appendix A is a detailed description of the discrete dipole approximation. It is intended to serve as a guide such that a user could carry out the various types of calculations discussed in this thesis simply by reading this appendix.

## CHAPTER I

### INTRODUCTION TO METALLIC NANOPARTICLES

Noble metal nanoparticles are of great interest due to their tunable optical and radiative properties. Intense localized fields can be induced at the surface of a noble metal nanoparticle by electromagnetic waves of appropriate energy. These fields are generated as a result of the electric field of resonant frequency light coupling with the conduction band electrons in a noble metal nanoparticle leading to an oscillation in these conduction band electrons. This oscillation is primarily localized on the surface and is termed a localized surface plasmon resonance (LSPR).<sup>1-4</sup> The specific wavelength at which the LSPR occurs is dependent upon the shape, size and composition (dielectric function) of the particle as well as the dielectric constant of the host medium. Thus, the optical properties of noble metal nanoparticles can be systematically tuned by altering these specific parameters. The tunability of the LSPR and the intense localized fields at the nanoparticle surface make noble metal nanoparticles extremely appealing for a wide range of applications in medicine,<sup>5-8</sup> optics<sup>9-12</sup> and sensing.<sup>6-8,13,14</sup>

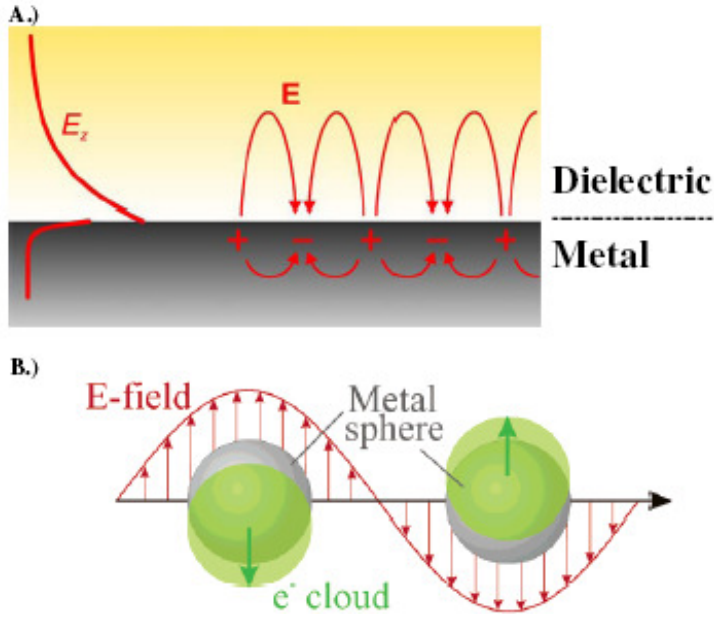
#### **1.1 Plasmonic Responses in Metallic Films and Nanoparticles**

Surface plasmons, also known as surface plasmon polaritons (SPPs), are electronic fluctuations at the interface between two materials in response to an applied electric field.

These fluctuations were first observed in thin metallic films in 1957.<sup>15</sup> The field propagates along the interface between the two materials and extends into the materials to a certain depth. The skin depth is the distance into the material at which the field decays to  $1/e$  and is a function of the dielectric permeability of the material. Figure 1 - 1A depicts the SPP as it propagates along the interface between a metal and dielectric and induces regions of fluctuating charge.

When the interface between the metal and the dielectric becomes small compared to the wavelength of light incident upon it, which occurs either when the size of the metal (metallic nanoparticles)<sup>2,16</sup> or the dielectric (nanoholes)<sup>17,18</sup> is reduced, a localized surface plasmon resonance (LSPR) occurs that is isolated at the interface (Figure 1 - 1B). The result of this localized plasmon is an intensely focused electric field that can be used for a wide range of applications. This thesis work concentrates exclusively on metallic nanoparticles, so the following discussion will be centered on phenomena associated with nanoparticles and their applications.





First, the fundamental equations that describe the interaction of light with a material will be discussed in reference to the plasmonic metal nanoparticle. Equation 1 gives the dipole polarizability of any particle that is small with respect to the wavelength of incident light ( $\text{size} \leq \lambda/4$ ).

$$\alpha = \epsilon_0 (1 + \gamma) \left( \frac{\epsilon - \epsilon_m}{\epsilon + \gamma \epsilon_m} \right) V \quad \text{Equation 1}$$

where  $\epsilon = \epsilon_{\text{Re}} + i\epsilon_{\text{Im}}$  is the frequency dependent dielectric permittivity of the particle material,  $\epsilon_m$  is the dielectric permittivity of the medium (usually assumed to be

independent of the frequency within the range of measurement),  $\gamma$  is a variable that depends on the shape of the particle (e.g.  $\gamma = 2$  for spheres), and  $V$  is the volume of the particle.

The conditions to establish a surface plasmon resonance (maximum polarizability) are satisfied when the denominator of Equation 1 goes to zero. In general, this condition is satisfied when

$$\mathcal{E} = -\gamma\mathcal{E}_m \quad \text{Equation 2}$$

The shape factor ( $\gamma$ ) is always positive, and the dielectric permittivity of air - as well as that of most solvents - is greater than zero. The consequence is that the dielectric permittivity of the particle material must be negative in order for Equation 2 to be satisfied and a surface plasmon supported. The dielectric permittivity of metals is negative in most regions of the electromagnetic spectrum, allowing metallic nanoparticles to support a LSPR. At the frequency of light that is in resonance with the localized surface plasmon, termed the localized surface plasmon frequency, the conduction band electrons within the particle are delocalized and oscillating in resonance with the light's electric field. In particular, the localized plasmon frequency for noble metals (gold, silver, copper) falls in the IR-visible region of the electromagnetic spectrum, making them appropriate for optical applications.

## 1.2 Radiative Applications of Noble Metal Nanoparticles

The tunability and longevity of noble metal nanoparticles makes them suitable for applications utilizing the visible and near-infrared (NIR) region of the electromagnetic spectrum. The coupling between metal nanoparticles and light, in the form of the LSPR, provides plasmonic nanoparticles distinct advantages over fluorescent dyes, which are often used as optical markers in biological and chemical applications but are susceptible to photo-bleaching. In addition to the durability of metallic nanoparticles, the time scale of scattering from a nanoparticle is much faster than fluorescence (femtosecond vs. nanosecond timescales),<sup>19-23</sup> making it possible to probe processes that occur on shorter timescales. Another distinct advantage of nanoparticles compared to fluorescent dyes is that nanoparticles have extinction coefficients that can be up to several orders of magnitude greater than those of fluorescent dyes.<sup>24</sup>

The strong absorption properties of plasmonic metal nanoparticles coupled with their efficient, non-radiative electronic relaxation characteristics give them powerful photo-thermal properties. The energy attenuated by the plasmonic nanoparticle upon irradiation of light at the plasmonic resonance is partially absorbed by the particle. The percentage of the light extinction that is absorbed is dependent on the size and shape of the nanoparticle. As the particle size increases, the ratio of scattered light to absorbed light increases.<sup>25</sup> The scattered light is elastically scattered from the particle, while the energy from the absorbed light is transferred to the hot electron gas that is oscillating in resonance with the light. At moderate intensities, the hot electron gas cools via electron-

phonon coupling (~1-10 ps) and transfers the energy to the positive nuclear lattice. The energy is then transferred to the surrounding medium (~100 ps) as the hot positive lattice cools through phonon-phonon coupling with the environment.<sup>22,26-29</sup> This is important in applications such as nanoparticle photothermal therapy, as only the absorbed light is converted to useful heat. One of the most well known applications of this technique has been the use of gold nanoparticles of various shapes to photo-thermally treat cancer.<sup>30-32</sup> The intense heating is localized to only a very small area around the nanoparticles, thereby only transferring heat to the local environment and allowing for discrete targeting of tumors without damaging the non-targeting healthy tissues.<sup>30-32</sup>

Another application that recently has become very important in science is surface enhanced spectroscopies, such as surface enhanced Raman scattering (SERS).<sup>7,31,33-37</sup> These techniques have become significant because the strong fields that are induced around the nanoparticle upon irradiation at the plasmon frequency can be used to enhance the intensity of the observed spectroscopic response. The main drawback to normal Raman spectroscopy is that very few photons undergo Raman scattering (~1 out of 1,000,000), resulting in very weak Raman signals in unenhanced systems. However, in SERS, the strong plasmonic near-fields at the surface of the nanoparticle amplify both the intensity of the incident light (excitation) as well as the scattered light (signal), resulting in a surface enhanced Raman scattering signal. The intensity of the SERS signal is most influenced by the strength of the near-field at the surface of the nanoparticle. For this reason, efforts to maximize the near-field strength around plasmonic nanoparticles have been a major research focus in the past decade.<sup>38,39</sup> This enhancement can be achieved in

two general ways: (1) by changing the shape of the particle to maximize the electromagnetic field intensity or (2) bringing multiple particles close enough together that their electromagnetic fields couple and produce regions of higher field intensity than the sum of the two independent fields.

The shape of the nanoparticle can be changed in order to focus the electronic cloud into a small spatial region (such as a sharp corner). This is referred to as the “lightning rod effect,”<sup>40,41</sup> which results from the relatively high surface area-to-volume ratios in regions such as corners and points. As shown in Figure 1 - 2 A and B, the maximum field strength for the nanosphere is 50x the incident intensity, whereas the maximum field strength of a nanoprism of comparable size is ~3500x the incident intensity.<sup>3,38</sup>

When the plasmonic near-fields of two particles couple with one another, the strength of the resultant field is greater than the sum of the two individual field strengths. This synergistic effect is mainly attributed to coupling of higher order multipoles (quadrupole, octopole, etc.).<sup>42,43</sup> In Figure 1 - 2 C and D the field between dimers of silver nanospheres and nanoprisms is enhanced far above what is seen for monomers of the same shapes (Figure 1 - 2 A and B). The maximum field strength enhancement between the dimer of spheres is ~11000x the incident intensity (compared to 50x for the single particle), and the maximum field strength enhancement between the dimer of nanoprisms is ~53000x the incident intensity (compared to 3500x).<sup>3,38</sup>

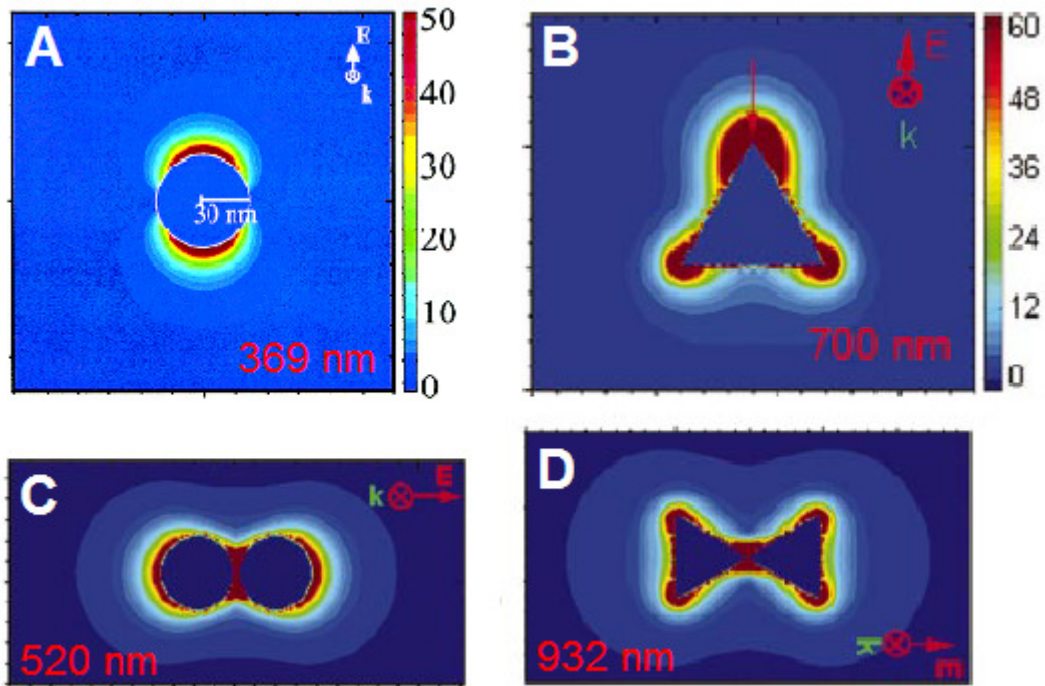


Figure 1 - 2. Electric field contour plots. A) Ag nanosphere of radius 30 nm. Maximum field enhancement is 50x initial intensity. B) Ag nanoprism with edge length of 60 nm. Maximum field enhancement is 3500x initial intensity. C) Dimer of 36 nm Ag nanospheres separated by 2 nm. Maximum enhancement 11,000 x the initial intensity. D) Tip-to-tip dimer of Ag prisms separated by 2 nm. Maximum enhancement is 53,000x initial intensity. The wavelengths in each panel are the resonant wavelengths for that particular system.<sup>3,38</sup>

### 1.3 Near-field Coupling between Plasmonic Nanoparticles

The ability of plasmonic nanomaterials to localize light in a sub-wavelength regime and to transport absorbed energy and information on a sub-wavelength level has recently made them the focus of intense research for their applications as optical waveguides.<sup>11,12,35,44-49</sup> It is important for these applications that fundamental and

systematic studies are performed in order to understand the effect of the external dielectric environment on the field coupling as well as how the plasmonic coupling, and therefore the energy transport, depends on geometric variables, such as particle shape, size, separation and orientation, which is the main focus of this thesis.

It has been demonstrated that as two plasmonic particles are brought together, their near-fields begin to overlap and couple, which affects the plasmon resonance of the overall system.<sup>5,50-52</sup> Additionally, when plasmonic particles are small compared to their interparticle separation, they can be treated as dipolar excitons,<sup>53</sup> a fact that allows for the use of the exciton-coupling model to describe the plasmonic coupling of two interacting particles. If the plasmon dipoles are aligned in an attractive configuration, e.g. head-to-tail in an axial alignment, the aggregate plasmon band is stronger and at a lower energy than that of a single particle. Conversely, if the dipoles are aligned in a repulsive configuration, e.g. head-to-head in an axial alignment, the plasmon band will occur at a higher energy.

Studies involving nanoparticles synthesized via colloidal techniques have provided some initial qualitative data on the nature and strength of near-field coupling between plasmonic nanoparticles.<sup>13,54,55</sup> However, in order to achieve quantitative measurements of the coupling of two plasmonic metal nanoparticles, fabrication techniques that allow for more precise control over the nanoparticles' size, shape and separation are necessary. The recent advances in electron beam lithography (EBL) have provided the technology

that allows for fabrication of nanoparticles of high homogeneity (in size, shape, separation and orientation) and low feature size.

Quantitative studies on the near field dipole plasmon coupling between two spheroidal gold nanoparticles as a function of interparticle separation were independently first reported by Su et al.<sup>51</sup> and Rechberger et al.<sup>5</sup> They concluded that when the LSPR peak shift ( $\Delta\lambda$ ) is scaled by the peak wavelength ( $\lambda$ ) and the interparticle separation ( $s$ ) is scaled by the particle diameter ( $D$ ), all data points fall on a common curve. The common curve is the exponential decay of the coupling, measured by the fractional shift in the plasmon resonance ( $\Delta\lambda/\lambda$ ) as a function of the scaled interparticle separation ( $s/D$ ) (Equation 3).<sup>5,51</sup>

$$\left(\frac{\Delta\lambda}{\lambda}\right) = Ae^{\left[\frac{(-s/D)}{\tau}\right]} \quad \text{Equation 3}$$

It was later shown that while a single exponential of the form shown in Equation 3 very nearly approximates the dependence of the dipole coupling on the scaled interparticle separation, the true dependence goes as  $(s/D)^{-3}$ .<sup>54</sup> The exponential approximation continues to be used, as it will be in this work, because it is suitable for quantifying the relative strength of the dipole field by the magnitude of the pre-exponential factor,  $A$ , and the decay length of the field away from the particle surface by the magnitude of  $\tau$ .

There has been much debate over the nature of Equation 3, and whether there is any universal law for the coupling of particles.<sup>42,56-58</sup> [ENREF 57](#) The general consensus has



become that there is no universal law, and that the final form of Equation 3 depends on all the unique features of a particle (i.e. size, shape, composition, surrounding medium, etc.).<sup>58</sup> [ENREF 58](#) Therefore fundamental investigations are needed for each new shape to discover and define its plasmonic properties, which is the main focus of this thesis.

## 1.4 References

- (1) Bohren, C. F.; Huffman, D. R. *Absorption and Scattering of Light by Small Particles*; Wiley: New York, 1983.
- (2) El-Sayed, M. A. Some interesting properties of metals confined in time and nanometer space of different shapes. *Accounts Chem. Res.* **2001**, *34*, 257-264.
- (3) Kelly, K. L.; Coronado, E.; Zhao, L. L.; Schatz, G. C. The optical properties of metal nanoparticles: The influence of size, shape, and dielectric environment. *J. Phys. Chem. B* **2003**, *107*, 668-677.
- (4) Link, S.; El-Sayed, M. A. Spectral properties and relaxation dynamics of surface plasmon electronic oscillations in gold and silver nanodots and nanorods. *J. Phys. Chem. B* **1999**, *103*, 8410-8426.
- (5) Rechberger, W.; Hohenau, A.; Leitner, A.; Krenn, J. R.; Lamprecht, B.; Aussenegg, F. R. Optical properties of two interacting gold nanoparticles. *Optics Communications* **2003**, *220*, 137-141.
- (6) Rosi, N. L.; Mirkin, C. A. Nanostructures in biodiagnostics. *Chemical Reviews* **2005**, *105*, 1547-1562.
- (7) Willets, K. A.; Van Duyne, R. P. Localized surface plasmon resonance spectroscopy and sensing. *Annual Review of Physical Chemistry* **2007**, *58*, 267-297.
- (8) Zou, S. L.; Schatz, G. C. Silver nanoparticle array structures that produce giant enhancements in electromagnetic fields. *Chemical Physics Letters* **2005**, *403*, 62-67.
- (9) Huang, W. Y.; Qian, W.; El-Sayed, M. A. Gigahertz optical modulation resulting from coherent lattice oscillations induced by femtosecond laser pumping of 2D photonic crystals of gold-capped polystyrene microspheres. *Adv. Mater.* **2008**, *20*, 733-+.
- (10) Lin, A. X.; Boo, S.; Moon, D. S.; Jeong, H. J.; Chung, Y.; Han, W. T. Luminescence enhancement by Au nanoparticles in Er<sup>3+</sup>-doped germano-silicate optical fiber. *Opt. Express* **2007**, *15*, 8603-8608.
- (11) Maier, S. A.; Brongersma, M. L.; Kik, P. G.; Meltzer, S.; Requicha, A. A. G.; Atwater, H. A. Plasmonics - A route to nanoscale optical devices. *Adv. Mater.* **2001**, *13*, 1501-+.

- (12) Maier, S. A.; Kik, P. G.; Atwater, H. A.; Meltzer, S.; Harel, E.; Koel, B. E.; Requicha, A. A. G. Local detection of electromagnetic energy transport below the diffraction limit in metal nanoparticle plasmon waveguides. *Nature Materials* **2003**, *2*, 229-232.
- (13) Jiang, J.; Bosnick, K.; Maillard, M.; Brus, L. Single molecule Raman spectroscopy at the junctions of large Ag nanocrystals. *J. Phys. Chem. B* **2003**, *107*, 9964-9972.
- (14) Nikoobakht, B.; El-Sayed, M. A. Surface-enhanced Raman scattering studies on aggregated gold nanorods. *Journal of Physical Chemistry A* **2003**, *107*, 3372-3378.
- (15) Ritchie, R. H. Plasma losses by fast electrons in thin films. *Physical Review* **1957**, *106*, 874-881.
- (16) Burda, C.; Chen, X. B.; Narayanan, R.; El-Sayed, M. A. Chemistry and properties of nanocrystals of different shapes. *Chemical Reviews* **2005**, *105*, 1025-1102.
- (17) Genet, C.; Ebbesen, T. W. Light in tiny holes. *Nature* **2007**, *445*, 39-46.
- (18) Hao, F.; Sonnefraud, Y.; Van Dorpe, P.; Maier, S. A.; Halas, N. J.; Nordlander, P. Symmetry Breaking in Plasmonic Nanocavities: Subradiant LSPR Sensing and a Tunable Fano Resonance. *Nano Lett.* **2008**, *8*, 3983-3988.
- (19) Landes, C. F.; Braun, M.; El-Sayed, M. A. On the nanoparticle to molecular size transition: Fluorescence quenching studies. *J. Phys. Chem. B* **2001**, *105*, 10554-10558.
- (20) Link, S.; Burda, C.; Wang, Z. L.; El-Sayed, M. A. Electron dynamics in gold and gold-silver alloy nanoparticles: The influence of a nonequilibrium electron distribution and the size dependence of the electron-phonon relaxation. *J. Chem. Phys.* **1999**, *111*, 1255-1264.
- (21) Link, S.; El-Sayed, M. A. Shape and size dependence of radiative, non-radiative and photothermal properties of gold nanocrystals. *Int. Rev. Phys. Chem.* **2000**, *19*, 409-453.
- (22) Link, S.; Hathcock, D. J.; Nikoobakht, B.; El-Sayed, M. A. Medium effect on the electron cooling dynamics in gold nanorods and truncated tetrahedra. *Adv. Mater.* **2003**, *15*, 393-+.
- (23) Yoo, S. I.; Lee, J. H.; Sohn, B. H.; Eom, I.; Joo, T.; An, S. J.; Yi, G. C. Enhancement and Concurrence of Emissions from Multiple Fluorophores in a Single Emitting Layer of Micellar Nanostructures. *Advanced Functional Materials* **2008**, *18*, 2984-2989.

- (24) Jain, P. K.; Huang, X.; El-Sayed, I. H.; El-Sayed, M. A. Review of some interesting surface plasmon resonance-enhanced properties of noble metal nanoparticles and their applications to biosystems. *Plasmonics* **2007**, *2*, 107-118.
- (25) Lee, K. S.; El-Sayed, M. A. Dependence of the enhanced optical scattering efficiency relative to that of absorption for gold metal nanorods on aspect ratio, size, end-cap shape, and medium refractive index. *J. Phys. Chem. B* **2005**, *109*, 20331-20338.
- (26) Bauer, C.; Abid, J. P.; Fermin, D.; Girault, H. H. Ultrafast chemical interface scattering as an additional decay channel for nascent nonthermal electrons in small metal nanoparticles. *J. Chem. Phys.* **2004**, *120*, 9302-9315.
- (27) Bauer, C.; Abid, J. P.; Girault, H. H. Size dependence investigations of hot electron cooling dynamics in metal/adsorbates nanoparticles. *Chemical Physics* **2005**, *319*, 409-421.
- (28) Link, S.; Burda, C.; Nikoobakht, B.; El-Sayed, M. A. How long does it take to melt a gold nanorod? A femtosecond pump-probe absorption spectroscopic study. *Chemical Physics Letters* **1999**, *315*, 12-18.
- (29) Link, S.; Furube, A.; Mohamed, M. B.; Asahi, T.; Masuhara, H.; El-Sayed, M. A. Hot electron relaxation dynamics of gold nanoparticles embedded in MgSO<sub>4</sub> powder compared to solution: The effect of the surrounding medium. *J. Phys. Chem. B* **2002**, *106*, 945-955.
- (30) Huang, X. H.; El-Sayed, I. H.; Qian, W.; El-Sayed, M. A. Cancer cell imaging and photothermal therapy in the near-infrared region by using gold nanorods. *J. Am. Chem. Soc.* **2006**, *128*, 2115-2120.
- (31) Huang, X. H.; El-Sayed, I. H.; Qian, W.; El-Sayed, M. A. Cancer cells assemble and align gold nanorods conjugated to antibodies to produce highly enhanced, sharp, and polarized surface Raman spectra: A potential cancer diagnostic marker. *Nano Lett.* **2007**, *7*, 1591-1597.
- (32) Huang, X. H.; Jain, P. K.; El-Sayed, I. H.; El-Sayed, M. A. Gold nanoparticles: interesting optical properties and recent applications in cancer diagnostic and therapy. *Nanomedicine* **2007**, *2*, 681-693.
- (33) Braun, G.; Lee, S. J.; Dante, M.; Nguyen, T. Q.; Moskovits, M.; Reich, N. Surface-enhanced Raman spectroscopy for DNA detection by nanoparticle assembly onto smooth metal films. *J. Am. Chem. Soc.* **2007**, *129*, 6378-+.
- (34) Jackel, F.; Kinkhabwala, A. A.; Moerner, W. E. Gold bowtie nanoantennas for surface-enhanced Raman scattering under controlled electrochemical potential. *Chemical Physics Letters* **2007**, *446*, 339-343.

- (35) Le, F.; Brandl, D. W.; Urzhumov, Y. A.; Wang, H.; Kundu, J.; Halas, N. J.; Aizpurua, J.; Nordlander, P. Metallic nanoparticle arrays: A common substrate for both surface-enhanced Raman scattering and surface-enhanced infrared absorption. *Acs Nano* **2008**, *2*, 707-718.
- (36) Nie, S. M.; Emery, S. R. Probing single molecules and single nanoparticles by surface-enhanced Raman scattering. *Science* **1997**, *275*, 1102-1106.
- (37) Su, K.-H.; Wei, Q.-H.; Zhang, X.; Mock, J. J.; Smith, D. R.; Schultz, S. Optical properties of coupled nano gold particles. *Proceedings of SPIE - The International Society for Optical Engineering* **2003**, *5221*, 108-115.
- (38) Hao, E.; Schatz, G. C. Electromagnetic fields around silver nanoparticles and dimers. *The Journal of Chemical Physics* **2004**, *120*, 357-366.
- (39) Kelly, K. L.; Lazarides, A. A.; Schatz, G. C. Computational electromagnetics of metal nanoparticles and their aggregates. *Comput. Sci. Eng.* **2001**, *3*, 67-73.
- (40) Gersten, J.; Nitzan, A. Electromagnetic theory of enhanced Raman-scattering by molecules adsorbed on rough surfaces. *J. Chem. Phys.* **1980**, *73*, 3023-3037.
- (41) Gersten, J. I. The effect of surface-roughness on surface enhanced Raman-scattering. *J. Chem. Phys.* **1980**, *72*, 5779-5780.
- (42) Gunnarsson, L.; Rindzevicius, T.; Prikulis, J.; Kasemo, B.; Kall, M.; Zou, S. L.; Schatz, G. C. Confined plasmons in nanofabricated single silver particle pairs: Experimental observations of strong interparticle interactions. *J. Phys. Chem. B* **2005**, *109*, 1079-1087.
- (43) Shuford, K. L.; Ratner, M. A.; Schatz, G. C. Multipolar excitation in triangular nanoprisms. *J. Chem. Phys.* **2005**, *123*.
- (44) Dionne, J. A.; Sweatlock, L. A.; Atwater, H. A.; Polman, A. Plasmon slot waveguides: Towards chip-scale propagation with subwavelength-scale localization. *Physical Review B* **2006**, *73*.
- (45) Dionne, J. A.; Verhagen, E.; Polman, A.; Atwater, H. A. Are negative index materials achievable with surface plasmon waveguides? A case study of three plasmonic geometries. *Opt. Express* **2008**, *16*, 19001-19017.
- (46) Oulton, R. F.; Sorger, V. J.; Genov, D. A.; Pile, D. F. P.; Zhang, X. A hybrid plasmonic waveguide for subwavelength confinement and long-range propagation. *Nature Photonics* **2008**, *2*, 496-500.

- (47) Quinten, M.; Leitner, A.; Krenn, J. R.; Aussenegg, F. R. Electromagnetic energy transport via linear chains of silver nanoparticles. *Optics Letters* **1998**, *23*, 1331-1333.
- (48) Rusina, A.; Durach, M.; Nelson, K. A.; Stockman, M. I. Nanoconcentration of terahertz radiation in plasmonic waveguides. *Opt. Express* **2008**, *16*, 18576-18589.
- (49) Zou, S. L.; Schatz, G. C. Metal nanoparticle array waveguides: Proposed structures for subwavelength devices. *Physical Review B* **2006**, *74*.
- (50) Maier, S. A.; Brongersma, M. L.; Kik, P. G.; Atwater, H. A. Observation of near-field coupling in metal nanoparticle chains using far-field polarization spectroscopy. *Physical Review B* **2002**, *65*.
- (51) Su, K. H.; Wei, Q. H.; Zhang, X.; Mock, J. J.; Smith, D. R.; Schultz, S. Interparticle coupling effects on plasmon resonances of nanogold particles. *Nano Lett.* **2003**, *3*, 1087-1090.
- (52) Sweatlock, L. A.; Maier, S. A.; Atwater, H. A.; Penninkhof, J. J.; Polman, A. Highly confined electromagnetic fields in arrays of strongly coupled Ag nanoparticles. *Physical Review B* **2005**, *71*.
- (53) Jain, P. K.; El-Sayed, M. A. Plasmonic coupling in noble metal nanostructures. *Chemical Physics Letters* **2010**, *487*, 153-164.
- (54) Jain, P. K.; Eustis, S.; El-Sayed, M. A. Plasmon coupling in nanorod assemblies: Optical absorption, discrete dipole approximation simulation, and exciton-coupling model. *J. Phys. Chem. B* **2006**, *110*, 18243-18253.
- (55) Reinhard, B. M.; Siu, M.; Agarwal, H.; Alivisatos, A. P.; Liphardt, J. Calibration of dynamic molecular ruler based on plasmon coupling between gold nanoparticles. *Nano Lett.* **2005**, *5*, 2246-2252.
- (56) Jain, P. K.; Huang, W. Y.; El-Sayed, M. A. On the universal scaling behavior of the distance decay of plasmon coupling in metal nanoparticle pairs: A plasmon ruler equation. *Nano Lett.* **2007**, *7*, 2080-2088.
- (57) Jain, P. K.; El-Sayed, M. A. Surface plasmon coupling and its universal size scaling in metal nanostructures of complex geometry: Elongated particle pairs and nanosphere trimers. *Journal of Physical Chemistry C* **2008**, *112*, 4954-4960.
- (58) Tabor, C.; Murali, R.; Mahmoud, M.; El-Sayed, M. A. On the Use of Plasmonic Nanoparticle Pairs As a Plasmon Ruler: The Dependence of the Near-Field Dipole Plasmon Coupling on Nanoparticle Size and Shape. *Journal of Physical Chemistry A* **2009**, *113*, 1946-1953.

## CHAPTER II

### FABRICATION AND INSTRUMENTATION

#### **2.1 Electron Beam Lithography Fabrication**

As mentioned in Chapter I, the localized surface plasmon resonance (LSPR) is very sensitive to the size, shape, and composition of a nanoparticle in addition to the interparticle separation if particles are within coupling range. Therefore, precise control over these factors is needed in the fabrication method for fundamental studies aimed at investigating how nanoparticle geometry and interparticle separation affect the plasmonic properties of noble metal nanoparticle arrays. Although colloidal synthesis techniques offer the advantages of high throughput and flexibility in three-dimensional shape and metal composition, electron beam lithography (EBL) offers the advantages of near-exact control over particle geometry and interparticle separation, particularly for interparticle separations ranging from 10-100 nm,

The EBL instrument is located in the microelectronic facility at the Georgia Institute of Technology. The instrument is a JEOL JBX-9300FS and has a minimum beam size of 4nm with a 50-100 kV acceleration and 50 pA-2 nA current range. For all experiments done here, the acceleration was 100 kV and the current used was 2 nA.

Unless otherwise noted, the substrates used were  $\text{Si}_3\text{N}_4/\text{Si}$  membrane wafers pre-fabricated by graduate students in Dr. Tolbert's laboratory. A layer of silicon nitride

(Si<sub>3</sub>N<sub>4</sub>) was deposited onto a prime grade double-side polished silicon wafer, followed by selective etching of the Si wafer to produce an array of freely supported silicon nitride membrane windows that were ~250 x 250 μm<sup>2</sup>. Each window was used for a single design pattern (this is discussed more fully later in this section).

These membrane samples, compared to traditional silicon wafers, minimize overexposure of the electron-sensitive polymer resist due to proximity effects in EBL. The substrate is coated with a polymer resist prior to exposure to the electron beam used to write the desired pattern (these steps are discussed further in the next paragraph). As the electrons in the beam pass through the polymer resist and enter the substrate, a portion of the electrons will undergo large angle scattering events. These electrons may return back into the resist at a significant distance from the incident beam causing additional, unwanted, resist exposure. This additional exposure from the backscattered electrons can detrimentally affect the resolution of the exposed pattern. Use of the thin (< 200 nm) Si<sub>3</sub>N<sub>4</sub> membranes as substrates for EBL significantly decreases the overexposure of the PMMA resist due to the proximity effect (Figure 2 - 1).



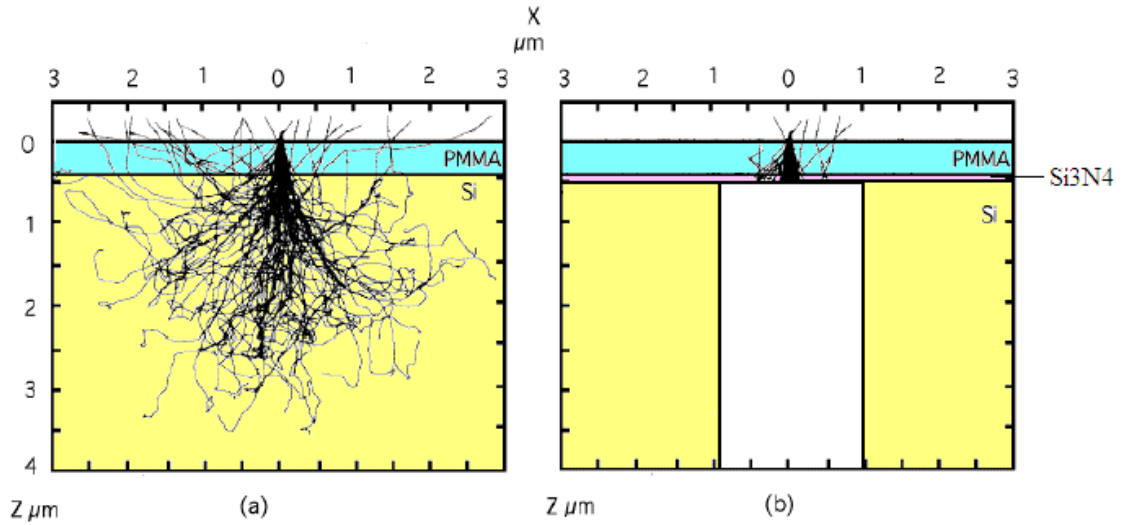


Figure 2 - 1. Diagram of proximity effect adapted from SPIE Handbook of Microlithography.<sup>1</sup> a) Monte Carlo simulation of the back and forward scattering caused by the substrate-electron interactions as the electron beam exposes a thin PMMA resist layer (shown in blue) that is supported on a silicon wafer (shown in yellow) with an acceleration voltage of 20kV. b) The same simulation as in (a) with the assumption that the substrate is only 50 nm thick at the spot of exposure (shown in pink), as is the case with the  $\text{Si}_3\text{N}_4$  substrates used in this work.

A schematic of the general EBL fabrication process is shown in Figure 2 - 2. The  $\text{Si}_3\text{N}_4/\text{Si}$  substrate was first cleaned with acetone for several minutes to remove any organic residues. then dried with  $\text{N}_2$  gas. Prior to spin-coating the substrate, a piece of single side tape was applied to the bottom surface of the substrate to protect the  $\text{Si}_3\text{N}_4$  windows from being shattered by the vacuum applied to the substrate during the spinning process. The substrate was then placed in the spin-coater and a thin layer of PMMA (several drops of a 2% solution of PMMA dissolved in anisole) was cast onto the surface using spin conditions of 4000 RPM and a rate of 500 R/s for 60 seconds. The tape was removed from the backside of the substrate, and the substrate was baked on a hot plate

for 2 minutes at 180°C to anneal the polymer. This procedure yielded a PMMA layer of approximately  $80 \pm 5$  nm as determined by contact profilometry.

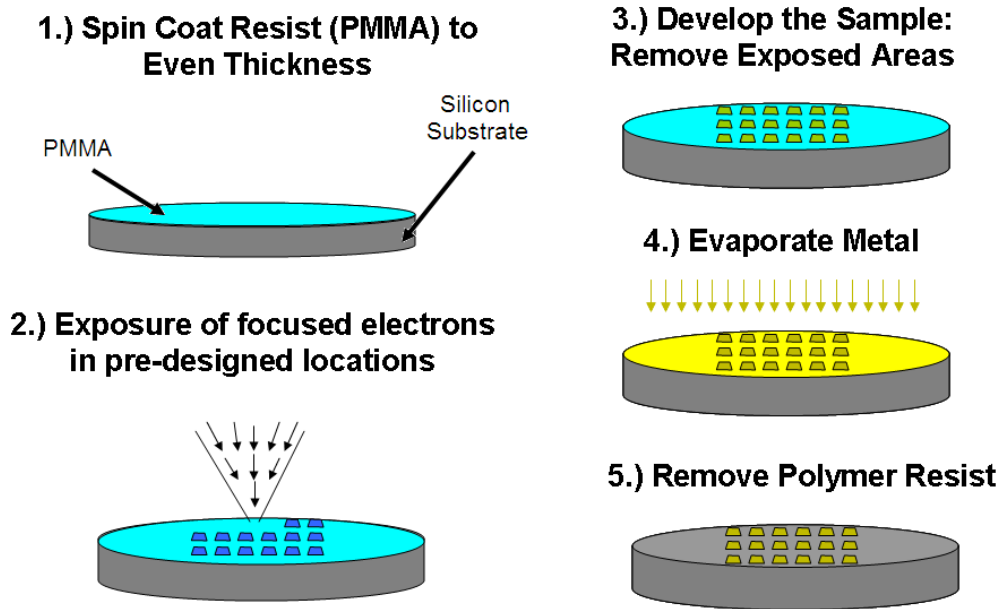


Figure 2 - 2. General electron beam lithography fabrication process. 1) Spin-coating of a thin layer ( $\sim 100$ nm) of an electron sensitive resist (PMMA) onto a conductive substrate (typically silicon). 2) Exposure of the PMMA resist with a focused beam of electrons. 3) Development of the sample (removal of exposed areas of PMMA). 4) Evaporation of metal onto the substrate and into the exposed areas of the PMMA resist. 5) Removal of all polymer resist leaving only the fabricated structures.

The polymer-coated  $\text{Si}_3\text{N}_4/\text{Si}$  substrate was then loaded into the EBL instrument. In addition to the standard EBL function, the JEOL JBX-9300FS is equipped with a scanning electron microscope (SEM), which was used to align the  $\text{Si}_3\text{N}_4$  membranes to

overlap the pattern, written in AutoCAD. Over-exposure of the polymer resist to the electrons used in the SEM imaging resulted in the sacrifice of several of the windows (at least 2 windows per sample).

The dose used for the exposures varied depending on the size and shape of the features being written, and is specified for each pattern in the appropriate chapter. Following the exposure, the sample was developed in a solution of isopropyl alcohol and methyl isobutyl ketone (3:1, IPA:MIBK) for 10 seconds, rinsed in an IPA bath for at least 60 seconds, and gently blown dry with a stream of N<sub>2</sub>. The developed EBL sample was then inserted into an electron beam deposition chamber. A thin adhesion layer of Cr (0.5 nm) was deposited on the sample at a rate of 0.1 Å/s followed by a layer of gold (18-22 nm) at a rate of 0.5 Å/s. After deposition of the metals, the remaining PMMA was removed with 1-methyl-2-pyrrolidinone, leaving only the gold nanostructures.

A schematic of the substrate and nanoparticle arrays are shown in Figure 2 - 3. The arrays were designed so that the nanoparticle dimer pairs were spaced more than 800 nm from one another to minimize far-field coupling between separate particle pairs. Within each window there are several thousand dimers, all with the same interparticle separation. This interparticle separation is varied from window to window. In these experimental samples with small interparticle gaps, the near-field coupling can be expected to be so significantly stronger than any far-field grating effects that the latter of the two can be ignored.

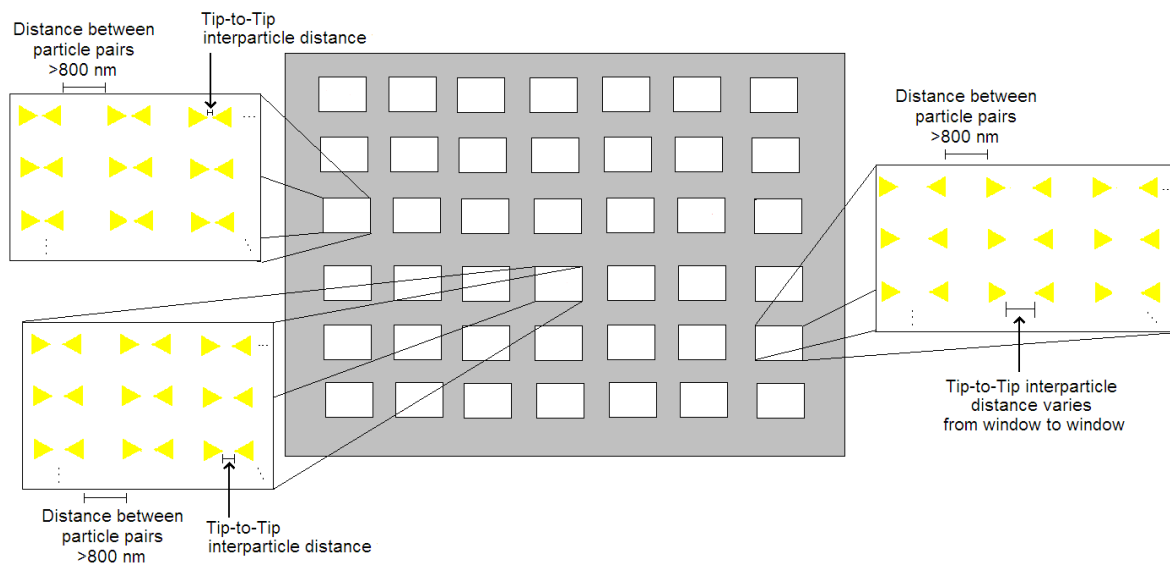


Figure 2 - 3. Schematic of the Si<sub>3</sub>N<sub>4</sub>/Si substrates used in the EBL fabrication. The Si<sub>3</sub>N<sub>4</sub> windows are shown as white rectangles and the surrounding Si substrate is shown in grey.

## 2.2 Electron and Surface Probe Microscopes: SEM

The samples fabricated via EBL were imaged using a scanning SEM (Zeiss Ultra 60 FE-SEM). All images were taken using a secondary electron detector and an accelerating voltage from 1-10 kV.

## 2.3 Spectroscopic Measurements

Extinction measurements were performed on a Craic Microspectra 121 UV-visible-NIR microspectrophotometer with an imaging range from 400-1700 nm at normal incidence in transmission mode under several polarization conditions (parallel and perpendicular to the interparticle axis and unpolarized). The aperture size selected for the measurements was  $625 \mu\text{m}^2$  with a 36X objective lens, and each reported spectrum is an average of at least 5 separate spectra taken across the sample.

## 2.4 Theoretical Modeling: Discrete Dipole Approximation

The discrete dipole approximation (DDA) is a popular theoretical method used to model the optical properties of systems. DDA is robust and flexible allowing one to model particles of arbitrary shape either as single particles or as groups of particles with assigned spatial positions and relative orientations.<sup>2-7</sup>

In DDA, the target particle is approximated as a three-dimensional finite lattice of point dipoles that is excited by an external field. The response of the dipoles to the external field and to one another is solved self-consistently using Maxwell's equations. Precise and accurate definition of the lattice used to represent the particle is crucial to achieve the best match with experimental conditions and results.<sup>4,8</sup>

Most of the work done so far has involved modeling the optical properties of solid nanoparticles of different shapes, with little emphasis on hollow structures.<sup>3,7,9,10</sup>

Preliminary work on the importance of realistic shape models in theoretical simulations has shown that DDA calculations can be improved by clipping sharp corners to give a more realistic representation of particle geometry,<sup>4</sup> there has been little focus on improving the representation of particle shape in DDA calculations. Improvement of shape modeling in DDA is therefore a topic that will become a main thrust of this thesis in the following chapters.

To carry out DDA calculations, the user defines: the arrangement of the point dipoles (i.e. the shape of the object), the polarizability of the dipoles (i.e. the material being represented), the energy range of the incident radiation (i.e. the wavelength range of the light) and the polarization of the incident radiation. The DDSCAT 6.1 code offered publicly by Draine and Flatau<sup>11</sup> allows for calculation of the absorption and scattering spectra separately, allowing for assessment of the contributions from each to the extinction spectra, which is the sum of these two components. Furthermore, using modifications to the code by Goodman<sup>12</sup> and Schatz,<sup>13</sup> it is possible to calculate the electric field enhancement contours and the individual dipole orientations at a specific wavelength. These plots can only be generated for one two-dimensional slice through the particle at a time, but the slice position can be chosen. These plots can be used to assign the different plasmon modes based on the shape of the fields around the particle as well as the orientation of the individual dipoles within the particle. However, most previous work has based these plasmon mode assignments on a single two-dimensional slice

through the particle. This does not give an accurate representation of the three-dimensional nature of the plasmon modes. Accordingly, one of the major topics of this thesis was the development of a technique to gain a better three-dimensional representation of the field by repeating the calculations for multiple two-dimensional slices through the particle and creating a composite three-dimensional plot.

## 2.5 References

- (1) *SPIE Handbook of Microlithography, Micromachining and Microfabrication*, [http://www.cnf.cornell.edu/cnf\\_spie3.html](http://www.cnf.cornell.edu/cnf_spie3.html).
- (2) Halas, N. J. Playing with plasmons. Tuning the optical resonant properties of metallic nanoshells. *MRS Bull.* **2005**, *30*, 362-367.
- (3) Jain, P. K.; Lee, K. S.; El-Sayed, I. H.; El-Sayed, M. A. Calculated absorption and scattering properties of gold nanoparticles of different size, shape, and composition: Applications in biological imaging and biomedicine. *J. Phys. Chem. B* **2006**, *110*, 7238-7248.
- (4) Kelly, K. L.; Coronado, E.; Zhao, L. L.; Schatz, G. C. The optical properties of metal nanoparticles: The influence of size, shape, and dielectric environment. *J. Phys. Chem. B* **2003**, *107*, 668-677.
- (5) Olson, T. Y.; Schwartzberg, A. M.; Orme, C. A.; Talley, C. E.; O'Connell, B.; Zhang, J. Z. Hollow gold-silver double-shell nanospheres: Structure, optical absorption, and surface-enhanced Raman scattering. *Journal of Physical Chemistry C* **2008**, *112*, 6319-6329.
- (6) Sun, Y. G.; Mayers, B.; Xia, Y. N. Metal nanostructures with hollow interiors. *Advanced Materials* **2003**, *15*, 641-646.
- (7) Wan, D. H.; Chen, H. L.; Lin, Y. S.; Chuang, S. Y.; Shieh, J.; Chen, S. H. Using Spectroscopic Ellipsometry to Characterize and Apply the Optical Constants of Hollow Gold Nanoparticles. *Acs Nano* **2009**, *3*, 960-970.
- (8) Near, R.; Tabor, C.; Duan, J. S.; Pachter, R.; El-Sayed, M. Pronounced Effects of Anisotropy on Plasmonic Properties of Nanorings Fabricated by Electron Beam Lithography. *Nano Lett.* **2012**, *12*, 2158-2164.
- (9) Jain, P. K.; Eustis, S.; El-Sayed, M. A. Plasmon coupling in nanorod assemblies: Optical absorption, discrete dipole approximation simulation, and exciton-coupling model. *J. Phys. Chem. B* **2006**, *110*, 18243-18253.
- (10) Tabor, C.; Murali, R.; Mahmoud, M.; El-Sayed, M. A. On the Use of Plasmonic Nanoparticle Pairs As a Plasmon Ruler: The Dependence of the Near-Field Dipole Plasmon Coupling on Nanoparticle Size and Shape. *Journal of Physical Chemistry A* **2009**, *113*, 1946-1953.
- (11) Draine, B. T.; Flatau, P. J. Discrete-Dipole Approximation for scattering calculations. *J. Opt. Soc. Am. A-Opt. Image Sci. Vis.* **1994**, *11*, 1491-1499.



- (12) Goodman, J. J.; Draine, B. T.; Flatau, P. J. Application of Fast-Fourier-Transform techniques to the Discrete-Dipole Approximation. *Optics Letters* **1991**, *16*, 1198-1200.
- (13) Shuford, K. L.; Ratner, M. A.; Schatz, G. C. Multipolar excitation in triangular nanoprisms. *J. Chem. Phys.* **2005**, *123*.

## CHAPTER III

### THIN TO THICK, SHORT TO LONG: ENERGETIC PROPERTIES OF GOLD NANORODS BY THEORETICAL MODELING

#### **3.1 Summary**

Recent advances in gold nanorod colloidal synthesis demand a theoretical model capable of predicting the energetic characteristics of gold nanorods with dimensions outside the realm of consideration of previous models. We employ the discrete dipole approximation to calculate the spectra and extinction intensities of a series of gold nanorods in water, with sizes ranging from 3 x 6 nm to 15 x 90 nm. We then present models to relate the plasmon resonant wavelength and extinction intensity to the nanoparticle aspect ratio and volume, respectively. These relationships will allow for facile determination of the dimensions necessary to generate the desired energetic characteristics for applications of gold nanorods in medicine and energy.

#### **3.2 Introduction**

Gold nanoparticles have wide applicability in medicine<sup>1-4</sup> and energy<sup>5-7</sup> due to the unique, tunable energetic properties that result from their localized surface plasmon resonance (LSPR).<sup>8-11</sup> The energy of the LSPR is a function of the nanoparticle geometry and

composition as well as the dielectric of the surrounding medium.<sup>9,11-14</sup> For example, rod-shaped gold nanoparticles of the proper dimensions have a strong plasmon resonance in the red wavelength region, coincident with the therapeutic window, where human tissue permittivity to light is relatively high. Thus, gold nanorods (AuNR) are often used as photothermal contrast agents for cancer therapy.<sup>2,4</sup> In therapy, the size of the AuNR is of defining importance, as size determines both (1) biocompatibility (*e.g.* circulation half-life, renal clearance, *etc.*), and (2) bioactivity (*i.e.* energetic characteristics and resultant therapeutic efficacy).

Typical colloidal synthetic techniques produce gold nanorods with adjustable lengths but widths confined to around 10 nm. Previous endeavors to model the relationship between nanorod dimensions and plasmon resonant wavelength have therefore focused on nanorods of ca. 10 nm diameter.<sup>11,15,16</sup> These efforts have used Gans and Mie equations in conjunction with experimental data and have shown a dependence of the plasmon peak position on the aspect ratio (AR),<sup>11</sup> defined as length divided by width. Recent advancement in colloidal synthetic techniques has yielded syntheses for AuNR of smaller diameters,<sup>17</sup> which are predicted to present numerous applicative boons in areas such as cancer therapeutics, where smaller nanorods would provide improved renal clearance and resultant decreased toxicity from accumulation in the tumor, spleen, *etc.*<sup>2,4</sup> These nanorods fall outside the size range encompassed by existing models for prediction of nanorod energetic characteristics and therefore call for a theoretical model that encompasses a larger size range.

### 3.3 Methods

The optical response of gold nanorods (diameters: 3, 5, 7, 10, 15 nm) with varying aspect ratio (AR: 2-6) was calculated using the discrete dipole approximation (DDA) method with the DDSCAT 6.1 code offered publicly by Draine and Flatau.<sup>18</sup> The dielectric values for gold reported by Johnson and Christy<sup>19</sup> were used. The incident light is always polarized along the length of the AuNR in this report, and the medium surrounding the particle was represented as water (refractive index,  $n = 1.333$ ).

### 3.4 Results and Discussion

We employ the discrete dipole approximation (DDA) method to theoretically model AuNR of 5 diameters and 6 aspect ratios (30 AuNR total). DDA has proven exceptionally accurate and flexible in modeling the energetic properties of nanoparticles of arbitrary shape through representation of the nanoparticle as a three-dimensional finite lattice of point dipoles.<sup>12,20,21</sup> This collection of dipoles is then excited by an external field, and Maxwell's equations are solved self-consistently to gauge the response of the dipoles both to the external field and to one another. The flexibility afforded by DDA has allowed us to model more exact replicas of the shape that these rods take experimentally in colloidal suspensions - cylinders with hemispherical end caps - whereas many other methods approximate the AuNR as an ellipsoidal structure. This direct, reliable theoretical technique allows us to avoid the use of multiple conjoined approximations,<sup>11,22</sup>

to choose an experimentally relevant solvent (water), and to avoid the error inherent in models based off of experimental colloidal suspensions of nanoparticles, which are known to exhibit high degrees of heterodispersity.<sup>15</sup>

The plasmon resonance of a gold nanorod displays two distinct bands, corresponding to the oscillation of free electrons along the transverse and longitudinal axes of the rod, respectively. The transverse oscillation is relatively weak in intensity, whereas the longitudinal oscillation not only generates an intense extinction band but also displays a high degree of sensitivity to the nanorod dimensions. This sensitivity allows for tunability of the resonant wavelength throughout the visible and NIR regions of the spectrum and therefore defines the utility of gold nanorods in applications. Consequently, we will focus our discussion herein on only the longitudinal plasmon resonance and its extinction wavelength ( $\lambda_2$ ) and intensity.

DDA calculations were carried out individually for AuNRs with diameters of 3, 5, 7, 10 and 15 nm and several aspect ratios (AR) for each diameter (AR = 2, 3, 4, 5, and 6). The DDA extinction spectrum for  $\lambda_2$  of each AuNR is shown in Figure 3 - 1A and Figure 3 - 1B, where they are colored by diameter and AR, respectively, to emphasize different trends that will be discussed forthwith.

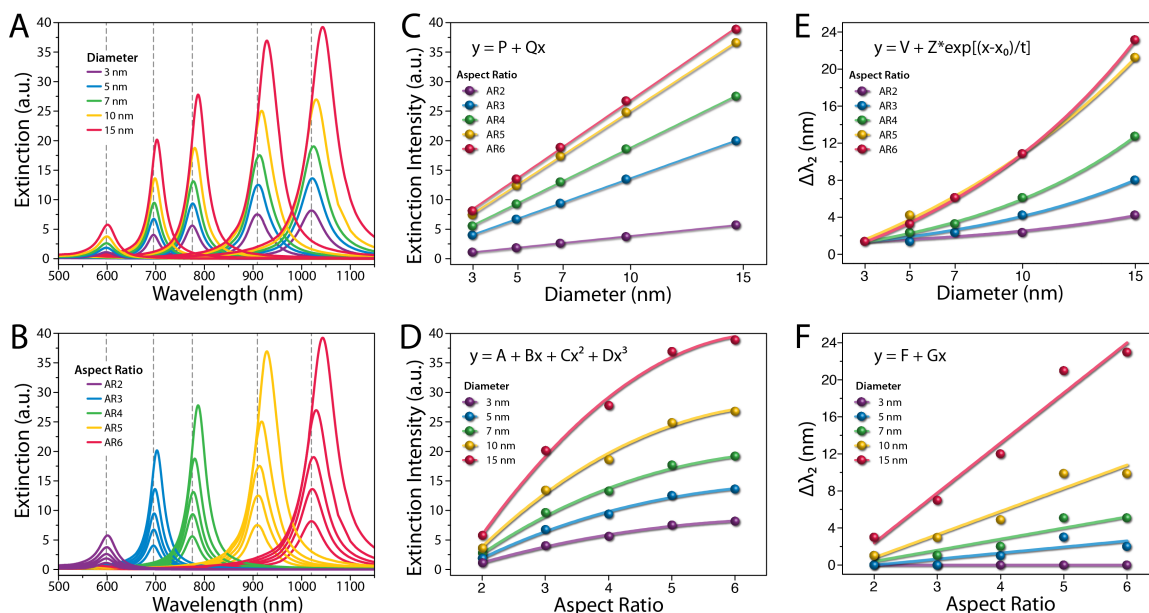












Figure 3 - 1. DDA extinction spectra for AuNRs in water of varying diameter and AR grouped by (A) diameter and (B) AR, as indicated by color. Extinction intensity trends (C) cubically by diameter and (D) linearly by AR, emphasizing the role of cubic volume. The change in the longitudinal plasmon wavelength is (E) linear by diameter, indicating a dependence on anisotropy, and (F) exponential by AR from electromagnetic retardation effects in large nanoparticles.

Table 3-1. Constants corresponding to the fits provided in Figure 3 - 1.

	 3 nm	 5 nm	 7 nm	 10 nm	 15 nm		 AR2	 AR3	 AR4	 AR5	 AR6
<b>A</b>	-6.37	-11.0	-15.3	-21.6	-29.8	<b>P</b>	-0.07	0.04	0.13	0.27	0.69
<b>B</b>	4.54	7.87	11.0	15.5	21.0	<b>Q</b>	0.39	1.35	1.85	2.46	2.59
<b>C</b>	-0.40	-0.75	-1.02	-1.39	-1.54	<b>V</b>	-0.94	-2.76	-3.71	-14.0	-10.1
<b>D</b>	0.01	0.02	0.03	0.03	-0.01	<b>Z</b>	0.36	0.62	1.05	4.41	2.85
<b>F</b>	0	-1.6	-2.0	-4.2	-8.4	<b>x<sub>0</sub></b>	5.01	-8.98	-7.25	-12.6	-9.72
<b>G</b>	0	0.7	1.2	2.5	5.4	<b>t</b>	8.39	8.70	8.23	13.3	10.1

### 3.4.1 Intensity of the longitudinal plasmon band

When we consider nanorods grouped by diameter (rods getting longer, not wider), we observe a large, cubic shift in intensity with increasing length (Figure 3 - 1C). When group by aspect ratio (rods becoming both longer and wider with the same L/W ratio), the trend in intensity remains large but becomes linear (Figure 3 - 1D). These observations are consistent with previous studies,<sup>11</sup> and they emphasize that extinction intensity is most directly related to nanoparticle volume. This relationship is a consequence of the increasing number of conduction band electrons involved in the plasmon resonance in increasingly voluminous particles. Over this size range, more electrons involved in the plasmon means a stronger electromagnetic field, which causes the nanorod to both absorb and scatter more photons.

### 3.4.2 Energy of the longitudinal plasmon resonance

When grouped by diameter, we observe a large, linear change in  $\lambda_2$  (Figure 3 - 1E). Thus, as previously demonstrated by our group and others,<sup>11,15,16,22,23</sup>  $\lambda_2$  is largely a function of the degree of nanorod anisotropy, with the length-to-width ratio, or aspect ratio (AR), determining the energy of the resonance. Thus, a longer, thinner nanorod will display a red-shifted  $\lambda_2$  relative to a shorter, thicker nanorod. This observation is consistent with the spectroscopic exciton coupling model,<sup>24</sup> which has been previously applied to gold nanorods.<sup>25</sup>

When grouped by AR,  $\lambda_2$  is expected to become constant, per previous predictions over more limited size regimes. In general, we do see a linear relationship between  $\lambda_2$

(Figure 3 - 2A), however, we observe a small but significant exponential shift in  $\lambda_2$  despite the constant L/W ratio (Figure 3 - 1F). This shift is likely the result of electromagnetic retardation effects, which result from the depolarization of the light field across the particle surface. Retardation becomes more pronounced in larger nanoparticles and results in both a red-shift and broadening of the plasmon resonance band.<sup>11</sup>

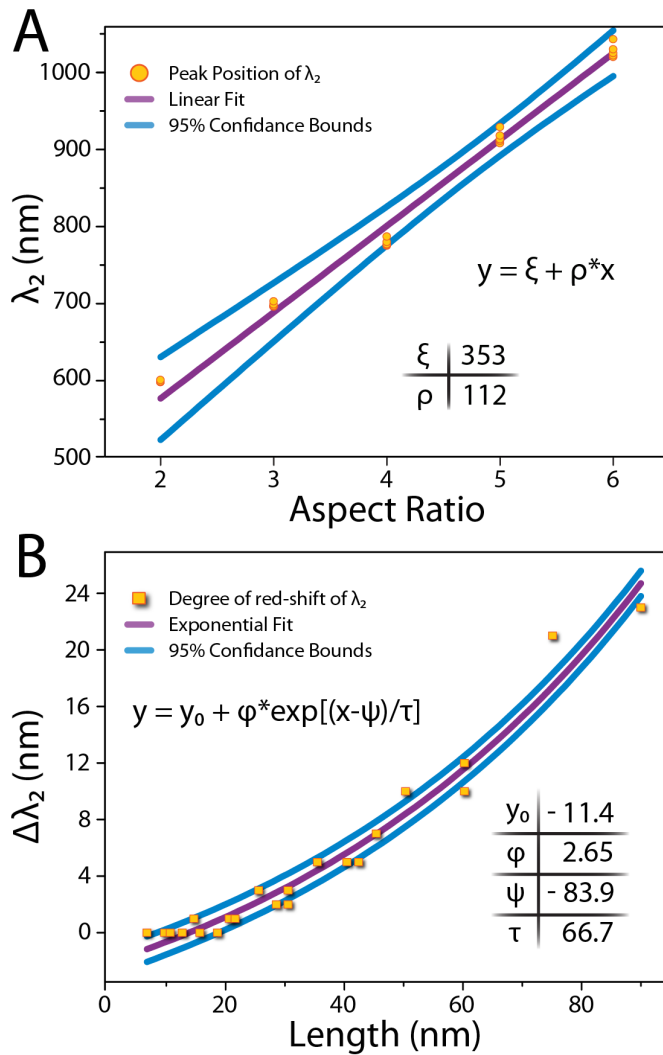


Figure 3 - 2. (A) The position of the longitudinal plasmon wavelength is linear by AR, indicating a dependence on anisotropy. (B) The change in the longitudinal wavelength is exponential by length from electromagnetic retardation effects in large nanoparticles.



We plotted the shift in  $\lambda_2$  against nanorod length and found good agreement along the same exponential relation for all the AuNRs considered here (Figure 3 - 2B). We then combined the linear relation between  $\lambda_2$  and AR with the exponential relation that accounts for retardation effects to produce Equation 1,

$$\lambda_2 = \alpha + \beta \times \frac{L}{W} + \gamma \times e^{\left[ \frac{(L+\delta)}{\kappa} \right]} \quad (1)$$

where  $\alpha = 342 \pm 28$ ,  $\beta = 112 \pm 5.57$ ,  $\gamma = 2.65$ ,  $\delta = 84$ , and  $\kappa = 67 \pm 0.8$ , and L and W are the nanorod length and width, respectively.

Equation 1 allows for the calculation of either (1) the necessary dimensions to produce the desired nanorod energetic characteristics or (2) what energetic characteristics can be expected from a given set of dimensions. This relationship should be exceedingly useful for applications, as it will allow for more targeted synthetic approaches. Conversely, if a sample of AuNRs of unknown dimensions has been synthesized using a method known to produce a certain diameter nanorod, the equation should allow for prediction of the average length of the sample.

### 3.5 Conclusions

We have used DDA theoretical methods to calculate the extinction spectra for AuNRs of varying diameter and aspect ratio. We have found that there is a modified linear relationship between the LSPR peak position of the longitudinal plasmon mode and the aspect ratio of the AuNR. Furthermore, we have found that within an aspect ratio, there

is a linear relationship between the AuNR diameter and peak intensity. A consequence is that  $\lambda_2$  can be maintained for rods of increasing length by concurrently increasing the diameter, according to the relationship presented in Equation 1. Such a relationship allows for target energetic characteristics to be achieved for a particular application and the nanoparticle dimensions altered to achieve the desired secondary effects. An example of this in photothermal therapy includes the ability to choose the plasmon resonant energy at the desired wavelength, calculate the aspect ratios that produce that specific plasmon resonance, and subsequently choose a nanoparticle size that provides good renal clearance.

### 3.6 References

- (1) Boisselier, E.; Astruc, D. Gold nanoparticles in nanomedicine: preparations, imaging, diagnostics, therapies and toxicity. *Chemical Society Reviews* **2009**, *38*, 1759-1782.
- (2) Dreaden, E. C.; Mackey, M. A.; Huang, X. H.; Kang, B.; El-Sayed, M. A. Beating cancer in multiple ways using nanogold. *Chemical Society Reviews* **2011**, *40*, 3391-3404.
- (3) Gobin, A. M.; Lee, M. H.; Halas, N. J.; James, W. D.; Drezek, R. A.; West, J. L. Near-infrared resonant nanoshells for combined optical imaging and photothermal cancer therapy. *Nano Lett.* **2007**, *7*, 1929-1934.
- (4) Oyelere, A. K.; Chen, P. C.; Huang, X. H.; El-Sayed, I. H.; El-Sayed, M. A. Peptide-conjugated gold nanorods for nuclear targeting. *Bioconjugate Chemistry* **2007**, *18*, 1490-1497.
- (5) Atwater, H. A.; Polman, A. Plasmonics for improved photovoltaic devices. *Nature Materials* **2010**, *9*, 205-213.
- (6) Kamat, P. V. Meeting the clean energy demand: Nanostructure architectures for solar energy conversion. *Journal of Physical Chemistry C* **2007**, *111*, 2834-2860.
- (7) Yen, C. W.; Hayden, S. C.; Dreaden, E. C.; Szymanski, P.; El-Sayed, M. A. Tailoring Plasmonic and Electrostatic Field Effects To Maximize Solar Energy Conversion by Bacteriorhodopsin, the Other Natural Photosynthetic System. *Nano Lett.* **2011**, *11*, 3821-3826.
- (8) Bohren, C. F.; Huffman, D. R. *Absorption and Scattering of Light by Small Particles*; Wiley: New York, 1983.
- (9) El-Sayed, M. A. Some interesting properties of metals confined in time and nanometer space of different shapes. *Accounts Chem. Res.* **2001**, *34*, 257-264.
- (10) Kelly, K. L.; Coronado, E.; Zhao, L. L.; Schatz, G. C. The optical properties of metal nanoparticles: The influence of size, shape, and dielectric environment. *J. Phys. Chem. B* **2003**, *107*, 668-677.
- (11) Link, S.; El-Sayed, M. A. Spectral properties and relaxation dynamics of surface plasmon electronic oscillations in gold and silver nanodots and nanorods. *J. Phys. Chem. B* **1999**, *103*, 8410-8426.

- (12) Jain, P. K.; Lee, K. S.; El-Sayed, I. H.; El-Sayed, M. A. Calculated absorption and scattering properties of gold nanoparticles of different size, shape, and composition: Applications in biological imaging and biomedicine. *J. Phys. Chem. B* **2006**, *110*, 7238-7248.
- (13) Rechberger, W.; Hohenau, A.; Leitner, A.; Krenn, J. R.; Lamprecht, B.; Aussenegg, F. R. Optical properties of two interacting gold nanoparticles. *Optics Communications* **2003**, *220*, 137-141.
- (14) Sweatlock, L. A.; Maier, S. A.; Atwater, H. A.; Penninkhof, J. J.; Polman, A. Highly confined electromagnetic fields in arrays of strongly coupled Ag nanoparticles. *Physical Review B* **2005**, *71*.
- (15) vanderZande, B. M. I.; Bohmer, M. R.; Fokkink, L. G. J.; Schonenberger, C. Aqueous gold sols of rod-shaped particles. *J. Phys. Chem. B* **1997**, *101*, 852-854.
- (16) Yu, Y. Y.; Chang, S. S.; Lee, C. L.; Wang, C. R. C. Gold nanorods: Electrochemical synthesis and optical properties. *J. Phys. Chem. B* **1997**, *101*, 6661-6664.
- (17) Ali, M. R. K.; Snyder, B.; El-Sayed, M. A. Synthesis and Optical Properties of Small Au Nanorods Using a Seedless Growth Technique. *Langmuir* **2012**, *28*, 9807-9815.
- (18) Flatau, P. J.; Stephens, G. L.; Draine, B. T. Light-scattering by rectangular solids in the Discrete-Dipole Approximation - A new algorithm exploiting the block-toeplitz structure. *J. Opt. Soc. Am. A-Opt. Image Sci. Vis.* **1990**, *7*, 593-600.
- (19) Johnson, P. B.; Christy, R. W. Optical-constants of noble-metals. *Physical Review B* **1972**, *6*, 4370-4379.
- (20) Halas, N. J. Playing with plasmons. Tuning the optical resonant properties of metallic nanoshells. *MRS Bull.* **2005**, *30*, 362-367.
- (21) Sun, Y. G.; Mayers, B.; Xia, Y. N. Metal nanostructures with hollow interiors. *Advanced Materials* **2003**, *15*, 641-646.
- (22) Yan, B. H.; Yang, Y.; Wang, Y. C. Comment on "Simulation of the optical absorption spectra of gold nanorods as a function of their aspect ratio and the effect of the medium dielectric constant". *J. Phys. Chem. B* **2003**, *107*, 9159-9159.
- (23) Brioude, A.; Jiang, X. C.; Pileni, M. P. Optical properties of gold nanorods: DDA simulations supported by experiments. *J. Phys. Chem. B* **2005**, *109*, 13138-13142.
- (24) Kasha, M.; Rawls, H. R.; El-Bayoumi, M. A. The Exciton Model in Molecular Spectroscopy. *Pure and Applied Chemistry* **1965**, *11*, 371 - 392.

- (25) Jain, P. K.; Eustis, S.; El-Sayed, M. A. Plasmon coupling in nanorod assemblies: Optical absorption, discrete dipole approximation simulation, and exciton-coupling model. *J. Phys. Chem. B* **2006**, *110*, 18243-18253.

## CHAPTER IV

### RAPID AND EFFICIENT PREDICTION OF OPTICAL EXTINCTION COEFFICIENTS FOR GOLD NANOSPHERES AND GOLD NANORODS

#### **4.1 Summary**

We have used DDA extinction spectra and experimental extinction coefficients for AuNSs and AuNRs to find shape dependent theoretical conversion factors that allow us to predict extinction coefficients from DDA calculations alone. We used these formulas to predict the extinction coefficient for a 40 nm AuNS and a 30x10 AuNR each in water, and found good agreement between our predictions and previously reported literature values. We also predicted the extinction coefficients for a series of 10 nm diameter AuNRs with varying AR. Our predicted values followed trends that have been previously reported. Experimental determination of extinction coefficients can be difficult and time consuming. Use of the formulas derived here allows for the determination of extinction coefficients from DDA spectra alone, which are easy and fast to produce. Increasing the speed and accuracy in determining extinction coefficients is desirable for many applications that are sensitive to concentration. Additionally, these formulas can be used in a predictive manner to predetermine the appropriate dimensions for a particular AuNS or AuNR to achieve specific energetic characteristics.

## 4.2 Introduction

The use of plasmonic noble metal nanoparticles (NP) in applications has exploded on the scientific landscape over the past few decades<sup>1-3</sup> as colloidal synthetic techniques have ameliorated to provide exquisite control over the size and shape of these nano-sized materials.<sup>4</sup> Precise control of NP geometry is of utmost importance, as this allows for tuning of the plasmon resonant energy throughout a relatively large electromagnetic range.<sup>5</sup> Gold nanoparticles, in particular, have a plasmon resonant energy that can be tuned in the visible spectrum from the green to the NIR. Gold NPs also benefit from high stability, intense local electromagnetic fields, and an incredible ability to generate local heat. These properties have led to the use of gold NPs in applications ranging from sensing and imaging to diagnostics and therapeutics.<sup>6-8</sup>

A limitation to the use of gold nanoparticles in applications is the determination of the concentration of any given batch of NPs. Traditionally, Beer's law is used to convert the measured optical density (OD) into NP concentration using an experimentally pre-determined extinction coefficient ( $\epsilon$ ). However, determination of this  $\epsilon$  requires a rigorous process of acid digestion and quantitative analytical techniques (e.g. ICP-MS) that is incredibly costly in terms of both time and money.

Facile determination of nanoparticle optical and electromagnetic properties can be achieved with theoretical methods, such as the Discrete Dipole Approximation (DDA).<sup>9,10</sup> This method requires minimal man-hours and allows for flexibility in modeled NP

composition and geometry. In DDA, the NP is represented by a three-dimensional finite lattice of point dipoles that is excited by an external field. The response of the point dipoles to the external field and to one another is solved self-consistently using Maxwell's equations. DDA also provides an extinction intensity for the single modeled particle, though this value is yet to be related to an actual physical quantity.

Herein, we systematically examine series of gold nanospheres (AuNS) and gold nanorods (AuNR) both experimentally and theoretically. We calculate the theoretical extinction intensity (TEI) using DDA. We also use literature values and our own experimental values for experimental extinction coefficients (EECs) for particles of the same dimensions we performed DDA calculations for. By combining the TEI and the EECs, we provide an equation to generate a predicted extinction coefficient (PEC) for each of the nanospheres and nanorods examined. These equations can then be used in the future to generate PECs from DDA calculations alone.

## **4.3 Methods**

### 4.3.1 Reagents

Chlorauric acid (CAS: 16961-25-4) was purchased from Alfa Aesar. Sodium Borohydride (CAS: 16940-66-2), silver nitrate (CAS: 7761-88-8), and CTAB (CAS: 57-



09-0) were purchased from Sigma-Aldrich. Ascorbic acid (CAS: 50-81-7) was purchased from Mallinckrodt Chemicals.

#### 4.3.2 Synthesis of gold nanorods

Gold nanorods (14 nm diameter, 54 nm length) were synthesized using a seed-mediated approach.<sup>8</sup> The seed solution was first prepared by dissolving cetyltrimethylammonium bromide (CTAB, 0.273 g) in water (deionized, 7.5 mL) with mild stirring and slight heating. Hydrogen tetrachloroaurate (250  $\mu$ L, 10 mM) was added, and the gold was reduced with sodium borohydride (600  $\mu$ L, 0.1 M). The solution was stirred for 5 mins before use.

The growth solution was prepared by dissolving CTAB (15.49 g) in water (deionized, 425 mL) with mild stirring and slight heating. Tetrachloroaurate trihydrate (20 mL, 10 mM) was then added, yielding a clear, bronze-colored solution. Silver nitrate (8.5 mL, 4 mM) was added, and then the gold was reduced with ascorbic acid (11.6 mL, 79 mM), yielding a clear, colorless solution. Seed solution (960  $\mu$ L) was injected, and the solution was left undisturbed overnight. The nanoparticles were cleaned via 2x successive centrifugation.

### 4.3.3 Thermal reshaping of gold nanorods

Gold nanorods of varying dimensions were synthesized via controlled thermal melting of AuNR@CTAB prepared as described above. A solution of CTAB (0.31 g, 100 mL) was prepared and heated to a gentle boil under gentle stirring (400 rpm) in a 250 mL trace-clean Erlenmeyer flask. The as-prepared AuNR@CTAB solution (25 mL) was injected, and heating/stirring was continued until the desired aspect ratio was achieved. The change in aspect ratio was monitored through observation of the longitudinal plasmon resonance peak (ca. 800 nm, initially), which moved exponentially slowly toward the transverse plasmon resonance peak (ca. 530 nm). Evidence of this change is also apparent in the color of the solution, which progresses from brown to purple to blue/green to red over the course of the rod-to-sphere transformation. The resulting nanoparticles were cleaned via 2x centrifugation with water. Extinction cross sections were measured using an Ocean Optics HR400CG-UV-NIR and Spectrasuite software.

### 4.3.4 Characterization of gold nanoparticles

Gold nanospheres and nanorods were cleaned via 2x centrifugation and redispersion in water. Optical characterization of the nanoparticles was carried out using an Ocean Optics HR400CG-UV-NIR spectrometer and Spectrasuite software. Size and morphology characterization was carried out using a JEOL 100 CX transmission electron microscope.

For ICP-MS, aliquots of each sample were then digested via dissolution in aqua regia (3:1 HCl:HNO<sub>3</sub>) and boiling to dryness. Dry salt samples were then redispersed in aqua regia, boiled to ca. 2 mL, and diluted to 5 mL with micropure water. Indium IS was prepared in a 50 mL volumetric by adding 24.96 uL of 10,010 ppm and diluting to the line to give a final concentration of 5 ppm In IS. For ICP-MS, an aliquot (1 mL) of each unknown sample was diluted with HNO<sub>3</sub> (8,980 uL, 2%) and IS (20 uL). The Au standard was 19,696.657 ppm. We made a 10 ppm in a 50 mL volumetric by adding 25.4 uL of Au standard and diluting to the line with 2% HNO<sub>3</sub>. We diluted this further to make a 1 ppm (or 1000ppb) stock in a 50 mL volumetric by adding 5 mL 10 ppm and diluting to the line with 2% HNO<sub>3</sub>.

Using respective 50 mL volumetrics we made the calibration curve by adding the following:

2000 ppb - 10 mL of 10 ppm Au standard

1000 ppb - 5 mL of 10 ppm Au standard

500 ppb - 2.5 mL of 10 ppm Au standard

100 ppb - 5 mL of 1 ppm Au standard

50 ppb - 2.5 mL of 1 ppm Au standard

10 ppb - 500 uL of 1 ppm Au standard

5 ppb - 250 uL of 1 ppm Au standard

1 ppb - 50 uL of 1 ppm Au standard

To each level we added 100 uL of In IS.

Gold ion concentrations were then determined using an inductively coupled plasma mass spectrometer (ICP-MS). A minimum of X# of ICP measurements were collected for each nanoparticle sample.

#### 4.3.5 Theoretical methods

The optical response of gold nanospheres (diameters of: 6, 10, 15, 23, 30, 50, 40, 60 and 80nm) and gold nanorods (54×15, 51×16, 50×18, 50×19, 46×23, 40×30, 42×10, 40×10, 30×10, 20×10, 50×10, and 60×10) was calculated using the DDA method with the DDSCAT 6.1 code offered publicly by Draine and Flatau.<sup>11</sup> The dielectric values for gold reported by Johnson and Christy<sup>12</sup> were used. The incident light is always polarized along the length of the AuNR in this report, and the medium surrounding the particle was represented as water with a refractive index of 1.333.

## 4.4 Results and Discussion

### 4.4.1 Modeling the optical properties of gold nanospheres

In DDA the user easily defines the size, shape, and composition of a particle as well as the number of particles and their location in the system. However, one obstacle is that the overall size of the system is not easily defined. In order to determine the extinction coefficient from the DDA calculations it is necessary to know the overall volume of the system in DDA. We know the number of particles in the system, but without knowing the overall size of the system, we cannot know the volume of virtual solution around the particle, and thus the concentration. Therefore, we need to develop a theoretical conversion factor by which to account for the overall volume of surrounding media in DDA and from that calculate the extinction coefficient.

DDA calculations were carried out for single AuNS with varying diameter (diameter = 6, 10, 15, 23, 30 50, 60, 80) in water. As the diameter of the AuNS increases, the peak intensity in the DDA extinction spectrum increases (Figure 4 - 1).

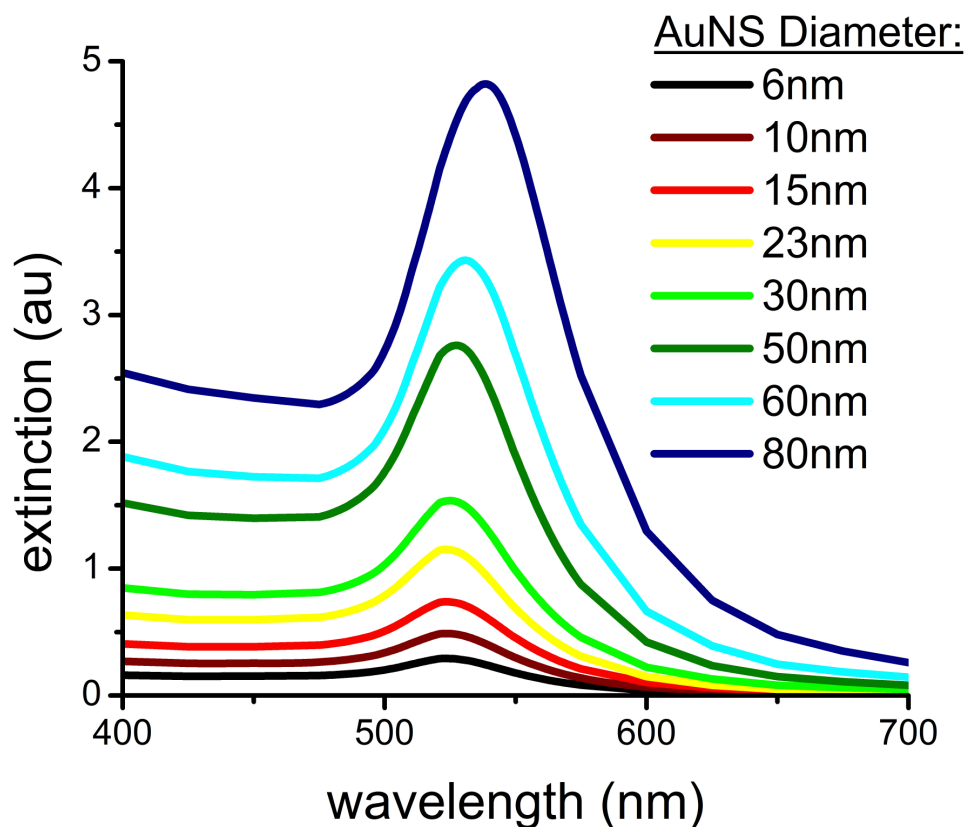


Figure 4 - 1. DDA extinction spectra for AuNS of varying diameter (indicated in legend) The extinction increases as the size of the AuNS increases with very little change in peak position.

We used the maximum extinction value from the DDA spectrum for each AuNS in Figure 4 - 1 and literature values for their extinction coefficients<sup>13-18</sup> to find an empirical formula relating the volume of the particle to the volume of the overall system. This empirical relation for the AuNS is shown in Figure 4 - 2, and takes the form of an allometric function. We will henceforth refer to this empirical relation as the theoretical

conversion factor, as it gives us the ability to relate our theoretical spectra to physical values.

In order to predict the extinction coefficients from theoretical spectra, we simply combine our theoretical conversion factor with a few constants to get:

$$PEC = TEI * 10^{-24} * N_A * f(x)$$

where PEC is the predicted extinction coefficient, TEI is the theoretical extinction intensity (obtained from the DDA spectrum),  $10^{-24}$  is a conversion factor for converting  $\text{nm}^3$  to L,  $N_A$  is Avogadro's number, and  $f(x)$  is our shape dependent theoretical conversion factor where the volume of the particle in  $\text{nm}^3$  is  $x$ . From Figure 4 - 2, for AuNS,

$$f(x) = a * x^b$$

where  $a = (5.90 \pm 1.33) * 10^6$  and  $b = (0.665 \pm 0.0186)$ .

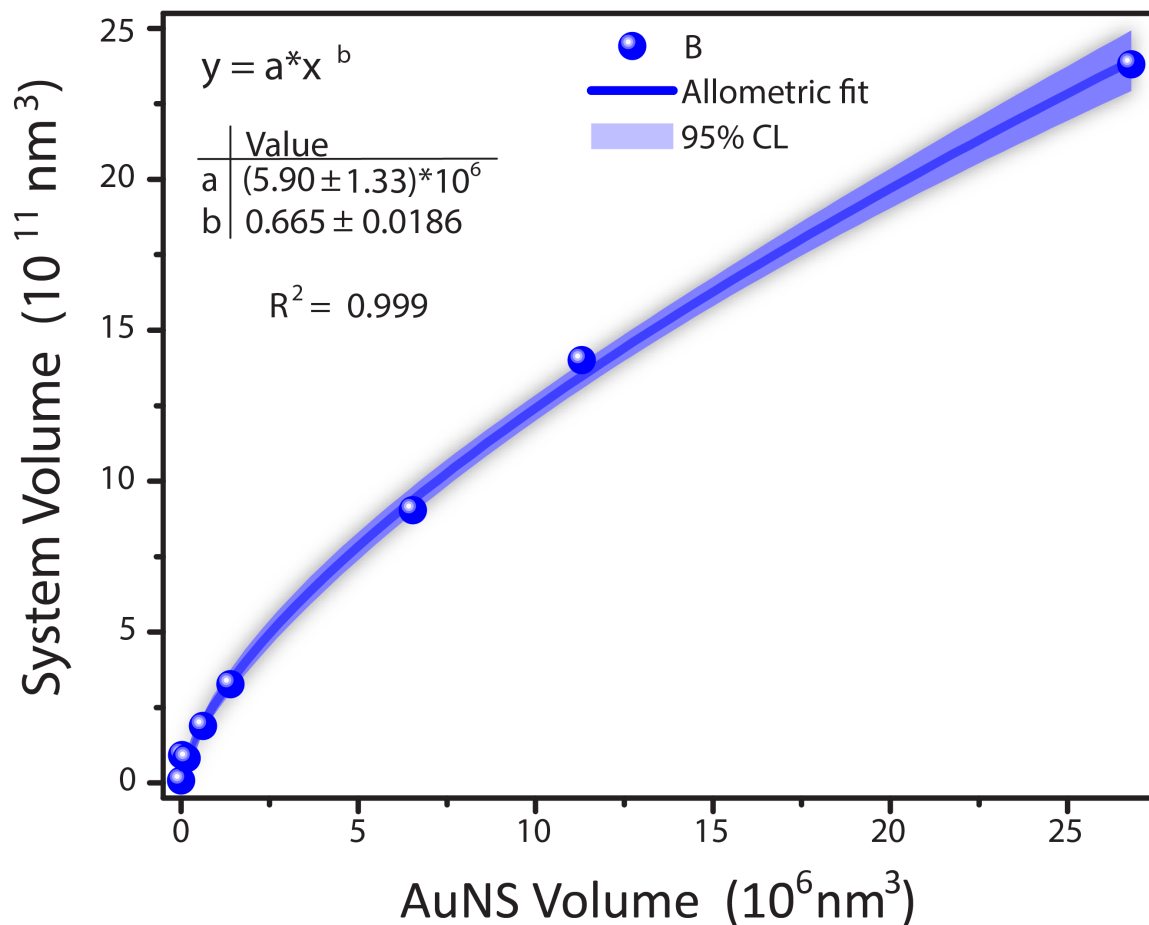


Figure 4 - 2. Empirical formula relating the volume of the AuNS to the volume of the system DDA. The data fit well ( $R^2 = 0.999$ ) to an allometric formula,  $y = a \cdot x^b$ .

We used our equation to generate the predicted extinction coefficients (PECs) for a range of nanosphere sizes (Figure 4 - 1), and plotted these as a blue line in Figure 4 - 3. We then overlaid these with experimental extinction coefficients (EECs) from the literature to show that these data points fall within the predicted confidence intervals.



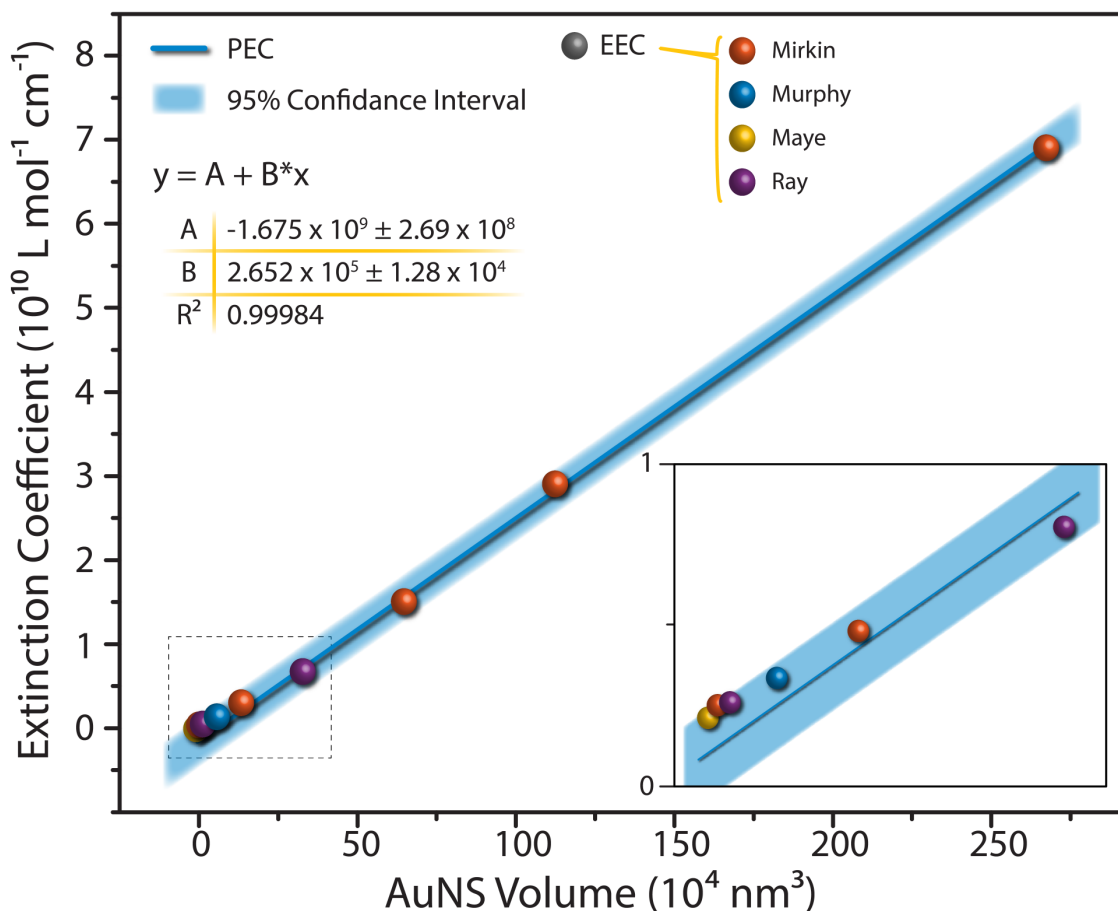


Figure 4 - 3. Fit of predicted extinction coefficients (PEC) against AuNS volume (blue line) with experimental extinction coefficients (EEC) from literature (colored spheres). All the experimental data points fall on the relation derived theoretically, indicating a good agreement.

To test the validity of this process, we will predict the extinction coefficient for a 40 nm AuNS in water from DDA. The theoretical conversion factor for a 40 nm AuNS is  $(6.01 \pm 2.92) \times 10^9 \text{ nm}^3$ . The DDA extinction spectrum for the 40 nm AuNS in water (Figure 4 - 4) has a peak extinction value of 2.12 at a wavelength of 526 nm. Using the equation relating TEI and PEC, the predicted extinction coefficient for a 40 nm AuNS from DDA

is  $(7.67 \pm 3.73) \times 10^9 \text{ M}^{-1} \text{ cm}^{-1}$ . The literature value for 40 nm AuNSs is  $6.7 \times 10^9 \text{ M}^{-1} \text{ cm}^{-1}$ ,<sup>1,13</sup> which falls within the values predicted via DDA.

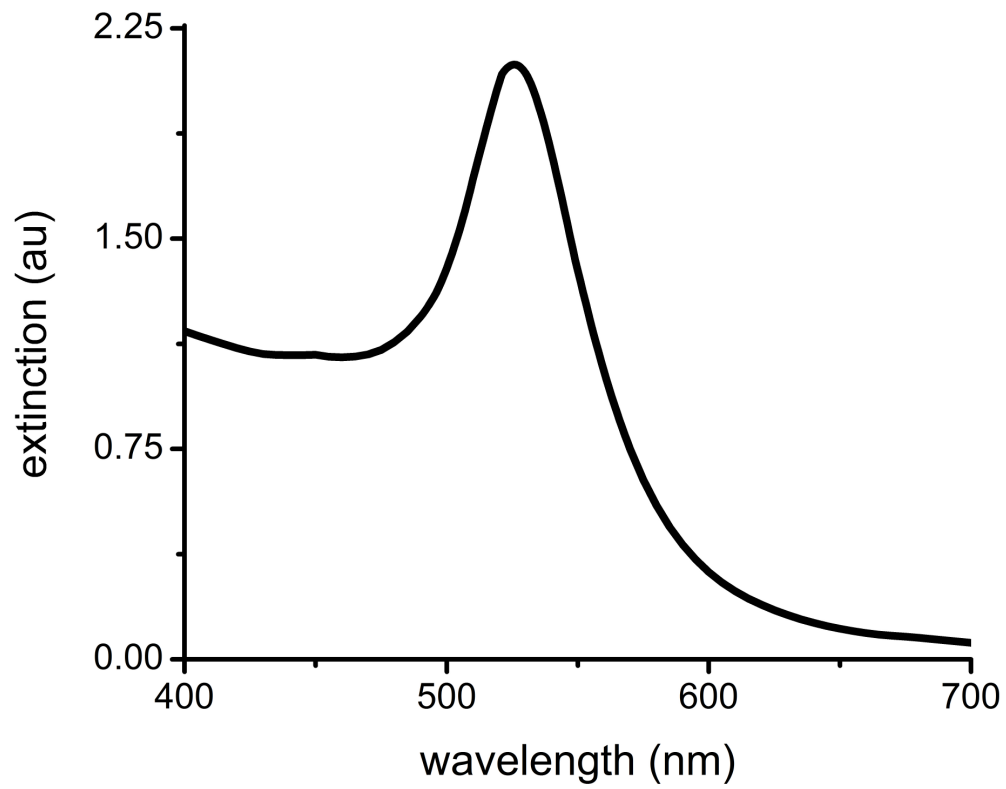


Figure 4 - 4. DDA extinction spectrum for a 40 nm AuNS in water.

#### 4.4.2 Thermal treatment of gold nanorods

The synthesis and handling of gold nanorods is less facile than gold nanospheres; thus extinction coefficients for AuNRs are not numerous enough in the literature for the purpose of building a robust model similar to that which we developed for AuNS.

Therefore, we supplemented literature-reported extinction coefficients<sup>17</sup> with our own examination of the extinction coefficients of AuNR with systematically varied dimensions prepared by a thermal reshaping process.

Our lab has previously reported the photothermal reshaping of gold nanorods into spherical particles via laser ablation.<sup>19</sup> When the nanorods are excited by a high power laser, the plasmon resonance is generated, and the nanorods melt from the inside out.<sup>20</sup> Conversely, when gold nanorods are heat-treated at low concentration and in the presence of excess CTAB, they melt the same as a bulk material - from the outside in. Moreover, this process is slower and occurs in all particles in the solution at once, rather than just the particles in the path of the laser beam. This slower timescale allows for the reaction to be arrested at any point during the melting, producing gold nanorods of desired dimensions and/or plasmon frequency.<sup>21</sup>

We fabricated a sample of AuNR via known methods.<sup>8</sup> Transmission Electron Microscopy (TEM) was used to determine the dimensions of the AuNRs were  $54.3 \pm 3.4 \times 15.1 \pm 1.0$  nm and the optical extinction spectrum showed a longitudinal plasmon resonance at ca. 800 nm (Figure 4 - 5). We used the simple heat-treatment method<sup>21</sup> to

systematically alter the dimensions of these AuNRs. We observed the thermal reshaping of nanorods over time via UV-vis and TEM (Figure 4 - 6). The progression produces increasingly shorter and fatter rods, until spheres are finally formed. The dimensions of the rods are given in Figure 4 - 7. Optically, the longitudinal plasmon band blue-shifts significantly as the rod length shortens. The transverse plasmon concurrently red-shifts, though to a much lesser degree. This effect is seen in the experimental extinction spectra in Figure 4 - 8.

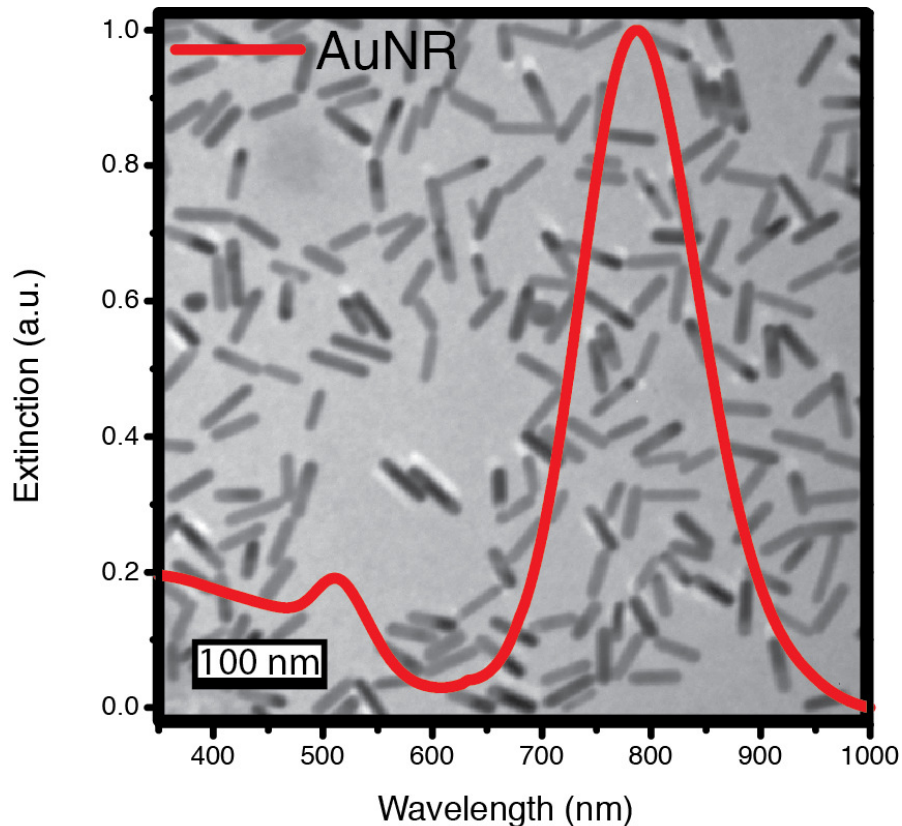


Figure 4 - 5. TEM micrograph of AuNRs  $54.3 \pm 3.4 \times 15.1 \pm 1.0$  nm capped with CTAB. The longitudinal plasmon band appears ca. 800 nm.

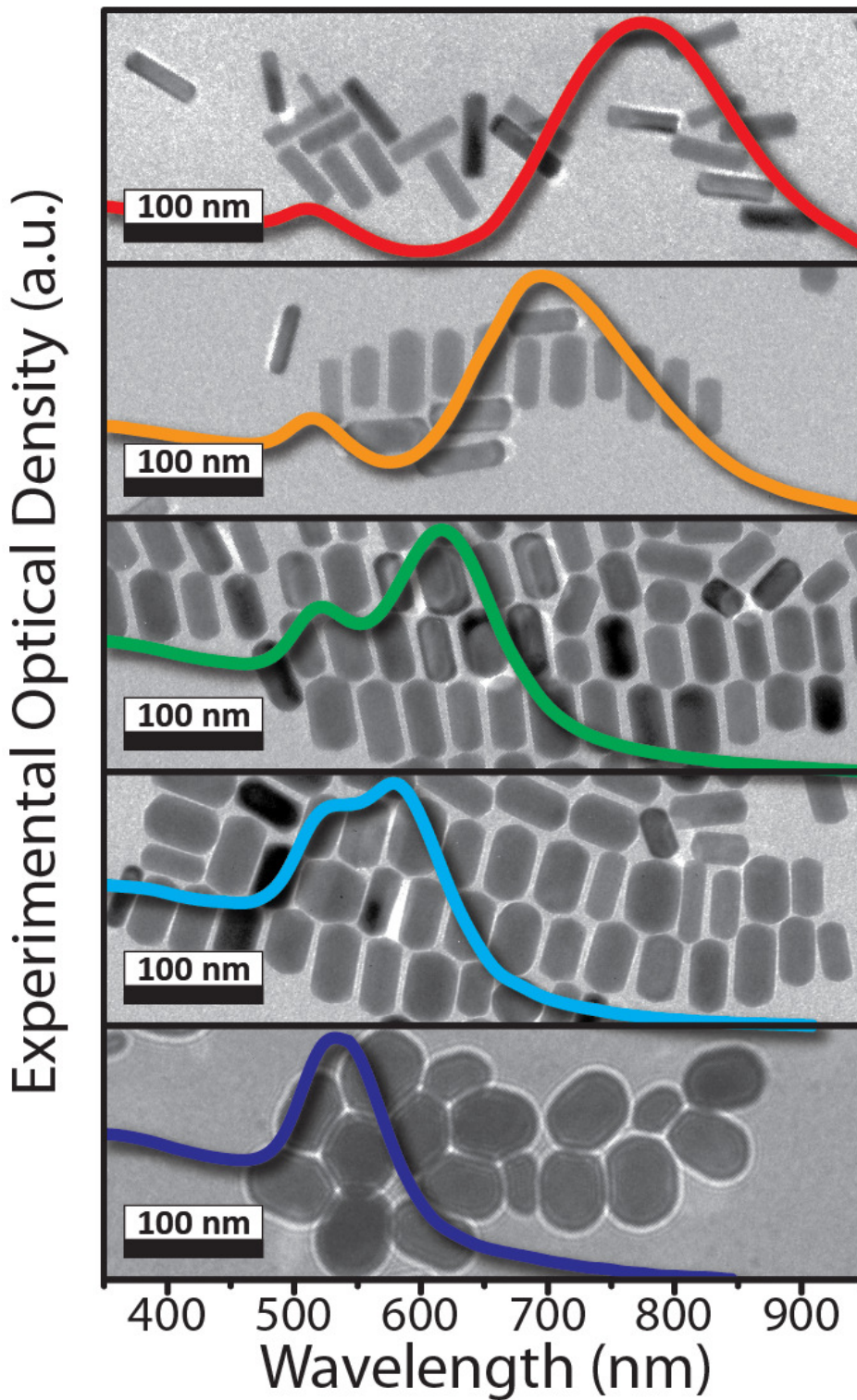


Figure 4 - 6. TEM micrographs with overlaid, corresponding optical extinction spectra showing the progression from gold nanorods (top) to gold nanospheres (bottom) over time with heat.

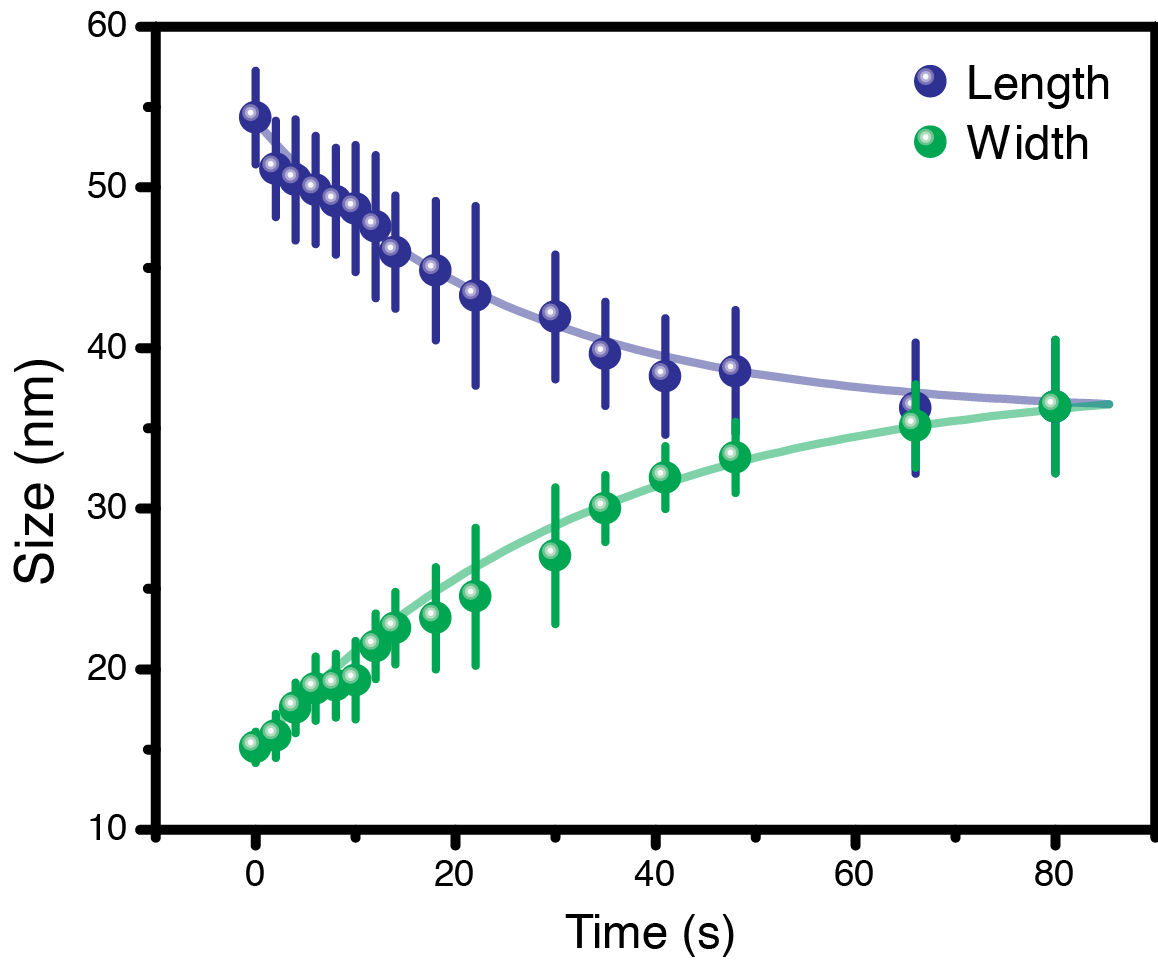


Figure 4 - 7. Length and width of gold nanorods over time. These nanorods become shorter and fatter as they thermally melt, finally producing nanospheres.

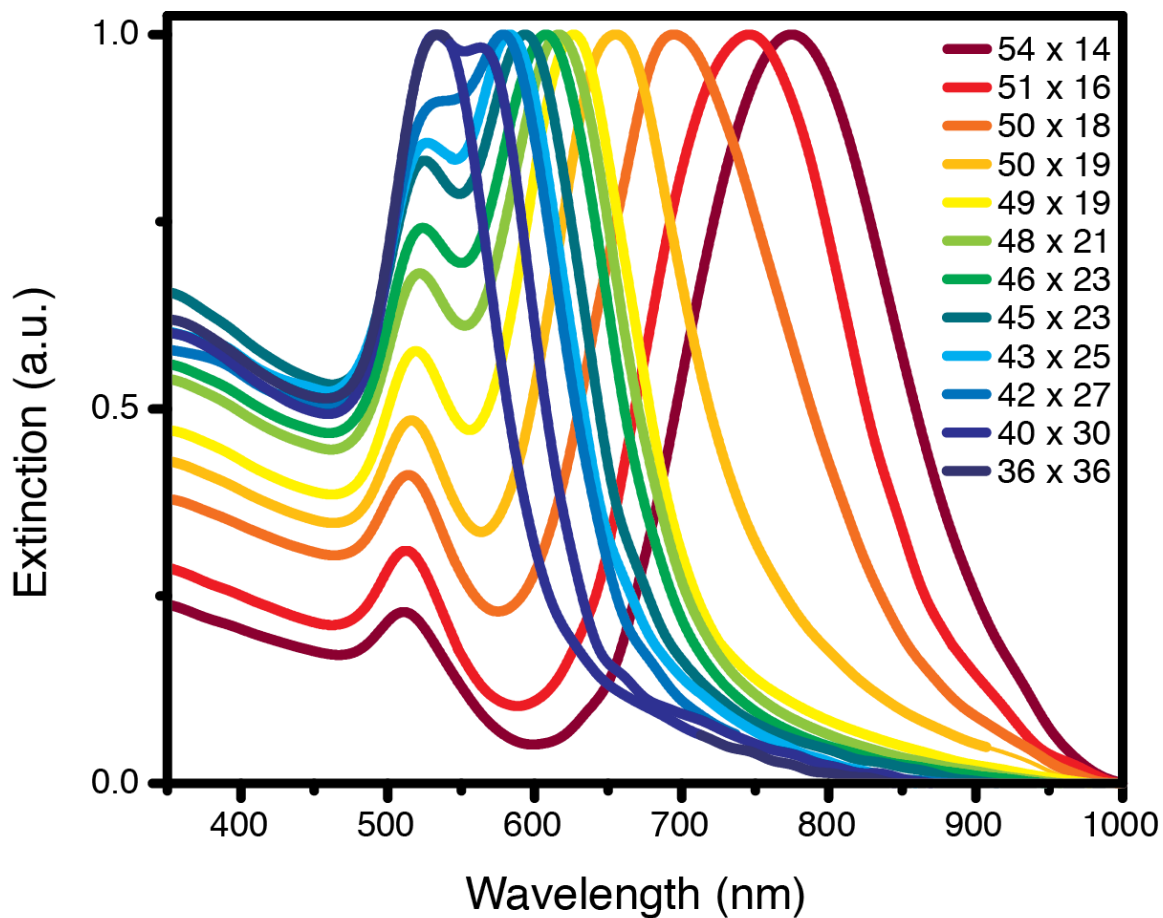


Figure 4 - 8. Experimental extinction spectra showing thermal transition from gold nanorods to gold nanospheres. The longitudinal plasmon resonance blue-shifts while the transverse plasmon resonance red-shifts.

ICP was used to determine the number of gold atoms per unit volume for each solution of nanorods. This in conjunction with the size of the rods (i.e. average volume of gold per rod) from the TEM measurements was used to determine the extinction coefficients for the different sized AuNRs. The extinction coefficients varied systematically with dimensions (Figure 4 - 9). We will use these and previously published experimentally determined extinction coefficients to predict extinction coefficients for AuNRs from DDA alone.

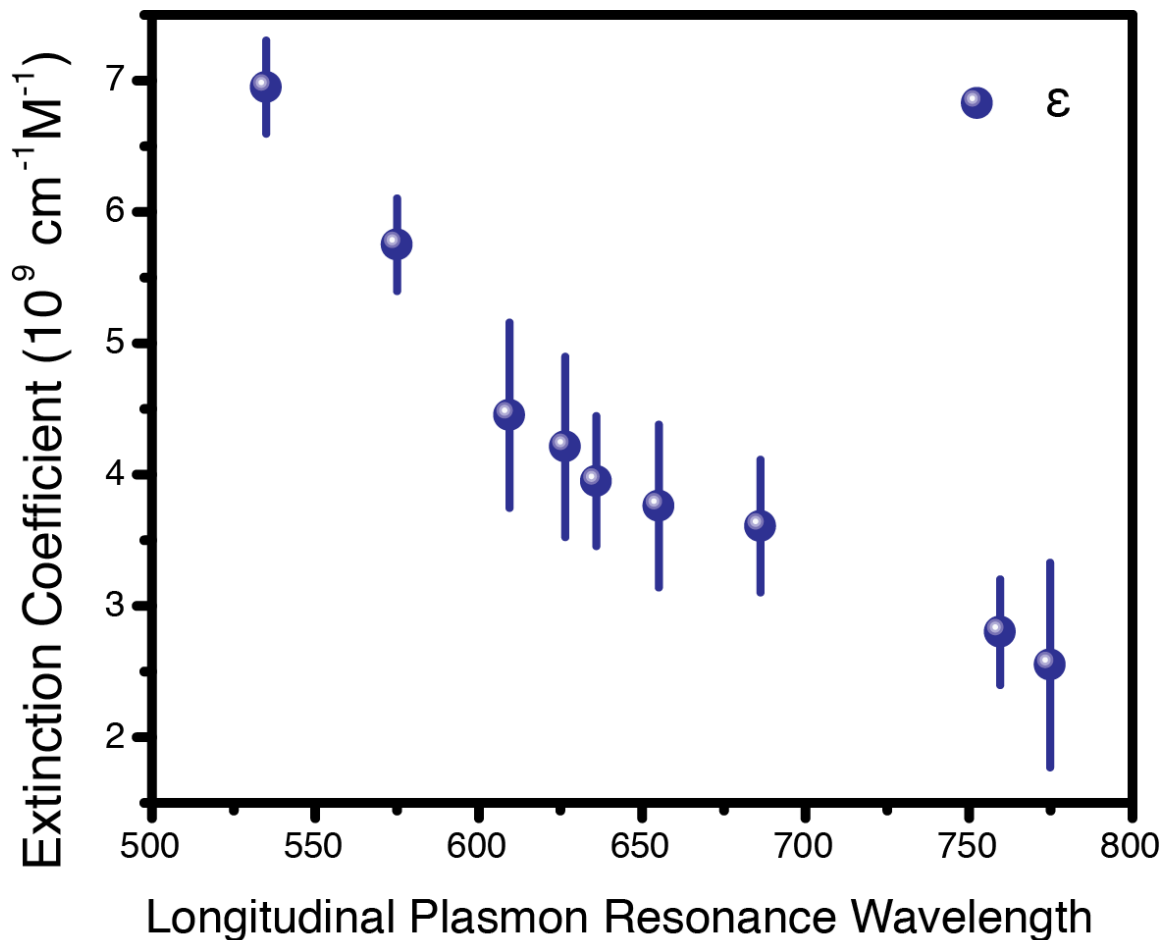


Figure 4 - 9. Experimental extinction coefficients by longitudinal plasmon resonance wavelength obtained via ICP-MS.

#### 4.4.3 Modeling the optical properties of gold nanorods

DDA calculations were carried out for single AuNR with varying dimensions (54×15, 51×16, 50×18, 50×19, 46×23, 40×30, 42×10, and 40×10) in water. The DDA extinction spectra for AuNRs are shown in Figure 4 - 10. The plasmon peak position is dependent



on both dimensions of AuNR, even though the light was polarized to isolate the longitudinal mode.

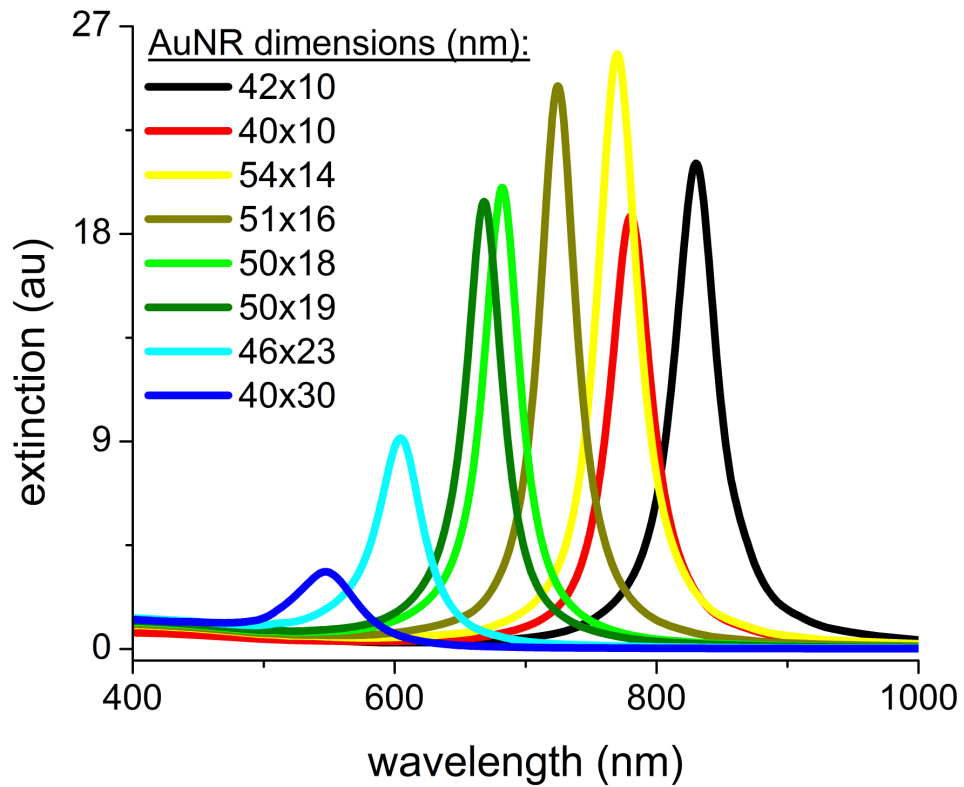


Figure 4 - 10. DDA extinction spectra for AuNR of varying dimensions (indicated in legend). The extinction intensity and peak position depend on both dimensions of the AuNR even though light is polarized along the length of the AuNR to isolate only the longitudinal mode.

As with the AuNS, we used the maximum extinction value from the DDA spectrum for each AuNR in Figure 4 - 10 and experimental values for their extinction coefficients<sup>17</sup> (Figure 4 - 9) to find an empirical formula relating the volume of the particle to the volume of the overall system. This empirical relation for the AuNR is shown in Figure 4 - 11, and takes the form of an exponential function.

In order to predict the extinction coefficients from theoretical spectra, we simply combine our theoretical conversion factor with a few constants to get:

$$PEC = TEI * 10^{-24} * N_A * f(x)$$

where  $10^{-24}$  is a conversion factor for converting  $\text{nm}^3$  to L,  $N_A$  is Avogadro's number, and  $f(x)$  is a shape dependent theoretical conversion factor where  $x$  is the volume of the particle in  $\text{nm}^3$ . For AuNR  $f(x)$  is:

$$f(x) = y_0 + A * e^{[(x-x_0)/t]}$$

where  $y_0 = (2.11 \pm 0.46) * 10^8$ ,  $A = 1.11 * 10^7$ ,  $x_0 = 2.61 * 10^3$  and  $t = (3.40 \pm 0.18) * 10^3$ .

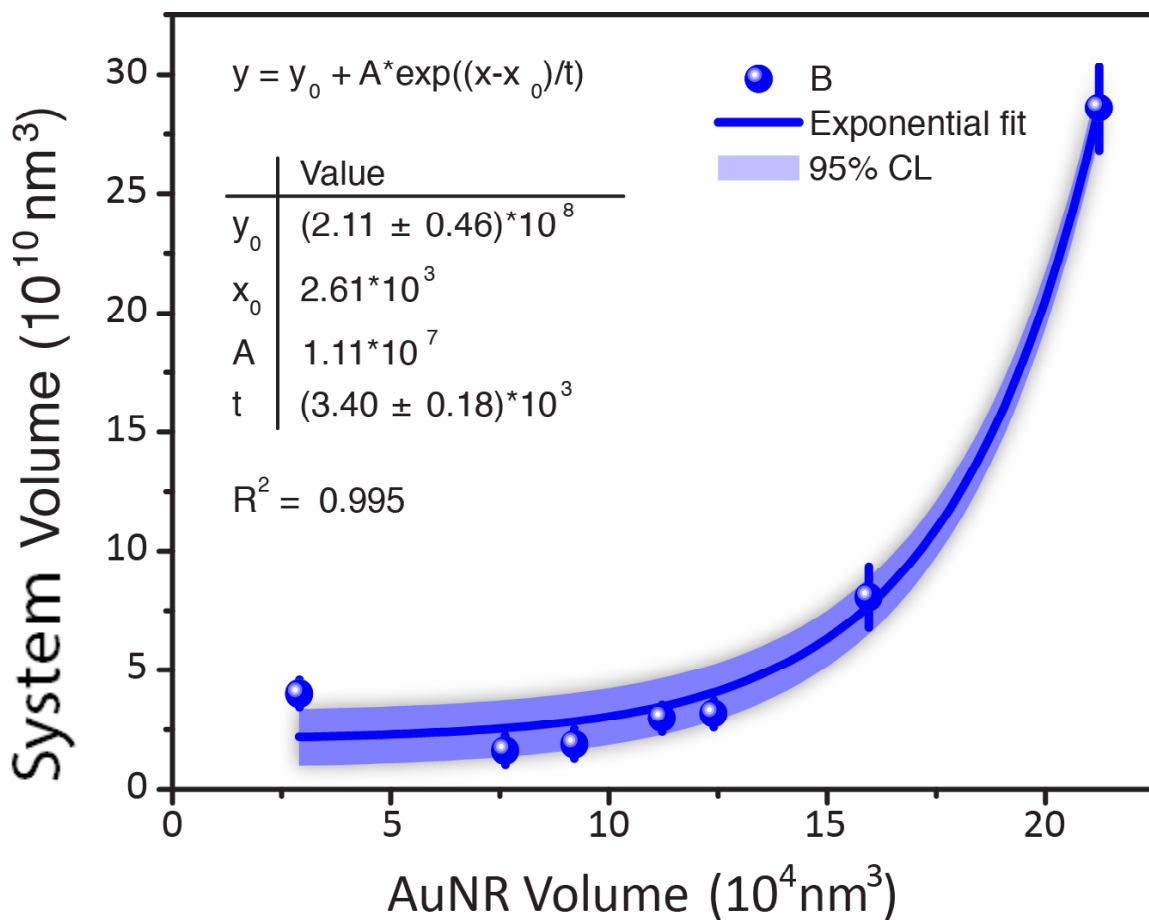


Figure 4 - 11. Empirical formula relating the volume of the AuNR to the system volume in DDA. The data fit well ( $R^2 = 0.995$ ) to an exponential formula,  $y = y_0 + A \cdot \exp[(x - x_0)/t]$ .

We used our equation for AuNRs to generate the predicted extinction coefficients (PECs) for a range of nanorod sizes (Figure 4 - 10), and plotted these as a blue line in Figure 4 - 12. We then overlaid these with experimental extinction coefficients (EECs) from the literature<sup>17</sup> and our own experiments (Figure 4 - 8) to show that these data points fall within the predicted confidence intervals.

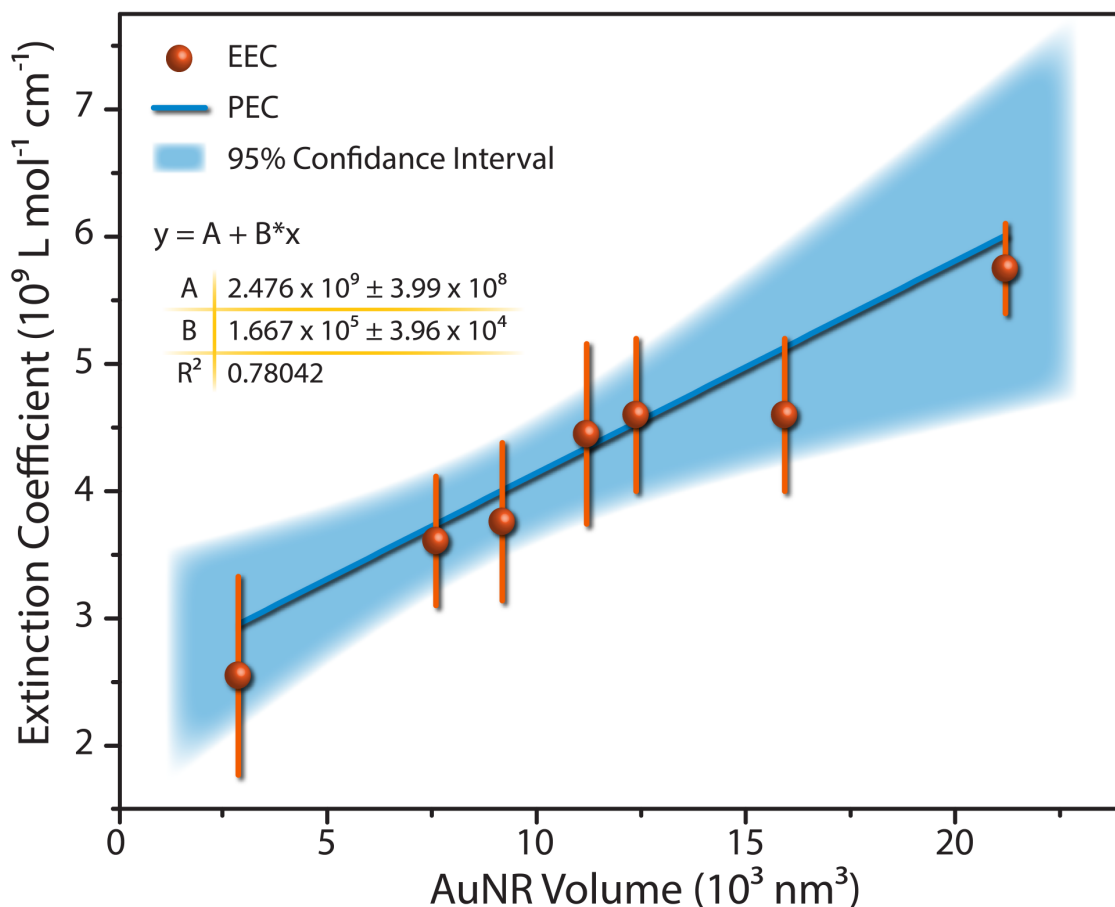


Figure 4 - 12. Fit of predicted extinction coefficients (PEC) against AuNR volume (blue line) with experimental extinction coefficients (EEC, orange spheres). All the experimental data points fall on the relation derived theoretically, indicating a good agreement.

To test the validity of this process, we will predict the extinction coefficient for a 30×10 nm AuNR in water from DDA. The theoretical conversion factor for a 30×10 nm AuNR is  $(2.21 \pm 0.45) \times 10^8 \text{ nm}^3$ . The DDA extinction spectrum for the 30x10 nm AuNS in water (Figure 4 - 13) has a peak extinction value of 13.615 at a wavelength of 699 nm. Using the equation relating TEI and PEC, the extinction coefficient for a 30×10 nm

AuNR from DDA is  $(1.81 \pm 0.37) \times 10^9 \text{ M}^{-1} \text{ cm}^{-1}$ . The literature value for 30 x 10 nm AuNRs is  $1.9 \times 10^9 \text{ M}^{-1} \text{ cm}^{-1}$ ,<sup>22</sup> which falls within the values predicted via DDA. In fact, the percent error between the average value predicted via DDA and the literature is only 5%.

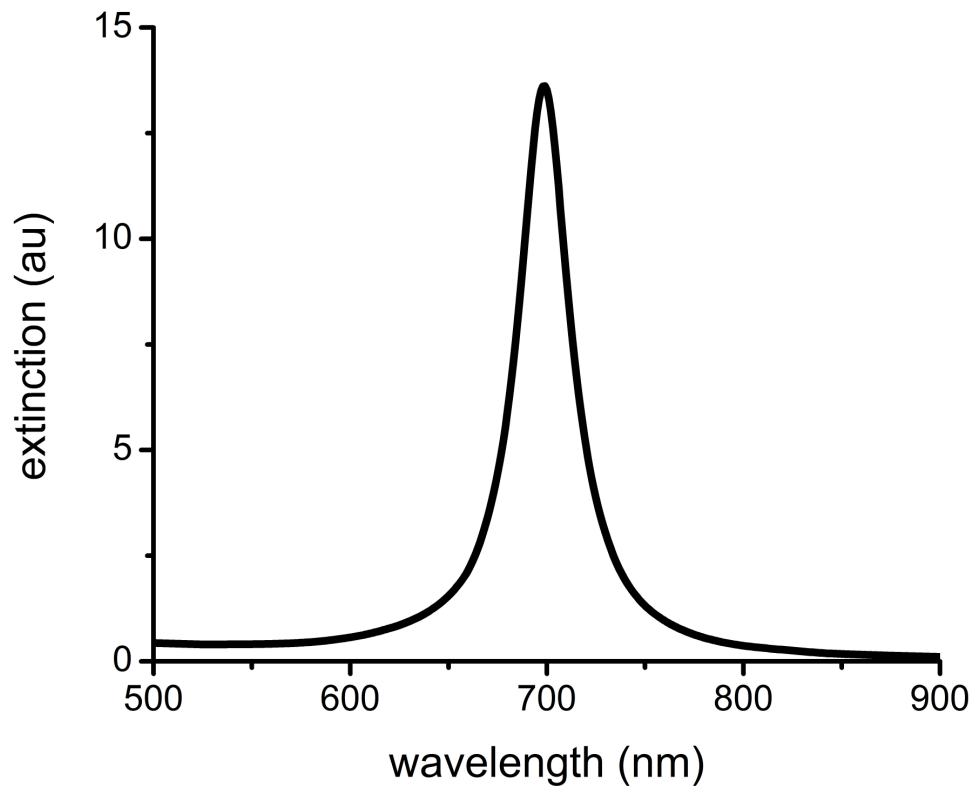


Figure 4 - 13. DDA extinction spectrum for the longitudinal mode of a 30x10 AuNR in water.

Now that we have developed a reliable way to predict extinction coefficients from DDA calculations alone, we applied this to a selection of AuNRs 10 nm in diameter at several aspect ratios (AR = 2, 3, 4, 5, and 6). The DDA extinction spectra for the various AuNRs are shown in Figure 4 - 14. The longitudinal plasmon peak red-shifts as the length increases (Figure 4 - 14, top right panel). Using our formulas, we were able to predict the extinction coefficients for these various AuNRs. The DDA predicted extinction coefficients are plotted against aspect ratio in the bottom right panel of Figure 4 - 14. The extinction coefficient increases as the aspect ratio increases, which agrees with what has been seen previously.<sup>17</sup> The order of magnitude of the extinction coefficients also agrees with those seen previously.<sup>17</sup>

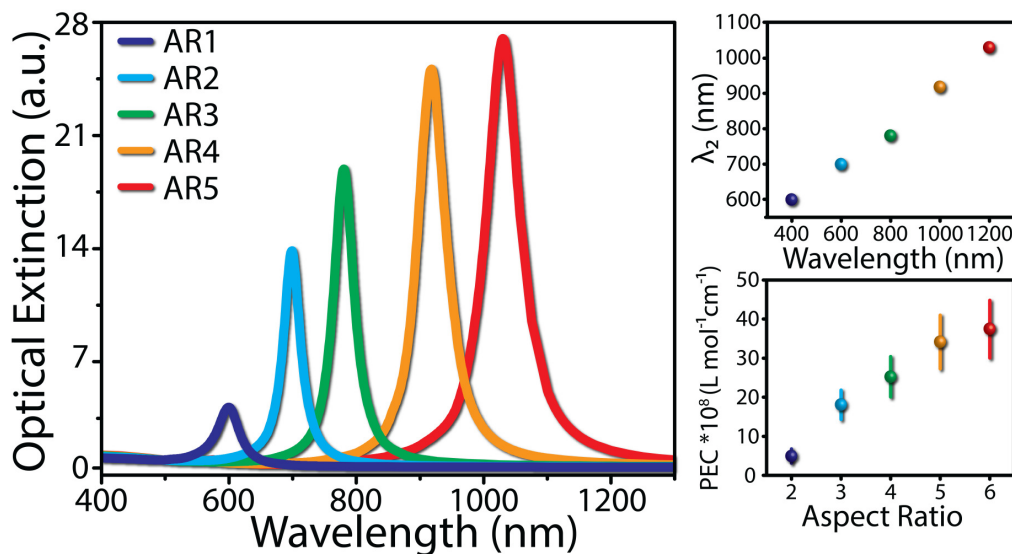


Figure 4 - 14. Theoretical extinction spectra of 10 nm diameter AuNR of indicated aspect ratio (AR). Extinction intensity increases with increasing AR; resonant wavelength red-shifts strongly with increasing AR (top right panel). The predicted extinction coefficients increase with increasing aspect ratio (bottom right panel).

## 4.5 Conclusions

We have used DDA extinction spectra and experimental extinction coefficients for AuNSs and AuNRs to find shape dependent theoretical conversion factors that allow us to predict extinction coefficients from DDA calculations alone.

$$PEC = TEI * 10^{-24} * N_A * f(x)$$

where PEC is the predicted extinction coefficient, TEI is the theoretical extinction intensity,  $10^{-24}$  is a conversion factor for converting  $\text{nm}^3$  to L,  $N_A$  is Avogadro's number, and  $f(x)$  is a shape dependent theoretical conversion factor where  $x$  is the volume of the particle in  $\text{nm}^3$ . For AuNS and AuNR  $f(x)$  is:

$$f(x) = \begin{cases} a * x^b & \text{for AuNS} \\ y_0 + A * e^{[(x-x_0)/t]} & \text{for AuNR} \end{cases}$$

where  $a = (5.90 \pm 1.33) * 10^6$ ,  $b = (0.665 \pm 0.0186)$ ,  $y_0 = (2.11 \pm 0.46) * 10^8$ ,  $A = 1.11 * 10^7$ ,  $x_0 = 2.61 * 10^3$  and  $t = (3.40 \pm 0.18) * 10^3$ . The shape dependent theoretical conversion factor is an empirical relation derived from comparing TEI to PEC for known cases.

We used these formulas to predict the extinction coefficient for a 40 nm AuNS and a 30x10 AuNR each in water, and found good agreement between our predictions and previously reported literature values. We also predicted the extinction coefficients for a

series of 10 nm diameter AuNRs with varying AR. Our predicted values followed trends that have been previously reported.<sup>17</sup>

Experimental determination of extinction coefficients can be difficult and time consuming. Use of the formulas derived here allows for the determination of extinction coefficients from DDA spectra alone, which are easy and fast to produce. Increasing the speed and accuracy in determining extinction coefficients is desirable for many applications that are sensitive to concentration. Additionally, these formulas can be used in a predictive manner to predetermine the appropriate dimensions for a particular AuNS or AuNR to achieve specific energetic characteristics.



## 4.6 References

- (1) Eustis, S.; El-Sayed, M. A. Why gold nanoparticles are more precious than pretty gold: Noble metal surface plasmon resonance and its enhancement of the radiative and nonradiative properties of nanocrystals of different shapes. *Chemical Society Reviews* **2006**, *35*, 209-217.
- (2) Daniel, M.-C.; Astruc, D. Gold nanoparticles: assembly, supramolecular chemistry, quantum-size-related properties, and applications toward biology, catalysis, and nanotechnology. *Chemical Reviews* **2004**, *104*, 293-639.
- (3) Yen, C.-W.; Hayden, S. C.; Dreaden, E. C.; Szymanski, P.; El-Sayed, M. A. Tailoring Plasmonic and Electrostatic Field Effects To Maximize Solar Energy Conversion by Bacteriorhodopsin, the Other Natural Photosynthetic System. *Nano Letters* **2011**, *11*, 3821-3826.
- (4) Hao, E.; Schatz, G. C.; Hupp, J. T. Synthesis and optical properties of anisotropic metal nanoparticles. *J. Fluoresc.* **2004**, *14*, 331-341.
- (5) Kelly, K. L.; Coronado, E.; Zhao, L. L.; Schatz, G. C. The optical properties of metal nanoparticles: The influence of size, shape, and dielectric environment. *J. Phys. Chem. B* **2003**, *107*, 668-677.
- (6) Schwartzberg, A. M.; Zhang, J. Z. Novel optical properties and emerging applications of metal nanostructures. *Journal of Physical Chemistry C* **2008**, *112*, 10323-10337.
- (7) Dickerson, E. B.; Dreaden, E. C.; Huang, X. H.; El-Sayed, I. H.; Chu, H. H.; Pushpanketh, S.; McDonald, J. F.; El-Sayed, M. A. Gold nanorod assisted near-infrared plasmonic photothermal therapy (PPTT) of squamous cell carcinoma in mice. *Cancer Letters* **2008**, *269*, 57-66.
- (8) Huang, X. H.; Neretina, S.; El-Sayed, M. A. Gold Nanorods: From Synthesis and Properties to Biological and Biomedical Applications. *Adv. Mater.* **2009**, *21*, 4880-4910.
- (9) Draine, B. T.; Flatau, P. J. Discrete-Dipole Approximation for scattering calculations. *J. Opt. Soc. Am. A-Opt. Image Sci. Vis.* **1994**, *11*, 1491-1499.
- (10) Near, R.; Hayden, S.; El-Sayed, M. Extinction vs Absorption: Which Is the Indicator of Plasmonic Field Strength for Silver Nanocubes? *The Journal of Physical Chemistry C* **2012**, *116*, 23019-23026.

- (11) Flatau, P. J.; Stephens, G. L.; Draine, B. T. Light-Scattering by rectangular solids in the Discrete-Dipole Approximation - A new algorithm exploiting the block-toeplitz structure. *J. Opt. Soc. Am. A-Opt. Image Sci. Vis.* **1990**, *7*, 593-600.
- (12) Johnson, P. B.; Christy, R. W. Optical-constants of noble-metals. *Physical Review B* **1972**, *6*, 4370-4379.
- (13) Griffin, J.; Singh, A. K.; Senapati, D.; Lee, E.; Gaylor, K.; Jones-Boone, J.; Ray, P. C. Sequence-Specific HCV RNA Quantification Using the Size-Dependent Nonlinear Optical Properties of Gold Nanoparticles. *Small* **2009**, *5*, 839-845.
- (14) Hurst, S. J.; Lytton-Jean, A. K. R.; Mirkin, C. A. Maximizing DNA loading on a range of gold nanoparticle sizes. *Anal. Chem.* **2006**, *78*, 8313-8318.
- (15) Jin, R. C.; Wu, G. S.; Li, Z.; Mirkin, C. A.; Schatz, G. C. What controls the melting properties of DNA-linked gold nanoparticle assemblies? *J. Am. Chem. Soc.* **2003**, *125*, 1643-1654.
- (16) Maye, M. M.; Han, L.; Kariuki, N. N.; Ly, N. K.; Chan, W. B.; Luo, J.; Zhong, C. J. Gold and alloy nanoparticles in solution and thin film assembly: spectrophotometric determination of molar absorptivity. *Anal. Chim. Acta* **2003**, *496*, 17-27.
- (17) Orendorff, C. J.; Gearheart, L.; Jana, N. R.; Murphy, C. J. Aspect ratio dependence on surface enhanced Raman scattering using silver and gold nanorod substrates. *Phys. Chem. Chem. Phys.* **2006**, *8*, 165-170.
- (18) Park, S. Y.; Lee, J. S.; Georganopoulou, D.; Mirkin, C. A.; Schatz, G. C. Structures of DNA-linked nanoparticle aggregates. *J. Phys. Chem. B* **2006**, *110*, 12673-12681.
- (19) Link, S.; Burda, C.; Mohamed, M. B.; Nikoobakht, B.; El-Sayed, M. A. Laser photothermal melting and fragmentation of gold nanorods: Energy and laser pulse-width dependence. *Journal of Physical Chemistry A* **1999**, *103*, 1165-1170.
- (20) Link, S.; Burda, C.; Nikoobakht, B.; El-Sayed, M. A. How long does it take to melt a gold nanorod? A femtosecond pump-probe absorption spectroscopic study. *Chemical Physics Letters* **1999**, *315*, 12-18.
- (21) Mohamed, M. B.; Ismail, K. Z.; Link, S.; El-Sayed, M. A. Thermal reshaping of gold nanorods in micelles. *J. Phys. Chem. B* **1998**, *102*, 9370-9374.
- (22) Nikoobakht, B.; Wang, J. P.; El-Sayed, M. A. Surface-enhanced Raman scattering of molecules adsorbed on gold nanorods: off-surface plasmon resonance condition. *Chemical Physics Letters* **2002**, *366*, 17-23.

## CHAPTER V

### EXTINCTION VS. ABSORPTION: WHICH IS THE INDICATOR OF PLASMONIC FIELD STRENGTH FOR SILVER NANOCUBES

#### 5.1 Summary

This investigation demonstrates the contributions of absorption and scattering to the extinction spectrum of silver nanocubes with multipole resonances and the complexity of the resulting plasmon field strengths for these varying modes. The three-dimensional plasmonic field distribution and orientation around a silver nanosphere (AgNS, 40 nm) and a silver nanocube (AgNC; 40, 60, 86 nm) were calculated in the visible via the Discrete Dipole Approximation. The three-dimensional nature of these particles allows for significant contribution from the quadrupole mode in some cases. The AgNS displays one plasmon band, its dipole mode, and has little contribution from scattering. The maximum plasmon field occurs at the extinction maximum, as expected. The 40 nm AgNC exhibits multiple plasmon bands, and the highest maximum field strength is attained from excitation of the quadrupole mode, not the dipole mode. As the size of the AgNC increases, the contribution from scattering increases. When the contribution from scattering is greater than the contribution from absorption in a AgNC, the field strength within a plasmon mode trends with the absorption and not with the extinction or scattering. This should be considered in applications of AgNCs, as excitation of the

largest peak in the experimental extinction spectrum will not always result in the strongest plasmon field strength.

## 5.2 Introduction

Plasmonic nanoparticles can interact with light in several different ways. The amount of light scattered by a particle relative to the amount of light absorbed by the particle is dependent on the particle's size, shape and composition.<sup>1-3</sup> Scattering of light by plasmonic particles is the key process in many diagnostic applications employing nanoparticles, as the large amount of scattering makes it easy to see the particles via dark field microscopy.<sup>1,4-9</sup> Many other applications (e.g. solar cells,<sup>10-12</sup> photothermal therapy,<sup>8,13-15</sup> drug delivery<sup>13,16-18</sup>) rely heavily on the absorption of light by plasmonic particles and the subsequent conversion of that energy to heat or strong electric fields.

In many applications involving the use of electric fields around nanoparticles, a specific wavelength or selection of wavelengths is used to excite the particle to give the strongest field. It has been shown elsewhere that excitation at the dipolar plasmon wavelength creates very strong fields,<sup>19,20</sup> and many applications exploit this, choosing wavelengths based on the largest peak from the experimentally collected extinction spectrum. Our results for silver nanocubes indicate that field strength trends with absorption and not extinction or scattering, which necessitates a thorough theoretical investigation to accurately determine the ideal excitation wavelength for applications.

The discrete dipole approximation (DDA) is a theoretical technique for modeling the spectral properties of systems. DDA has the advantage of being able to model particle(s) of arbitrary shape.<sup>1,20-24</sup> In this method, the particle is represented by a three-dimensional finite lattice of point dipoles that is excited by an external field. The response of the point dipoles to the external field and to one another is solved self-consistently using Maxwell's equations. The DDSCAT 6.1 code offered publicly by Draine and Flatau<sup>25</sup> allows for calculation of the absorption and scattering spectra separately, allowing for assessment of the contributions from each to the extinction spectra, which is the sum of these two components. Furthermore, with modifications to the code by Goodman<sup>26</sup> and Schatz,<sup>27</sup> it is possible to calculate the electric field enhancement contours and the individual dipole orientations at a specific wavelength. These plots can only be generated for one slice through the particle at a time, but the slice position can be chosen. Thus, by repeating the calculations for multiple slices through the particle, a three-dimensional representation of the field can be obtained at a particular resonance wavelength.

Using DDA, we calculate the absorption and scattering components of the extinction as well as the three-dimensional field plots for whole particles. We show that an in-depth investigation of the three-dimensional field enhancement contours is needed to accurately assign the plasmonic modes and determine which wavelength results in the largest field enhancement for silver nanocubes. We also elucidate the relationship between the absorption spectrum and maximum field enhancement within a single plasmon mode for a silver nanosphere and for silver nanocubes of varying size.

### 5.3 Methods

The optical response of a silver sphere (40 nm diameter) and a silver nanocube with varying edge length (40 nm, 60 nm and 86 nm) was calculated using the DDA method with the DDSCAT 6.1 code offered publicly by Draine and Flatau<sup>25</sup> with modifications by Goodman<sup>26</sup> and Schatz<sup>27</sup>. The dielectric values for silver reported by Johnson and Christy<sup>28</sup> were used. The incident light was always polarized left to right along the edge of the AgNC for these calculations, and the medium surrounding the particle was represented as water with a refractive index of 1.333.

### 5.4 Results and Discussion

#### 5.4.1 40 nm Silver Nanosphere

The extinction, absorption, and scattering spectra for a 40 nm AgNS in water are shown in Figure 5 - 1a. Here, there is only one plasmon band, which has some contribution from scattering but is dominated by absorption. The maximum of this plasmon band occurs at 393 nm. To accurately assign the plasmon modes, multiple field contour plots were generated at each wavelength for five evenly spaced slices through the particle. When combined (as in, Figure 5 - 2), these five slices give a good three-dimensional representation of the field location and orientation at a particular resonance wavelength. The composite field plot at 393 nm, is shown in Figure 5 - 2 along with its field enhancement scale. The maximum enhancement for this wavelength is 1085 and occurs

on the middle slice of the particle. A summary of the spectral and field information for the 40 nm AgNS is plotted in Figure 5 - 1b. In addition to the field contour, a plot of the individual dipoles that make up the particle and their orientation was generated for each particle slice. Hereafter, a minus sign will be used to represent when the field vectors are pointing away from an area and a plus sign will be used to represent when the field vectors are all pointing towards an area (Figure 5 - 3).

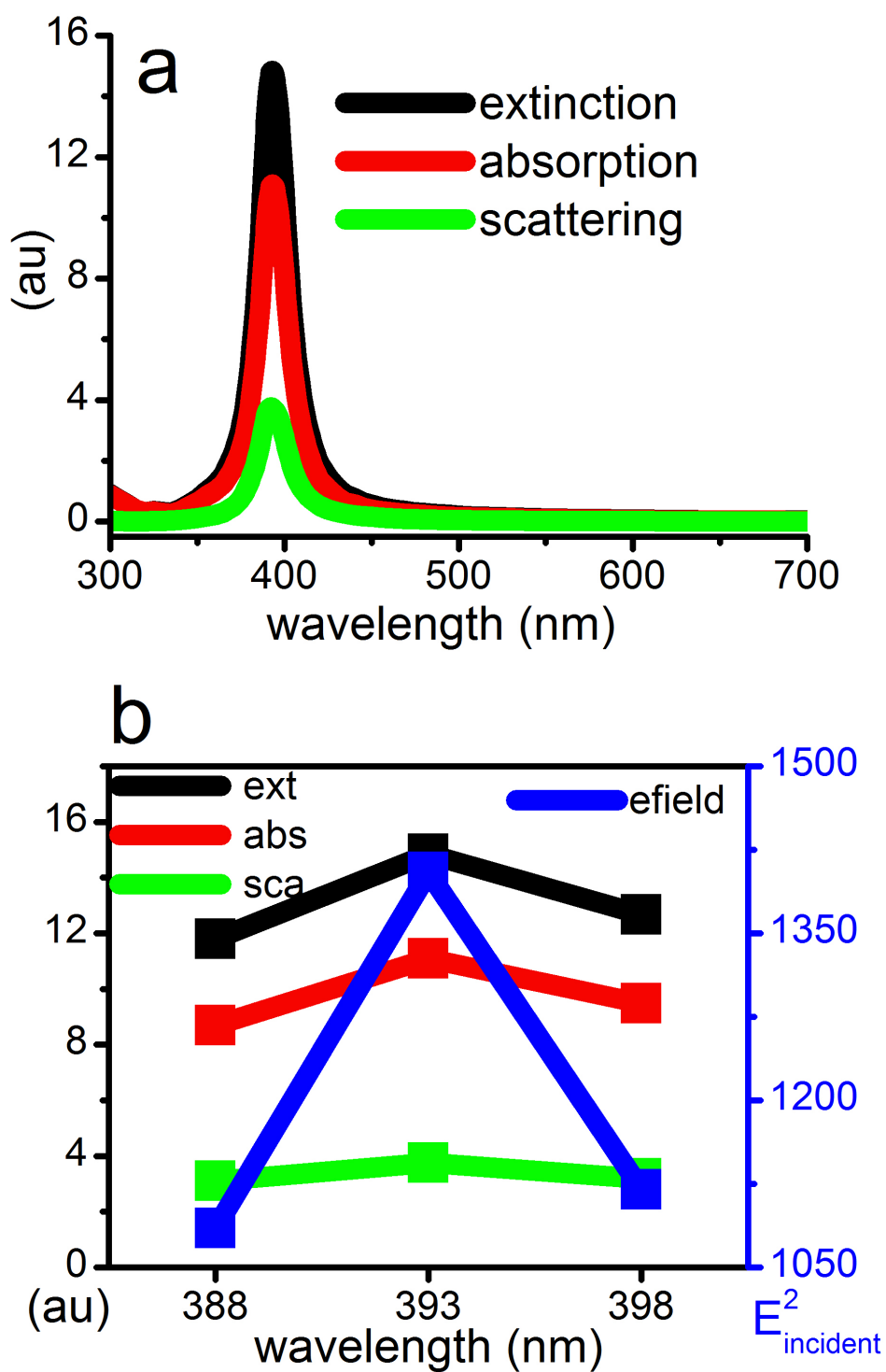


Figure 5 - 1. a) DDA extinction (black), absorption (red) and scattering (green) spectra for a 40 nm AgNS in water. b) Comparison of spectral value trends with field enhancement trends for the dipole mode of a 40 nm AgNS. It can be seen that the maximum in field strength corresponds to the maximum spectral values.



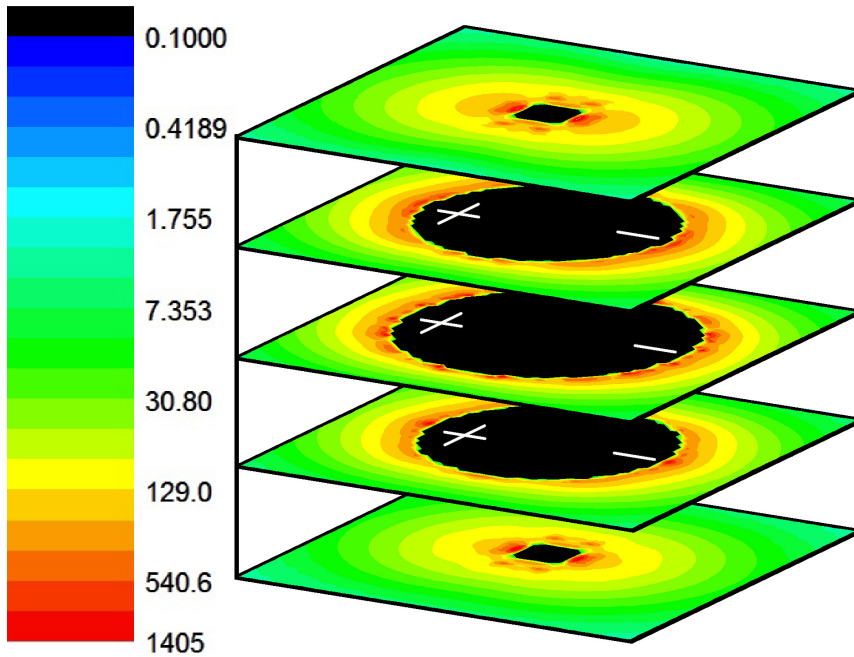


Figure 5 - 2. Three-dimensional representation for the electric field enhancement of a 40 nm AgNS when excited with a wavelength of 393 nm. The field location and field vector orientations indicate that this is the dipole mode.

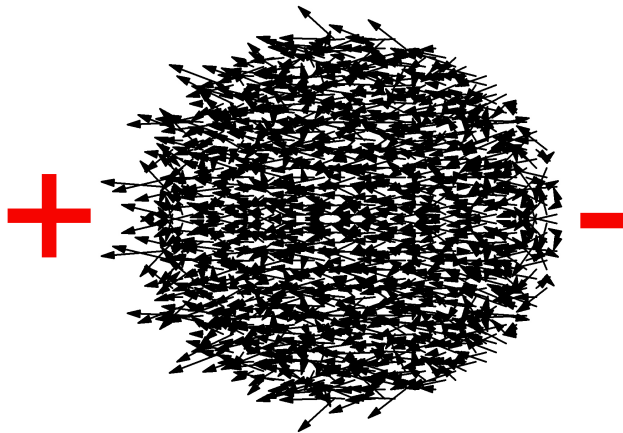


Figure 5 - 3. Representative field vector plot (middle slice of a 40 nm AgNS at 393 nm). As shown, a plus sign will indicate when all the vectors are pointing towards an area, and a minus sign indicates when all the vectors are pointing away from an area.

The composite field plot for the AgNS at 393 nm has the field vectors pointing away from the left side and towards the right side throughout the entire particle. This corresponds to the most primitive dipole mode for the particle, which is the largest extinction peak. Similar investigations were carried out slightly off resonance at 388 nm and 398 nm (Figure 5 - 4 and Figure 5 - 5). The field location and orientation is the same as that seen at 393 nm; these two wavelengths also correspond to the dipole mode. The spectral values and field intensities for all three wavelengths are plotted in Figure 5 - 1b, and the highest field enhancement is found where the maximum extinction and absorption values occur at 393 nm.

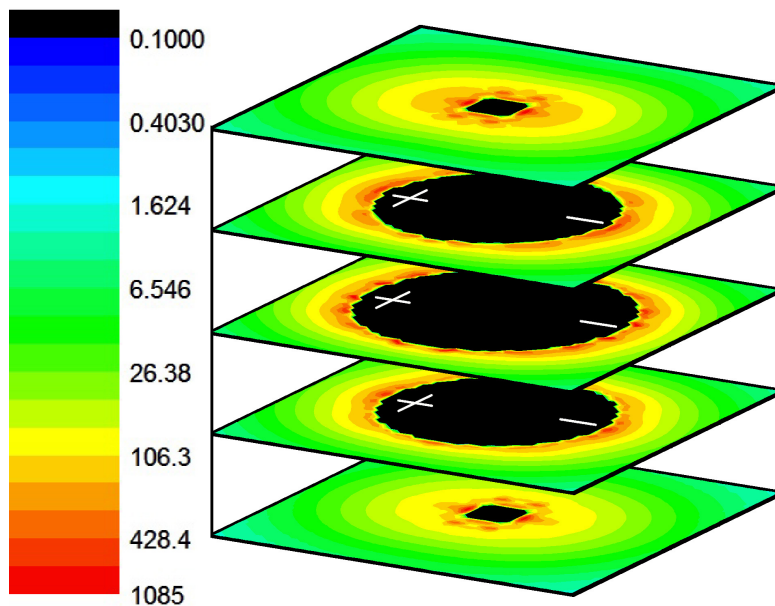


Figure 5 - 4. Three-dimensional representation for the electric field enhancement of a 40 nm AgNS when excited with a wavelength of 388 nm.

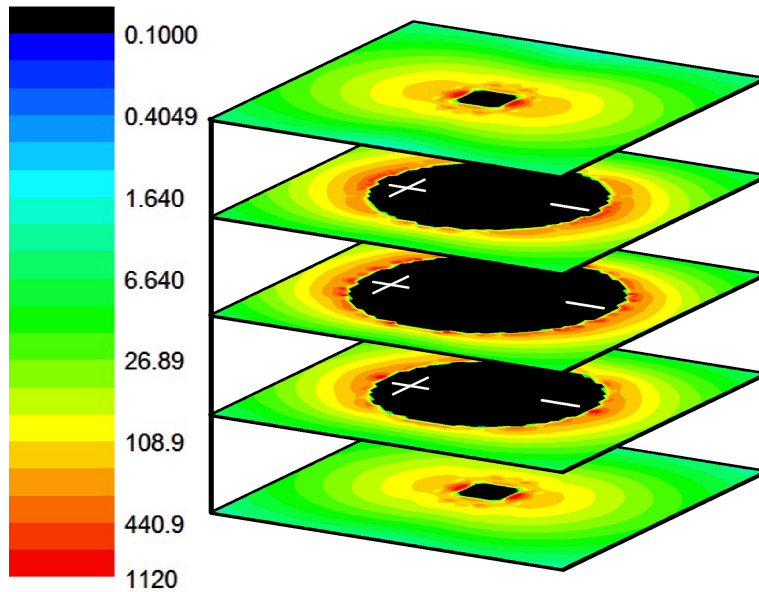


Figure 5 - 5. Three-dimensional representation for the electric field enhancement of a 40 nm AgNS when excited with a wavelength of 398 nm.

In the case of the 40 nm silver nanosphere, we see that the three-dimensional field modeling can be used to accurately assign different plasmon modes based on the field contour and orientation. Additionally, the field maximum occurs at the absorbance maximum, which in this case coincides with the extinction maximum, as there is very little contribution from scattering.

#### 5.4.2 40 nm Silver Nanocube

Next, we wanted to use this three-dimensional field mapping to examine particles with more complex spectral features. It has previously been shown that silver nanocubes (AgNCs) exhibit multiple spectral peaks and can have a significant contribution from

scattering when the AgNC is of sufficient size (>30 nm).<sup>29-32</sup> Therefore, we first considered a silver nanocube (AgNC) with a 40 nm edge length.

The DDA extinction (black), absorption (red) and scattering (green) spectra for a 40 nm AgNC are shown in Figure 5 - 6a. At this size, absorption dominates scattering, but there is still a substantial contribution from scattering. It is also apparent that there are multiple bands, though at this size they are reasonably well separated. The first wavelength investigated was 475 nm, which is slightly off resonance for the peak appearing furthest to the red. The composite field plot for 475 nm is shown in Figure 5 - 7. It can be seen that the field is located at the corners of the particle in each slice. Also, the orientation of the field vectors corresponds to the most primitive dipole mode for the particle; this is also the largest extinction peak occurring furthest to the red.

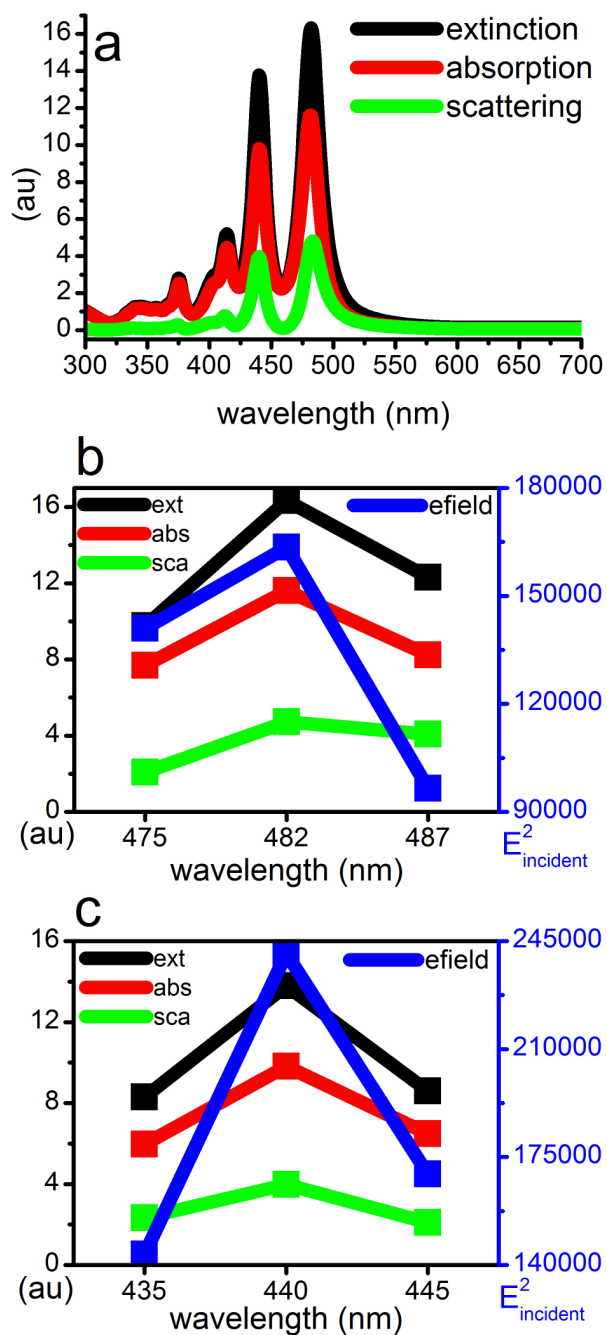


Figure 5 - 6. a) DDA extinction (black), absorption (red) and scattering (green) spectra for a AgNC in water with a 40 nm edge length. Higher order modes are present, but the modes are well separated. Absorption dominates scattering. b) Comparison of spectral value trends with field enhancement trends for the dipole mode of a 40 nm AgNC. The maximum field strength occurs at the spectral maxima, which all coincide. c) Comparison of spectral value trends with field enhancement trends for the quadrupole mode of a 40 nm AgNC. The maximum field strength occurs at the spectral maxima, which all coincide.

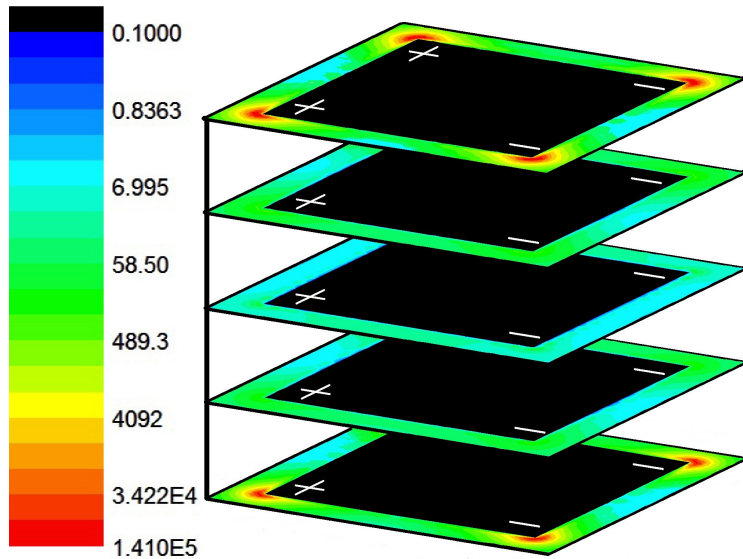


Figure 5 - 7. Three-dimensional representation for the electric field enhancement of a 40 nm AgNC when excited with a wavelength of 475 nm. The field locations and field vector orientations indicate that this is the dipole mode.

The next two wavelengths considered for the 40 nm AgNC were 482 nm and 487 nm (Figure 5 - 8 and Figure 5 - 9, respectively). Both wavelengths have the same field location and orientation as was seen for 475 nm, meaning both 482 nm and 487 nm also correspond to the dipole mode for the 40 nm AgNC. There is an increase in the field enhancement maximum from 475 nm to 482 nm and a decrease from 482 nm to 487 nm, with corresponding trends in the spectral values (Figure 5 - 6b).

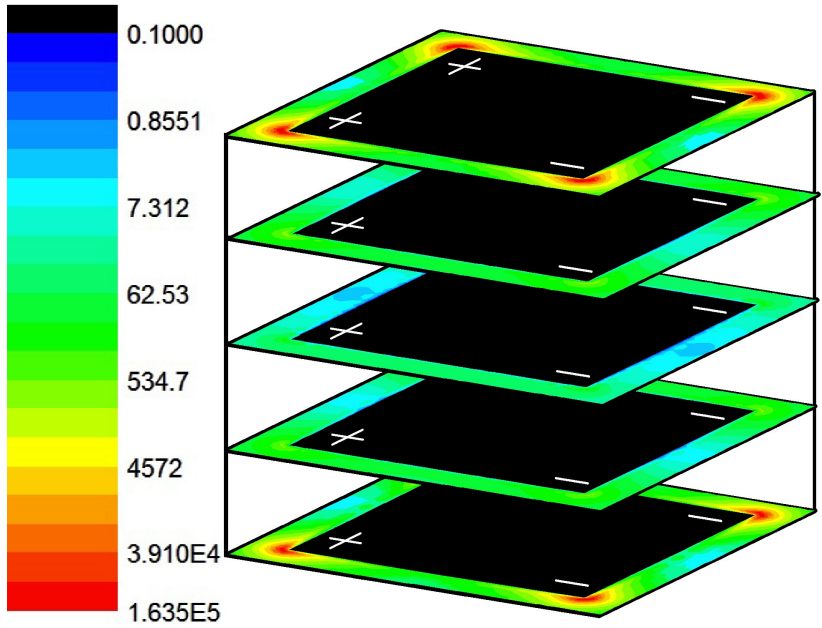


Figure 5 - 8. Three-dimensional representation for the electric field enhancement of a 40 nm AgNC when excited with a wavelength of 482 nm.

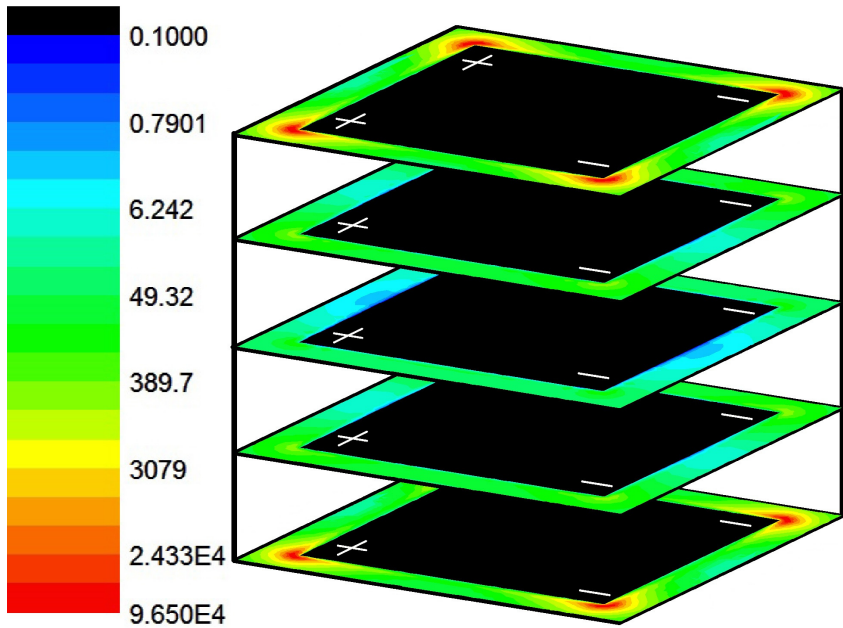


Figure 5 - 9. Three-dimensional representation for the electric field enhancement of a 40 nm AgNC when excited with a wavelength of 487 nm.

Next, we considered the band at 435 nm. Unlike what has been seen previously, the field orientation is not the same for all five slices (Figure 5 - 10). Here, the top and bottom of the particle have the same field orientation, with the field vectors pointing away from the left and towards the right, while the interior of the particle has the opposite field vector orientation, pointing away from the right and towards the left. These field orientations suggest a quadrupole mode.

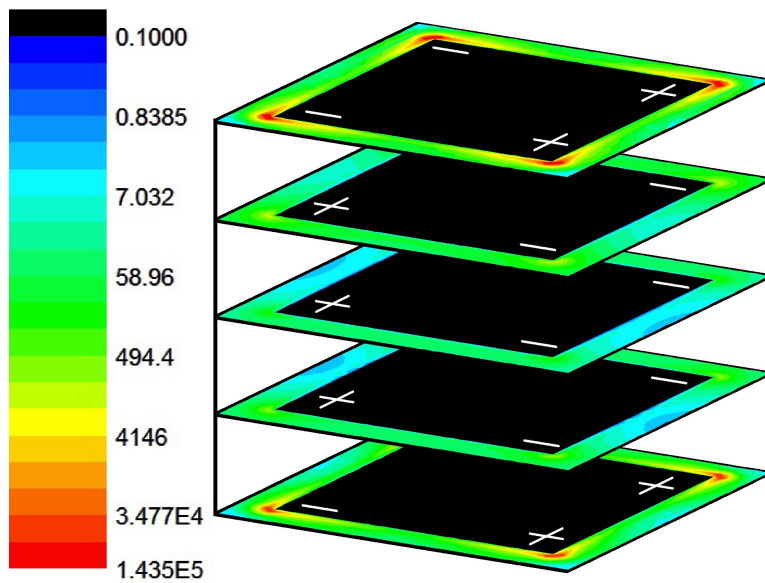


Figure 5 - 10. Three-dimensional representation for the electric field enhancement of a 40 nm AgNC when excited with a wavelength of 435 nm. The field location and field vector orientations indicate that this is the quadrupole mode.



The wavelengths 440 nm and 445 nm were both found to correspond to the quadrupole mode, as indicated by their composite field plots (Figure 5 - 11 and Figure 5 - 12). For the 40 nm AgNC, the field enhancement maximum increases from 435 nm to 440 nm, then decreases from 440 nm to 445 nm with corresponding trends in the spectral values (Figure 5 - 6c). It is interesting to note that the maximum field enhancement for the quadrupole mode is greater than what is seen for the dipole mode.

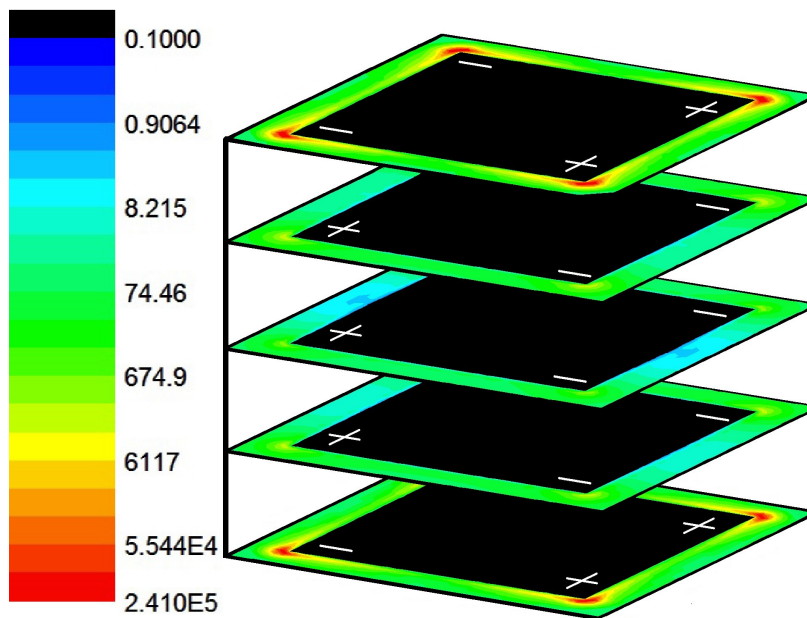


Figure 5 - 11. Three-dimensional representation for the electric field enhancement of a 40 nm AgNC when excited with a wavelength of 440 nm.

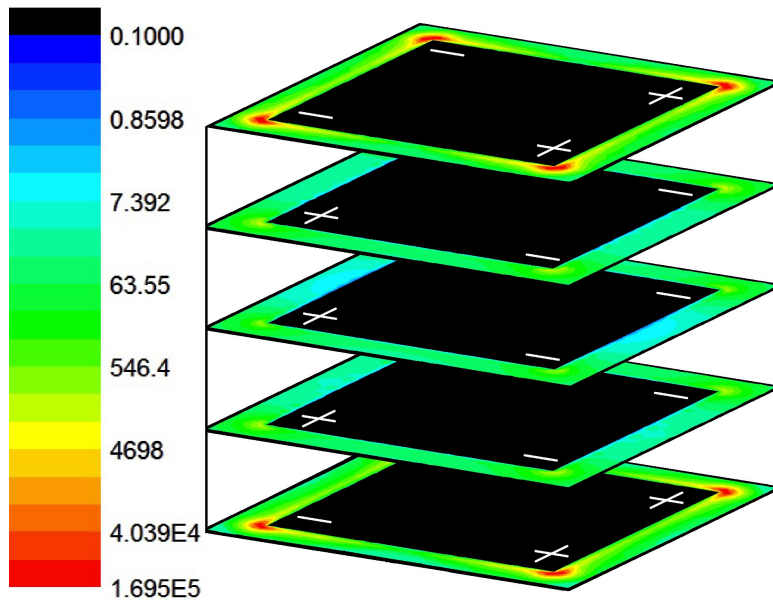


Figure 5 - 12. Three-dimensional representation for the electric field enhancement of a 40 nm AgNC when excited with a wavelength of 445 nm.

#### 5.4.3 60 nm Silver Nanocube

The 40 nm AgNC allows for investigation of multiple modes, but the spectra are still fairly simple; the modes are well separated from one another, and absorption still dominates scattering. Next we considered an even larger silver cube (60 nm), to increase the contribution from scattering (Figure 5 - 13a).<sup>1-3</sup> By comparison with the spectra for the 40 nm AgNC (Figure 5 - 6a) there is considerably higher contribution from scattering than was seen for the smaller particle, as expected. Despite the increase in contribution from scattering, the multiple bands still remain fairly well distinguished.

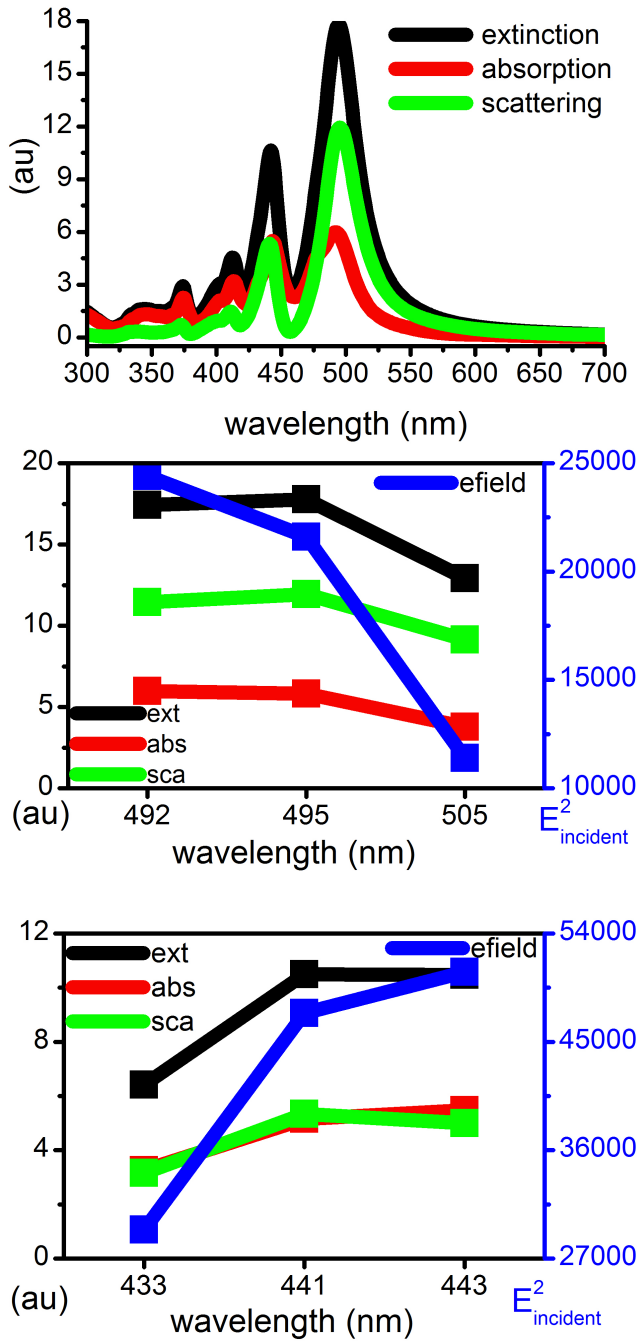


Figure 5 - 13. a) DDA extinction (black), absorption (red) and scattering (green) spectra for a AgNC in water with a 60 nm edge length. Higher order modes are present, but the modes are well separated. Scattering dominates absorption. b) Comparison of spectral value trends with field enhancement trends for the dipole mode of a 60 nm AgNC. The maximum field strength trends with the absorption, not the scattering or extinction. c) Comparison of spectral value trends with field enhancement trends for the quadrupole mode of a 60 nm AgNC. The maximum field strength trends with the absorption, not the scattering or extinction.

It was found that wavelengths 433 nm, 441 nm and 443 nm all corresponded to the quadrupole mode for the 60 nm AgNC, as indicated by their composite field plots (Figure 5 - 14, Figure 5 - 15 and Figure 5 - 16). However, an interesting trend was observed for the field strength. It can be seen in Figure 5 - 13c that the field increases from 433 nm to 441 nm and reaches a maximum at 443 nm. The absorption value follows the same trend as the field strength maximum, increasing from 433 nm to 443 nm, while the extinction and scattering values do not. Thus, for this particle whose scattering contributes more to the extinction than the absorption does, the absorption value is a better indicator of field strength within a single plasmon mode than is the extinction.

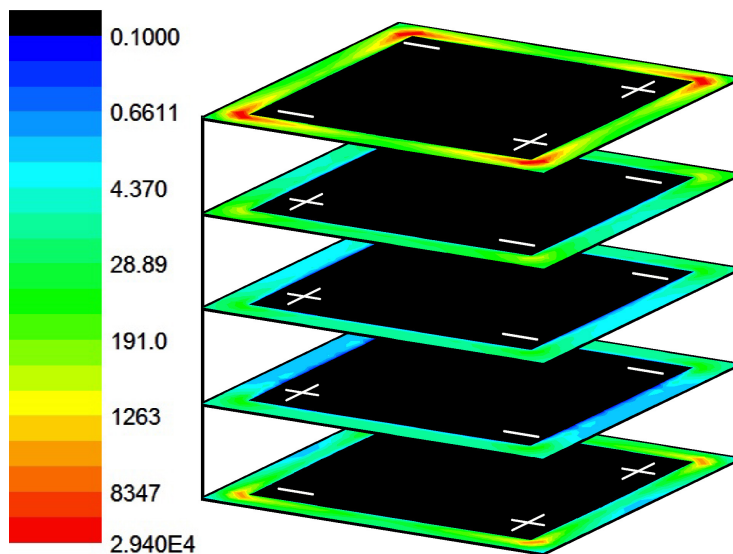


Figure 5 - 14. Three-dimensional representation for the electric field enhancement of a 60 nm AgNC when excited with a wavelength of 433 nm. The field location and field vector orientations indicate that this is the quadrupole mode.

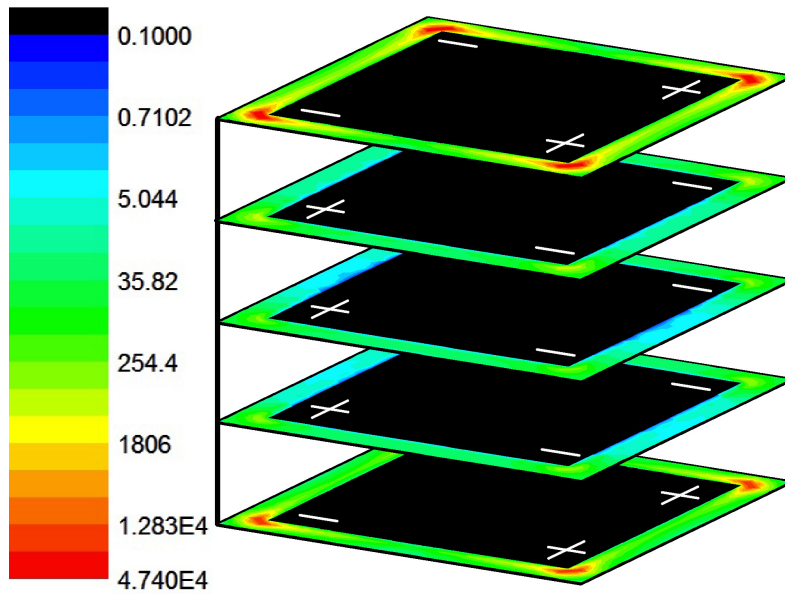


Figure 5 - 15. Three-dimensional representation for the electric field enhancement of a 60 nm AgNC when excited with a wavelength of 441 nm.

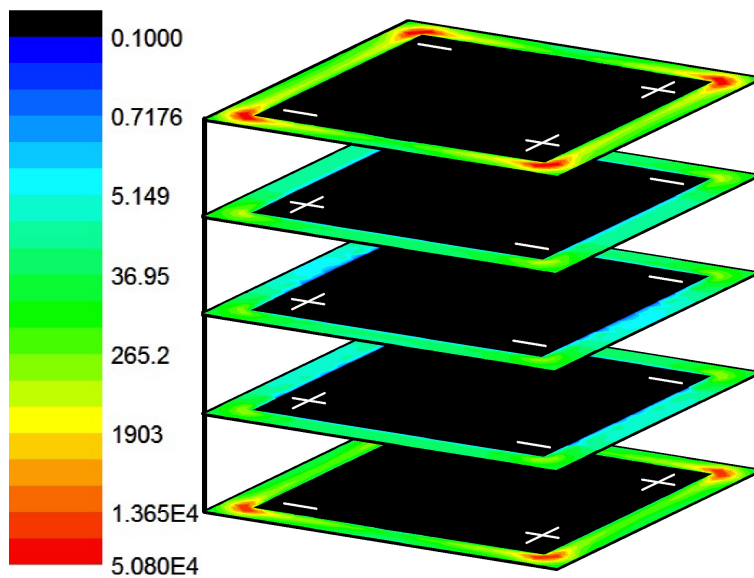


Figure 5 - 16. Three-dimensional representation for the electric field enhancement of a 60 nm AgNC when excited with a wavelength of 443 nm.

Next, we examined the dipole mode at 492, 495 and 505 nm (Figure 5 - 17, Figure 5 - 18 and Figure 5 - 19). Again we see that the field strength trends with the absorption and not with the scattering or extinction for this plasmon mode (Figure 5 - 13b).

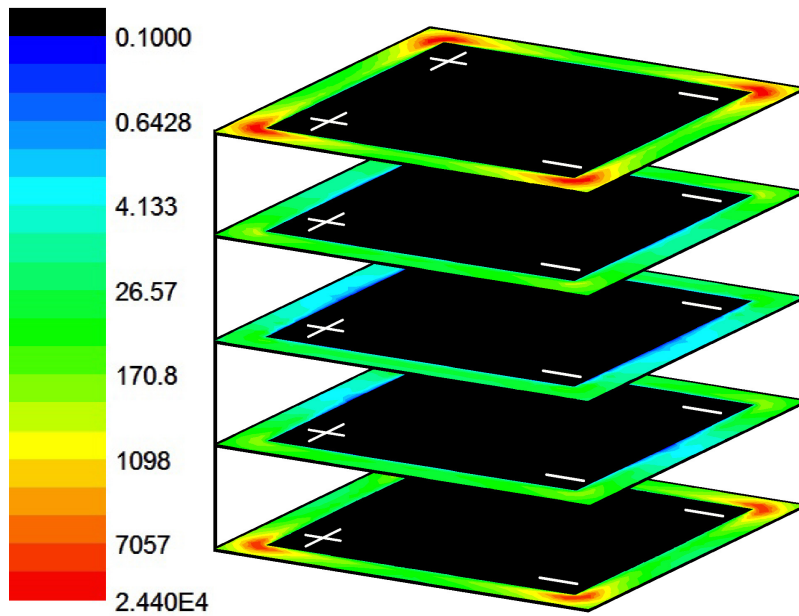


Figure 5 - 17. Three-dimensional representation for the electric field enhancement of a 60 nm AgNC when excited with a wavelength of 492 nm. The field location and field vector orientation indicate that this is the dipole mode.

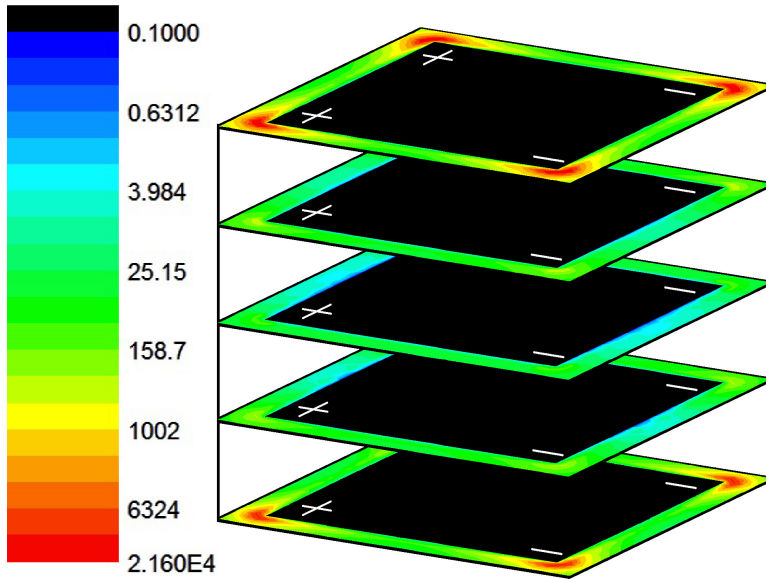


Figure 5 - 18. Three-dimensional representation for the electric field enhancement of a 60 nm AgNC when excited with a wavelength of 495 nm.

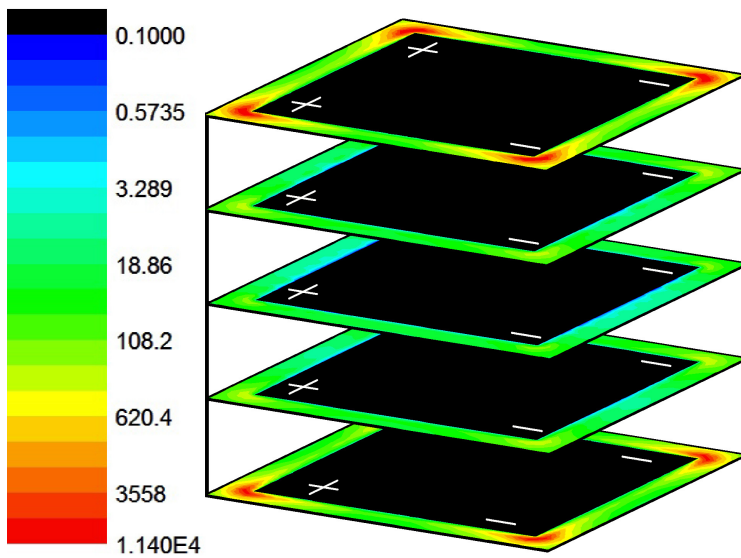


Figure 5 - 19. Three-dimensional representation for the electric field enhancement of a 60 nm AgNC when excited with a wavelength of 505 nm.

#### 5.4.4 86 nm Silver Nanocube

Finally, an even larger AgNC (86 nm) was studied to see if the plasmon modes could be distinguished despite a further increase in scattering as well as to further investigate the relation between field enhancement and absorption. For this particle, the scattering dominates the absorption to the point that the different plasmon bands begin to overlap in the extinction spectrum (Figure 5 - 20a). Here, more modes than the quadrupole and dipole were considered to determine the robustness of the three-dimensional particle composite field plot in distinguishing between modes. The data are presented in detail in Table 5-1 and discussed forthwith.



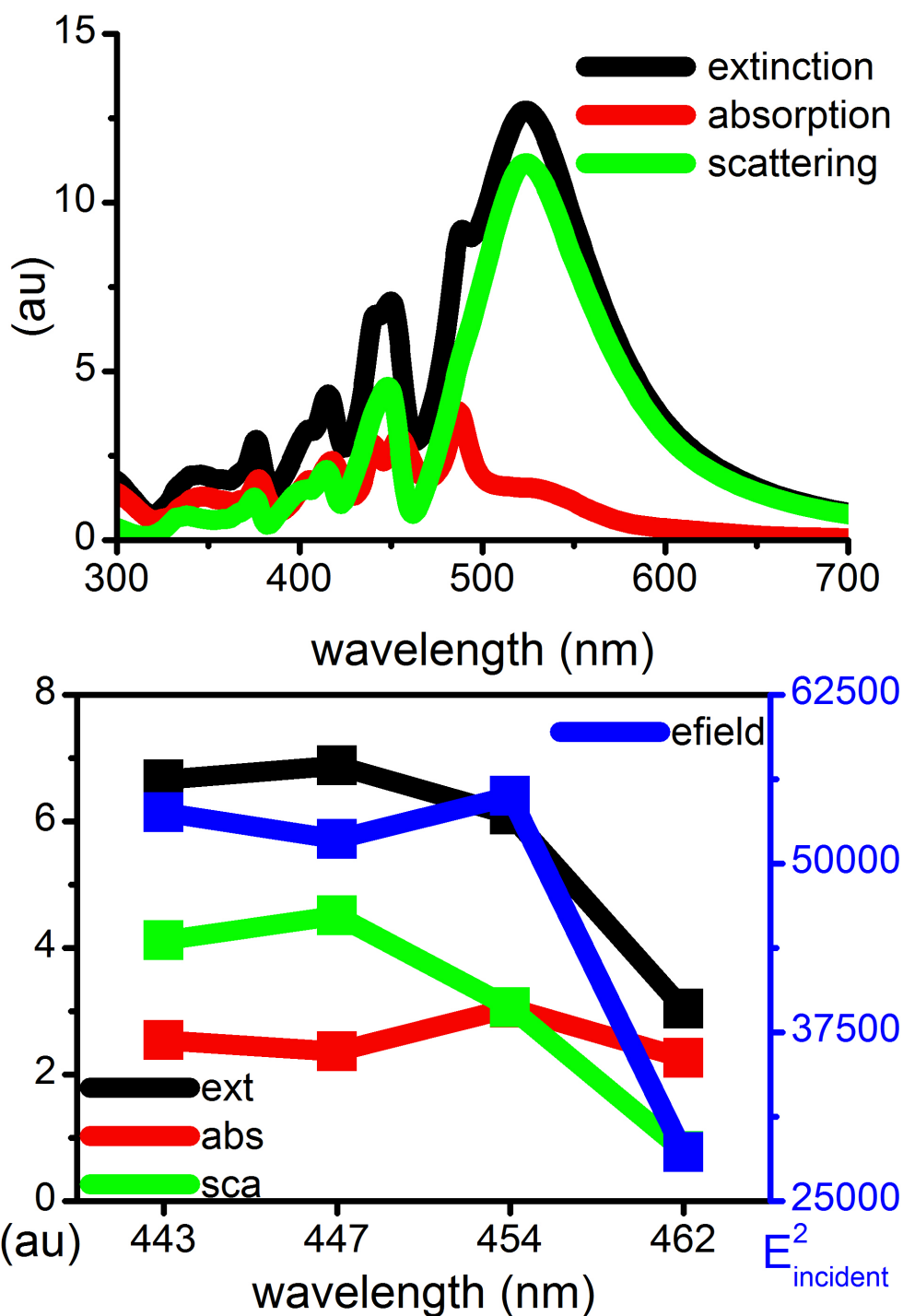


Figure 5 - 20. a) DDA extinction (black), absorption (red) and scattering (green) spectra for a AgNC in water with an 86 nm edge length. Higher order modes are present and there is considerable overlap between the modes. Scattering dominates absorption. b) Comparison of spectral value trends with field enhancement trends for the quadrupole mode of an 86 nm AgNC. The maximum field strength trends with the absorption, not the scattering or extinction.

Table 5-1. Summary of field plot data at different wavelength for 86 nm AgNC. "Extinction", "Absorption" and "Scattering" refer to the value for those spectra at the wavelength of interest. "Max. field" is the largest field enhancement value observed for any slice of the particle.

Wavelength (nm)	Extinction (au)	Absorption (au)	Scattering (au)	Max. field ( $E^2_{\text{incident}}$ )
377.5	2.8798	1.8112	1.0686	1035
405	3.2813	1.7844	1.4969	1080
417	4.2174	2.3387	1.8787	7640
440	6.5549	2.8394	3.7156	48400
443	6.6572	2.5413	4.1159	53800
447	6.8790	2.3658	4.5132	51800
454	6.106	3.0495	3.0565	55000
462	3.0401	2.256	0.7841	28600
470.5	3.6499	1.8359	1.814	15500
487	9.0214	3.8126	5.2088	35600
523	12.727	1.5617	11.165	6400

#### 5.4.4.1 Higher Order Multipoles

It was found that the wavelengths 377.5, 405, 417 and 440 nm all corresponded to distinct higher order plasmon modes (Figure 5 - 21, Figure 5 - 22, Figure 5 - 23 and Figure 5 - 24), as indicated by their complex but distinct field locations and field vector orientations. These results show that the three-dimensional modeling can be applied to distinguish between even very complicated higher order plasmon modes.

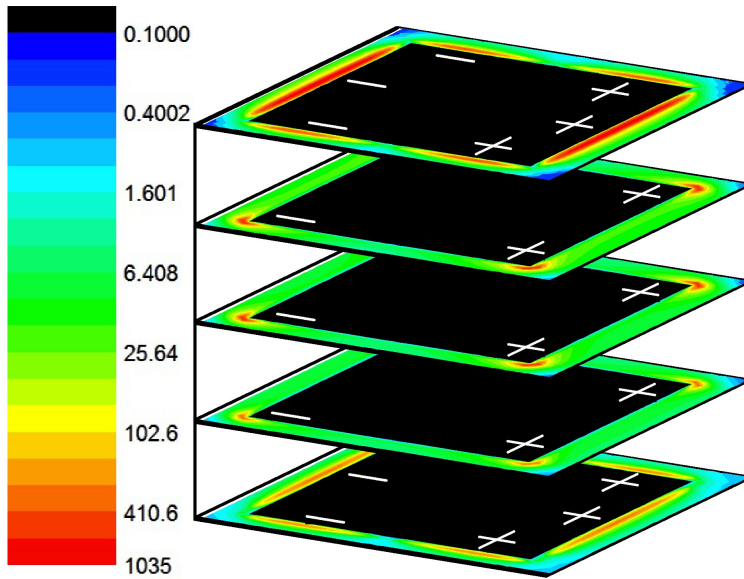


Figure 5 - 21. Three-dimensional representation for the electric field enhancement of an 86 nm AgNC when excited with a wavelength of 377.5 nm. The field locations and field vector orientations indicate that this is a higher order multipole mode.

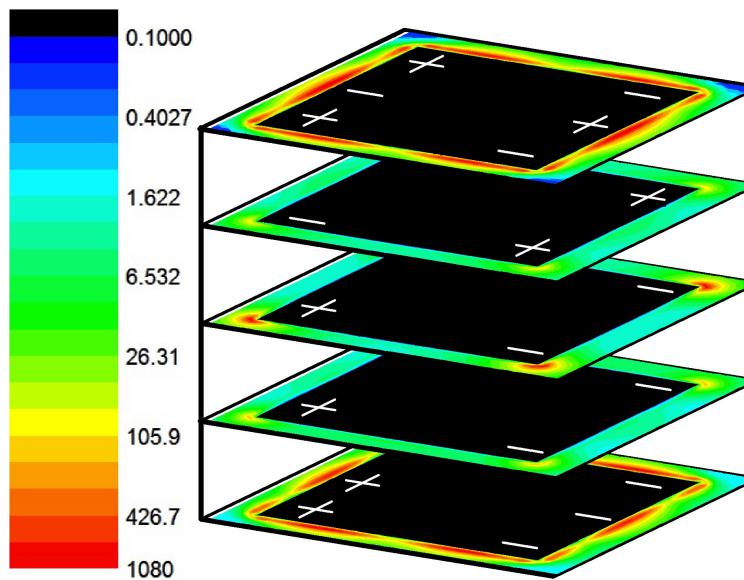


Figure 5 - 22. Three-dimensional representation for the electric field enhancement of an 86 nm AgNC when excited with a wavelength of 405 nm. The field locations and field vector orientations indicate that this is a higher order multipole mode.

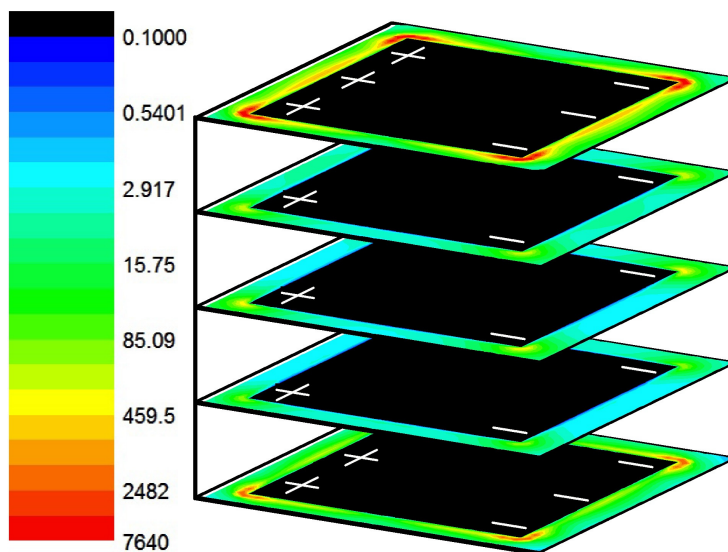


Figure 5 - 23. Three-dimensional representation for the electric field enhancement of an 86 nm AgNC when excited with a wavelength of 417 nm. The field locations and field vector orientations indicate that this is a higher order multipole mode.

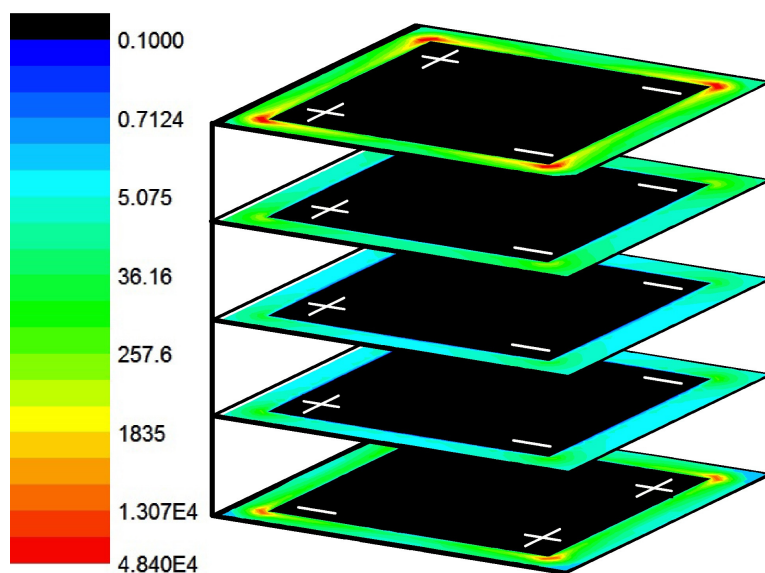


Figure 5 - 24. Three-dimensional representation for the electric field enhancement of an 86 nm AgNC when excited with a wavelength of 440 nm. The field locations and field vector orientations indicate that this is a higher order multipole mode.

#### 5.4.4.2 Quadrupole and Dipole Modes

The wavelengths 443, 447, 454 and 462 nm were all found to correspond to the quadrupole mode (Figure 5 - 25, Figure 5 - 26, Figure 5 - 27 and Figure 5 - 28), as indicated by the field contour and field vector orientations. As was previously seen, the maximum field strength trends with the absorbance and not with the scattering or extinction values (Figure 5 - 20b).

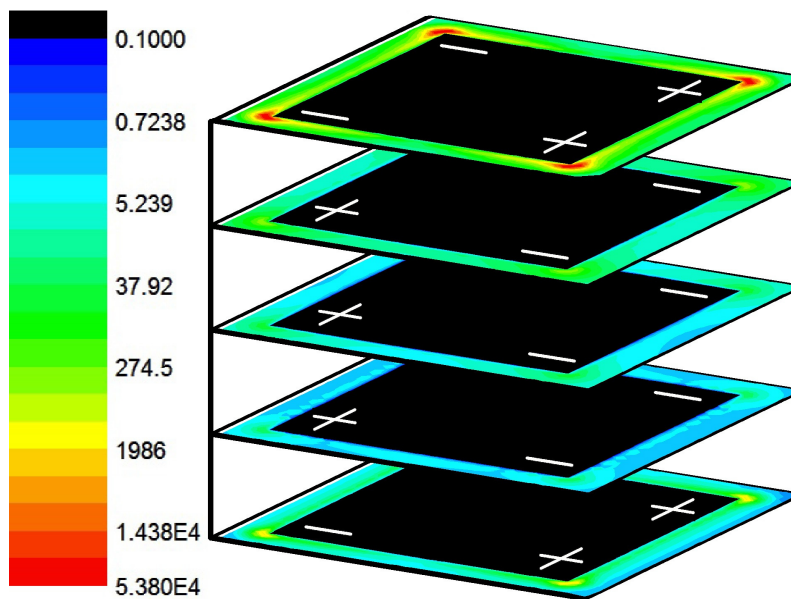


Figure 5 - 25. Three-dimensional representation for the electric field enhancement of an 86 nm AgNC when excited with a wavelength of 443 nm. The field locations and field vector orientations indicate that this is the quadrupole mode.

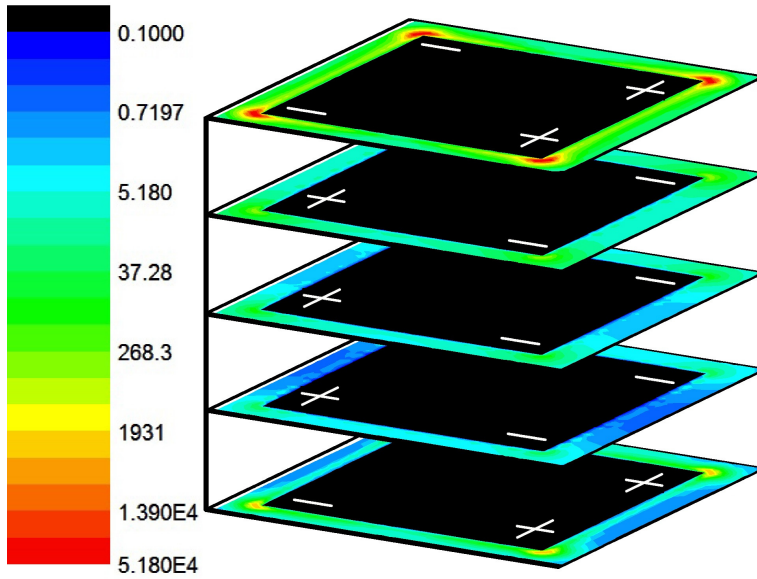


Figure 5 - 26. Three-dimensional representation for the electric field enhancement of an 86 nm AgNC when excited with a wavelength of 447 nm.

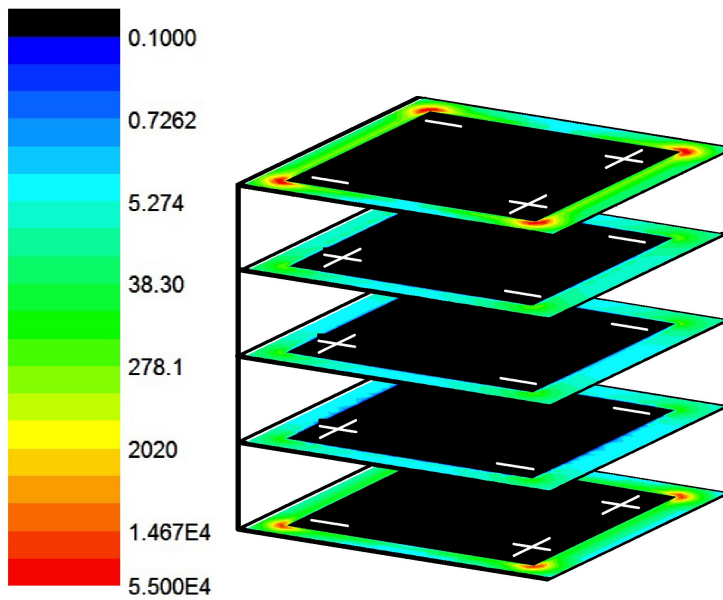


Figure 5 - 27. Three-dimensional representation for the electric field enhancement of an 86 nm AgNC when excited with a wavelength of 454 nm.

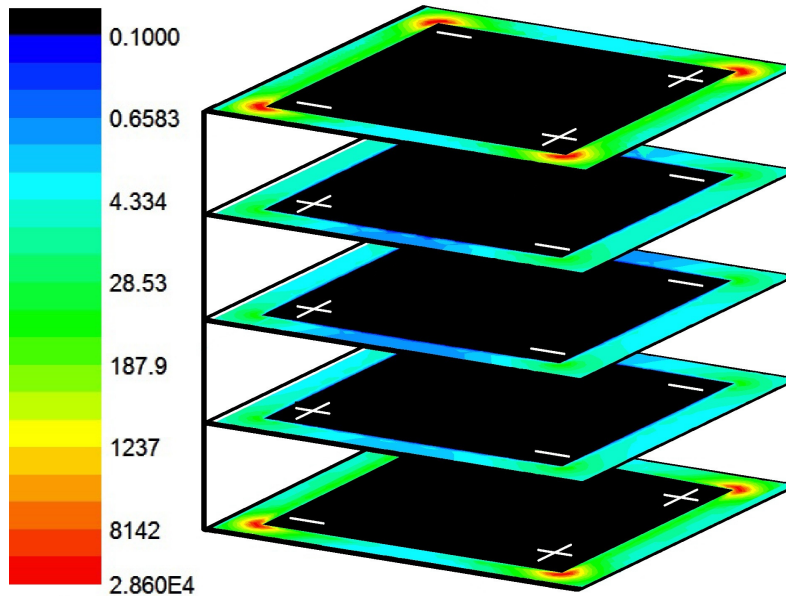


Figure 5 - 28. Three-dimensional representation for the electric field enhancement of an 86 nm AgNC when excited with a wavelength of 462 nm.

The wavelengths 470.5 and 487 nm were found to correspond to a different mode that is a mixture of the quadrupole and dipole modes (Figure 5 - 29 and Figure 5 - 30). For this mode, if only the field enhancement locations had been considered, then it might appear that this wavelength represented the same mode as the previous four (443, 447, 454 and 462 nm). Similarly, if only the top slice had been considered, which shows the strongest field enhancement in all cases, this mode would have appeared to be the quadrupole mode even if the dipole orientations had also been considered. These results in particular show the importance of basing mode assignments on thorough theoretical results.

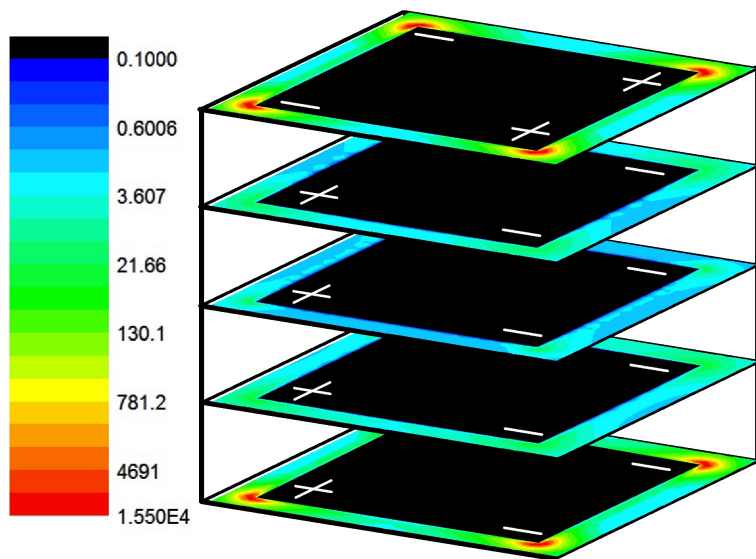


Figure 5 - 29. Three-dimensional representation for the electric field enhancement of an 86 nm AgNC when excited with a wavelength of 470.5 nm. The field locations and field vector orientations indicate that this is a hybrid between the quadrupole and dipole modes.

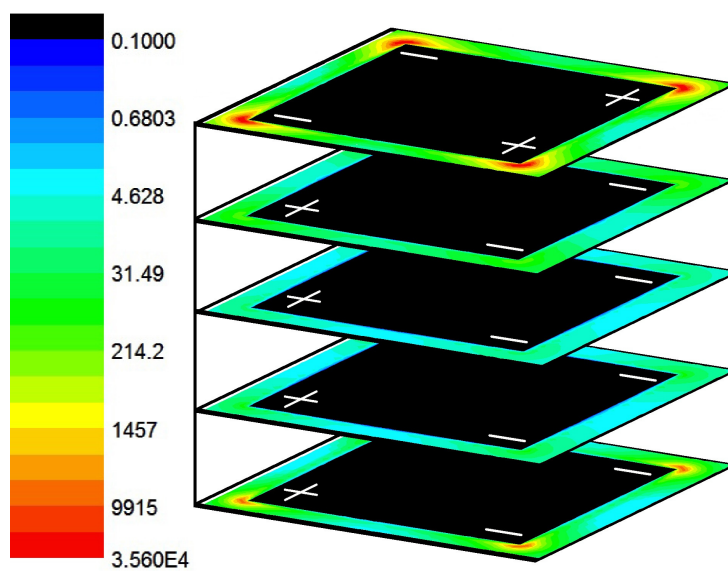


Figure 5 - 30. Three-dimensional representation for the electric field enhancement of an 86 nm AgNC when excited with a wavelength of 487 nm.



Finally, we examined 523 nm, which corresponds to the maximum of the large extinction peak. Here, the location of the field is focused at the corners and the field vectors are pointing away from the left and towards the right throughout the entirety of the particle (Figure 5 - 31). This corresponds to the most primitive dipole mode for the particle, which agrees with the fact that this is also the largest extinction peak. Interestingly, the maximum field enhancement is only 6400, which is an order of magnitude less than that seen for the last seven wavelengths. Although 523 nm corresponds to large peak in the extinction and scattering (Figure 5 - 20a), there is very little contribution from the absorption, thus there is little field enhancement. This agrees with our previous results that indicate the absorption is one of the key factors in determining which mode will give the highest field enhancement for AgNCs.

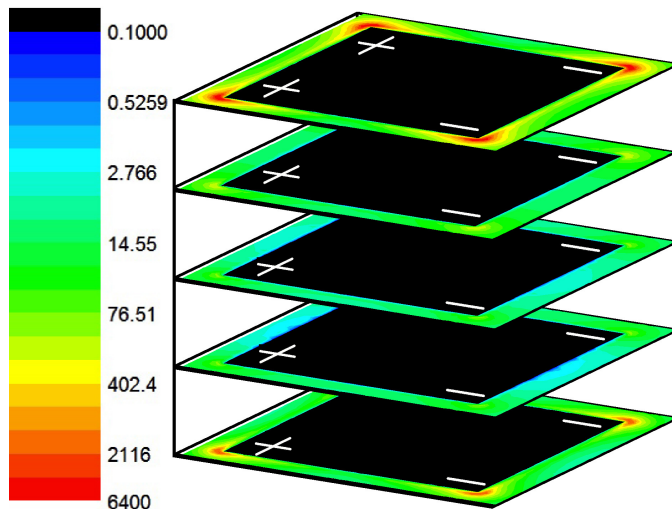


Figure 5 - 31. Three-dimensional representation for the electric field enhancement of an 86 nm AgNC when excited with a wavelength of 523 nm. The field locations and field vector orientations indicate that this is the dipole mode.

In the case of silver nanocubes, we see we can accurately assign multiple plasmon modes from more complicated spectra using the three-dimensional field modeling. As the contribution from scattering increases (i.e. as the size of the AgNC increases) it becomes apparent that the field strength depends on the absorption, and not the extinction or scattering.

## **5.5 Conclusions**

We have completed a thorough and systematic investigation of the plasmon modes of a 40 nm AgNS and various sizes of AgNCs. Our results show that there are multiple distinct plasmon modes for AgNCs, and specifically that there is a significant contribution to the spectra from the quadrupole and dipole modes. We also showed that consideration of the field distribution and orientation in three dimensions is necessary for accurate description and assignment of the plasmon modes for AgNCs.

We found for all three AgNC sizes considered that the quadrupole mode results in a higher maximum field enhancement than the dipole mode. Further, we found an interesting relationship between the spectral values and field intensity for the AgNCs. Specifically, when the contribution from scattering is greater than that from absorption, the field strength within a plasmon mode of a AgNC trends with the absorption values and not with the extinction or scattering. It seems safe to conclude that this is always the case for AgNCs. However, this distinction becomes less necessary when there is a small

contribution from scattering, as the extinction and absorption peaks become more coincidental. Experimentally, it is typically the extinction spectrum that is collected, and this could be misleading in choosing the resonance wavelength for maximum field enhancement of AgNCs if there is a significant contribution from scattering (e.g. in large AgNCs).

We should now point out that the relationship between absorption and field strength is not absolute, but only can be used within one mode for one particle at a time. This means that for the same mode in two different-sized AgNCs, a higher absorption value for one particle size does not necessarily indicate a higher maximum field enhancement for that particle compared to the other. Second, the absorption values cannot be compared between modes within a single AgNC to determine which will have a higher field. In fact, our results for all three sizes of AgNC considered show that the quadrupole mode results in the highest maximum field enhancement, not the dipole mode, even though in some cases the absorption value for the dipole peak was higher than the quadrupole peak. All these trends simply point out that a thorough theoretical investigation is needed to accurately assign the plasmon modes and choose the wavelength most appropriate for applications using AgNCs.

Our results indicate that plasmon field strength of AgNCs trends with absorption, which indicates the necessity of thorough theoretical investigation to choose the appropriate wavelength for maximum field enhancement for applications using AgNCs. This is

especially true for particles with a significant quadrupole mode and/or a substantial contribution from scattering

## 5.6 References

- (1) Jain, P. K.; Lee, K. S.; El-Sayed, I. H.; El-Sayed, M. A. Calculated absorption and scattering properties of gold nanoparticles of different size, shape, and composition: Applications in biological imaging and biomedicine. *J. Phys. Chem. B* **2006**, *110*, 7238-7248.
- (2) Lee, K. S.; El-Sayed, M. A. Dependence of the enhanced optical scattering efficiency relative to that of absorption for gold metal nanorods on aspect ratio, size, end-cap shape, and medium refractive index. *J. Phys. Chem. B* **2005**, *109*, 20331-20338.
- (3) Lee, K. S.; El-Sayed, M. A. Gold and silver nanoparticles in sensing and imaging: Sensitivity of plasmon response to size, shape, and metal composition. *J. Phys. Chem. B* **2006**, *110*, 19220-19225.
- (4) Alivisatos, P. The use of nanocrystals in biological detection. *Nature Biotechnology* **2004**, *22*, 47-52.
- (5) Corot, C.; Robert, P.; Idee, J. M.; Port, M. Recent advances in iron oxide nanocrystal technology for medical imaging. *Advanced Drug Delivery Reviews* **2006**, *58*, 1471-1504.
- (6) El-Sayed, I. H.; Huang, X. H.; El-Sayed, M. A. Surface plasmon resonance scattering and absorption of anti-EGFR antibody conjugated gold nanoparticles in cancer diagnostics: Applications in oral cancer. *Nano Lett.* **2005**, *5*, 829-834.
- (7) Gao, X. H.; Cui, Y. Y.; Levenson, R. M.; Chung, L. W. K.; Nie, S. M. In vivo cancer targeting and imaging with semiconductor quantum dots. *Nature Biotechnology* **2004**, *22*, 969-976.
- (8) Gobin, A. M.; Lee, M. H.; Halas, N. J.; James, W. D.; Drezek, R. A.; West, J. L. Near-infrared resonant nanoshells for combined optical imaging and photothermal cancer therapy. *Nano Lett.* **2007**, *7*, 1929-1934.
- (9) Ito, A.; Shinkai, M.; Honda, H.; Kobayashi, T. Medical application of functionalized magnetic nanoparticles. *Journal of Bioscience and Bioengineering* **2005**, *100*, 1-11.
- (10) Atwater, H. A.; Polman, A. Plasmonics for improved photovoltaic devices. *Nature Materials* **2010**, *9*, 205-213.
- (11) Kamat, P. V. Meeting the clean energy demand: Nanostructure architectures for solar energy conversion. *Journal of Physical Chemistry C* **2007**, *111*, 2834-2860.

- (12) Yen, C. W.; Hayden, S. C.; Dreaden, E. C.; Szymanski, P.; El-Sayed, M. A. Tailoring Plasmonic and Electrostatic Field Effects To Maximize Solar Energy Conversion by Bacteriorhodopsin, the Other Natural Photosynthetic System. *Nano Lett.* **2011**, *11*, 3821-3826.
- (13) Boisselier, E.; Astruc, D. Gold nanoparticles in nanomedicine: preparations, imaging, diagnostics, therapies and toxicity. *Chemical Society Reviews* **2009**, *38*, 1759-1782.
- (14) Huang, X. H.; Kang, B.; Qian, W.; Mackey, M. A.; Chen, P. C.; Oyelere, A. K.; El-Sayed, I. H.; El-Sayed, M. A. Comparative study of photothermalysis of cancer cells with nuclear-targeted or cytoplasm-targeted gold nanospheres: continuous wave or pulsed lasers. *Journal of Biomedical Optics* **2010**, *15*.
- (15) Loo, C.; Lowery, A.; Halas, N. J.; West, J.; Drezek, R. Immunotargeted nanoshells for integrated cancer imaging and therapy. *Nano Lett.* **2005**, *5*, 709-711.
- (16) Dreaden, E. C.; Mwakwari, S. C.; Sodji, Q. H.; Oyelere, A. K.; El-Sayed, M. A. Tamoxifen-Poly(ethylene glycol)-Thiol Gold Nanoparticle Conjugates: Enhanced Potency and Selective Delivery for Breast Cancer Treatment. *Bioconjugate Chemistry* **2009**, *20*, 2247-2253.
- (17) Giljohann, D. A.; Seferos, D. S.; Daniel, W. L.; Massich, M. D.; Patel, P. C.; Mirkin, C. A. Gold Nanoparticles for Biology and Medicine. *Angew. Chem.-Int. Edit.* **2010**, *49*, 3280-3294.
- (18) West, J. L.; Halas, N. J. Engineered nanomaterials for biophotonics applications: Improving sensing, imaging, and therapeutics. *Annual Review of Biomedical Engineering* **2003**, *5*, 285-292.
- (19) Hao, E.; Schatz, G. C. Electromagnetic fields around silver nanoparticles and dimers. *J. Chem. Phys.* **2004**, *120*, 357-366.
- (20) Kelly, K. L.; Coronado, E.; Zhao, L. L.; Schatz, G. C. The optical properties of metal nanoparticles: The influence of size, shape, and dielectric environment. *J. Phys. Chem. B* **2003**, *107*, 668-677.
- (21) Halas, N. J. Playing with plasmons. Tuning the optical resonant properties of metallic nanoshells. *MRS Bull.* **2005**, *30*, 362-367.
- (22) Olson, T. Y.; Schwartzberg, A. M.; Orme, C. A.; Talley, C. E.; O'Connell, B.; Zhang, J. Z. Hollow gold-silver double-shell nanospheres: Structure, optical absorption, and surface-enhanced Raman scattering. *Journal of Physical Chemistry C* **2008**, *112*, 6319-6329.

- (23) Sun, Y. G.; Mayers, B.; Xia, Y. N. Metal nanostructures with hollow interiors. *Advanced Materials* **2003**, *15*, 641-646.
- (24) Wan, D. H.; Chen, H. L.; Lin, Y. S.; Chuang, S. Y.; Shieh, J.; Chen, S. H. Using Spectroscopic Ellipsometry to Characterize and Apply the Optical Constants of Hollow Gold Nanoparticles. *ACS Nano* **2009**, *3*, 960-970.
- (25) Draine, B. T.; Flatau, P. J. Discrete-Dipole Approximation for scattering calculations. *J. Opt. Soc. Am. A-Opt. Image Sci. Vis.* **1994**, *11*, 1491-1499.
- (26) Goodman, J. J.; Draine, B. T.; Flatau, P. J. Application of Fast-Fourier-Transform techniques to the Discrete-Dipole Approximation. *Optics Letters* **1991**, *16*, 1198-1200.
- (27) Shuford, K. L.; Ratner, M. A.; Schatz, G. C. Multipolar excitation in triangular nanoprisms. *J. Chem. Phys.* **2005**, *123*.
- (28) Johnson, P. B.; Christy, R. W. Optical-constants of noble-metals. *Physical Review B* **1972**, *6*, 4370-4379.
- (29) Mahmoud, M. A.; Tabor, C. E.; El-Sayed, M. A. Surface-Enhanced Raman Scattering Enhancement by Aggregated Silver Nanocube Monolayers Assembled by the Langmuir-Blodgett Technique at Different Surface Pressures. *Journal of Physical Chemistry C* **2009**, *113*, 5493-5501.
- (30) Siekkinen, A. R.; McLellan, J. M.; Chen, J. Y.; Xia, Y. N. Rapid synthesis of small silver nanocubes by mediating polyol reduction with a trace amount of sodium sulfide or sodium hydrosulfide. *Chemical Physics Letters* **2006**, *432*, 491-496.
- (31) Wiley, B. J.; Im, S. H.; Li, Z. Y.; McLellan, J.; Siekkinen, A.; Xia, Y. N. Maneuvering the surface plasmon resonance of silver nanostructures through shape-controlled synthesis. *J. Phys. Chem. B* **2006**, *110*, 15666-15675.
- (32) Zhou, F.; Li, Z. Y.; Liu, Y.; Xia, Y. N. Quantitative Analysis of Dipole and Quadrupole Excitation in the Surface Plasmon Resonance of Metal Nanoparticles. *Journal of Physical Chemistry C* **2008**, *112*, 20233-20240.

## CHAPTER VI

### PRONOUNCED EFFECTS OF ANISOTROPY ON THE PLASMONIC PROPERTIES OF NANORINGS FABRICATED BY ELECTRON BEAM LITHOGRAPHY

#### 6.1 Summary

Gold nanoring dimers were fabricated via EBL with dimensions of  $127.6 \pm 2.5$  nm and  $57.8 \pm 2.3$  nm for the outer and inner diameters, respectively, with interparticle separations ranging from  $17.8 \pm 3.4$  nm to  $239.2 \pm 3.7$  nm. The coupling between the inner and outer surfaces of a single nanoring renders it very sensitive to any anisotropy. We found that anisotropy in the particle geometry and anisotropy introduced by the substrate combine to create very unique spectral features in this system.

#### 6.2 Introduction

A unique feature of noble metal nanoparticles is their ability to support a localized surface plasmon resonance (LSPR) in response to an applied electric field, i.e. light.<sup>1-6</sup> The LSPR imbues the nanoparticles with intense near-field and far-field optical properties that make them attractive for a wide variety of applications including sensing,<sup>7-13</sup> imaging,<sup>14-20</sup> drug delivery,<sup>21-27</sup> and cancer therapy.<sup>22,28-31</sup> Recently, there has been increased interest in hollow nanostructures, as these can be more tunable and sensitive to



their environment than their solid particle analogs.<sup>30-33</sup> This sensitivity results from the strong intraparticle coupling that arises from the interaction between the plasmon supported on the outer surface and the plasmon supported on the inner surface of each hollow nanostructure.

The plasmonic properties of metal nanoparticles are dependent upon their size, shape, and composition as well as the dielectric of the surrounding medium.<sup>2,6,19</sup> It has been demonstrated that as two plasmonic particles are brought together, their near-fields begin to overlap and couple, which affects the plasmon resonance of the overall system.<sup>34-37</sup> Additionally, when plasmonic particles are small compared to their interparticle separation, they can be treated as dipolar excitons,<sup>38</sup> a fact that allows for the use of the exciton-coupling model to describe the plasmonic coupling of two interacting particles. If the plasmon dipoles are aligned in an attractive configuration, e.g. head-to-tail in an axial alignment, the aggregate plasmon band is stronger and at a lower energy than that of a single particle. Conversely, if the dipoles are aligned in a repulsive configuration, e.g. head-to-head in an axial alignment, the plasmon band will occur at a higher energy. The magnitude of the shift in the frequency of the LSPR for two interacting particles has been found to depend on the particle size and interparticle separation. This can be approximated<sup>35,39</sup> by:

$$\left( \frac{\Delta\lambda}{\lambda} \right) = A e^{\left[ \frac{(-s/D)}{\tau} \right]}$$

where  $\Delta\lambda$  is the fractional shift in the LSPR wavelength,  $\lambda_0$  is the wavelength of the LSPR for an isolated particle, A is the pre-exponential fitting factor, s is the separation

between the particles,  $D$  is the dimension of the particle along the interparticle axis and  $\tau$  is the exponential decay length of the coupled particle pair.

High sensitivity to the above factors necessitates precise control of the nanoparticle shape is needed in the fabrication method for fundamental studies aimed at investigating how nanoparticle geometry and interparticle separation affect the plasmonic properties of noble metal nanoparticle arrays. Although colloidal synthesis techniques offer the advantages of high throughput and flexibility in three-dimensional shape and metal composition, electron beam lithography (EBL) offers the advantages of near-exact control over particle geometry and interparticle separation, particularly for interparticle separations ranging from 20-100 nm.

Hollow nanostructures support two plasmons, one on their inner surface and one on their outer surface.<sup>40</sup> These two plasmons can interact strongly with one another, making hollow nanostructures much more sensitive to structural inhomogeneity than their solid analogs. In particular, changing the wall thickness in a hollow nanostructure greatly affects its optical properties.<sup>40-42</sup> This extreme sensitivity to structural inhomogeneity in the wall thickness adds a geometrical constraint that is not an issue for solid structures and therefore makes accurate representation of the particle geometry vital for the theoretical modeling of hollow nanostructures. In addition, it has been shown that placing a nanoparticle on a substrate results in some degree of symmetry breaking and can introduce coupling and hybridization of the plasmon modes.<sup>43</sup> Therefore, in order to

accurately model the system, the calculations should reproduce the particle sitting on a substrate.

The discrete dipole approximation (DDA) and the finite-difference time-domain (FDTD) method are two of the most widely used approaches for modeling plasmonic systems. DDA is an attractive method for simulating the extinction spectra of metal particles of arbitrary shape.<sup>4,19,42,44-46</sup> In this method, the solid target particle is approximated as a three-dimensional finite lattice of point dipoles that is excited by an external field. The response of the dipoles to the external field and to one another is solved self-consistently using Maxwell's equations. Most of the work done so far has involved modeling the optical properties of solid nanoparticles of different shapes, with little emphasis on hollow structures.<sup>19,46-48</sup> While it has been shown that DDA calculations can be improved by clipping sharp corners to give a more realistic representation of particle geometry,<sup>4</sup> there has been little focus on improving the representation of particle shape in DDA calculations, a topic which is addressed in this work.

Finite-difference time-domain (FDTD) simulations<sup>49</sup> are another practical approach to simulate large nanostructures. Using the Yee algorithm, propagation of the electromagnetic field is defined on a spatial grid through consecutive time steps, and the spectrum obtained from a single run. By analyzing the nanoring system using DDA and FDTD calculations, a better understanding of the features in the experimentally observed spectra was achieved.

### 6.3 Methods

Nanoring arrays were fabricated using a JEOL JBX-9300FS 100 kV electron beam lithography (EBL) system. The nanorings were supported on an array of free-standing silicon nitride ( $\text{Si}_3\text{N}_4$ ) membrane windows, whose fabrication has been described elsewhere.<sup>50</sup> Each  $\text{Si}_3\text{N}_4$  membrane window measured  $150 \times 150 \mu\text{m}^2$  and was used for a single design pattern, which measured  $200 \times 200 \mu\text{m}^2$  to ensure overlap with the window. An 80 nm thick layer of poly(methyl methacrylate) (PMMA), a positive electron resist, was spin coated onto the top  $\text{Si}_3\text{N}_4$  side of the wafer. The doses used to write the pattern ranged between 500 and 4000  $\mu\text{C}/\text{cm}^2$ , with a beam current of 1.98 nA. A solution of 1:3 methyl isobutyl ketone:isopropyl alcohol (MIBK:IPA) was used to develop the exposed sample for 10 s, after which it was rinsed in IPA for 30 s and gently dried with  $\text{N}_2$ . A CVC electron beam evaporator was then used to deposit an adhesion layer of chrome (0.5 Å at 0.1 Å/s), followed by a layer of gold (220 Å at 0.5 Å/s). Finally, the sample was placed in 1165 remover (MicroChem) for several hours to achieve lift-off.

In order to minimize any far-field coupling, the nanoring array was designed so that within an array the center-to-center distance between each neighboring dimer in any direction was at least 1000 nm. Additionally, the interparticle spacing never exceeded five particle diameters to ensure that the near-field coupling dominated the sample properties.<sup>35</sup>

The supported nanoring arrays were imaged using a Zeiss Ultra60 scanning electron microscope (SEM). Extinction measurements were performed on a Craic Microspectra 121 UV-visible-NIR microspectrophotometer with an imaging range from 400-1700 nm in transmission mode under several polarization conditions (parallel and perpendicular to the interparticle axis and unpolarized). The aperture size selected for the measurements was  $625 \mu\text{m}^2$  with a 36x objective lens, and each reported spectrum is an average of at least five separate spectra taken across the sample.

The optical response of the nanoring dimer arrays has been calculated using the DDA method with the DDSCAT 6.1 code offered publicly by Draine and Flatau.<sup>51</sup> The bulk values of the dielectric constants for gold and silicon nitride reported by Johnson and Christy<sup>52</sup> and Palik<sup>53</sup> were used.

Finite-difference time-domain (FDTD) simulations were performed with the Lumerical software package<sup>49,54</sup> using the Yee algorithm.<sup>55</sup> The propagation of the electromagnetic field was defined on a spatial grid through consecutive time steps, and the spectrum obtained from a single run. The time step was determined by increments according to the time stepping stability criterion, and the simulation time estimated so that the field components decayed to nearly zero. To assure accuracy, the grid size was set to 1 nm in the x and y directions and to 0.6 nm in z direction. Experimental data characterized for thin films was fitted to the dielectric function expression, where an expansion of Lorentzian terms was included to account for inter-band transitions and the other non-Drude contributions.<sup>56</sup> Size correction to the bulk mean collision rate of the conduction

electrons, necessary for nanoparticle sizes comparable to the mean free path of the electrons, was achieved by a modified expression for the collision rate  $\gamma$ . This expression is  $\gamma = \gamma_{\infty} + Av_F/r$ , where  $\gamma_{\infty}$  is the value in bulk metal,  $v_F$  the Fermi velocity in bulk metal, and A is a geometric parameter that relates the mean electron free path to the particle's average radius r. Equivalence of the time-domain equations to those in the frequency domain using analytical forms of the dielectric function were described by Gray et al.<sup>57</sup> The dispersive material data for the dielectric substrate reported by Palik<sup>53</sup> were used.

#### **6.4 Results and Discussion**

A few representative SEM images of the nanoring arrays are shown in Figure 6 - 1. The average dimensions of the rings were  $127.6 \pm 2.5$  nm and  $57.8 \pm 2.3$  nm for the outer and inner diameters, respectively, with interparticle separations ranging from  $17.8 \pm 3.4$  nm to  $239.2 \pm 3.7$  nm.

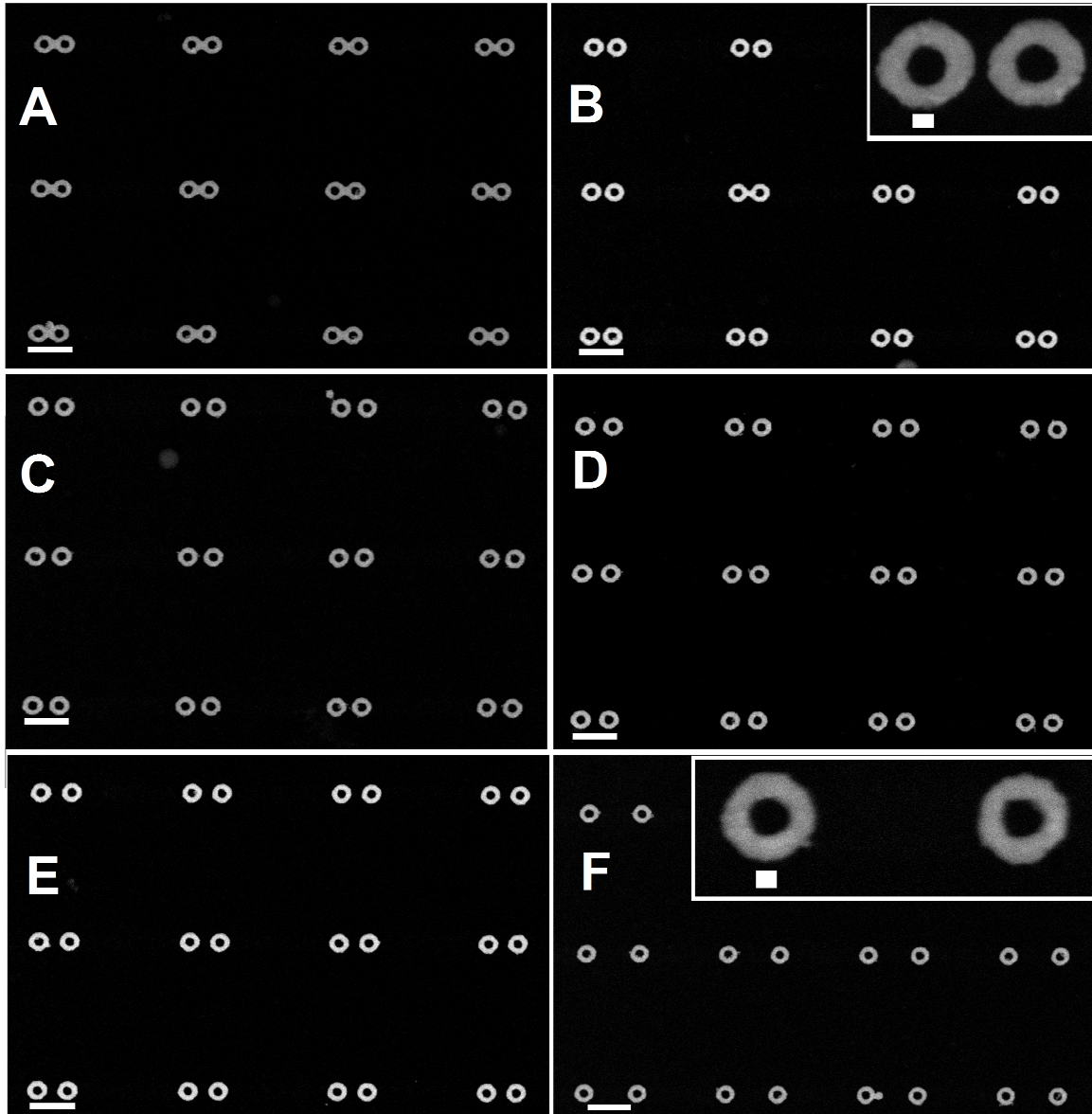


Figure 6 - 1. Selected SEM images of nanoring dimers fabricated by EBL. The average dimensions of the rings are  $127.6 \pm 2.5$  nm and  $57.8 \pm 2.3$  nm for the outer and inner diameters, respectively. The interparticle separations are 0,  $17.8 \pm 3.4$ ,  $37.5 \pm 2.9$ ,  $53.8 \pm 1.7$ ,  $68.3 \pm 3.4$ , and  $239.2 \pm 3.7$  nm for A-F respectively. The scale bars in A-F are all 300 nm. The insets in B and F are highly magnified images of one dimer. The scale bars in the insets are both 30 nm.

DDA calculations were carried out to model the optical properties of the fabricated nanorings. The particles were modeled, in air, as symmetric rings with the average dimensions determined from SEM images. The results of the DDA calculations for a nanoring dimer with interparticle separation of 240 nm are shown for two polarization modes in Figure 6 - 2; at this distance, the particles should have negligible interaction with each other. It can be seen that the peak position for the two polarization modes is practically identical, which is expected for a symmetric structure and occurs around 715 nm. Approximately 31% of the surface area of a single ring is exposed to the silicon nitride substrate in the experimental sample. The calculated sensitivity factor, defined as the change in LSPR peak position per unit refractive index unit change, for the nanorings is ~530 nm/RIU, which means that the extinction band for the experimental sample should be red shifted by approximately 170 nm relative to the DDA results in air, causing the band to appear around 900 nm.



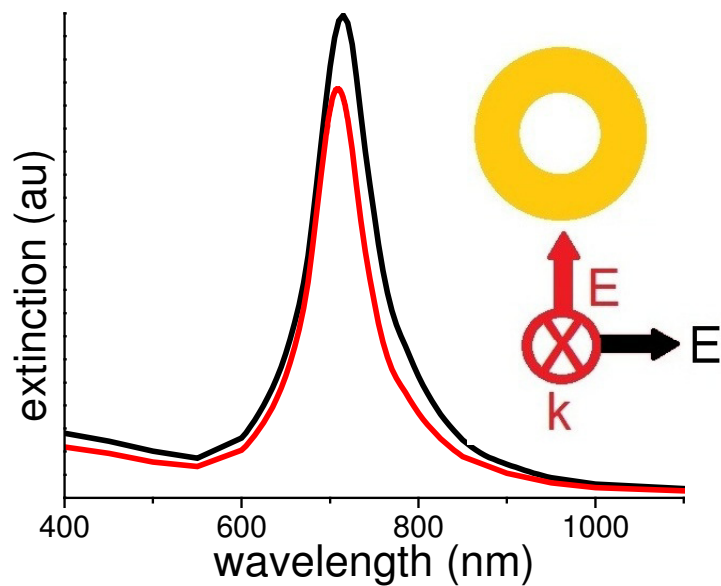


Figure 6 - 2. Initial DDA results for a ring dimer with an interparticle separation of 240 nm, simulating an isolated structure. The position of the peaks is practically the same for the two different polarization conditions.

The experimental unpolarized extinction spectra of the nanoring arrays at several interparticle separations is shown in Figure 6 - 3. Based on the DDA calculations, only one peak was expected; however two distinct peaks are present in the unpolarized spectra for the experimental sample. The fractional shift of the two peaks with respect to interparticle distance is shown in Figure 6 - 4. The peak at ~1100 nm exhibits a red shift as the interparticle distance is decreased. However, the equally intense peak that is located at ~1000 nm does not exhibit any distinguishable shift as the interparticle distance changes.

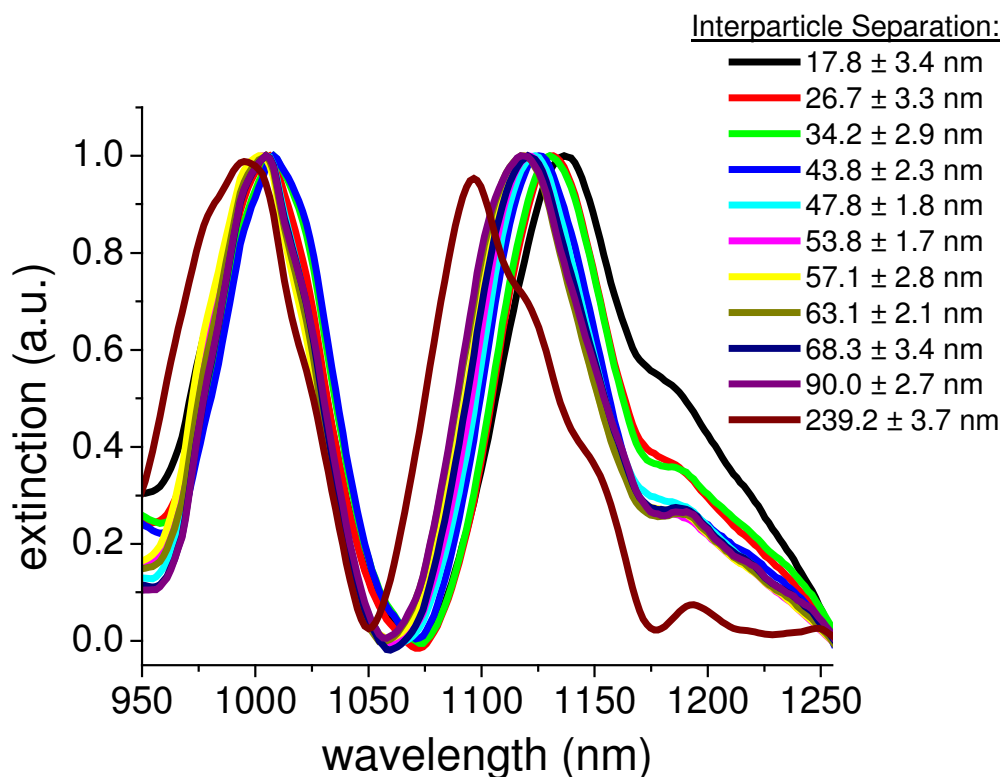


Figure 6 - 3. Normalized experimental extinction spectra for nanoring dimers with a range of interparticle separations irradiated with unpolarized light. Two distinct bands are observed, one appearing around 1000 nm, whose position does not appreciably change with interparticle separation, and one appearing between 1100 and 1200 nm, whose position red shifts significantly as the interparticle separation is decreased.

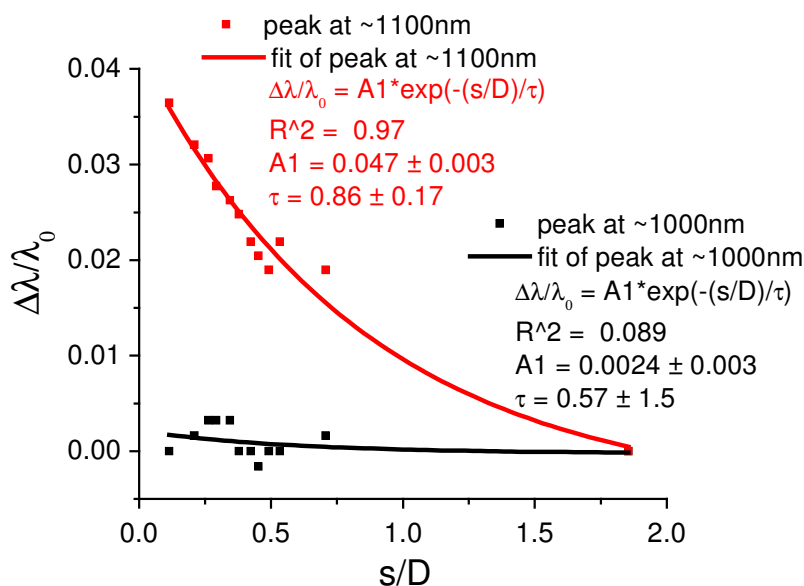


Figure 6 - 4. Fractional shift of the wavelength ( $\Delta\lambda/\lambda_0$ ) plotted against the interparticle separation scaled by the outer diameter ( $s/D$ ) for the peak at 1000 nm (black) and the peak at 1100 nm (red). The solid line of the same color as the corresponding data set shows the exponential fit of each plot.

In our previous work on nanodiscs, the solid analogues to rings, there was no mismatch between the experimentally observed optical properties and those predicted by DDA.<sup>39</sup> Experimentally, only one extinction band was observed for the discs. This band showed the expected red shift for light polarized parallel to the interparticle axis and blue shift for light polarized perpendicular to the interparticle axis. Furthermore, all the experimentally observed behaviors for the discs were predicted via DDA.

Recently, the plasmonic coupling in gold nanoring dimers was investigated by Tsai *et al.*<sup>42</sup> They found that nanorings are more sensitive to changes in refractive index than

nanodiscs of similar dimensions, but in general the plasmonic properties of the nanorings behaved in a similar fashion to solid nanostructures.<sup>42</sup> Namely, the resonance band red shifted when the light was polarized parallel to the interparticle axis, blue shifted when the light was polarized perpendicular to the interparticle axis, and the magnitude of the shifts falls along the expected exponential relationship with gap distance. For their dimers with large gap distances, the resonance peak position for both polarization conditions occurred at practically the same wavelength, meaning if the spectra had been collected with unpolarized light they would only expect to see one band. The dimensions of their nanorings (400 nm diameter, 100 nm wall thickness, 50 nm height) are much larger than the ones discussed here (120 nm diameter, 60 nm wall thickness, 22 nm height). The smaller size of our nanorings may cause them to be more sensitive than those discussed by Tsai *et al.*<sup>42</sup>

To clarify the experimental spectra of the rings, further extinction spectra were collected under specific polarization conditions for all interparticle separations. When the incident light was polarized parallel to the interparticle axis, only the peak around 1100 nm was observed (Figure 6 - 5) and displayed the expected red shift (Figure 6 - 6). Conversely, when the incident light was polarized perpendicular to the interparticle axis, only the peak at ~1000 nm was observed (Figure 6 - 7). A slight blue shift in the peak at ~1000 nm is also discernable in the polarized spectra (Figure 6 - 8). These results suggest that at least one cause of the two peaks is a slight anisotropy in the nanoring shapes along the two different axes. This was confirmed through careful analysis of high resolution SEM images of the rings.

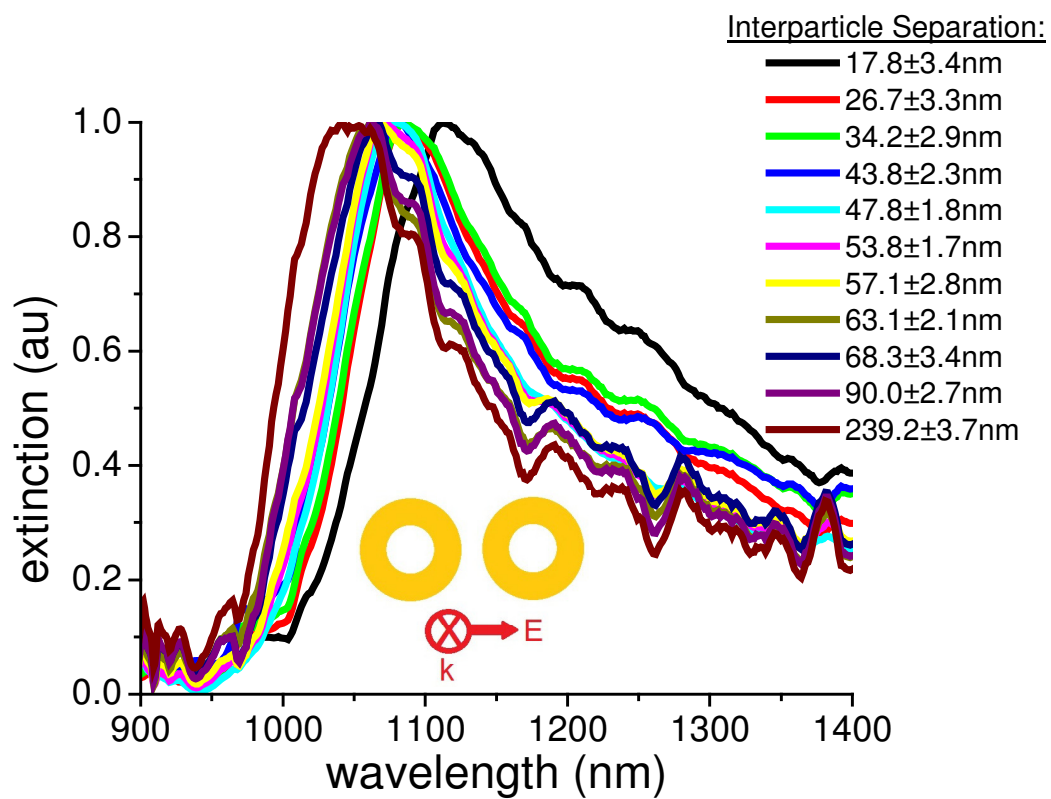


Figure 6 - 5. Normalized experimental extinction spectra for nanoring dimers of varying interparticle separations with polarization parallel and to the interparticle axis (as indicated in inset). Only one extinction band is observed. As the interparticle separation decreases, the extinction band red shifts.

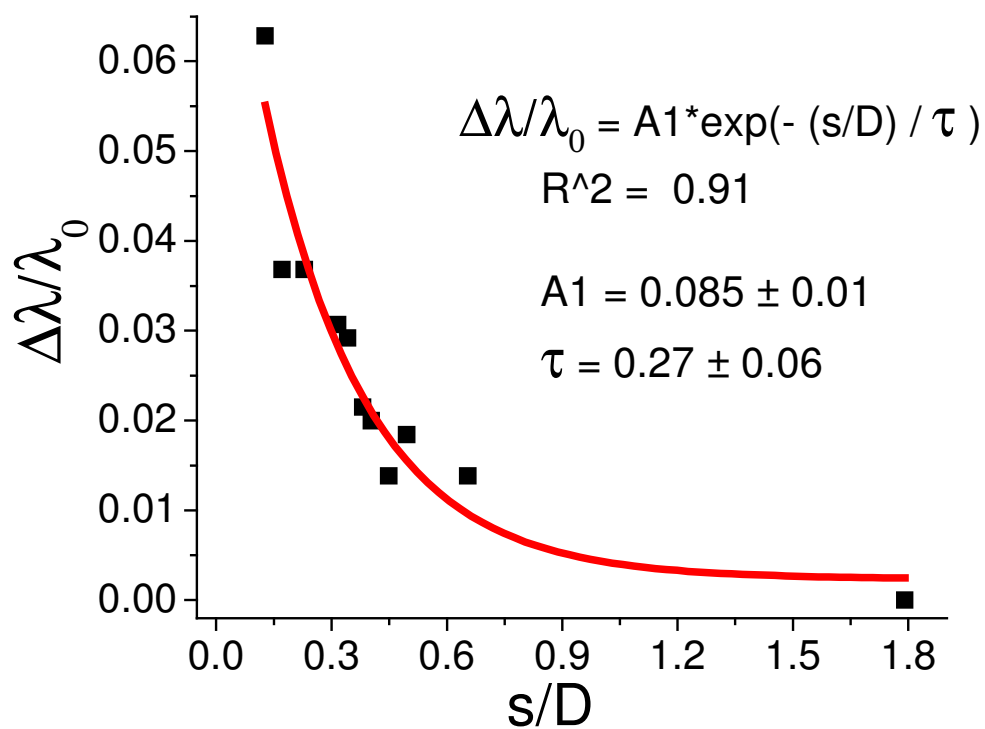


Figure 6 - 6. The fractional shift of the band isolated under parallel polarization plotted against the interparticle separation scaled by the outer diameter. The data fits well ( $R^2 = 0.91$ ) to the exponential model.

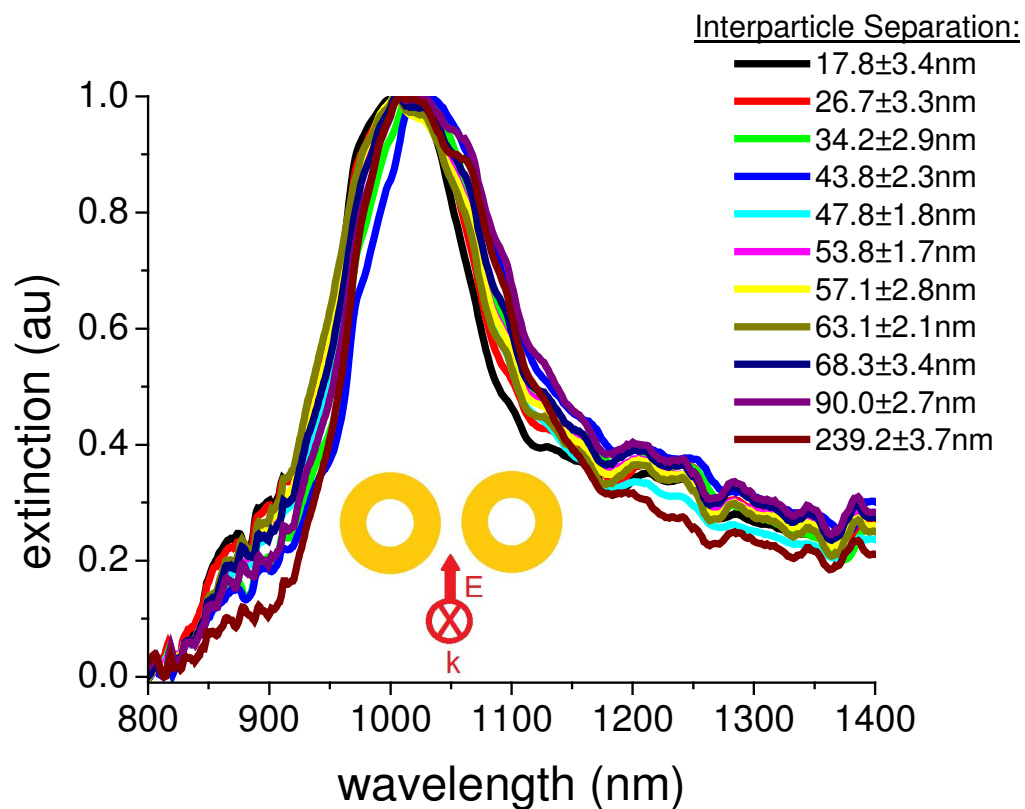


Figure 6 - 7. Normalized experimental extinction spectra for nanoring dimers of varying interparticle separations with polarization perpendicular to the interparticle axis (as indicated in inset). Only one extinction band is observed. As the interparticle separation decreases, the extinction band blue shifts.

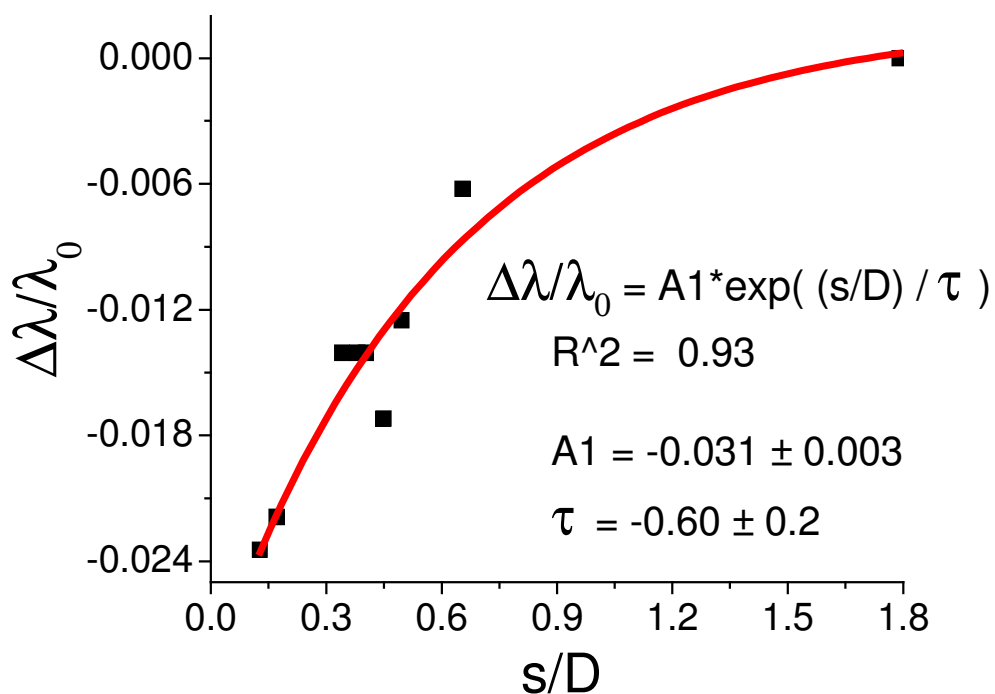


Figure 6 - 8. The fractional shift of the band isolated under perpendicular polarization plotted against the interparticle separation scaled by the outer diameter. The data fits well ( $R^2 = 0.93$ ) to the exponential model.

The SEM image shown in Figure 6 - 9a displays the ring dimers with the smallest interparticle separation ( $17.8 \pm 3.4$  nm, also shown in Figure 6 - 1B). It was found that the wall thickness of the particles along the interparticle axis, i.e. the left and right sides of the rings, was  $36.00 \pm 2.45$  nm, whereas the thickness of the walls perpendicular to the interparticle axis, i.e. the top and bottom walls of the rings, was  $32.86 \pm 1.93$  nm. An unpaired t-test gave a two-tailed p-value of less than 0.0001, indicating that the difference in wall thickness along the two different axes is extremely statistically significant.



Similar analysis of the SEM images for other interparticle separations showed the same average difference in the thickness of the walls. A higher resolution SEM image of a single nanoring is shown in Figure 6 - 9b where the anisotropy is more clearly seen. This difference in wall thickness most likely arises from a slight tilt of the sample perpendicular to the interparticle axis during the metal deposition step, which would create a shadowing effect. Indeed, a tilt of only  $3^\circ$  would account for the 4 nm difference in the thickness of the walls in the rings.

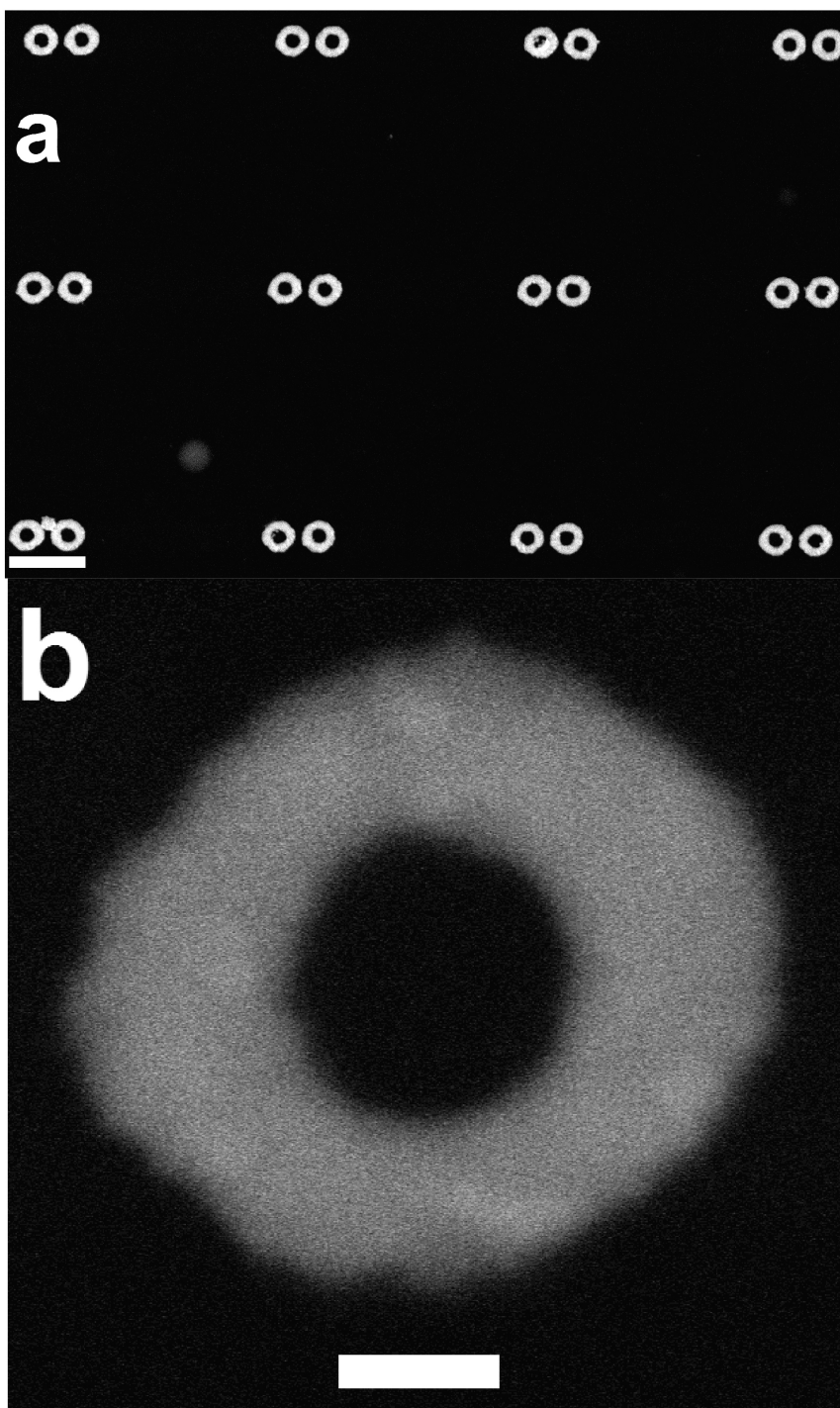


Figure 6 - 9. a) SEM image of nanoring dimers with interparticle separation is  $17.8 \pm 3.4$  nm. The scale bar is 300 nm. b) High resolution SEM image of a single nanoring demonstrating the particle anisotropy. The scale bar is 30 nm.

The resonance bands for both polarization directions have a Fano lineshape (i.e., an asymmetric lineshape), which is more dominantly present in the parallel resonance band (Figure 6 - 5) and demonstrates an interference of the allowed and dark dipolar modes.<sup>58</sup> This is to be expected, as interference of the dipolar and higher-order modes through image charges induced in the dielectric leads to symmetry breaking,<sup>59</sup> which is dependent on the inter-particle distance in this case. For the fully separated dimer for example, the Fano line shape is less pronounced than the closely spaced particles. For the perpendicular polarization, the emergence of the Fano interference is much weaker (Figure 6 - 7), possibly due to the weaker coupling for this polarization mode.

The possibility that anisotropy in the ring geometry is leading to the two peaks means that this same anisotropy needs to be accurately represented in the description of the shape used in the theoretical calculations. In the previous DDA calculations for the rings, an ideal ring shape was used (symmetric, no surface irregularities, etc) whose dimensions were acquired by averaging the dimensions from several SEM images. It is very apparent from the disparity between the experimental and theoretical results, however, that this method has not provided an accurate representation of the particle geometry. Our solution to this problem was to directly convert the SEM image of the nanoring into the file that is used to define the particle shape in the theoretical calculations. ImageJ was used to convert an SEM image into a text file of the XY coordinates for the pixels of each particle in the image. These XY coordinates were directly used to define the shape of the particle for the theoretical calculations. An immediate benefit of this process was the ability to model several particle pairs from the same sample. Although EBL gives

very precise control over particle shape in theory, there are always some fabrication inconsistencies from one particle to the next. These small inconsistencies are lost in the traditional shape file preparation methods. These normally average out in the experimental data, however, if they occur consistently enough they could potentially impact the experimental spectra as the spectrometer spot size usually covers several neighboring particle pairs.

The shape files for 10 single nanorings derived from SEM images were used to run DDA calculations to model the gold nanorings in air. The results of these calculations are shown in Figure 6 - 10. When the light is polarized parallel to the interparticle axis, the extinction peak is located at  $763 \pm 8$  nm (Figure 6 - 10a), whereas when the light is polarized perpendicular to the axis, the extinction peak is located around  $730 \pm 10$  nm (Figure 6 - 10b). It can be seen that for both polarization conditions, there is a slight difference in the peak location for each of the 10 particles, but this difference is quite small ( $\sim 1\%$  deviation). These results suggest that the slight surface irregularities from one particle to the next are not affecting the spectra in a major way. These results also strongly suggest that anisotropy in the particle shape along the two axes plays a role in the cause of the two peaks observed experimentally.

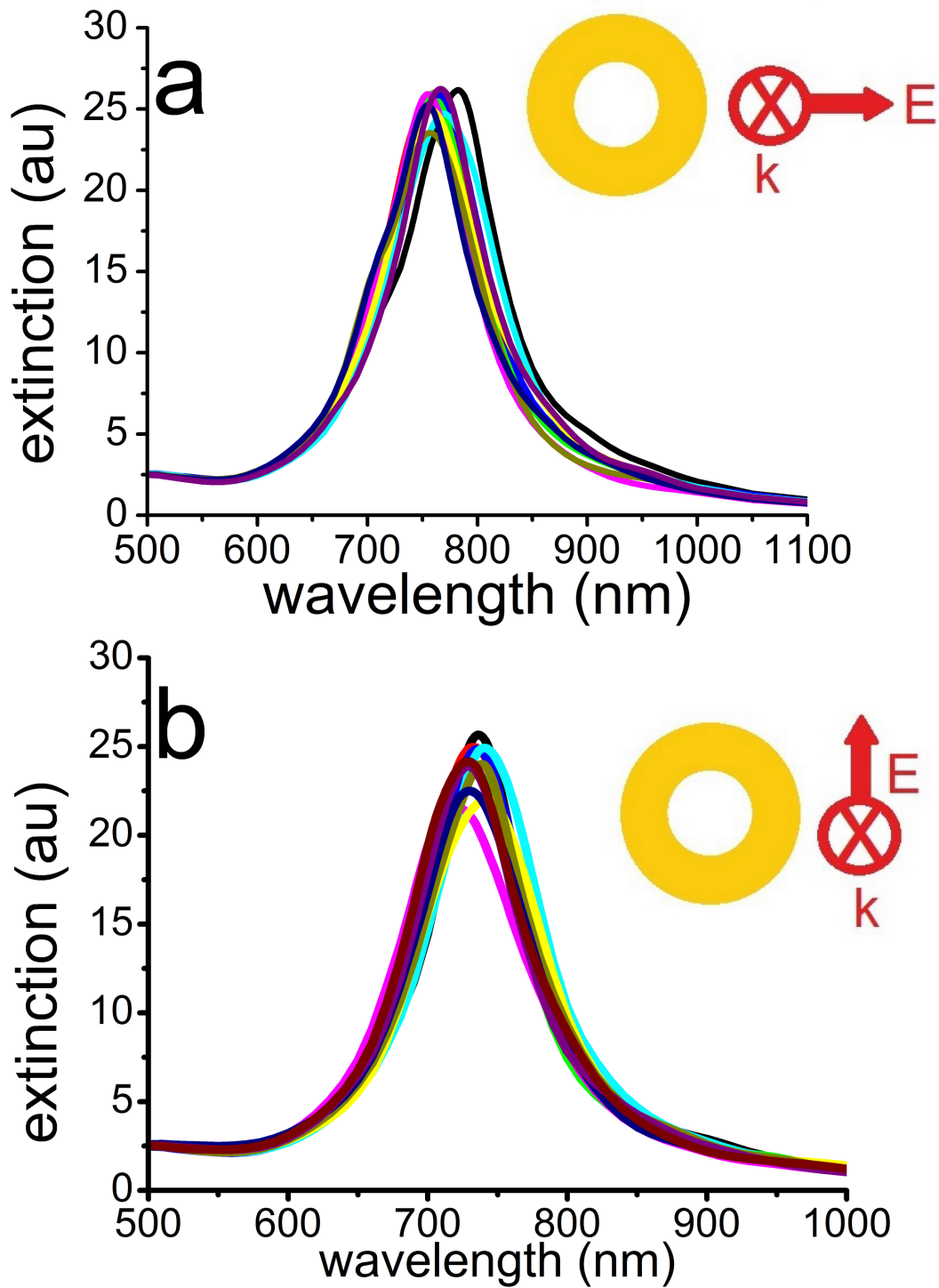


Figure 6 - 10. DDA-simulated extinction spectra (in air) of ten single nanorings calculated using the SEM based shape files with light polarized a) parallel and b) perpendicular to the interparticle axis (as indicated in insets).

FDTD simulations were also used to investigate this system. The FDTD extinction spectra for two samples, both of which represent the smallest interparticle separation observed experimentally ( $17.8 \pm 3.4$  nm) in the absence of a substrate and in vacuum are shown in Figure 6 - 11. Interestingly, upon using the SEM-based geometry for a nanoring dimer, the emergence of a slight Fano lineshape (i.e., asymmetric lineshape) is noted, due to the asymmetry in geometry of the two nanorings. This Fano lineshape was observed experimentally, but was not reproduced via DDA calculations.

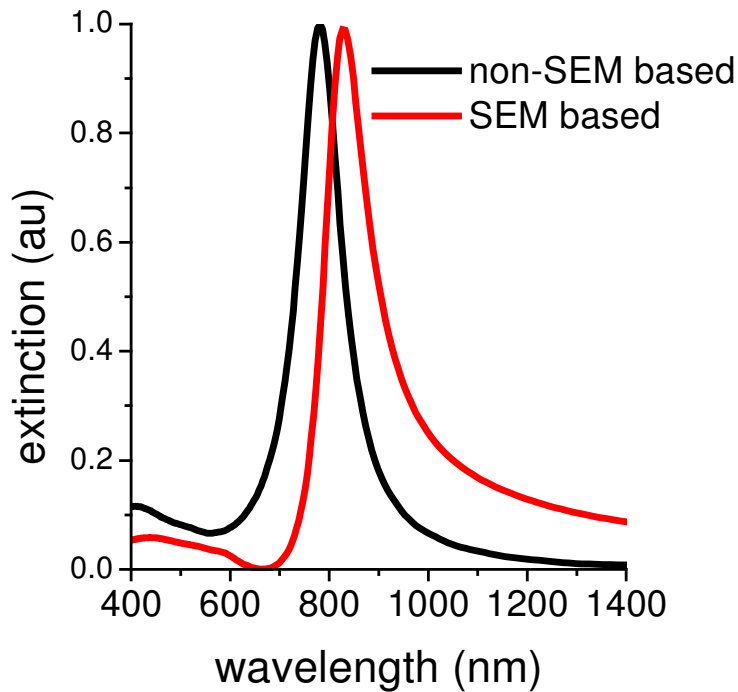


Figure 6 - 11. FDTD calculated spectra for a perfect nanoring dimer (black), and an SEM based nanoring dimer (red), both representing the sample with the smallest interparticle separation ( $17.8 \pm 3.4$  nm). All spectra are done in vacuum with no substrate present.

As discussed previously, it has been shown that placing a nanoparticle on a substrate can introduce anisotropy effects to the system, and the resulting break in symmetry affects the spectral properties of the system. Accordingly, in order to accurately model such a system, any theoretical calculations should reproduce the particle(s) sitting on a substrate, as opposed to considering them immersed in an effective medium.

The FDTD simulations of the spectra of perfect gold nanoring dimers deposited on a  $\text{Si}_3\text{N}_4$  substrate were compared to the experimental spectra, with specific focus on the position and lineshape of the LSPRs. Upon introduction of the substrate, the LSPRs were red-shifted compared to the previous results in vacuum (Figure 6 - 11) because of the increase in refractive index. This response can be understood qualitatively using an image charge model, modulated by the permittivity of the substrate.<sup>60</sup> Such an effect was demonstrated experimentally by changing the distance to gold nanodiscs when incorporating dielectric pillars on the substrate.<sup>61</sup> As expected, the effect is larger for the parallel polarization. Therefore, a larger difference between the LSPRs for the two polarizations for dimers on a high dielectric substrate is observed.

The FDTD extinction spectra for a selection of dimers with varying interparticle distance and light polarized parallel to the interparticle axis are shown in Figure 6 - 12. It can be seen that as the interparticle separation is decreased, the expected red shift is reproduced in the FDTD spectra.

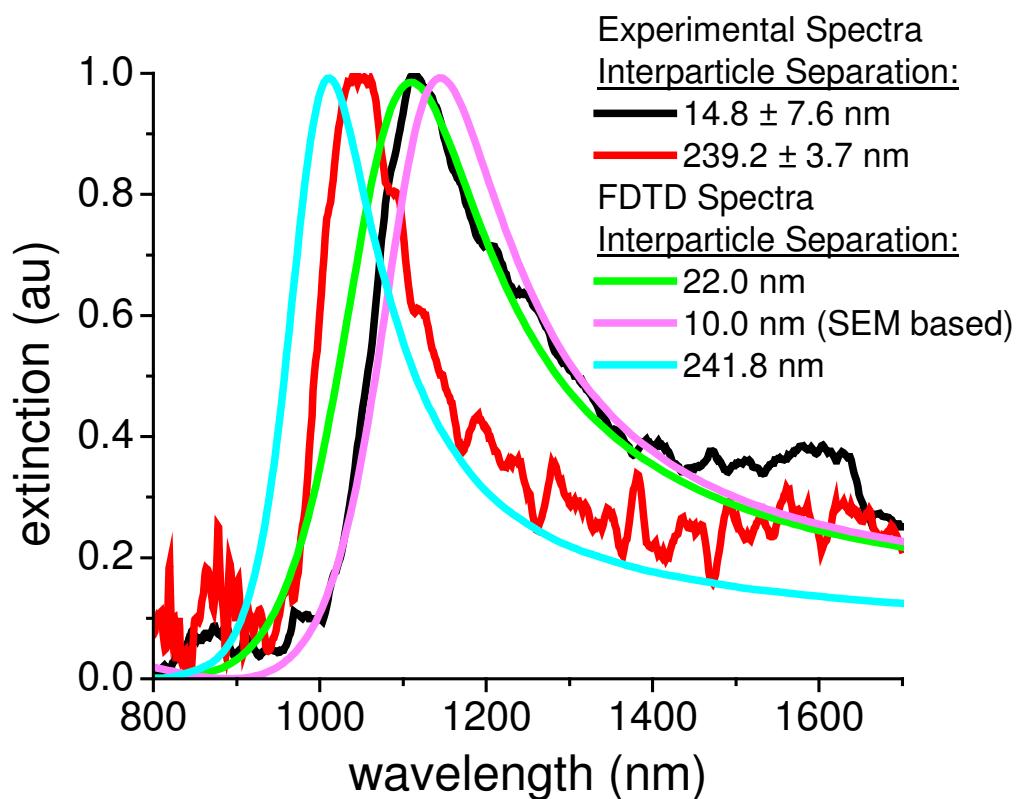


Figure 6 - 12. FDTD extinction spectra for nanoring dimers of varying interparticle separations with polarization parallel to the interparticle axis. Introduction of the substrate induces a Fano lineshape in the model for the dimer with an interparticle separation of 22.0 nm. Furthermore, use of the SEM-based dimer in the calculations has increased the Fano lineshape and most closely resembles the corresponding experimental spectra.

As mentioned before, the experimental data for parallel polarization (Figure 6 - 5) show a Fano resonance that is blue shifted compared to the broad dipolar mode excitation and is dependent on the interparticle separation. For the fully separated dimer, the effect was noted to be smaller experimentally, and this result was reproduced theoretically (Figure 6 - 12). Furthermore, it can be seen in Figure 6 - 12 that when the SEM based particle is



used, the Fano lineshape becomes more pronounced and more closely resembles the experimental spectrum. This is to be expected, as this most accurately represents the experimental system. It is worthwhile to note that the emergent resonance around 900 nm in the experimental spectra in Figure 6 - 12 was not observed in any of our models. This resonance is likely due to additional asymmetry in the system and will be further investigated in future work.

## **6.5 Conclusions**

We have demonstrated the exceptional sensitivity of nanorings to their anisotropic environment, namely asymmetries in the particle shape and high index substrate effects. This results in a Fano lineshape for the dipolar plasmon resonance bands. The slight anisotropy in our fabricated nanoring structures is most likely due to a shadowing effect during the metal deposition step. We have also shown that the traditional shape generation methods were unable to accurately represent this slight anisotropy. Accordingly, we developed a method for preparing the files describing the nanoparticle shape for theoretical calculations wherein an SEM image of the particle(s) is directly used to create the file. This method is easy to execute and should therefore become the new paradigm for particle shape descriptions in future calculations. We have also shown the pronounced effect that the substrate has on the spectra of the nanorings. Consideration of this high index substrate into our models allows us to model the experimentally observed Fano lineshape, which was more significant as the particle

coupling increased at smaller interparticle separations. The improved sensitivity of these nanorings due to their geometry and increased field enhancement in the cavity make them attractive for absorption or fluorescence enhancement applications in the future.

## 6.6 References

- (1) Bohren, C. F.; Huffman, D. R. *Absorption and Scattering of Light by Small Particles*; Wiley: New York, 1983.
- (2) El-Sayed, M. A. Some interesting properties of metals confined in time and nanometer space of different shapes. *Accounts Chem. Res.* **2001**, *34*, 257-264.
- (3) Hutter, E.; Fendler, J. H. Exploitation of localized surface plasmon resonance. *Advanced Materials* **2004**, *16*, 1685-1706.
- (4) Kelly, K. L.; Coronado, E.; Zhao, L. L.; Schatz, G. C. The optical properties of metal nanoparticles: The influence of size, shape, and dielectric environment. *J. Phys. Chem. B* **2003**, *107*, 668-677.
- (5) Kreibig, U.; Vollmer, M. *Optical Properties of Metal Clusters*; Springer: Berlin, 1995; Vol. 25.
- (6) Link, S.; El-Sayed, M. A. Spectral properties and relaxation dynamics of surface plasmon electronic oscillations in gold and silver nanodots and nanorods. *J. Phys. Chem. B* **1999**, *103*, 8410-8426.
- (7) Alivisatos, P. The use of nanocrystals in biological detection. *Nature Biotechnology* **2004**, *22*, 47-52.
- (8) Haes, A. J.; Hall, W. P.; Chang, L.; Klein, W. L.; Van Duyne, R. P. A localized surface plasmon resonance biosensor: First steps toward an assay for Alzheimer's disease. *Nano Lett.* **2004**, *4*, 1029-1034.
- (9) Jiang, J.; Bosnick, K.; Maillard, M.; Brus, L. Single molecule Raman spectroscopy at the junctions of large Ag nanocrystals. *J. Phys. Chem. B* **2003**, *107*, 9964-9972.
- (10) Nikoobakht, B.; El-Sayed, M. A. Surface-enhanced Raman scattering studies on aggregated gold nanorods. *Journal of Physical Chemistry A* **2003**, *107*, 3372-3378.
- (11) Rosi, N. L.; Mirkin, C. A. Nanostructures in biodiagnostics. *Chemical Reviews* **2005**, *105*, 1547-1562.
- (12) Willets, K. A.; Van Duyne, R. P. In *Annual Review of Physical Chemistry*; Annual Reviews: Palo Alto, 2007; Vol. 58, p 267-297.
- (13) Zou, S. L.; Schatz, G. C. Silver nanoparticle array structures that produce giant enhancements in electromagnetic fields. *Chemical Physics Letters* **2005**, *403*, 62-67.

- (14) Corot, C.; Robert, P.; Idee, J. M.; Port, M. Recent advances in iron oxide nanocrystal technology for medical imaging. *Advanced Drug Delivery Reviews* **2006**, *58*, 1471-1504.
- (15) El-Sayed, I. H.; Huang, X. H.; El-Sayed, M. A. Surface plasmon resonance scattering and absorption of anti-EGFR antibody conjugated gold nanoparticles in cancer diagnostics: Applications in oral cancer. *Nano Lett.* **2005**, *5*, 829-834.
- (16) Gao, X. H.; Cui, Y. Y.; Levenson, R. M.; Chung, L. W. K.; Nie, S. M. In vivo cancer targeting and imaging with semiconductor quantum dots. *Nature Biotechnology* **2004**, *22*, 969-976.
- (17) Gobin, A. M.; Lee, M. H.; Halas, N. J.; James, W. D.; Drezek, R. A.; West, J. L. Near-infrared resonant nanoshells for combined optical imaging and photothermal cancer therapy. *Nano Lett.* **2007**, *7*, 1929-1934.
- (18) Ito, A.; Shinkai, M.; Honda, H.; Kobayashi, T. Medical application of functionalized magnetic nanoparticles. *Journal of Bioscience and Bioengineering* **2005**, *100*, 1-11.
- (19) Jain, P. K.; Lee, K. S.; El-Sayed, I. H.; El-Sayed, M. A. Calculated absorption and scattering properties of gold nanoparticles of different size, shape, and composition: Applications in biological imaging and biomedicine. *J. Phys. Chem. B* **2006**, *110*, 7238-7248.
- (20) West, J. L.; Halas, N. J. Engineered nanomaterials for biophotonics applications: Improving sensing, imaging, and therapeutics. *Annual Review of Biomedical Engineering* **2003**, *5*, 285-292.
- (21) Chen, W.; Xu, N. F.; Xu, L. G.; Wang, L. B.; Li, Z. K.; Ma, W.; Zhu, Y. Y.; Xu, C. L.; Kotov, N. A. Multifunctional Magnetoplasmonic Nanoparticle Assemblies for Cancer Therapy and Diagnostics (Theranostics). *Macromolecular Rapid Communications* **2010**, *31*, 228-236.
- (22) Dreaden, E. C.; Mwakwari, S. C.; Sodji, Q. H.; Oyelere, A. K.; El-Sayed, M. A. Tamoxifen-Poly(ethylene glycol)-Thiol Gold Nanoparticle Conjugates: Enhanced Potency and Selective Delivery for Breast Cancer Treatment. *Bioconjugate Chemistry* **2009**, *20*, 2247-2253.
- (23) Ghosn, B.; van de Ven, A. L.; Tam, J.; Gillenwater, A.; Sokolov, K. V.; Richards-Kortum, R.; Roy, K. Efficient mucosal delivery of optical contrast agents using imidazole-modified chitosan. *Journal of Biomedical Optics* **2010**, *15*.
- (24) Khlebtsov, N. G.; Dykman, L. A. Optical properties and biomedical applications of plasmonic nanoparticles. *J. Quant. Spectrosc. Radiat. Transf.* **2010**, *111*, 1-35.

- (25) Kogan, B.; Andronova, N.; Khlebtsov, N.; Khlebtsov, B.; Rudoy, V.; Dement'eva, O.; Sedykh, E.; Bannykh, L. *Pharmacokinetic study of PEGylated plasmon resonant gold nanoparticles in tumor-bearing mice*, 2008.
- (26) von Maltzahn, G.; Park, J. H.; Lin, K. Y.; Singh, N.; Schwoppe, C.; Mesters, R.; Berdel, W. E.; Ruoslahti, E.; Sailor, M. J.; Bhatia, S. N. Nanoparticles that communicate in vivo to amplify tumour targeting. *Nature Materials* **2011**, *10*, 545-552.
- (27) Yin, P. G.; Chen, Y.; Jiang, L.; You, T. T.; Lu, X. Y.; Guo, L.; Yang, S. H. Controlled Dispersion of Silver Nanoparticles into the Bulk of Thermosensitive Polymer Microspheres: Tunable Plasmonic Coupling by Temperature Detected by Surface Enhanced Raman Scattering. *Macromolecular Rapid Communications* **2011**, *32*, 1000-1006.
- (28) Dickerson, E. B.; Dreaden, E. C.; Huang, X. H.; El-Sayed, I. H.; Chu, H. H.; Pushpanketh, S.; McDonald, J. F.; El-Sayed, M. A. Gold nanorod assisted near-infrared plasmonic photothermal therapy (PPTT) of squamous cell carcinoma in mice. *Cancer Letters* **2008**, *269*, 57-66.
- (29) Huang, X. H.; Jain, P. K.; El-Sayed, I. H.; El-Sayed, M. A. Gold nanoparticles: interesting optical properties and recent applications in cancer diagnostic and therapy. *Nanomedicine* **2007**, *2*, 681-693.
- (30) Huang, X. H.; Kang, B.; Qian, W.; Mackey, M. A.; Chen, P. C.; Oyelere, A. K.; El-Sayed, I. H.; El-Sayed, M. A. Comparative study of photothermalolysis of cancer cells with nuclear-targeted or cytoplasm-targeted gold nanospheres: continuous wave or pulsed lasers. *Journal of Biomedical Optics* **2010**, *15*.
- (31) Lee, K. S.; El-Sayed, M. A. Dependence of the enhanced optical scattering efficiency relative to that of absorption for gold metal nanorods on aspect ratio, size, end-cap shape, and medium refractive index. *J. Phys. Chem. B* **2005**, *109*, 20331-20338.
- (32) Jain, P. K.; El-Sayed, M. A. Surface plasmon coupling and its universal size scaling in metal nanostructures of complex geometry: Elongated particle pairs and nanosphere trimers. *Journal of Physical Chemistry C* **2008**, *112*, 4954-4960.
- (33) Mahmoud, M. A.; Snyder, B.; El-Sayed, M. A. Surface Plasmon Fields and Coupling in the Hollow Gold Nanoparticles and Surface-Enhanced Raman Spectroscopy. Theory and Experiment. *Journal of Physical Chemistry C* **2010**, *114*, 7436-7443.
- (34) Maier, S. A.; Brongersma, M. L.; Kik, P. G.; Atwater, H. A. Observation of near-field coupling in metal nanoparticle chains using far-field polarization spectroscopy. *Physical Review B* **2002**, *65*.

- (35) Rechberger, W.; Hohenau, A.; Leitner, A.; Krenn, J. R.; Lamprecht, B.; Aussenegg, F. R. Optical properties of two interacting gold nanoparticles. *Optics Communications* **2003**, *220*, 137-141.
- (36) Su, K. H.; Wei, Q. H.; Zhang, X.; Mock, J. J.; Smith, D. R.; Schultz, S. Interparticle coupling effects on plasmon resonances of nanogold particles. *Nano Lett.* **2003**, *3*, 1087-1090.
- (37) Sweatlock, L. A.; Maier, S. A.; Atwater, H. A.; Penninkhof, J. J.; Polman, A. Highly confined electromagnetic fields in arrays of strongly coupled Ag nanoparticles. *Physical Review B* **2005**, *71*.
- (38) Jain, P. K.; El-Sayed, M. A. Plasmonic coupling in noble metal nanostructures. *Chemical Physics Letters* **2010**, *487*, 153-164.
- (39) Jain, P. K.; Huang, W. Y.; El-Sayed, M. A. On the universal scaling behavior of the distance decay of plasmon coupling in metal nanoparticle pairs: A plasmon ruler equation. *Nano Lett.* **2007**, *7*, 2080-2088.
- (40) Prodan, E., Radloff, C., Halas, N. J., Nordlander, P. *Science* **2003**, *302*, 419.
- (41) Halas, N. J. Playing with plasmons. Tuning the optical resonant properties of metallic nanoshells. *MRS Bull.* **2005**, *30*, 362-367.
- (42) Tsai, C.-Y.; Lin, J.-W.; Wu, C.-Y.; Lin, P.-T.; Lu, T.-W.; Lee, P.-T. Plasmonic Coupling in Gold Nanoring Dimers: Observation of Coupled Bonding Mode. *Nano Lett.* **2012**, *12*, 1648-1654.
- (43) Zhang, S. P.; Bao, K.; Halas, N. J.; Xu, H. X.; Nordlander, P. Substrate-Induced Fano Resonances of a Plasmonic Nanocube: A Route to Increased-Sensitivity Localized Surface Plasmon Resonance Sensors Revealed. *Nano Lett.* **2011**, *11*, 1657-1663.
- (44) Olson, T. Y.; Schwartzberg, A. M.; Orme, C. A.; Talley, C. E.; O'Connell, B.; Zhang, J. Z. Hollow gold-silver double-shell nanospheres: Structure, optical absorption, and surface-enhanced Raman scattering. *Journal of Physical Chemistry C* **2008**, *112*, 6319-6329.
- (45) Sun, Y. G.; Mayers, B.; Xia, Y. N. Metal nanostructures with hollow interiors. *Advanced Materials* **2003**, *15*, 641-646.
- (46) Wan, D. H.; Chen, H. L.; Lin, Y. S.; Chuang, S. Y.; Shieh, J.; Chen, S. H. Using Spectroscopic Ellipsometry to Characterize and Apply the Optical Constants of Hollow Gold Nanoparticles. *Acs Nano* **2009**, *3*, 960-970.

- (47) Jain, P. K.; Eustis, S.; El-Sayed, M. A. Plasmon coupling in nanorod assemblies: Optical absorption, discrete dipole approximation simulation, and exciton-coupling model. *J. Phys. Chem. B* **2006**, *110*, 18243-18253.
- (48) Tabor, C.; Murali, R.; Mahmoud, M.; El-Sayed, M. A. On the Use of Plasmonic Nanoparticle Pairs As a Plasmon Ruler: The Dependence of the Near-Field Dipole Plasmon Coupling on Nanoparticle Size and Shape. *Journal of Physical Chemistry A* **2009**, *113*, 1946-1953.
- (49) *Computational Electrodynamics: The Finite-Difference Time-Domain Method*, Artech House, Norwood, MA; Taflove, A., S. C. Hagness, S. C. , Ed., 2005.
- (50) Lee, C. T.; Wang, M. X.; Jarnagin, N. D.; Gonsalves, K. E.; Roberts, J. M.; Yueh, W.; Henderson, C. L. In *Advances in Resist Materials and Processing Technology XXIV*; Lin, Q., Ed. 2007; Vol. 6519, p E5191-E5191.
- (51) Flatau, P. J.; Stephens, G. L.; Draine, B. T. Light-scattering by rectangular solids in the Discrete-Dipole Approximation - A new algorithm exploiting the block-toeplitz structure. *J. Opt. Soc. Am. A-Opt. Image Sci. Vis.* **1990**, *7*, 593-600.
- (52) Johnson, P. B.; Christy, R. W. Optical-constants of noble-metals. *Physical Review B* **1972**, *6*, 4370-4379.
- (53) Palik, E. D. *Handbook of Optical Constants of Solids*; Academic Press: San Diego, 1985; Vol. 1.
- (54) Lumerical Solutions, I.
- (55) Yee, K. S. *IEEE Trans. Antennas Propag.* **1966**, *14*, 302.
- (56) Hao, F., Nordlander, P. . *Chem. Phys. Lett.* **2007**, *446*, 115.
- (57) Gray, S. K.; Kupka, T. Propagation of light in metallic nanowire arrays: Finite-difference time-domain studies of silver cylinders. *Physical Review B* **2003**, *68*.
- (58) Giannini, V., Francescato, Y., Amrania, H., Phillips, C. C., Maier, S. A. *Nano Lett.*, *11*, 2835.
- (59) Zhang, S., Bao, K., Halas, N. J., Xu, H., Nordlander, P. *Nano Lett.* **2011**, *11*, 1657.
- (60) Wu, Y., Nordlander, P. *J. Phys. Chem. C* **2010**, *114*, 7302.
- (61) Dmitriev, A., Hagglund, C., Chen, S., Fredriksson, H., Pakizeh, T., Kall, M., Sutherland, D. S. *Nano Lett.* **2008**, *8*, 3893.

## CHAPTER VII

### HOLLOW GOLD NANORECTANGLES: THE ROLES OF POLARIZATION, SUBSTRATE AND ORIENTATION

#### **7.1 Summary**

Dimers of hollow gold nanorectangles (ca. 200 by 140 nm outside and 110 by 55 nm inside) were fabricated via Electron Beam Lithography with two different particle orientations and varying interparticle separations. Spectroscopic investigation of these arrays showed multiple peaks under illumination polarized both parallel and perpendicular to the interparticle axis. Discrete Dipole Approximation theoretical calculations were used to investigate the nature of these multiple peaks. These calculations demonstrate that the multiple peaks arise due to a combination of multiple plasmon modes and interactions with the substrate. Next, we show how these peaks change as the hollow nanorectangles are brought within coupling range of one another. In this endeavor, we make use of our previously-reported method to directly convert SEM images of the nanoparticles into the shape files for the theoretical calculations.



## 7.2 Introduction

Noble metal nanoparticles have been an area of intense research due to their unique optical properties. These include the localized surface plasmon resonance (LSPR),<sup>1-6</sup> which can be tuned by the size, shape, and medium of the nanoparticles as well as the spacing between nanoparticles.<sup>2,6-11</sup> Hollow nanostructures are even more sensitive than their solid analogues, as they have an extra degree of tunability afforded via control of the wall width.<sup>12-17</sup> The wall width of a hollow nanostructure determines how the inner and outer surface plasmons of a single nanoparticle interact with one another and how they interact with the plasmons on other nanoparticles within coupling range.<sup>2,6-11,16,17</sup>

It has been demonstrated that as two plasmonic particles are brought together, their near-fields begin to overlap and couple, which affects the plasmon resonance of the overall system.<sup>8-11</sup> Additionally, when plasmonic particles are small compared to their interparticle separation, they can be treated as dipolar excitons,<sup>18</sup> a fact that allows for the use of the exciton-coupling model to describe the plasmonic coupling of two interacting particles. If the plasmon dipoles are aligned in an attractive configuration, for example, head-to-tail in an axial alignment, the aggregate plasmon band is stronger and at a lower energy than that of a single particle. Conversely, if the dipoles are aligned in a repulsive configuration, for example, head-to-head in an axial alignment, the plasmon band will occur at a higher energy. The magnitude of the shift in the frequency of the LSPR for two interacting particles had been found to depend on the particle size and interparticle separation. This can be approximated<sup>9,19</sup> by  $\Delta\lambda/\lambda_0 = A \cdot \exp(-(s/D)/\tau)$  where  $\Delta\lambda$  is the

fractional shift in the LSPR wavelength,  $\lambda_0$  is the wavelength of the LSPR for an isolated particle,  $A$  is the pre-exponential fitting factor,  $s$  is the separation between the particles,  $D$  is the dimension of the particle along the interparticle axis, and  $\tau$  is the exponential decay length of the coupled particle pair.

Because of the high sensitivity of the plasmon resonant energy of hollow nanoparticles, very precise control over their geometry and interparticle separation is needed during their fabrication in order to study them systematically. Although colloidal synthesis techniques allow for high throughput and more flexibility with metal composition and three-dimensional shape, electron beam lithography (EBL) allows for nanometer-scale control over particle geometry and interparticle separations. However, a consequence of using EBL to fabricate nanoparticles is the introduction of a support substrate. It has previously been shown that placing nanoparticles on certain substrates (e.g. high-index) can lead to symmetry breaking as well as coupling or hybridization of plasmon modes,<sup>13,20,21</sup> so it is crucial to consider the effect of the substrate on the plasmon modes of the EBL-fabricated system. This can be accomplished by theoretically modeling the optical properties of the plasmonic nanoparticles in the presence and absence of a substrate.

The discrete dipole approximation (DDA) is a popular method to theoretically model the optical properties of systems due to the robustness and flexibility of this method, which allows for modeling of particles of arbitrary shape.<sup>4,7,12,14,15,22</sup> In this method, the particle is represented by a three-dimensional finite lattice of point dipoles that is then excited by

an external field. The response of the point dipoles to the external field and to one another is solved self-consistently using Maxwell's equations. Precise and accurate definition of the lattice used to represent the particle is crucial to achieve the best match with experimental conditions and results.<sup>4,13</sup> It has previously been shown that the use of SEM images as shape templates for theoretical calculations gives more accurate results than the traditional shape file preparation methods.<sup>13,16</sup> Another strength of DDA lies in the fact that this method allows for the consideration of substrate effects on the optical properties of the system. Furthermore, with modifications by Goodman<sup>23</sup> and Schatz<sup>24</sup> it is possible to calculate both the electric field enhancement contours and the individual dipole orientations at a specific wavelength. These plots can only be generated for one two-dimensional slice through the particle at a time, but the slice position can be chosen. Thus, by repeating the calculations for multiple slices through the particle, a three-dimensional representation of the field can be obtained at a particular resonant wavelength.

A sample of hollow gold nanorectangles was fabricated on silicon nitride substrates via electron beam lithography (EBL). The optical properties of the system were investigated experimentally and theoretically under parallel and perpendicular light polarization and in the presence and absence of a substrate.

### 7.3 Methods

Hollow gold nanorectangle arrays were fabricated using a JEOL JBX-9300FS 100 kV electron beam lithography (EBL) system. The substrate upon which the hollow rectangles were supported was an array of free-standing silicon nitride ( $\text{Si}_3\text{N}_4$ ) membrane windows, whose fabrication has been described elsewhere.<sup>25</sup> The  $\text{Si}_3\text{N}_4$  membrane was fabricated to a thickness of ca. 80 nm. Each  $\text{Si}_3\text{N}_4$  membrane window measured  $150 \times 150 \mu\text{m}^2$  and was used for a single design pattern, which measured  $200 \times 200 \mu\text{m}^2$  to ensure overlap with the window. An 80 nm thick layer of poly(methyl methacrylate) (PMMA), a positive electron resist, was spin coated onto the top  $\text{Si}_3\text{N}_4$  side of the wafer. The pattern was written using a base dose of  $1200 \mu\text{C}/\text{cm}^2$  and a beam current of 1.98 nA. A solution of 1:3 methyl isobutyl ketone:isopropyl alcohol (MIBK:IPA) was used to develop the exposed sample for 10 s, after which it was rinsed in IPA and gently dried with  $\text{N}_2$ . A CVC electron beam evaporater was then used to deposit an adhesion layer of chrome ( $0.5 \text{ \AA}$  at  $0.1 \text{ \AA}/\text{s}$ ), followed by a layer of gold ( $220 \text{ \AA}$  at  $0.5 \text{ \AA}/\text{s}$ ). Finally, the sample was placed in 1165 remover (MicroChem) to achieve lift-off, wherein all remaining PMMA was removed, including the metal film deposited on top of the PMMA, leaving just the metal particles on the substrate.

In order to minimize any far-field coupling, the hollow rectangle arrays were designed so that, within an array, the center-to-center distance between each neighboring dimer in any direction was at least 2000 nm. Additionally, the interparticle spacing never exceeded 5 particle diameters to ensure that the near-field coupling dominated the sample properties.<sup>9</sup>

The supported hollow rectangle arrays were imaged using a Zeiss Ultra60 scanning electron microscope (SEM). Extinction measurements were performed on a Craic Microspectra 121 UV-visible-NIR microspectrophotometer with an imaging range from 400-1700 nm at normal incidence in transmission mode under several polarization conditions (parallel and perpendicular to the interparticle axis and unpolarized). The aperture size selected for the measurements was  $625 \mu\text{m}^2$  with a 36X objective lens, and each reported spectrum is an average of at least 5 separate spectra taken across the sample.

The optical response of the hollow rectangle dimer arrays has been calculated using the DDA method with the DDSCAT 6.1 code offered publicly by Draine and Flatau<sup>26</sup> with modifications by Goodman<sup>23</sup> and Schatz.<sup>24</sup> The bulk values of the dielectric constants for gold and silicon nitride reported by Johnson and Christy<sup>27</sup> and Palik,<sup>28</sup> respectively, were used. At least 100,000 dipoles were used in the calculations to ensure accuracy of the results. In order to most accurately represent the experimental system, direct conversion of SEM images of the hollow rectangles were used as the shape descriptors for the DDA calculations. We have described this technique elsewhere.<sup>13</sup> Briefly, ImageJ (image processing software) was used to convert an SEM image into a text file of the XY coordinates for the pixels of the particle in the image. These XY coordinates were directly used to define the shape of the particle for the theoretical calculations. When included, the  $\text{Si}_3\text{N}_4$  substrate was simulated as a slab that extended ca. 30 nm beyond the particle(s) in the XY plane and was ca. 80 nm thick to mimic the experimental sample.

## 7.4 Results and Discussion

Two samples of hollow rectangle samples were fabricated by Electron beam Lithography. The rectangles in both samples had similar dimensions and interparticle separations, but the orientation of the particles is opposite in the two samples. In the first sample, the rectangles are oriented with their long axis parallel to the interparticle axis. In the second sample, the rectangles are oriented with their long axis perpendicular to the interparticle axis. For clarity, when discussing the polarization direction of light, the direction will always be defined with respect to the interparticle axis. Meaning, parallel polarization indicates light polarized along the interparticle axis and perpendicular polarization indicates light polarized perpendicular to the interparticle axis. Herein, the two samples or particles will be discussed separately and the effect of orientation assessed afterwards.

### 7.4.1 Long Orientation

A selection of SEM images of the hollow rectangles is shown in Figure 7 - 1. The average outer dimensions of the hollow rectangles are  $197\pm 4$  by  $134\pm 6$  nm, and the average inner dimensions are  $109\pm 5$  by  $53\pm 3$  nm, giving an average wall width of  $42\pm 3$  nm. The particles are 22 nm thick, and the interparticle separations range from  $27\pm 2$  nm to  $596\pm 8$  nm for the long configuration. The interparticle separation is measured as edge-to-edge (i.e. the smallest distance between edges) in the dimer throughout.

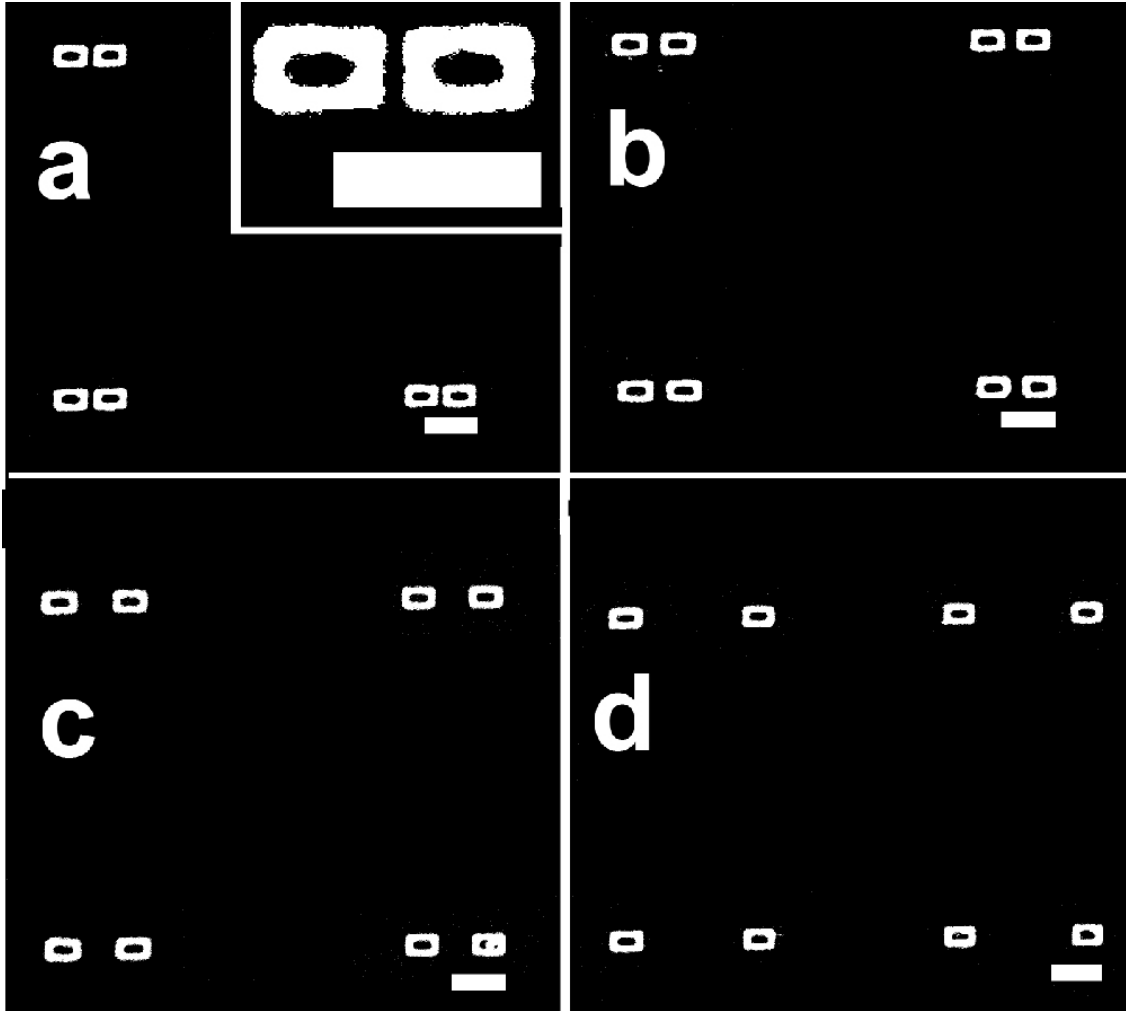


Figure 7 - 1. Selected SEM images of gold hollow rectangle pairs fabricated via EBL on  $\text{Si}_3\text{N}_4$  membranes. The particles have outer dimensions of  $197 \pm 4$  by  $134 \pm 6$  nm and inner dimensions of  $109 \pm 5$  by  $53 \pm 3$  nm. The interparticle separations are a)  $27 \pm 2$  nm, b)  $71 \pm 2$  nm, c)  $191 \pm 3$  nm, and d)  $596 \pm 8$  nm. The scale bars are 300 nm.

We have shown previously for gold nanorings that direct conversion of the SEM images for use in calculations led to better agreement between theory and experiment.<sup>13</sup>

Accordingly, the direct conversion of the SEM images was used in the DDA calculations

here as well. The simplest case was considered first, an isolated particle in air. The results indicate that when light is polarized along the long axis of the particle (hereafter referred to as parallel polarization as in the dimers it corresponds to along the interparticle axis), only one peak is present at 936 nm (Figure 7 - 2, black).

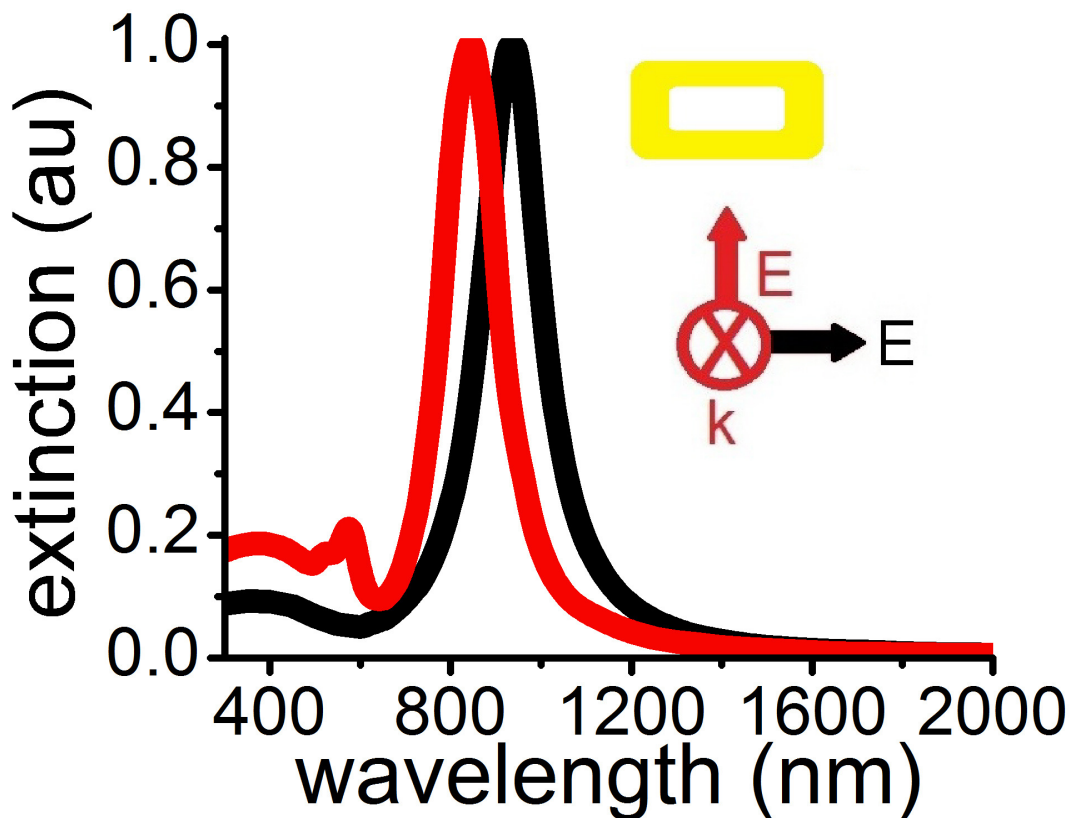


Figure 7 - 2. DDA in air for isolated particle with light polarized parallel (black) and perpendicular (red) to the long axis of the particle. For parallel polarization, only one peak is present at 936 nm. For perpendicular polarization, one major peak is present at 844 nm and one minor peak is present at 574 nm.



Field contour and vector plots were generated to elucidate which surface plasmon mode of the particle this peak represented. To accurately assign plasmon modes, multiple field contour plots were generated at each wavelength for evenly spaced slices through the particle(s). When combined (as in Figure 7 - 3), we can achieve a good three-dimensional representation of the field location and orientation at a particular resonance wavelength. The composite field plot for the isolated particle in air with parallel polarization is shown in Figure 7 - 3 along with its field enhancement scale. The field is concentrated at the outer corners of the particle in each slice. The concentration of the field at the corners is expected due to the lightning rod effect, and has also been seen in similar solid structures.<sup>29-32</sup> The maximum enhancement for this wavelength is 2060 and occurs at the top and bottom slices of the particle. In addition to the field contour, a plot of the individual dipoles that make up the particle and their orientation was generated for each particle slice. Hereafter, a minus sign will be used to represent when the field vectors are pointing away from an area. Conversely, a plus sign will be used to represent when the field vectors are pointing toward an area, as shown in Figure 7 - 4. The composite plot for the hollow rectangle at 936 nm has the field vectors pointing away from the right side and toward the left side throughout the entire particle. This corresponds to the most primitive dipole mode for the particle, which is the largest extinction peak.

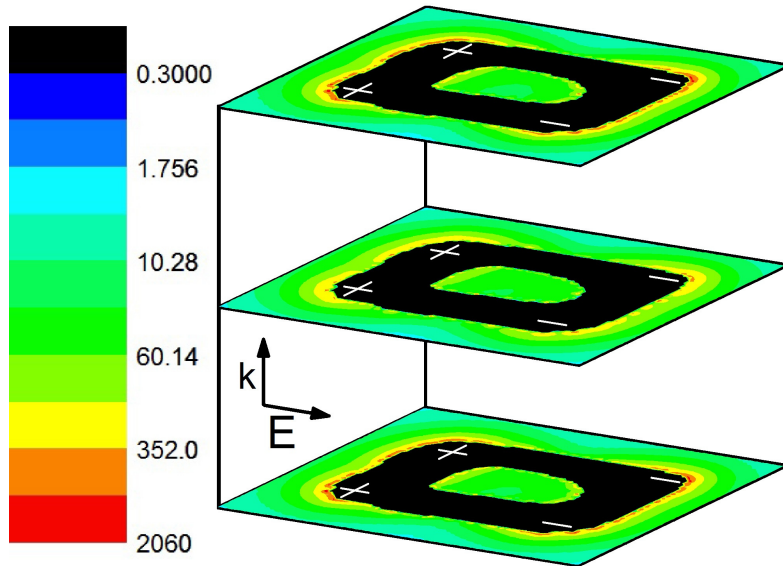


Figure 7 - 3. Composite field plot for isolated particle in air with parallel polarization at 936 nm. The field is located at the corners of the particle in each slice. The field vectors are pointing away from the right of the particle and towards the left in each slice. The field location and orientation indicates this is the dipole mode.

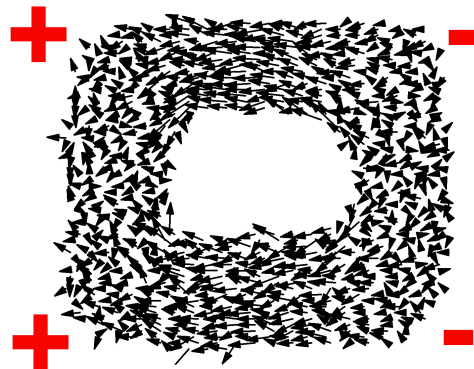


Figure 7 - 4. Representative field vector plot (top slice of a hollow rectangle) for an isolated hollow rectangle in air with parallel polarization at  $\lambda = 936\text{nm}$ . As shown, a plus sign will indicate when all the vectors are pointing towards an area, and a minus sign indicate when all the vectors are pointing away from an area.

For the perpendicular polarization, two peaks are present: a major peak at 844 nm and a minor peak at 574 nm (Figure 7 - 2, red). The peak at 574 nm is weaker in intensity than the peak at 844 nm by a factor of 4. Similar investigations of the field location and orientation were carried out for the perpendicular polarization case at 844 nm (Figure 7 - 5 and Figure 7 - 6) and 574 nm (Figure 7 - 7 and Figure 7 - 8). The maximum enhancement is at 844 nm is 1060 and occurs at the top and bottom slices of the particle. At 844 nm, the field is concentrated at the outer corners of the particle and the field vectors are pointing away from the far side of the particle and toward the near side throughout the entire particle (Figure 7 - 5 and Figure 7 - 6). This corresponds to the dipole mode at this polarization, which is different than the dipole mode seen for the opposite polarization because of the different dimensions of the particle along these two directions. The maximum enhancement at 574 nm is 247 and occurs at the top and bottom slices of the particle. At 574 nm the field is concentrated at the outer corners and along the interior walls while field vectors alternate in orientation from the corners to the included side (Figure 7 - 7 and Figure 7 - 8). This corresponds to the quadrupole mode. The asymmetric particle shape and the corners of the particle allow the quadrupole mode to contribute, as there is still a net moment for this mode on this particle. We have seen contributions for the quadrupole mode for other particles (e.g. prisms, cubes)<sup>29,32</sup> with one or more of these features (i.e. sharp corners and/or asymmetric shape) but have not seen the quadrupole mode on spherical or ring like structures.<sup>13,19</sup>

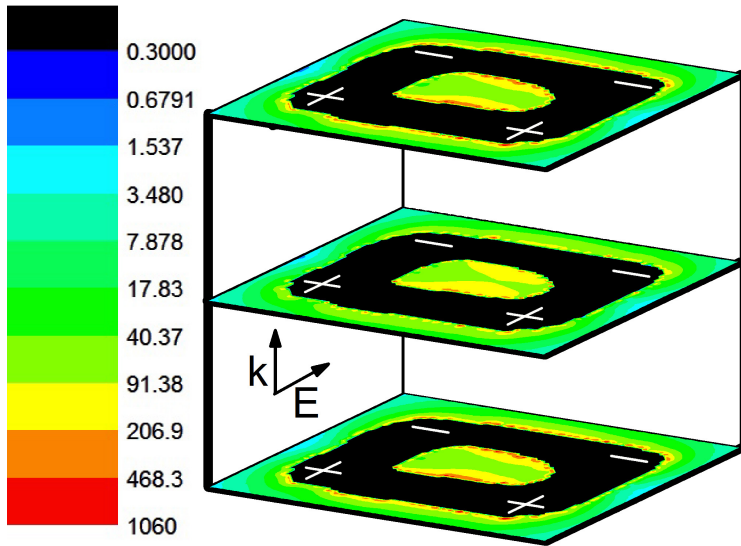


Figure 7 - 5. Composite field plots for isolated particle in air with perpendicular polarization at 844 nm (main peak). The field is located at the corners of the particle in each slice. The field vectors are pointing away from the back of the particle and towards the front in each slice. The field location and orientation indicates this is the dipole mode.

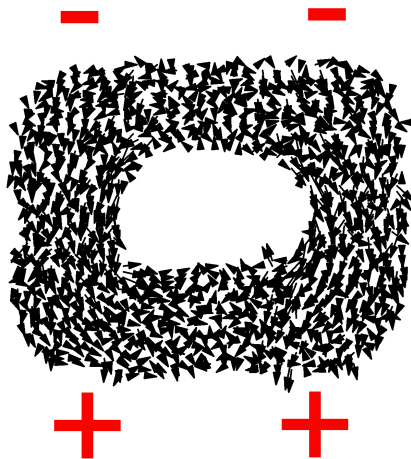


Figure 7 - 6. Representative field vector plot (top slice of a hollow rectangle) for an isolated hollow rectangle in air with perpendicular polarization at  $\lambda = 844$  nm. As shown, a plus sign will indicate when all the vectors are pointing towards an area, and a minus sign indicate when all the vectors are pointing away from an area.

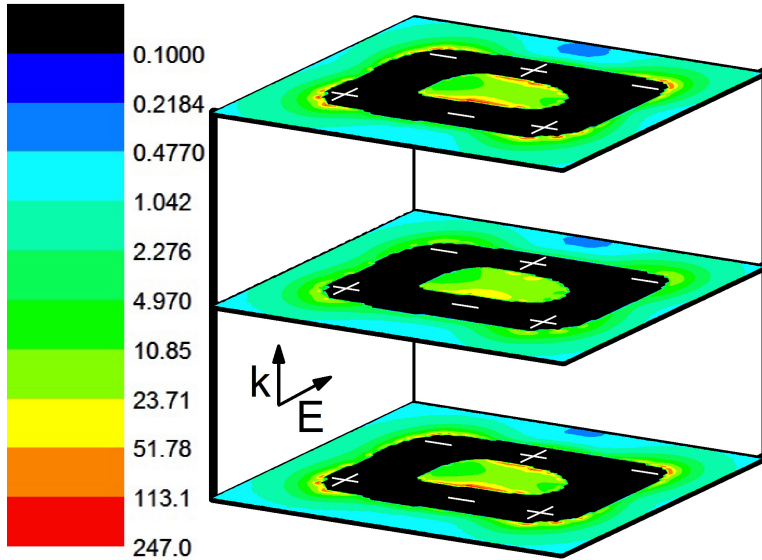


Figure 7 - 7. Composite field plots for isolated particle in air with perpendicular polarization at 574 nm (minor peak). The field is located at the outer corners and the interior long sides of the particle in each slice. The field vectors alternate orientation along the sides and corners. The field location and orientation indicates this is the quadrupole mode.

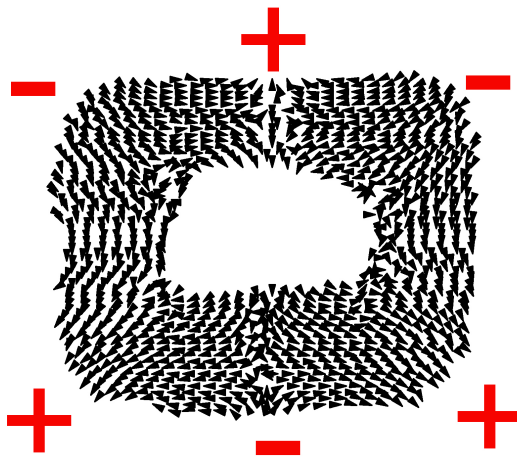


Figure 7 - 8. Representative field vector plot (top slice of a hollow rectangle) for an isolated hollow rectangle in air with perpendicular polarization at  $\lambda = 574$  nm. As shown, a plus sign will indicate when all the vectors are pointing towards an area, and a minus sign indicate when all the vectors are pointing away from an area.

After explaining the peaks present at different polarizations in air for the isolated particle, we next investigated the effects of coupling by looking at dimers with varying interparticle separations. It has previously been shown that bringing two nanoparticles closer together when the light is polarized parallel to the interparticle axis results in a red shift of the overall plasmon mode for the dimer as the interparticle separation decreases.<sup>2,6-11</sup> Conversely, if the light is polarized perpendicular to the interparticle axis, the overall plasmon mode for the dimer blue shifts as the interparticle separation decreases.<sup>2,6-11</sup> The results for all interparticle separations with parallel polarization are shown in Figure 7 - 9a and display a single peak that red shifts as the interparticle separation decreases, as expected. For the perpendicular polarization (Figure 7 - 9b) both the dipole and quadrupole peaks are present at all interparticle separations, and the dipole peak shows a slight blue shift, as expected. We expect the substrate supporting the experimental sample to affect the optical properties of the system, causing deviations from the properties predicted for the plasmonic system in air.

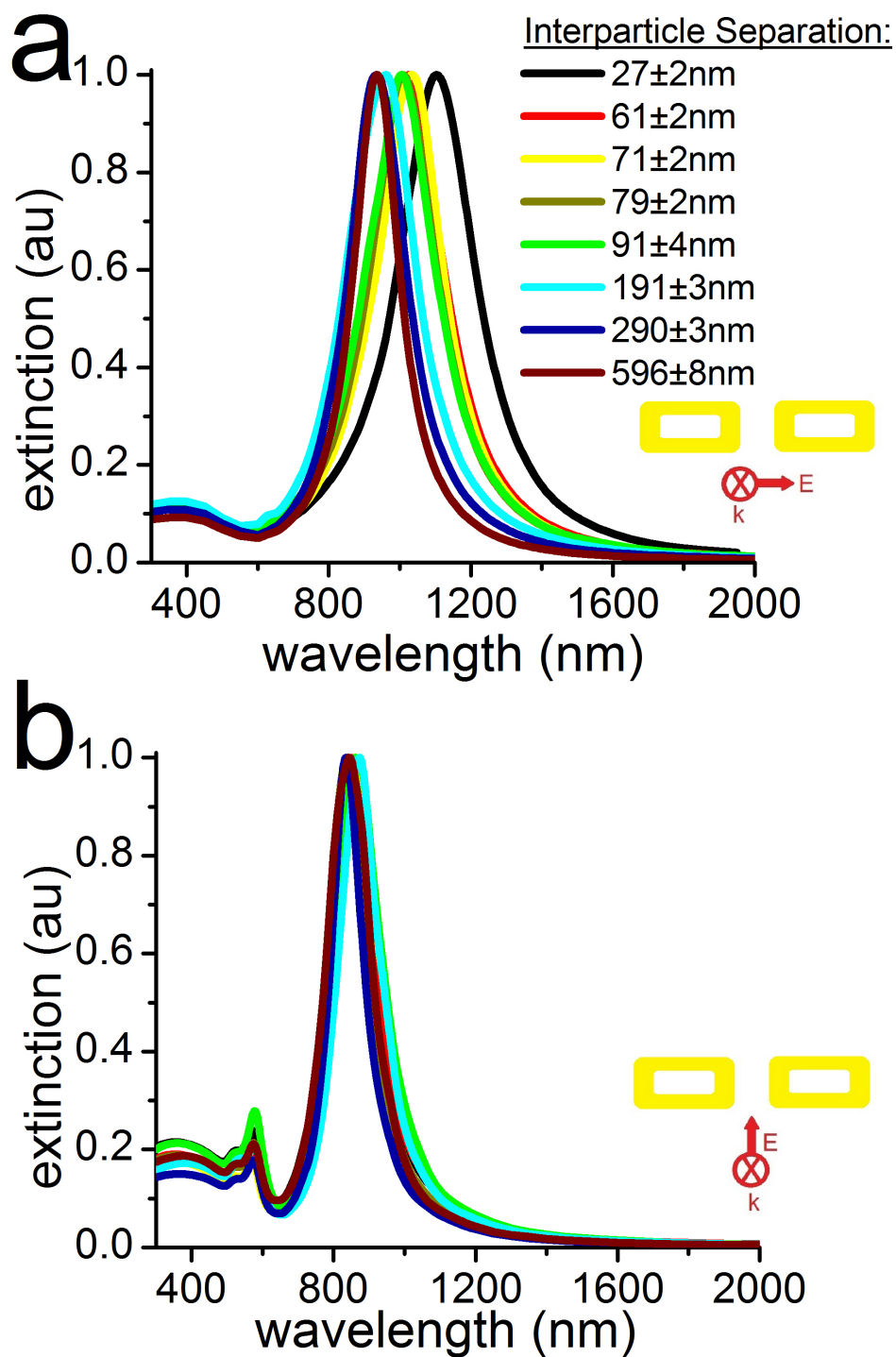


Figure 7 - 9. DDA extinction spectra for hollow gold nanorectangles with long orientation in air ( i.e. no substrate) and light polarized a) parallel and b) perpendicular to the interparticle axis (as indicated in the insets). The interparticle separations are indicated in the legend. The spectra show the expected red shift and blue shift for parallel and perpendicular polarization, respectively.

The experimental extinction spectra for the hollow rectangles are shown in Figure 7 - 10. It can be seen that there are two distinct peaks in the spectra with the light polarized parallel to the interparticle axis: one located at ca. 1200 nm and the other at ca. 1500 nm. As the interparticle separation decreases, both bands red shift and the intensity of the band at ca. 1200 nm decreases while the intensity of the band at ca. 1500 nm increases. This is in contrast with the DDA results in air, where only one peak was present. This is not due to variation in the sample, as there was very little variation (<1% RSD) in the spectra taken across one area of the sample (Figure 7 - 11). This suggests that there is a definite effect from the substrate for this polarization. For the perpendicular polarization, the spectra are simpler, with one major peak at ca. 1150 nm and two minor peaks at ca. 700 nm and ca. 1450 nm (Figure 7 - 10b). The major peak shows a slight blue shift as the interparticle separation is decreased. The minor peak at ca. 1450 increases in intensity as the interparticle separation is decreased. The minor peak at ca. 700 nm does not change significantly in position or intensity as the interparticle separation is varied. The peaks at ca. 1150 nm and 700 nm are most likely the dipole and quadrupole peaks that were predicted from the DDA calculations in air, just shifted due to the presence of the substrate. The intensity of the peak at ca. 1150 nm is approximately 4 times that for the peak at ca. 700 nm, which was the same intensity ratio that was predicted for the DDA calculations in air. However, the peak at 1450 nm was not predicted from the calculations in air. This suggests that the peak at 1450 is most likely due to substrate effects.



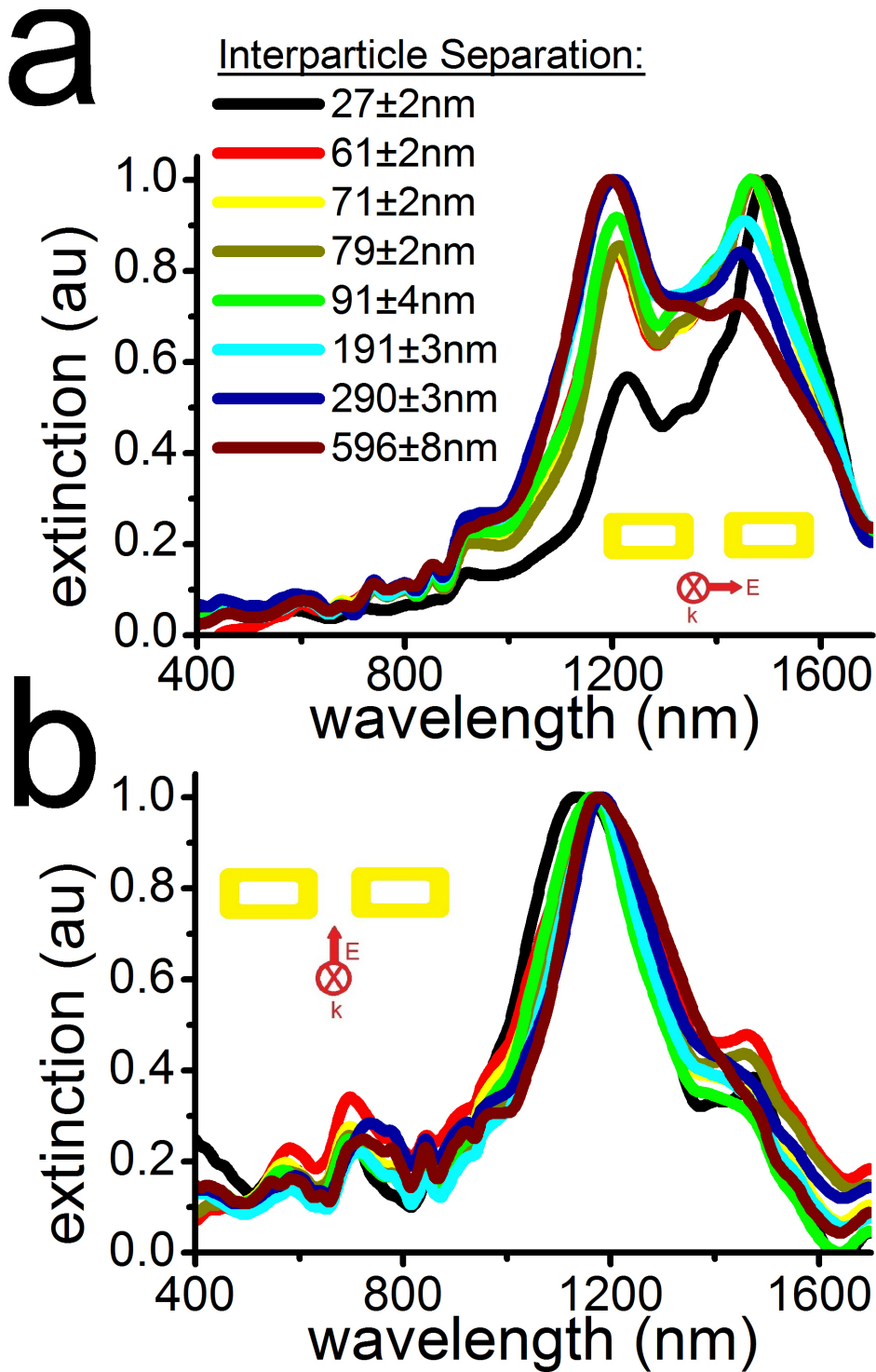


Figure 7 - 10. Experimental extinction spectra for hollow gold nanorectangles with long orientation and polarization a) parallel and b) perpendicular (as indicated in the insets) to the interparticle axis. The interparticle separations are indicated in the legend. There are two distinct peaks present for the parallel polarization, which red shift and change in intensity as the interparticle separation decreases. For the perpendicular polarization the expected blue shift is seen as the interparticle separation decreases.

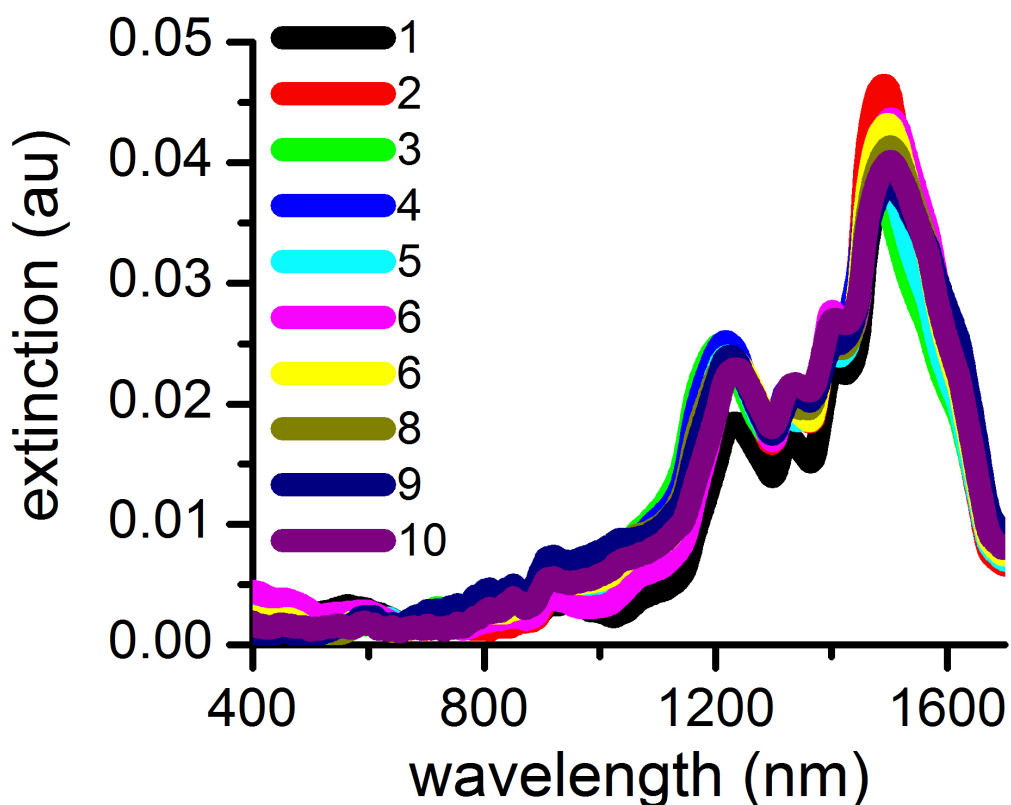


Figure 7 - 11. Ten raw experimental extinction spectra for hollow gold nanorectangles with an interparticle separation of  $27 \pm 2$  nm long orientation and polarization parallel to the interparticle axis. The spectra are very similar to one another, indicating good uniformity across the entire sample. The main peak position occurs at 1496 nm with a relative standard deviation of only 0.5%.

To determine how the substrate is interacting with the particles and if it is indeed causing the multiple peaks, we performed DDA calculations on a substrate. The DDA extinction spectra for the hollow rectangles on a substrate are shown in Figure 7 - 12. The spectra with light polarized parallel to the interparticle axis (Figure 7 - 12a) do show a shoulder that becomes a more pronounced second peak as the interparticle separation increases. In fact, comparing the experimental (Figure 7 - 10a) and DDA (Figure 7 - 12a) spectra for

light polarized parallel to the interparticle axis, it can be seen that the dip separating the two peaks occurs around 1300-1350 nm for all cases. The spectra with light polarized perpendicular to the interparticle axis (Figure 7 - 12b) have a major peak ca. 1150 nm and two minor peaks at ca. 700 nm and 1450 nm, just as was seen in the experimental spectra. The results for the DDA calculations on the substrate for both polarizations closely resemble what was seen experimentally, suggesting the extra spectral features not seen for calculations in air are indeed due to substrate effects.

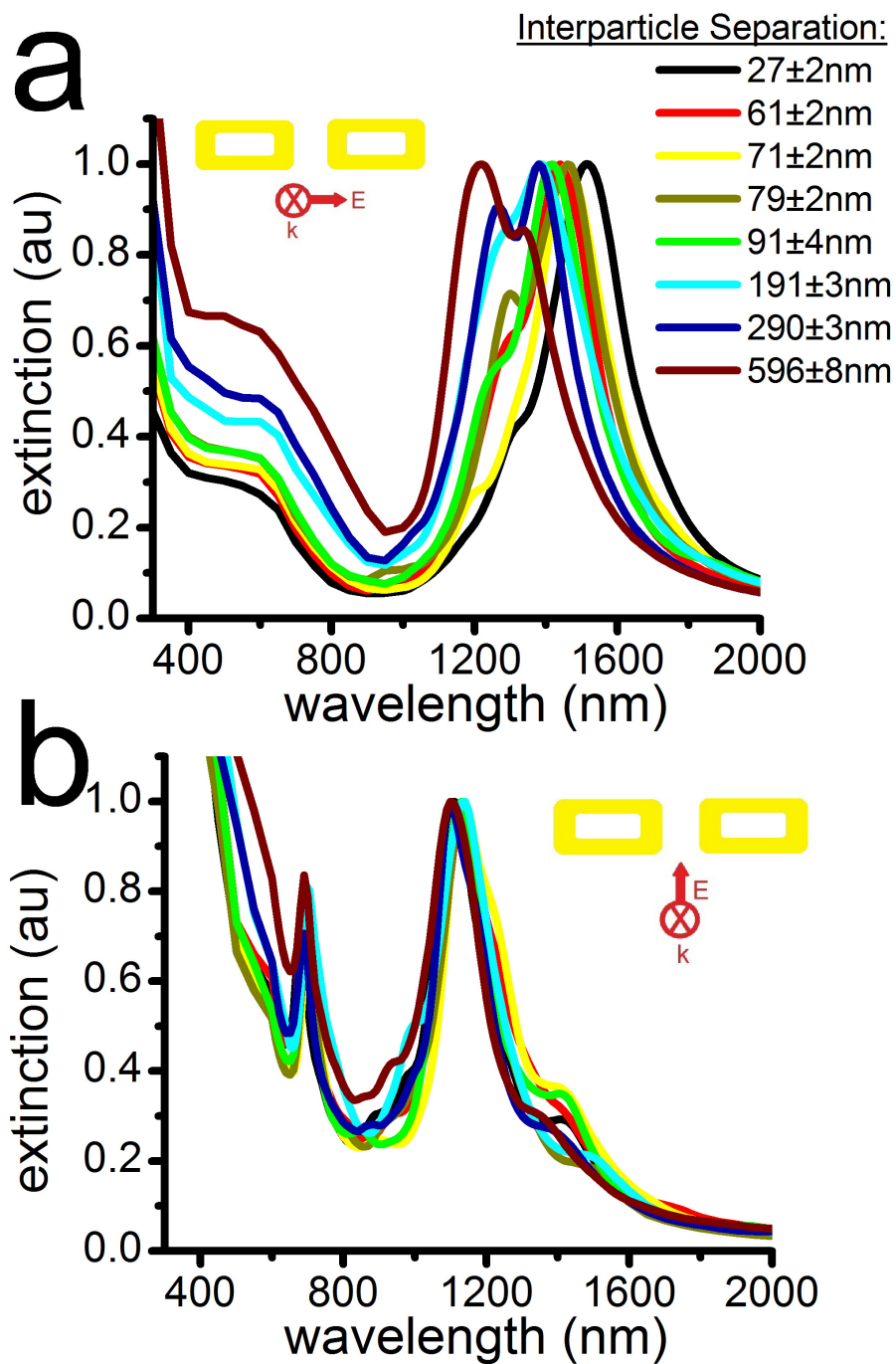


Figure 7 - 12. DDA extinction spectra for hollow gold nanorectangles with long orientation on a substrate light polarized a) parallel and b) perpendicular to the interparticle axis (indicated in the insets). The interparticle separations are indicated in the legend.

To determine which spectral features are due to substrate effects for the parallel polarization we will compare the field plots for the different peaks. First we will consider our DDA calculations in air, as these calculate the energy of the nanoparticles in an unperturbed state. Field plots were generated for multiple two-dimensional slices along the z-axis (top, middle and bottom) for the particles at each interparticle separation in air at the resonant wavelengths. For all interparticle separations in air, the field maximum for the resonant wavelength was located at the top and bottom of the nanoparticle (Figure 7 - 13). The propagation of the light is along the z-axis, so it makes sense that, in air, the field is concentrated at the surfaces of the particle along that axis (i.e. the top and bottom). Next, field plots were generated for several wavelengths for the dimer with an interparticle separation of  $596\pm 8$  nm on a substrate. At this interparticle separation ( $596\pm 8$  nm), the particles are far enough apart (ca. 3 particle lengths) to be considered isolated. The dip in the DDA extinction spectrum for this particle pair on a substrate under parallel polarization occurs at 1300 nm (Figure 7 - 12a, dark blue spectrum). Field plots indicate that the peaks at 1220 nm (Figure 7 - 14) and 1340 nm (Figure 7 - 15) both correspond to the dipole mode. The only difference between the two peaks is that at 1220 nm the field maximum occurs in the middle z slice of the particle whereas at 1340 nm the field maximum occurs at the bottom z slice. Field plots at several other wavelengths also correspond to the dipole mode, with the field maximum fluctuating between the bottom and middle of the particle, depending on the wavelength. The results are summarized in Figure 7 - 16 and indicate that for wavelengths to the blue of the dip ( $\lambda < 1300$  nm), the field maximum occurs in the middle of the particle, whereas for wavelengths to the red of the dip ( $\lambda > 1300$  nm) the field maximum occurs at the bottom of

the particle (Figure 7 - 16). The field maximum for the particle in air, i.e. the "unperturbed" particle, was located at the top and bottom of the particle, which would indicate that the peaks at which the field maximum is perturbed away from this location are those due to substrate effects. This indicates that the peak to the blue of the dip ( $\lambda=1220$  nm) is due to interactions with the substrate. On the other hand, the peak to the red ( $\lambda=1340$  nm) seems to be the same dipole peak seen for the calculations in air, just shifted due to the change in the refractive index of the surrounding medium due to the presence of the substrate. This is further illustrated in Figure 7 - 17, which shows that for the particle in air the field was most intense at the corners of the particle for the top and bottom. But when placed on a substrate, the field at the bottom of the particle interacts more strongly with the substrate than the field at the top of the particle, which leads to the formation of the two peaks observed experimentally and confirmed via DDA calculations where the substrate is included.

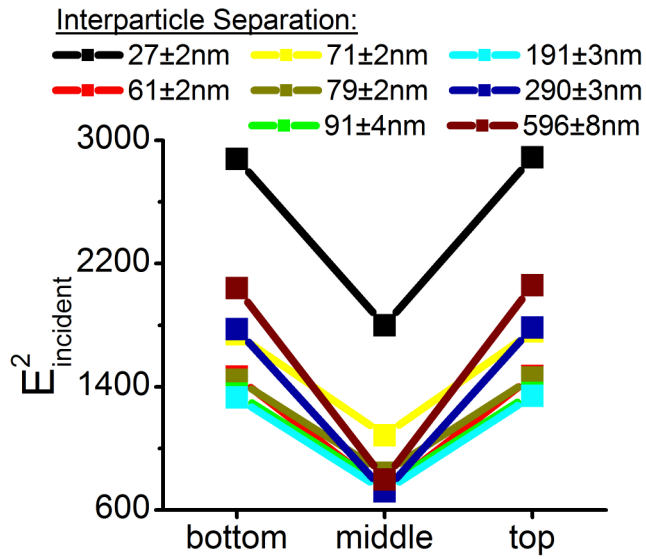


Figure 7 - 13. Field enhancement values at the resonant wavelength for the dipole mode of the particles in air with light polarized parallel to the interparticle axis. The interparticle separations are indicated in the legend. For all cases, the field enhancement is greatest at the top and bottom of the particles, and reaches a minimum in the middle.

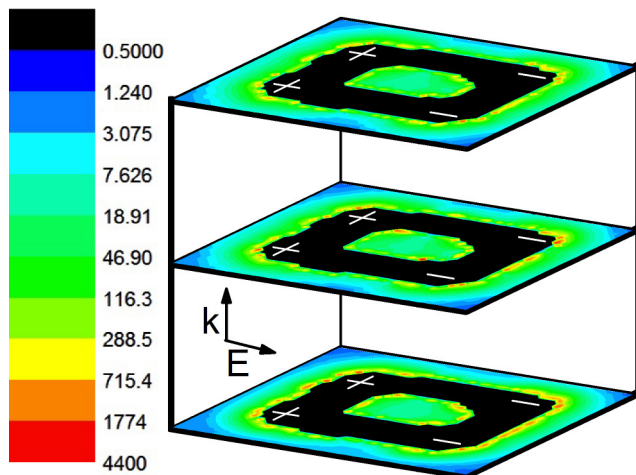


Figure 7 - 14. Composite field plot for isolated particle on a substrate with parallel polarization at 1220 nm. The field is located at the corners of the particle in each slice. The field vectors are pointing away from the right of the particle and towards the left in each slice. The field location and orientation indicates this is the dipole mode.

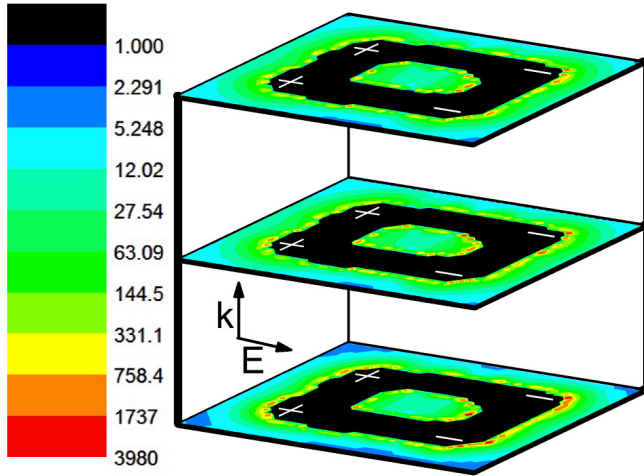


Figure 7 - 15. Composite field plot for isolated particle on a substrate with parallel polarization at 1340 nm. The field is located at the corners of the particle in each slice. The field vectors are pointing away from the right of the particle and towards the left in each slice. The field location and orientation indicates this is the dipole mode.

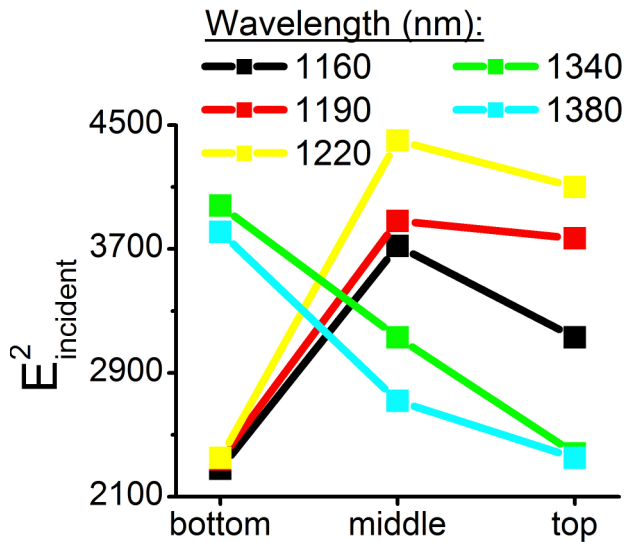


Figure 7 - 16. Field enhancement values for the particle pair with an interparticle separation of  $596 \pm 8$  nm on a substrate with light polarized parallel to the interparticle axis at several wavelengths (as indicated in the legend). For the wavelengths to the blue of 1300 nm, the field is most intense in the middle z slice of the particle. Meanwhile, for wavelengths to the red of 1300 nm, the field is most intense at the bottom z slice of the particle.



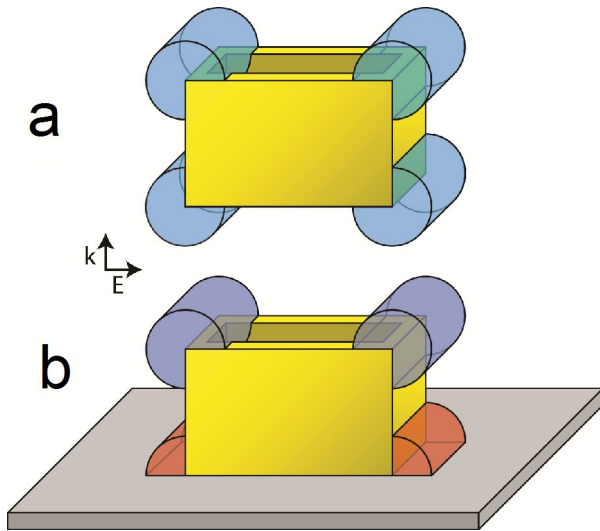


Figure 7 - 17. Diagram illustrating substrate effect for a single particle under parallel polarization. a) In air, the field is symmetric and most intense at the top and bottom of the particle. b) In the presence of the substrate, the field at the bottom of the particle interacts with the substrate and leads to the two peaks observed experimentally.

Similarly, we investigated the fields around the particle pair with smallest interparticle separation and light polarized perpendicular to the interparticle axis. We were able to confirm that the minor peak at 680 nm corresponded to the quadrupole mode (Figure 7 - 18) and the major peak at 1110 nm corresponded to the dipole mode (Figure 7 - 19), as was seen for the particles in air. Also, for both these modes, the maximum field enhancement occurred at the bottom slice of the particle. Meanwhile, the peak at 1420 nm also corresponded to the dipole mode but the maximum field occurred at the middle slice of the particle (Figure 7 - 20). This suggests that the peak at ca. 1450 nm is due to substrate interactions as the field is perturbed away from the extremities of the particle.

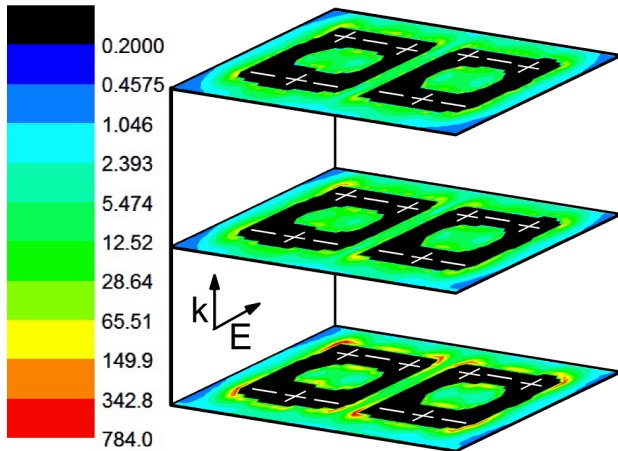


Figure 7 - 18. Composite field plot for particle pair with an interparticle separation of  $27\pm 2$  nm on a substrate with perpendicular polarization at 680 nm. The field is located at the corners and sides of the particle in each slice. The field vectors are pointing away from the front corners and middle of the back side and towards the back corners and middle of the front side. The field location and orientation indicates this is the quadrupole mode. The field is most intense at the bottom slice of the particle.

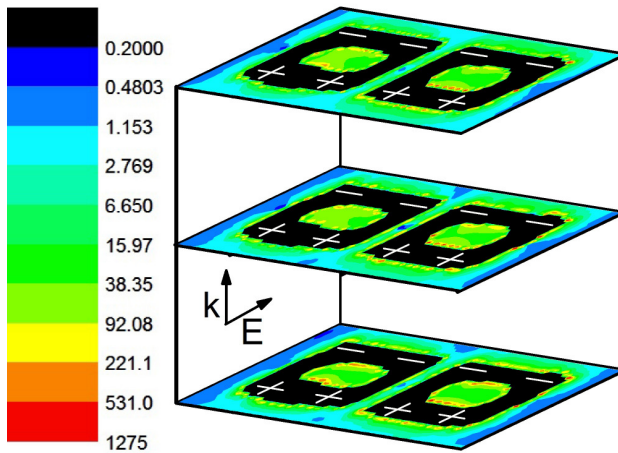


Figure 7 - 19. Composite field plot for particle pair with an interparticle separation of  $27\pm 2$  nm on a substrate with perpendicular polarization at 1110 nm. The field is located at the corners of the particle in each slice. The field vectors are pointing away from the back of the particle and towards the front in each slice. The field location and orientation indicates this is the dipole mode. The field is most intense at the bottom slice of the particle.

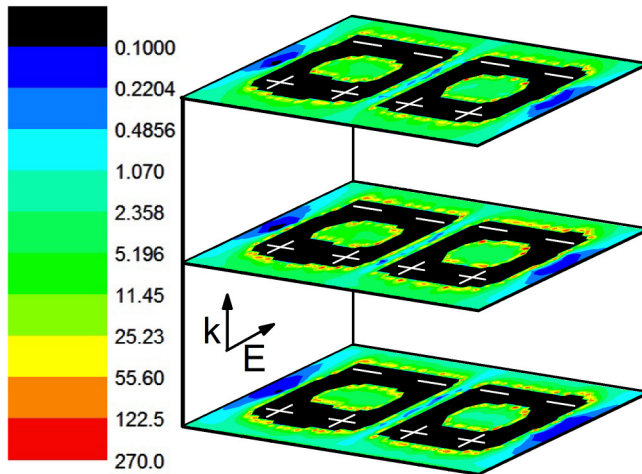


Figure 7 - 20. Composite field plot for particle pair with an interparticle separation of  $27 \pm 2$  nm on a substrate with perpendicular polarization at 1420 nm. The field is located at the corners of the particle in each slice. The field vectors are pointing away from the back of the particle and towards the front in each slice. The field location and orientation indicates this is the dipole mode. The field is most intense at the middle slice of the particle.

It has previously been shown that the fractional shift in the wavelength of the plasmon dipole mode can be approximated<sup>9,19</sup> by  $\Delta\lambda/\lambda_0 = A \cdot \exp(-(s/D)/\tau)$  where  $\Delta\lambda$  is the shift in the plasmon wavelength,  $\lambda_0$  is the plasmon wavelength for an isolated particle,  $A$  is the pre-exponential fitting factor,  $s$  is the separation between the particles,  $D$  is the dimension of the particle along the interparticle axis, and  $\tau$  is the exponential decay length of the coupled particle pair. Therefore, we would only expect the dipole peak of the particle, and not that due to the strong interaction with the substrate, to fit well to this exponential trend. So to confirm that we have assigned the two peaks seen experimentally and in the DDA calculations on a substrate to the appropriate modes (i.e. which is due to strong interactions with the substrate), the fractional shift of the peak not due to the substrate

interaction is shown in Figure 7 - 21 for the DDA and experimental data. In both cases the data fits the expected exponential decay<sup>2,6-11</sup> well ( $R^2 > 0.93$ ), confirming that the peak further to the red corresponds with the dipole mode of the particle.

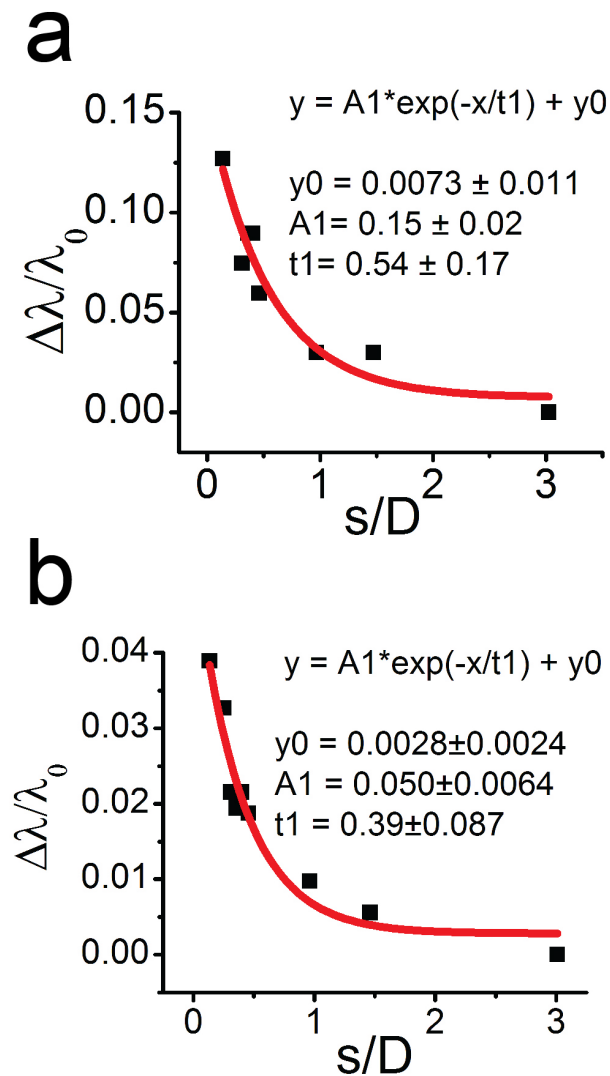


Figure 7 - 21. a) Fractional shift of calculated dipolar plasmon peak. The data fits the expected exponential decay well ( $R^2 = 0.93$ ). b) Fractional shift of experimental dipolar plasmon peak. The data fits the expected exponential decay well ( $R^2 = 0.95$ ).

#### 7.4.2 Tall Orientation

A selection of SEM images of the tall hollow rectangles is shown in Figure 7 - 22. The average outer dimensions of the hollow rectangles are  $140\pm 6$  by  $197\pm 4$  nm, and the average inner dimensions are  $53\pm 4$  by  $106\pm 5$  nm, giving an average wall width of  $45\pm 2$  nm. The particles are 22 nm thick, and the interparticle separations range from  $25\pm 2$  nm to  $284\pm 8$  nm. The interparticle separation is measured as edge-to-edge (i.e. the smallest distance between edges) in the dimer throughout.

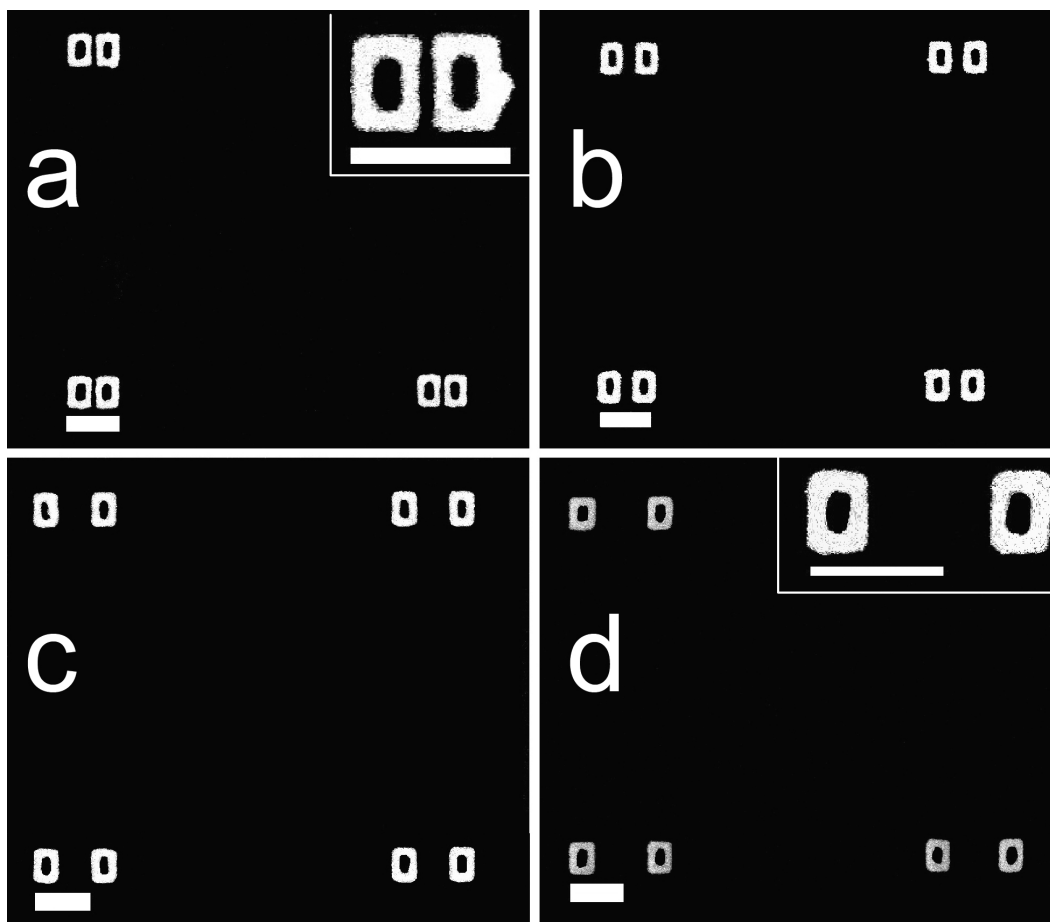


Figure 7 - 22. Selected SEM images of gold hollow rectangle pairs fabricated via EBL on  $\text{Si}_3\text{N}_4$  membranes. The particles have outer dimensions of  $140\pm 6$  by  $197\pm 4$  nm and inner dimensions of  $53\pm 4$  by  $106\pm 5$  nm. The interparticle separations are a)  $25\pm 2$  nm, b)  $73\pm 3$  nm, c)  $189\pm 7$  nm, and d)  $284\pm 8$  nm. The scale bars are 300 nm.

We have shown previously for gold nanorings that direct conversion of the SEM images for use in calculations led to better agreement between theory and experiment.<sup>13</sup>

Accordingly, the direct conversion of the SEM images was used in the DDA calculations here as well. The simplest case was considered first, an isolated particle in air. The results indicate that when light is polarized along the short axis of the particle (hereafter

referred to as parallel polarization), only one major peak is present at 855 nm and one minor peak is present at 570 nm (Figure 7 - 23, black).

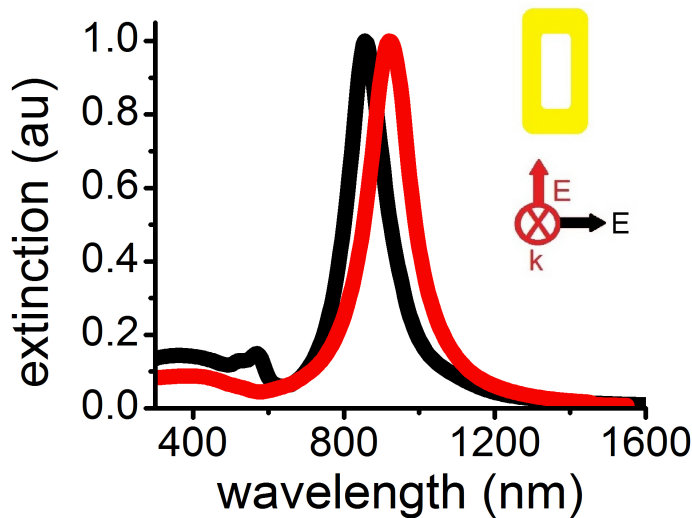


Figure 7 - 23. DDA in air for isolated particle with light polarized parallel (black) and perpendicular (red) to the short axis of the particle. For parallel polarization, one major peak is present at 855 nm and one minor peak is present at 570. For perpendicular polarization, only one peak is present at 920 nm.

Field contour and vector plots were generated to elucidate which surface plasmon mode of the particle this peak represented. To accurately assign plasmon modes, multiple field contour plots were generated at each wavelength for evenly spaced slices through the particle(s). When combined (as in Figure 7 - 24), we can achieve a good three-dimensional representation of the field location and orientation at a particular resonance wavelength. The composite field plot for the major peak at 855 nm for the

isolated particle in air is shown in Figure 7 - 24 along with its field enhancement scale. The field is concentrated at the outer corners of the particle in each slice. The concentration of the field at the corners is expected due to the lightning rod effect, and has also been seen in similar solid structures.<sup>29-32</sup> The maximum enhancement for this wavelength is 1340 and occurs at the top and bottom slices of the particle. In addition to the field contour, a plot of the individual dipoles that make up the particle and their orientation was generated for each particle slice. Hereafter, a minus sign will be used to represent when the field vectors are pointing away from an area. Conversely, a plus sign will be used to represent when the field vectors are pointing toward an area. The composite plot for the hollow rectangle at 855 nm has the field vectors pointing away from the right side and toward the left side throughout the entire particle (Figure 7 - 25). This corresponds to the most primitive dipole mode for the particle, which is the largest extinction peak. The field contour plot for the minor peak at 570 nm for the isolated particle in air with parallel polarization is shown in Figure 7 - 26. The maximum enhancement for this peak is only 160 and occurs at the top and bottom slices of the particle. At 570 nm the field is concentrated at the outer corners and along the interior walls while field vectors alternate in orientation from the corners to the included side (Figure 7 - 27). This corresponds to the quadrupole mode. The asymmetric particle shape and the corners of the particle allow the quadrupole mode to contribute, as there is still a net moment for this mode on this particle. We have seen contributions for the quadrupole mode for other particles (e.g. prisms, cubes)<sup>29,32</sup> with one or more of these features (i.e. sharp corners and/or asymmetric shape) but have not seen the quadrupole mode on spherical or ring like structures.<sup>13,19</sup>



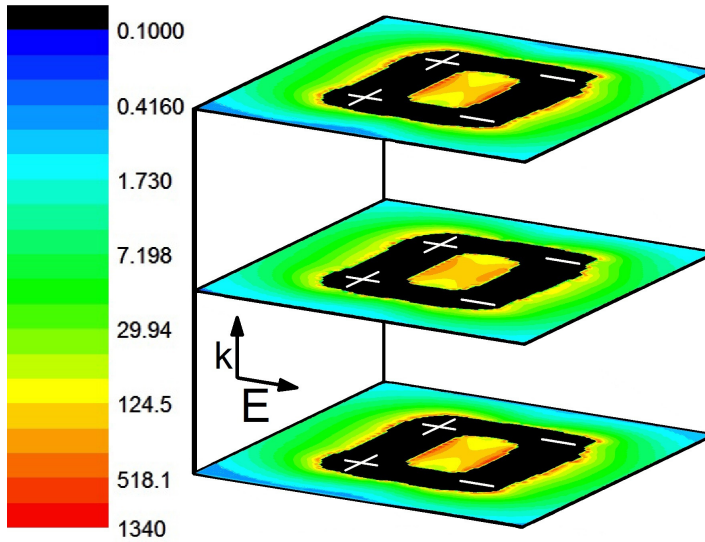


Figure 7 - 24. Composite field plots for isolated particle in air with parallel polarization at 855 nm (main peak). The field is located at the corners of the particle in each slice. The field vectors are pointing away from the right of the particle and towards the left in each slice. The field location and orientation indicates this is the dipole mode.

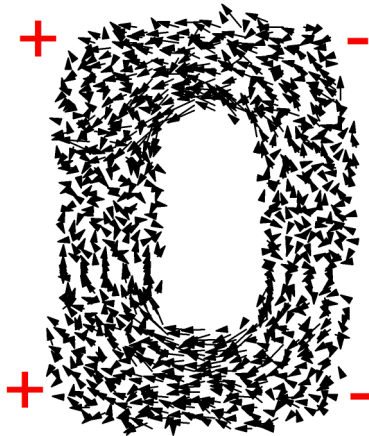


Figure 7 - 25. Representative field vector plot (top slice of a hollow rectangle) for an isolated hollow rectangle in air with parallel polarization at  $\lambda = 855$  nm. As shown, a plus sign will indicate when all the vectors are pointing towards an area, and a minus sign indicate when all the vectors are pointing away from an area.

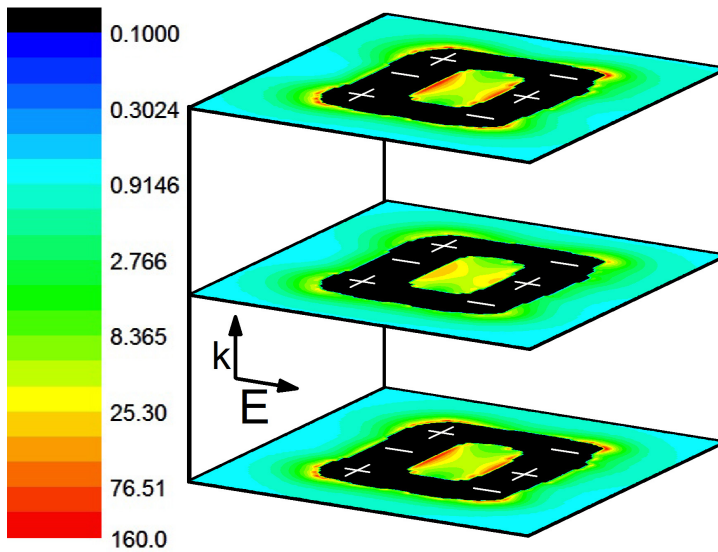


Figure 7 - 26. Composite field plots for isolated particle in air with parallel polarization at 570 nm (minor peak). The field is located at the outer corners and the interior long sides of the particle in each slice. The field vectors alternate orientation along the sides and corners. The field location and orientation indicates this is the quadrupole mode.

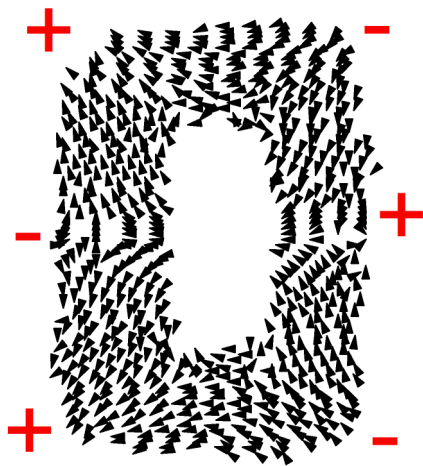


Figure 7 - 27. Representative field vector plot (top slice of a hollow rectangle) for an isolated hollow rectangle in air with parallel polarization at  $\lambda = 570$  nm. As shown, a plus sign will indicate when all the vectors are pointing towards an area, and a minus sign indicate when all the vectors are pointing away from an area.

For the perpendicular polarization, only one peak is present at 920 nm. Similar investigations of the field location and orientation were carried out for the perpendicular polarization case at 920 nm (Figure 7 - 28). The maximum enhancement is at 920 nm is 2170 and occurs at the top and bottom slices of the particle. At 920 nm, the field is concentrated at the outer corners of the particle and the field vectors are pointing away from the far side of the particle and toward the near side throughout the entire particle (Figure 7 - 29). This corresponds to the dipole mode at this polarization, which is different than the dipole mode seen for the opposite polarization because of the different dimensions of the particle along these two directions.

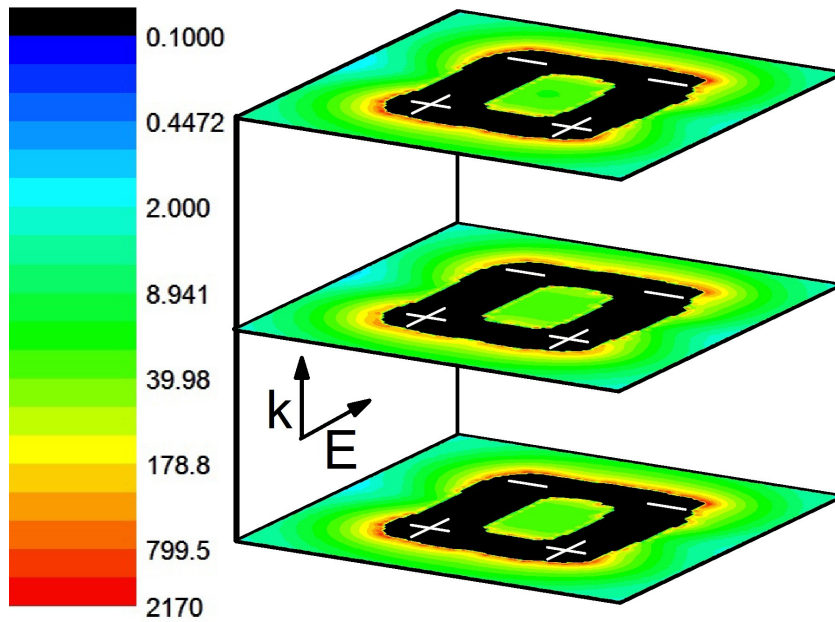


Figure 7 - 28. Composite field plots for isolated particle in air with perpendicular polarization at 920 nm. The field is located at the corners of the particle in each slice. The field vectors are pointing away from the back of the particle and towards the front in each slice. The field location and orientation indicates this is the dipole mode.

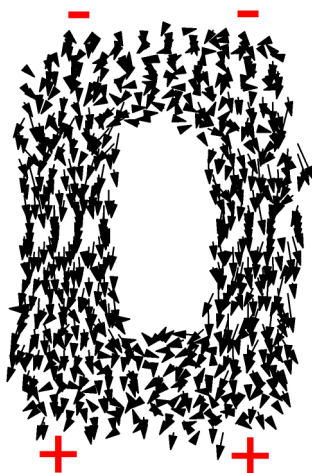


Figure 7 - 29. Representative field vector plot (top slice of a hollow rectangle) for an isolated hollow rectangle in air with perpendicular polarization at  $\lambda = 920$  nm. As shown, a plus sign will indicate when all the vectors are pointing towards an area, and a minus sign indicate when all the vectors are pointing away from an area.

After explaining the peaks present at different polarizations in air for the isolated particle, we next investigated the effects of coupling by looking at dimers with varying interparticle separations. It has previously been shown that bringing two nanoparticles closer together when the light is polarized parallel to the interparticle axis results in a red shift of the overall plasmon mode for the dimer as the interparticle separation decreases.<sup>2,6-11</sup> Conversely, if the light is polarized perpendicular to the interparticle axis, the overall plasmon mode for the dimer blue shifts as the interparticle separation decreases.<sup>2,6-11</sup> The results for the different interparticle separations with parallel polarization are shown in Figure 7 - 30a. Both the dipole and quadrupole peaks are present at all interparticle separations. The dipole peak red shifts as the interparticle separation decreases, as expected. There is little change in the position of the quadrupole peak as the interparticle separations decreases. It has previously been shown that the influence of interparticle separation on the coupling of higher order modes is not as pronounced as on the dipole mode.<sup>19</sup> For the perpendicular polarization (Figure 7 - 30b) the dipole peak shows a slight blue shift as the interparticle separation is decreased, as expected. We expect the substrate supporting the experimental sample to affect the optical properties of the system, causing deviations from the properties predicted for the plasmonic system in air.

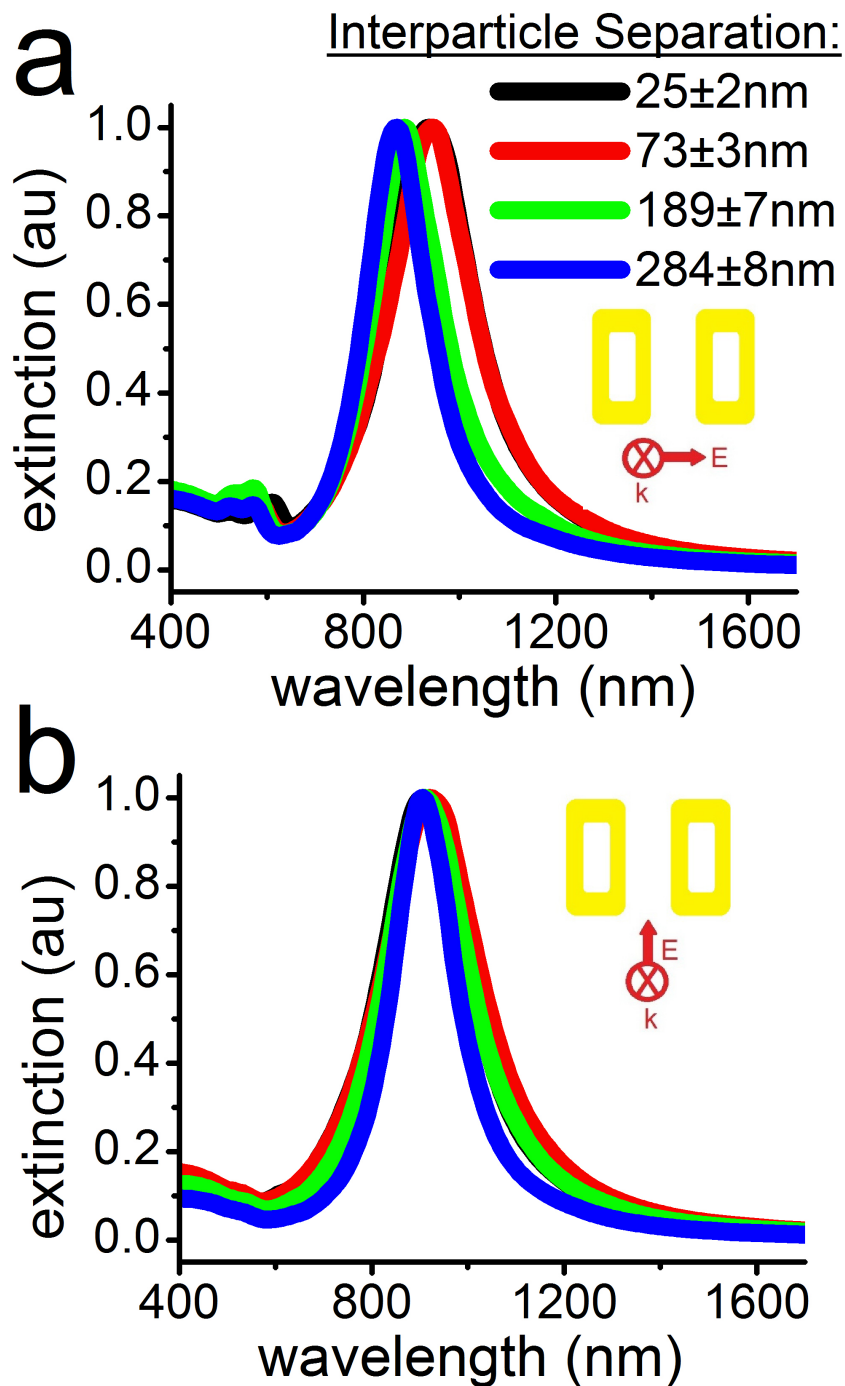


Figure 7 - 30. DDA extinction spectra for hollow gold nanorectangles in air (i.e. no substrate) with light polarized a) parallel and b) perpendicular to the interparticle axis (as indicated in the insets). The interparticle separations are indicated in the legend. As the interparticle separation decreases, we observe the expected red shift for parallel polarization and the expected slight blue shift for perpendicular polarization.

The experimental extinction spectra for the hollow rectangles are shown in Figure 7 - 31. It can be seen that there are two distinct major peaks in the spectra with the light polarized parallel to the interparticle axis: one located at ca. 1200 nm and the other at ca. 1500 nm. As the interparticle separation decreases, both bands red shift and the intensity of the band at ca. 1200 nm decreases while the intensity of the band at ca. 1500 nm increases. This is in contrast with the DDA results in air, where only one major peak was present. This suggests that there is a definite effect from the substrate for this polarization. In addition, a minor peak is present at 750 nm, which most likely corresponds to the quadrupole mode. For the perpendicular polarization, the spectra are simpler, with one major peak at ca. 1300 nm that shows a slight blue shift as the interparticle separation is decreased, as expected.

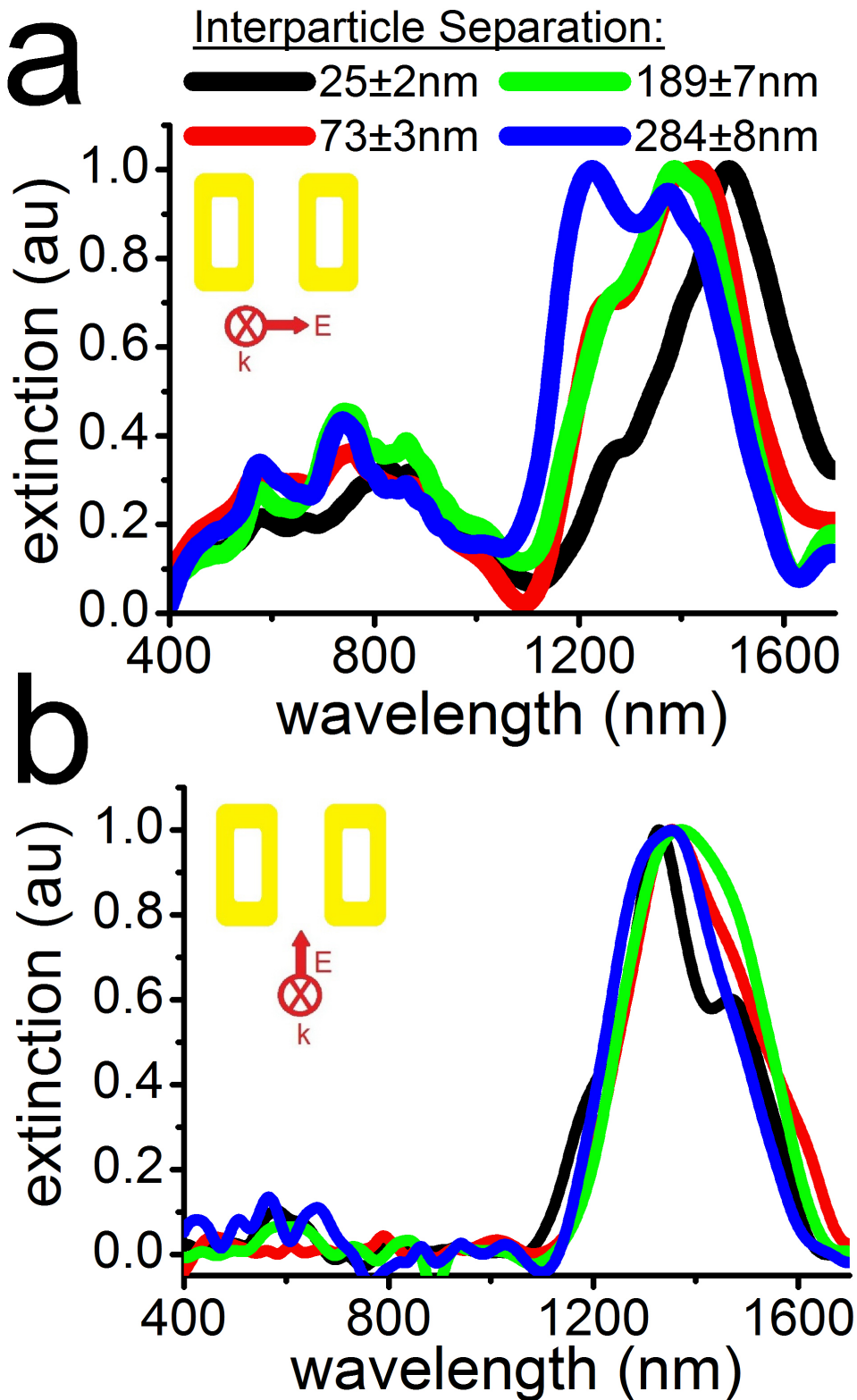


Figure 7 - 31. Experimental extinction spectra for hollow gold nanorectangles with light polarized a) parallel and b) perpendicular to the interparticle axis (as indicated in the insets). The interparticle separations are indicated in the legend.



To determine how the substrate is interacting with the particles and if it is indeed causing the multiple peaks, we performed DDA calculations on a substrate. The DDA extinction spectra for the hollow rectangles on a substrate are shown in Figure 7 - 32. The spectra with light polarized parallel to the interparticle axis (Figure 7 - 32a) do show a shoulder that becomes a more pronounced second peak as the interparticle separation increases. There is also a minor peak present at 710 nm. Field contour plots confirm this minor peak is the quadrupole mode, just shifted in wavelength due to the presence of the substrate (Figure 7 - 33). The spectra with light polarized perpendicular to the interparticle axis (Figure 7 - 32b) have one major peak ca. 1300 nm that shows a slight blue shift as the interparticle separation is decreased, just as was seen in the experimental spectra. Field contour plots confirm this is the dipole mode, just shifted in wavelength due to the presence of the substrate (Figure 7 - 34). The results for the DDA calculations on the substrate for both polarizations closely resemble what was seen experimentally, suggesting the extra spectral features not seen for calculations in air are indeed due to substrate effects.

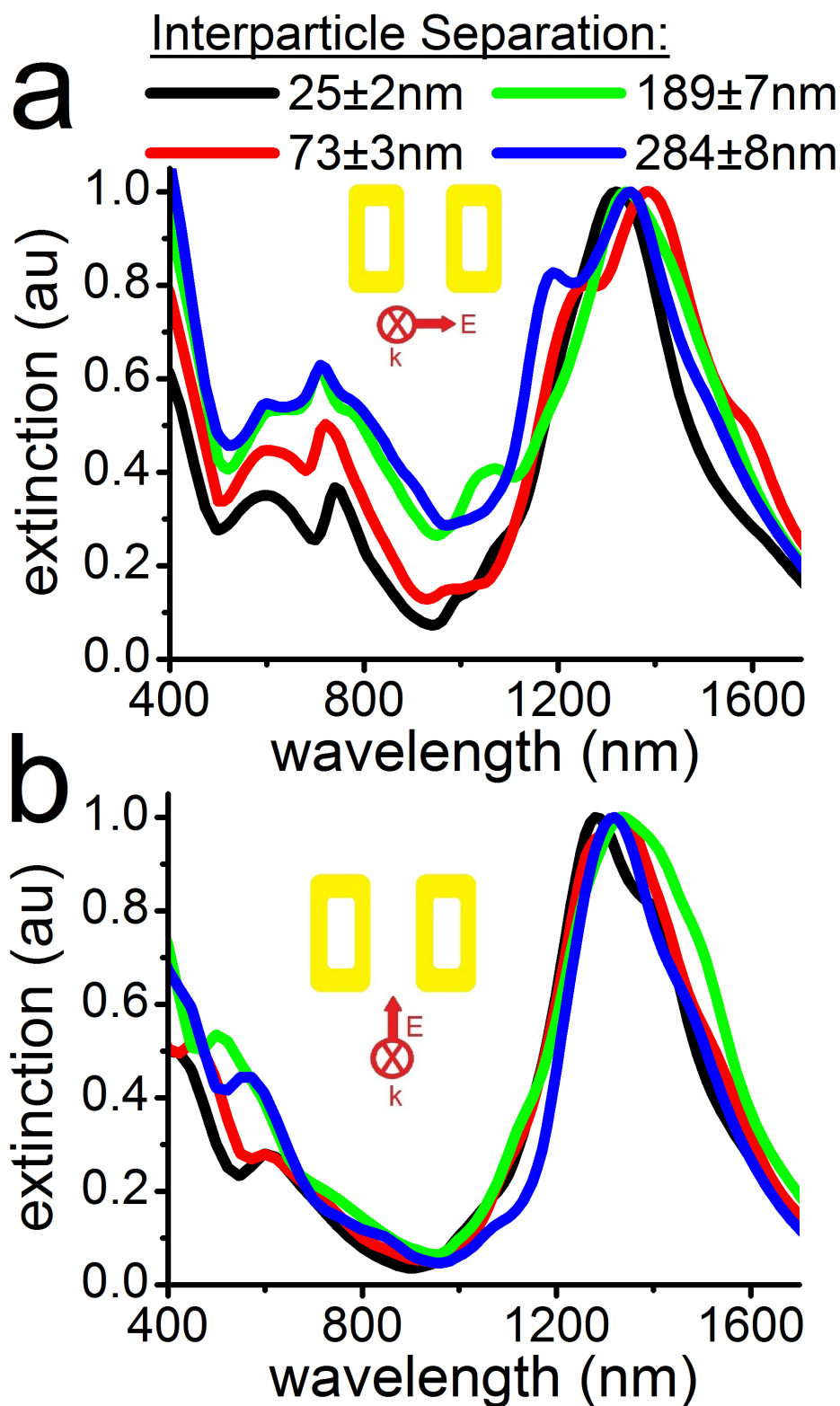


Figure 7 - 32. DDA extinction spectra for hollow gold nanorectangles on a substrate with polarization a) parallel and b) perpendicular to the interparticle axis (as indicated in the insets). The interparticle separations are indicated in the legend.

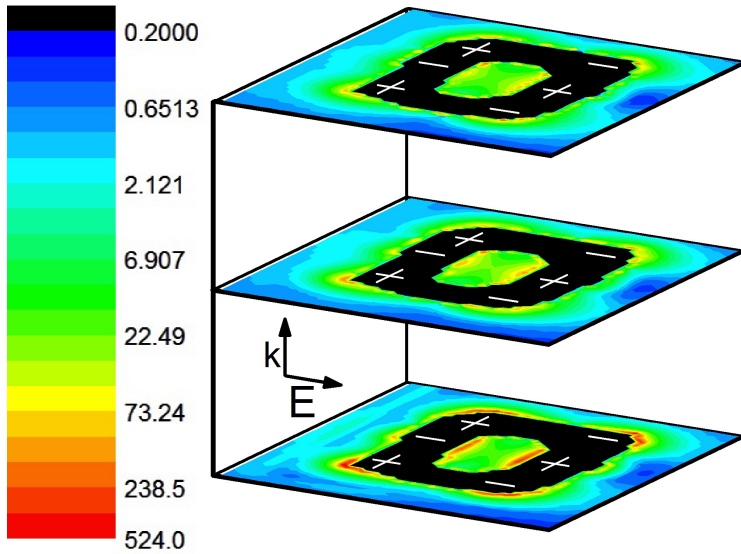


Figure 7 - 33. Composite field plot for particle on a substrate with an interparticle separation of  $284 \pm 8$  nm with parallel polarization at 710 nm (minor peak). The field is located at the outer corners and the interior long sides of the particle in each slice. The field vectors alternate orientation along the sides and corners. The field location and orientation indicates this is the quadrupole mode.

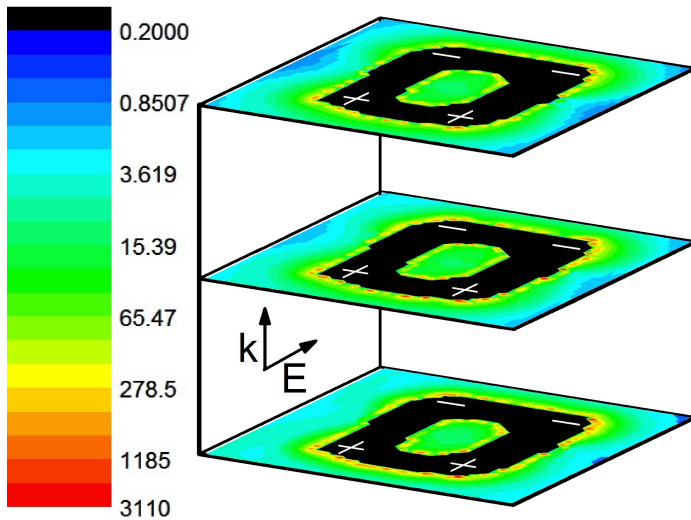


Figure 7 - 34. Composite field plot for particle on a substrate with an interparticle separation of  $284 \pm 8$  nm with perpendicular polarization at 920 nm. The field is located at the corners of the particle in each slice. The field vectors are pointing away from the back of the particle and towards the front in each slice. The field location and orientation indicates this is the dipole mode.

To determine which spectral features are due to substrate effects for the parallel polarization we will compare the field plots for the different peaks. First we will consider our DDA calculations in air, as these calculate the energy of the nanoparticles in an unperturbed state. Field plots were generated for multiple two-dimensional slices along the z-axis (top, middle and bottom) for the particles at each interparticle separation in air at the resonant wavelengths. For all interparticle separations in air, the field maximum for the resonant wavelength was located at the top and bottom of the nanoparticle (Figure 7 - 35). The propagation of the light is along the z-axis, so it makes sense that, in air, the field is concentrated at the surfaces of the particle along that axis (i.e. the top and bottom).

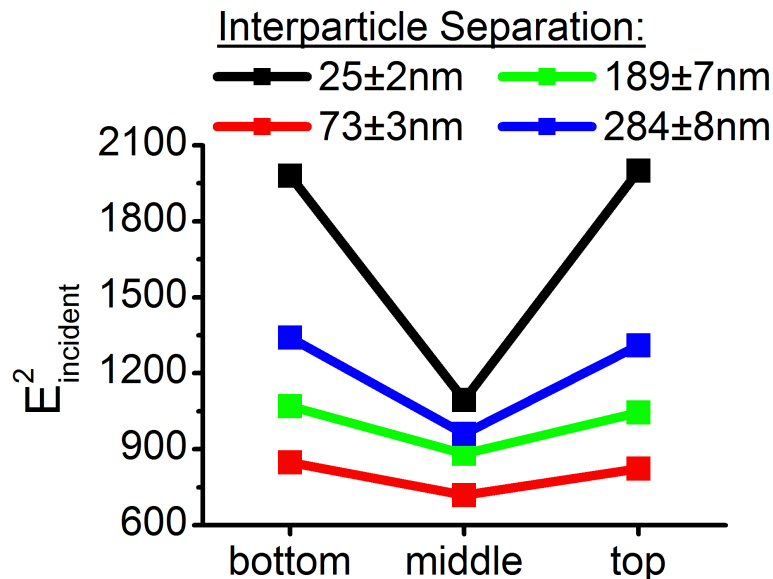


Figure 7 - 35. Field enhancement values at the resonant wavelength for the dipole mode of the particles in air with light polarized parallel to the interparticle axis. The interparticle separations are indicated in the legend. For all cases, the field enhancement is greatest at the top and bottom of the particles, and reaches a minimum in the middle.

Next, field plots were generated for several wavelengths for the dimer with an interparticle separation of  $284 \pm 8$  nm on a substrate. At this interparticle separation, the particles are far enough apart (ca. 2 particle dimensions along the interparticle axis) to be considered isolated. The dip in the DDA extinction spectrum for this particle pair on a substrate under parallel polarization occurs at 1230 nm (Figure 7 - 32a, blue spectrum). Field plots indicate that the peaks at 1190 nm (Figure 7 - 36) and 1350 nm (Figure 7 - 37) both correspond to the dipole mode. The only difference between the two peaks is that at 1190 nm the field maximum occurs at the bottom z slice of the particle whereas at 1350 nm the field maximum occurs in the middle z slice. Field plots at several other wavelengths also correspond to the dipole mode, with the field maximum fluctuating between the bottom and middle of the particle, depending on the wavelength. The results are summarized in Figure 7 - 38 and indicate that for wavelengths to the blue of the dip ( $\lambda \leq 1230$  nm), the field maximum occurs at the bottom of the particle, whereas for wavelengths to the red of the dip ( $\lambda > 1230$  nm) the field maximum occurs at the middle of the particle. The field maximum for the particle in air, i.e. the "unperturbed" particle, was located at the top and bottom of the particle, which would indicate that the peaks at which the field maximum is perturbed away from this location are those due to substrate effects. This indicates that the peak to the red of the dip ( $\lambda = 1340$  nm) is due to interactions with the substrate. On the other hand, the peak to the blue ( $\lambda = 1190$  nm) seems to be the same dipole peak seen for the calculations in air, just shifted due to the change in the refractive index of the surrounding medium due to the presence of the substrate. It is interesting that the peak that is due to the interaction with the substrate becomes more pronounced as the interparticle separation is decreased. This is mostly

likely due to the fact that the field intensity increases as the interparticle separation decreases, making interaction with the substrate more pronounced.

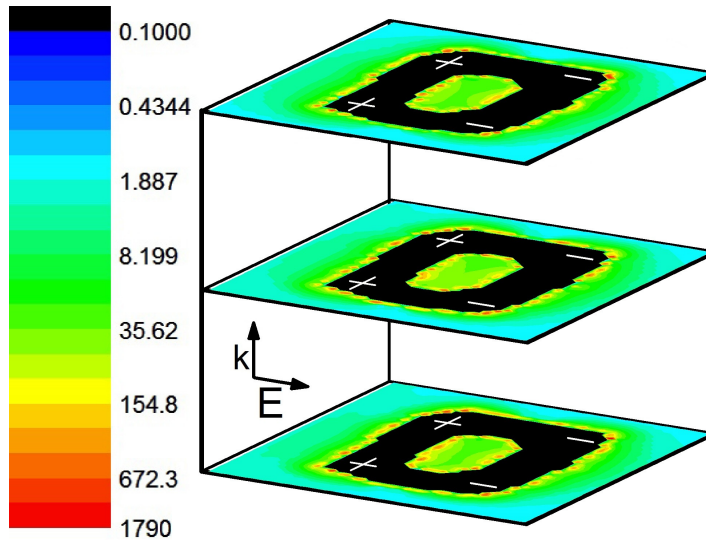


Figure 7 - 36. Composite field plot for isolated particle on a substrate with parallel polarization at 1190 nm. The field is located at the corners of the particle in each slice. The field vectors are pointing away from the right of the particle and towards the left in each slice. The field location and orientation indicates this is the dipole mode.

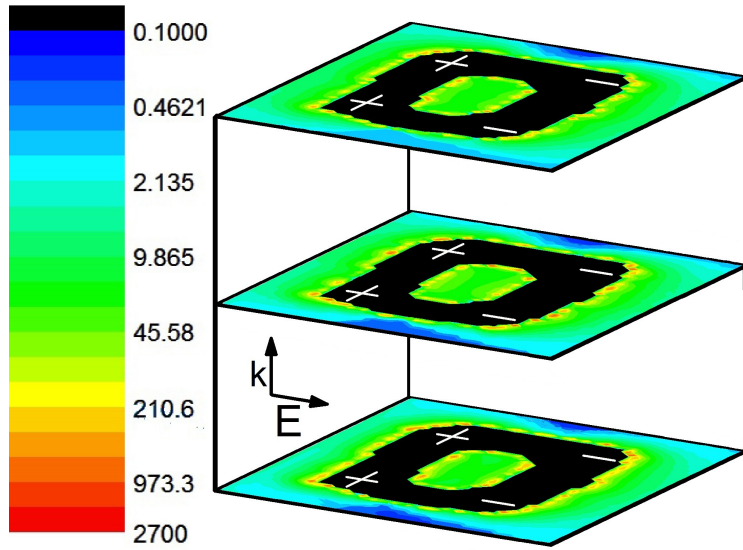


Figure 7 - 37. Composite field plot for isolated particle on a substrate with parallel polarization at 1350 nm. The field is located at the corners of the particle in each slice. The field vectors are pointing away from the right of the particle and towards the left in each slice. The field location and orientation indicates this is the dipole mode.

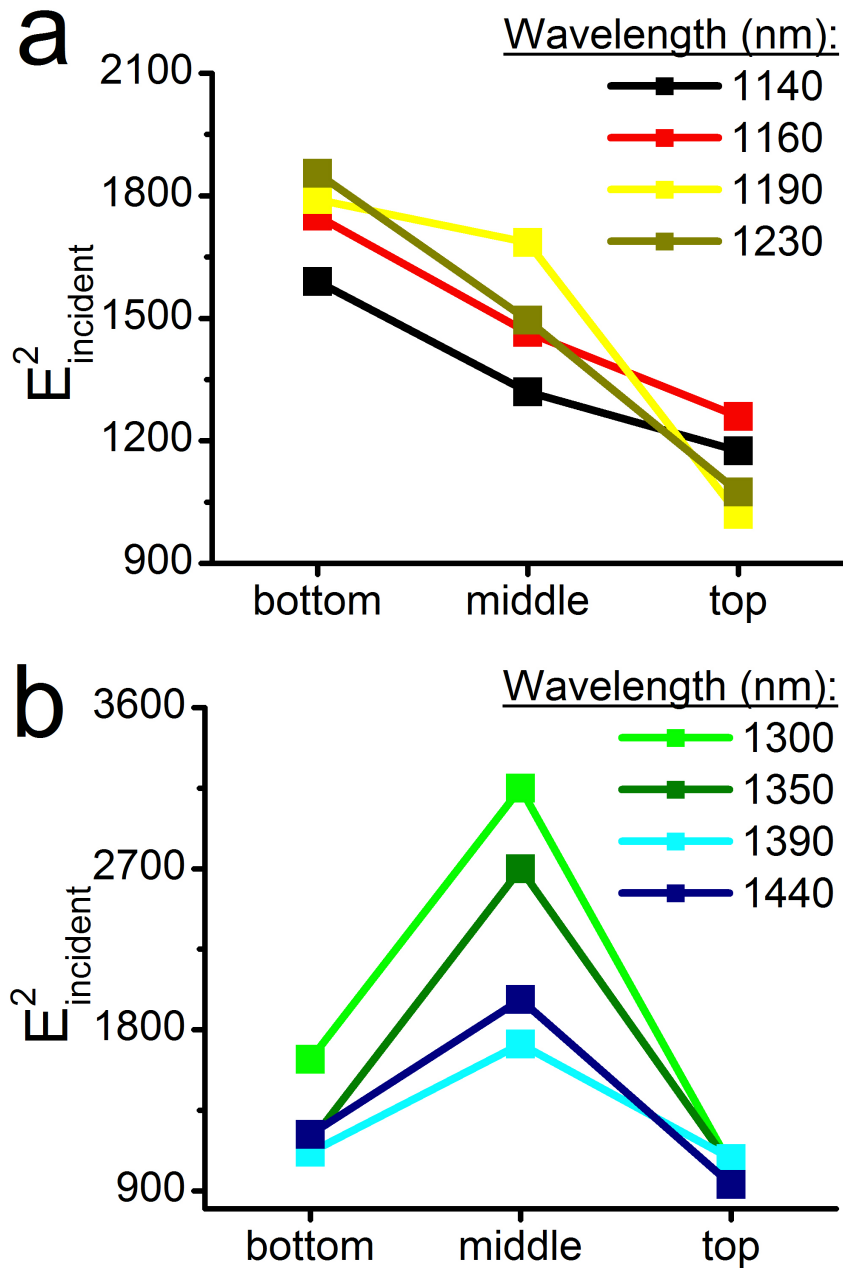


Figure 7 - 38. Field enhancement values for the particle pair with an interparticle separation of  $284 \pm 8$  nm on a substrate with light polarized parallel to the interparticle axis at several wavelengths (as indicated in the legend). a) For the wavelengths to the blue of 1240 nm, the field is most intense at the bottom z slice of the particle. b) Meanwhile, for wavelengths to the red of 1240 nm, the field is most intense at the middle z slice of the particle.



## 7.5 Conclusions

We have demonstrated the sensitivity of the resonant energy of hollow gold nanorectangles fabricated by EBL to polarization and their surroundings. We have confirmed that directly converting SEM images for use in DDA calculations greatly improves the fit to experimental data. For both the tall and long particle orientations, changing the interparticle separation leads to the expected shifts for the peaks due to the dipole plasmon modes of the particles.

For both particle orientations, the dipole and quadrupole mode are present when the light is polarized along the short axis of the particle, but only the dipole mode is present when the light is polarized along the long axis of the particle. This is most likely because the dipole mode of the long axis is so strong that any higher order modes are dwarfed in comparison.

Also for both particle orientations, the substrate plays a significant role when the light is polarized along the interparticle axis. For the long particle orientation, the substrate causes two significant dipole peaks, with the peak further to the blue being caused by the substrate (as indicated by the field distribution along the z-axis). For the tall orientation of the particles, we also see two dipole peaks for polarization along the interparticle axis. However, in this case the field distributions along the z-axis indicate that the peak further to the red is caused by substrate interactions. For the tall orientation, parallel polarization is along the short axis of the particle; this results in a much weaker dipole mode than for

light polarized along the long axis of the particle. As the particles are brought closer together, they are able to couple in a favorable manner, increasing the strength of the overall field and allowing for more significant substrate effects. For the particles with the long orientation, the parallel polarization (i.e. along the long axis of the particle) results in a dipole mode that is already so strong that even the isolated particle sees significant substrate interactions. Bringing the particles closer together increases the field strength even more. The substrate is only 80 nm thick, so increasing the field strength beyond a certain amount will cause the field to extend beyond the substrate entirely, resulting in the substrate effects decreasing as the interparticle separation is decreased for the parallel polarization of the particles with long orientation.

Our results indicate that by modifying the thickness of the substrate, we can control the degree of substrate effects. Also, the substrate effects mainly affect the dipole mode, and not the quadrupole mode. Therefore, assessment of these substrate effects can also be used to help distinguish between different plasmon modes.

## 7.6 References

- (1) Bohren, C. F.; Huffman, D. R. *Absorption and Scattering of Light by Small Particles*; Wiley: New York, 1983.
- (2) El-Sayed, M. A. Some interesting properties of metals confined in time and nanometer space of different shapes. *Accounts Chem. Res.* **2001**, *34*, 257-264.
- (3) Hutter, E.; Fendler, J. H. Exploitation of localized surface plasmon resonance. *Advanced Materials* **2004**, *16*, 1685-1706.
- (4) Kelly, K. L.; Coronado, E.; Zhao, L. L.; Schatz, G. C. The optical properties of metal nanoparticles: The influence of size, shape, and dielectric environment. *J. Phys. Chem. B* **2003**, *107*, 668-677.
- (5) Kreibig, U.; Vollmer, M. *Optical Properties of Metal Clusters*; Springer: Berlin, 1995; Vol. 25.
- (6) Link, S.; El-Sayed, M. A. Spectral properties and relaxation dynamics of surface plasmon electronic oscillations in gold and silver nanodots and nanorods. *J. Phys. Chem. B* **1999**, *103*, 8410-8426.
- (7) Jain, P. K.; Lee, K. S.; El-Sayed, I. H.; El-Sayed, M. A. Calculated absorption and scattering properties of gold nanoparticles of different size, shape, and composition: Applications in biological imaging and biomedicine. *J. Phys. Chem. B* **2006**, *110*, 7238-7248.
- (8) Maier, S. A.; Brongersma, M. L.; Kik, P. G.; Atwater, H. A. Observation of near-field coupling in metal nanoparticle chains using far-field polarization spectroscopy. *Physical Review B* **2002**, *65*.
- (9) Rechberger, W.; Hohenau, A.; Leitner, A.; Krenn, J. R.; Lamprecht, B.; Aussenegg, F. R. Optical properties of two interacting gold nanoparticles. *Optics Communications* **2003**, *220*, 137-141.
- (10) Su, K. H.; Wei, Q. H.; Zhang, X.; Mock, J. J.; Smith, D. R.; Schultz, S. Interparticle coupling effects on plasmon resonances of nanogold particles. *Nano Lett.* **2003**, *3*, 1087-1090.
- (11) Sweatlock, L. A.; Maier, S. A.; Atwater, H. A.; Penninkhof, J. J.; Polman, A. Highly confined electromagnetic fields in arrays of strongly coupled Ag nanoparticles. *Physical Review B* **2005**, *71*.

- (12) Halas, N. J. Playing with plasmons. Tuning the optical resonant properties of metallic nanoshells. *MRS Bull.* **2005**, *30*, 362-367.
- (13) Near, R.; Tabor, C.; Duan, J. S.; Pachter, R.; El-Sayed, M. Pronounced Effects of Anisotropy on Plasmonic Properties of Nanorings Fabricated by Electron Beam Lithography. *Nano Lett.* **2012**, *12*, 2158-2164.
- (14) Olson, T. Y.; Schwartzberg, A. M.; Orme, C. A.; Talley, C. E.; O'Connell, B.; Zhang, J. Z. Hollow gold-silver double-shell nanospheres: Structure, optical absorption, and surface-enhanced Raman scattering. *Journal of Physical Chemistry C* **2008**, *112*, 6319-6329.
- (15) Sun, Y. G.; Mayers, B.; Xia, Y. N. Metal nanostructures with hollow interiors. *Advanced Materials* **2003**, *15*, 641-646.
- (16) Large, N.; Aizpurua, J.; Lin, V. K.; Teo, S. L.; Marty, R.; Tripathy, S.; Mlayah, A. Plasmonic properties of gold ring-disk nano-resonators: fine shape details matter. *Opt. Express* **2011**, *19*, 5587-5595.
- (17) Tsai, C.-Y.; Lin, J.-W.; Wu, C.-Y.; Lin, P.-T.; Lu, T.-W.; Lee, P.-T. Plasmonic Coupling in Gold Nanoring Dimers: Observation of Coupled Bonding Mode. *Nano Lett.* **2012**, *12*, 1648-1654.
- (18) Jain, P. K.; El-Sayed, M. A. Plasmonic coupling in noble metal nanostructures. *Chemical Physics Letters* **2010**, *487*, 153-164.
- (19) Jain, P. K.; Huang, W. Y.; El-Sayed, M. A. On the universal scaling behavior of the distance decay of plasmon coupling in metal nanoparticle pairs: A plasmon ruler equation. *Nano Lett.* **2007**, *7*, 2080-2088.
- (20) Zhang, S. P.; Bao, K.; Halas, N. J.; Xu, H. X.; Nordlander, P. Substrate-Induced Fano Resonances of a Plasmonic Nanocube: A Route to Increased-Sensitivity Localized Surface Plasmon Resonance Sensors Revealed. *Nano Lett.* **2011**, *11*, 1657-1663.
- (21) Knight, M. W.; Wu, Y. P.; Lassiter, J. B.; Nordlander, P.; Halas, N. J. Substrates Matter: Influence of an Adjacent Dielectric on an Individual Plasmonic Nanoparticle. *Nano Lett.* **2009**, *9*, 2188-2192.
- (22) Wan, D. H.; Chen, H. L.; Lin, Y. S.; Chuang, S. Y.; Shieh, J.; Chen, S. H. Using Spectroscopic Ellipsometry to Characterize and Apply the Optical Constants of Hollow Gold Nanoparticles. *Acs Nano* **2009**, *3*, 960-970.

- (23) Goodman, J. J.; Draine, B. T.; Flatau, P. J. Application of Fast-Fourier-Transform techniques to the Discrete-Dipole Approximation. *Optics Letters* **1991**, *16*, 1198-1200.
- (24) Shuford, K. L.; Ratner, M. A.; Schatz, G. C. Multipolar excitation in triangular nanoprisms. *J. Chem. Phys.* **2005**, *123*.
- (25) Lee, C. T.; Wang, M. X.; Jarnagin, N. D.; Gonsalves, K. E.; Roberts, J. M.; Yueh, W.; Henderson, C. L. In *Advances in Resist Materials and Processing Technology XXIV*; Lin, Q., Ed. 2007; Vol. 6519, p E5191-E5191.
- (26) Flatau, P. J.; Stephens, G. L.; Draine, B. T. Light-scattering by rectangular solids in the Discrete-Dipole Approximation - A new algorithm exploiting the block-toeplitz structure. *J. Opt. Soc. Am. A-Opt. Image Sci. Vis.* **1990**, *7*, 593-600.
- (27) Johnson, P. B.; Christy, R. W. Optical-constants of noble-metals. *Physical Review B* **1972**, *6*, 4370-4379.
- (28) Palik, E. D. *Handbook of Optical Constants of Solids*; Academic Press: San Diego, 1985; Vol. 1.
- (29) Dreaden, E. C.; Near, R. D.; Abdallah, T.; Talaat, M. H.; El-Sayed, M. A. Multimodal plasmon coupling in low symmetry gold nanoparticle pairs detected in surface-enhanced Raman scattering. *Appl. Phys. Lett.* **2011**, *98*.
- (30) Mahmoud, M. A.; El-Sayed, M. A. Aggregation of Gold Nanoframes Reduces, Rather Than Enhances, SERS Efficiency Due to the Trade-Off of the Inter- and Intraparticle Plasmonic Fields. *Nano Lett.* **2009**, *9*, 3025-3031.
- (31) Mahmoud, M. A.; El-Sayed, M. A. Gold Nanoframes: Very High Surface Plasmon Fields and Excellent Near-Infrared Sensors. *J. Am. Chem. Soc.* **2010**, *132*, 12704-12710.
- (32) Near, R.; Hayden, S.; El-Sayed, M. Extinction vs Absorption: Which Is the Indicator of Plasmonic Field Strength for Silver Nanocubes? *Journal of Physical Chemistry C* **2012**, *116*, 23019-23026.

## APPENDIX A

### DISRECTE DIPOLE APPROXIMATION METHODOLOGY

#### **A.1 Summary**

The purpose of this chapter is an in depth discussion of the DDA procedure. A more general discussion can be found in the previous chapters of this thesis. To review, the discrete dipole approximation (DDA) is a method for computing scattering of radiation by particles of arbitrary shape. In this method a continuum target is approximated by a finite array of polarizable points. The points acquire dipole moments in response to the applied local electric field. The response of the system to the applied field and to one another is the solved self-consistently.

#### **A.2 Introduction**

For the purposes of this appendix, all procedures will be described using the programs and files that are currently available. If these files or programs have changed, adjustments may need to be made to the procedures discussed below. We use the DDSCAT 6.1 code (<http://www.astro.princeton.edu/~draine/DDSCAT.6.1.html>). The data processing software used will be Origin 5. Microsoft Excel is capable of some of the processing procedures, but the limits to the number of rows and columns in Excel make it inappropriate for the majority of the more complex processing procedures.

### *A.2.1 Computer Cluster*

Although it is possible to run these calculations on a personal computer, it is easiest and fastest to run them on a computer cluster or super computer. In the past we have used the CCMST cluster (<http://www.ccmst.gatech.edu/>), as it is fairly easy to get access to that cluster.

Once an account on the cluster is acquired, we use a file transfer program called WinSCP to remotely connect to the cluster to transfer files and run the calculations. Currently, it is possible to access the CCMST cluster from any wired internet connection on the Georgia Tech campus. To access the cluster from a wireless network on campus or from any internet connection not on campus, it is necessary to set up a VPN account as well.

When new files are copied via WinSCP from a personal computer to the super computer, the default permission setting on the files will be readable and writable by the owner (rw-r--r--). To change the permission, right click on the file, go to properties and check the appropriate boxes to give the files the right permissions. The ddscat and ddscat.pbs files need to be readable, writable and executable by the owner and the group, but not others (rwxr-xr-r). All the other files only need to be readable and writable by the owner (rw-r--r--).

A few final points about the cluster, in the current set up of the CCMST cluster no spaces are allowed in any of the folder or file names. Also, once a set of files has been

successfully set up on the cluster, it is easiest to simply duplicate the files over and over on the cluster, rather than continually copy them from a personal computer and have to reset the permissions constantly.

### **A.3 Two types of calculations and the required files**

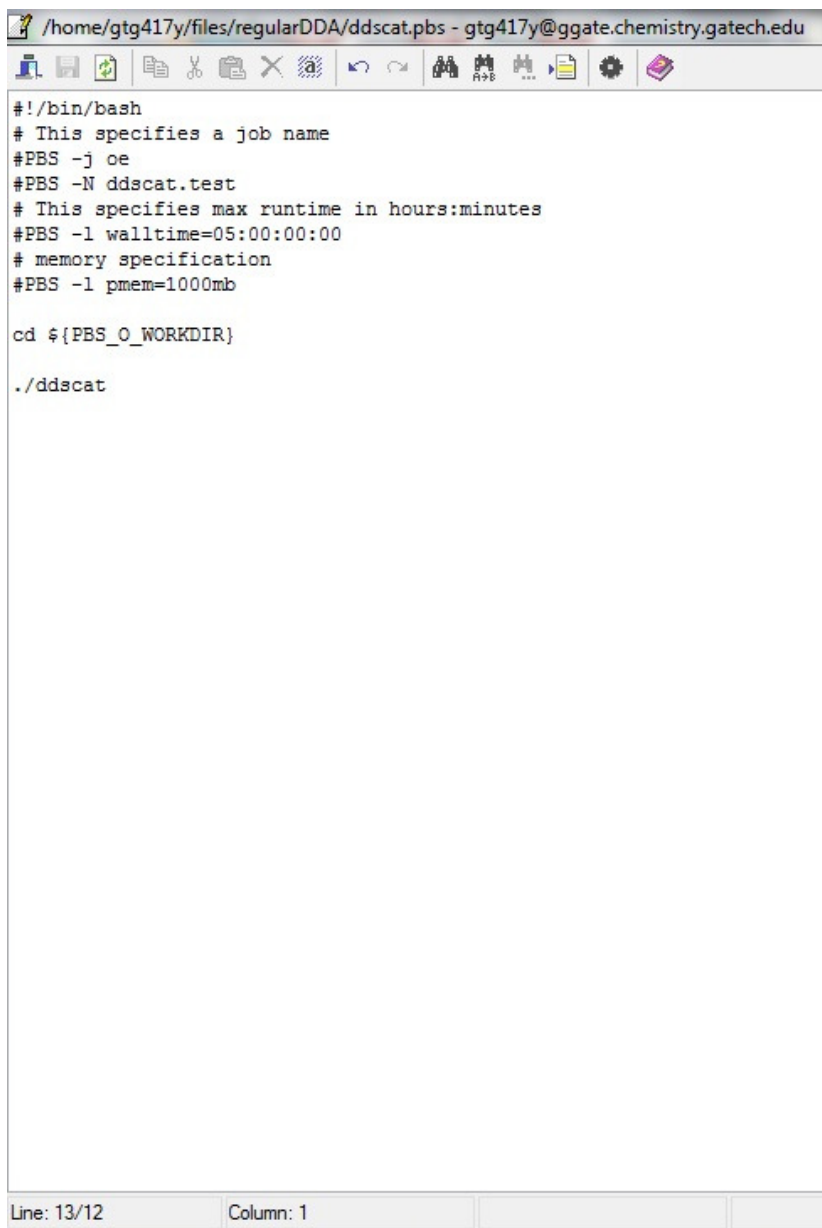
There are two different versions of the DDSCAT that are used to run different types of calculations. The original version from Draine and Flatau<sup>1</sup> is the code used for generating the spectra for the system. In these calculations, the extinction, absorption and scattering spectra are generated concurrently. We also have a copy of the DDSCAT code modified by Goodman<sup>2</sup> and Schatz<sup>3</sup> that generates the field contour and vector plots.

For the spectral calculations five files need to be included in the same folder on the cluster: `ddscat`, `ddscat.pbs`, `shape.dat`, `diel.tab` and `ddscat.par`. For the field calculations seven files are needed: `ddscat` (modified version), `ddscat.pbs`, `shape.dat`, `diel.tab`, `ddsact.par`, `a_0.f`, and `a.pbs`.

The `ddscat` file is the code that runs the calculations, and there are two different versions though the file name is the same. To avoid the confusion, it is best to keep them in separate folders. The two versions generate different output files, so if they do get mixed up it is possible to determine which is which by running a calculation and looking at the output.



The `ddscat.pbs` file is the call for the code, and this is the file that is submitted to run on the cluster (this process will be discussed more in section A.8). The contents can be seen in Figure A - 1. The only line in the file we usually make changes to is line 8, which specifies the memory allotted to run the calculations. The memory needed to run the calculations depends on how big the system is, how complicated it is, and which type of calculation you are running. Larger systems or systems with many particles or materials take more memory. For simple systems, that spectral calculations may need as little as 100 mb of memory. If the calculations don't run, or quit unexpectedly, try increasing the memory specified in the `ddscat.pbs` file. The other specifications in this file depend on terminology being used by computer cluster, so if that terminology changes or a different cluster is being used, some of the values in this file will change. In order to make those changes, someone who is more familiar with the cluster will need to be consulted.



```
#!/bin/bash
# This specifies a job name
#PBS -j oe
#PBS -N ddscat.test
# This specifies max runtime in hours:minutes
#PBS -l walltime=05:00:00:00
# memory specification
#PBS -l pmem=1000mb

cd ${PBS_O_WORKDIR}

./ddscat
```

Line: 13/12      Column: 1

Figure A - 1. An example of the ddscat.pbs file.

The other 3 files that both calculations have in common are where we define various properties of our system. The shape.dat file (i.e. the shape file) essentially contains the x, y, z coordinates of all the dipoles that make up the system. The diel.tab file (i.e. the

dielectric file) is where we define what materials the system contains. The `ddscat.par` file (i.e. the parameter file) is where we define many other properties of the system: number of materials, size of the particle(s), wavelengths, polarization. The `a_0.f` file is another code file that is used to define many of the parameters needed to generate the field contour and vector plots. The `a.pbs` file is the call for the formatted `a_0.f` file. All these files will be discussed more thoroughly in the following sections.

The first step chronologically in setting up a new calculation is usually generating the shape file. However, we must first discuss the parameter file, as several properties in the parameter file are helpful in deciding how to orient your particle(s) in the shape file.

#### **A.4 Parameter file**

An example parameter file is shown in Figure A - 2. A very thorough description of the file can be found in the DDA user guide,<sup>4</sup> but will describe the various important aspects we use in our lab.

```

/home/gtg417y/files/regularDDA/ddscat.par - gtg417y@ggate.chemistry.gatech.edu
Parameter file
***** PRELIMINARIES *****
NOTORQ= CMTORQ*6 (DOTORQ, NOTORQ) -- either do or skip torque calculations
PBCGST= CMDSOL*6 (PBCGST, PETRKP) -- select solution method
GPFAFT= CMETHD*6 (GPFAFT, FFTWJ, CONVEX)
LATTDR= CALPHA*6 (LATTDR, SCLDR)
NOTBIN= CBINFLAG (ALLBIN, ORIBIN, NOTBIN)
NOTCDF= CNETFLAG (ALLCDF, ORICDF, NOTCDF)
FRMFIL= CSHAPE*6 (FRMFIL, ELLIPS, CYLNDR, RCTNGL, HEXGON, TETRAH, UNICYL, UNIELL)
'shape.dat' = shape parameters PAR1, PAR2, PAR3
2 = NCOMP = number of dielectric materials
TABLES= CDIEL*6 (TABLES, H2OICE, H2OLIQ; if TABLES, then filenames follow...)
'dielAu.tab' = name of file containing dielectric function
'dielSiN100.tab'
***** CONJUGATE GRADIENT DEFINITIONS *****
0 = INIT (TO BEGIN WITH |X0> = 0)
1.00e-5 = TOL = MAX ALLOWED (NORM OF |G>=AC|E>-ACA|X>)/(NORM OF AC|E>)
***** Angular resolution for calculation of <cos>, etc. *****
0.5 = ETASCA (number of angles is proportional to [(3+x)/ETASCA]^2 )
***** Wavelengths *****
0.300 2.000 35 'LIN' = wavelengths (first, last, how many, how=LIN, INV, LOG)
***** Effective Radii *****
.124048 .124048 1 'LIN' = eff. radii (first, last, how many, how=LIN, INV, LOG)
***** Define Incident Polarizations *****
(0,0) (1.,0.) (0.,0.) = Polarization state e01 (k along x axis)
1 = IORTH (=1 to do only pol. state e01; =2 to also do orth. pol. state)
0 = IWRKSC (=0 to suppress, =1 to write ".sca" file for each target orient.
***** Prescribe Target Rotations *****
0. 0. 1 = BETAMI, BETAMX, NBETA (beta=rotation around a1)
0. 0. 1 = THETMI, THETMX, NTHETA (theta=angle between a1 and k)
0. 0. 1 = PHIMIN, PHIMAX, NPHI (phi=rotation angle of a1 around k)
***** Specify first IWAV, IRAD, IORI (normally 0 0 0) *****
0 0 0 = first IWAV, first IRAD, first IORI (0 0 0 to begin fresh)
***** Select Elements of S_ij Matrix to Print *****
6 = NSMELTS = number of elements of S_ij to print (not more than 9)
11 12 21 22 31 41 = indices ij of elements to print
***** Specify Scattered Directions *****
0. 0. 180. 10 = phi, thetan_min, thetan_max, dtheta (in degrees) for plane A
90. 0. 180. 10 = phi, ... for plane B
|
Line: 40/39 Column: 1

```

Figure A - 2. The ddscat.par or parameter file.

The first line of interest is line 9, which we always keep as it appears in Figure A - 2.

The FRMFIL indicates that the user will be providing a file wherein the shape is defined.

The name of that file is then listed on line 10. My experience indicates that this file must always be named shape.dat.

Line 11 gives a number that indicates the number of dielectric materials in the system. If only one material is present in the system (i.e. a gold particle in air) then this will be 1.

However, if there are two materials (i.e. a gold particle on a silicon substrate) this will be 2, and so on. Then the files containing the various dielectrics are listed on lines 13 on.

The materials should be listed in the order they are called in the shape file (see section A.5).

The next line of interest is the line immediately under the heading "wavelengths". On this line we define the starting and ending wavelengths, how many steps occur between those values and how to divide the steps. We typically do linear divisions of the steps, as indicated by the phrase 'LIN' on this line. The wavelengths are in micrometers for this file. So, as seen in the example (Figure A - 2) the first wavelength is 0.3  $\mu\text{m}$  (300 nm) and the last wavelength is 2.0  $\mu\text{m}$  (2000 nm). These can be set to any number; however, the wavelength range should be within that defined in the diel.tab file (see section A.6).

The number of divisions tells the code how often to repeat the calculations. To choose the number of divisions, find the difference between the first and last wavelengths, divide by the desired increment between wavelengths, and add one.

$$\frac{\lambda_f - \lambda_i}{\delta\lambda} + 1 = \#divisions$$

In this example (Figure A - 2), the number of divisions is 35, which will run the calculation for wavelengths in 50 nm increments starting at 300 nm and ending at 2000 nm. We usually start with a coarse set of divisions over the wavelength region of interest. Then the calculations can be repeated as many times as necessary to get finer divisions where needed.

The line following the header "Effective radii" is where we define the size of our system. To do this, calculate the total volume of all the material in the system (i.e. all the materials for the dipoles in the shape file). Then think of turning all that material into a sphere, and find what the radius of that sphere would be.

$$r_{effective} = \left[ \frac{3V}{4\pi} \right]^{1/3}$$

Again, this value should be in micrometers. We always define one effective radius at a time, so this line should have the same number twice, followed by a 1 and 'LIN', as seen in the example (Figure A - 2).

The lines immediately following the header "Define incident polarizations" are where we define how the incident light is polarized. It is important here to note that the xyz directions in the parameter file and the shape file are different. I find it easiest to think in terms of the shape file. As such, the propagation direction is along the x axis of the shape file. The polarization direction can then be altered anywhere in the yz plane. Setting the

polarization to (0,0) (1,0) (0,0) results in polarization along the y axis in the shape file (or zero degrees) whereas (0,0) (0,0) (1,0) results in polarization along the z axis in the shape file (or 90 degrees). Some other examples are:

(0,0) (0.707,0) (0.707,0) = 45 degrees

(0,0) (0.866,0) (0.5,0) = 30 degrees

(0,0) (0.5,0) (0.866,0) = 60 degrees

The next line (1 = IORTH...) tells the calculations whether to do just the polarization that was defined on the previous line (1 = IORTH) or to simultaneously do the polarization perpendicular to that (2 = IORTH). It should be noted that setting IORTH to 2 will not give two sets of data for the two polarizations. It will give one set of data as if the sample had been illuminated by light that is a combination of two plane-polarized waves that are perpendicular to one another. Setting IORTH to 2 also makes the calculation runtime very long. I have found it faster to set IORTH to 1 and run the two polarizations separately, then the results can be averaged to get the same results as if IORTH was set to 2.

These are the only sections of the parameter file we usually change, for a fuller description see DDA User guide provided by Draine and Flatau.<sup>4</sup>

## A.5 Shape File

This file only defines the shape of the particle/ system components, not the final size. The final size is defined in the parameter file (section A.4). A certain number of dipoles is needed in order to get reliable results. In my experience, around 10,000 dipoles per component is needed for good results. More dipoles means better (or at least more reliable) results, but it also means an increase in computation time. As such, systems with many particles or that include a substrate take longer to run as more dipoles are needed to accurately represent the system. One other limitation to note, if there are multiple particles there is a minimum separation the calculation seems to be able to handle. It seems that this minimum separation is at least two dipole units.

An example shape.dat file is shown in Figure A - 3. The first line contains a description of the shape being defined; the first 67 characters will be read and printed in various output statements. The second line gives a number (N) that is equal to the total number of dipoles in the target. The calculation will only read N number of rows in shape file, so N must equal the total number of rows for the whole file to be read. The next four lines we always keep as they are shown in Figure A - 3. The remaining lines are the definitions of the dipoles that make up the target (i.e. position and composition).



```

shape - Notepad
File Edit Format View Help
>TARELL ellipsoid1 grain; AX,AY,AZ= 40.0000 40.0000 40.0000
33552 = NAT
1.0000 0.0000 0.0000 = A_1 vector
0.0000 1.0000 0.0000 = A_2 vector
1.000000 1.000000 1.000000 = lattice spacings (d_x,d_y,d_z)/d
JA IX IY IZ ICOMP(x,y,z)
1 -3 -4 -20 1 1 1
2 -2 -4 -20 1 1 1
3 -1 -4 -20 1 1 1
4 0 -4 -20 1 1 1
5 1 -4 -20 1 1 1
6 2 -4 -20 1 1 1
7 -4 -3 -20 1 1 1
8 -3 -3 -20 1 1 1
9 -2 -3 -20 1 1 1
10 -1 -3 -20 1 1 1
11 0 -3 -20 1 1 1
12 1 -3 -20 1 1 1
13 2 -3 -20 1 1 1
14 3 -3 -20 1 1 1
15 -4 -2 -20 1 1 1
16 -3 -2 -20 1 1 1
17 -2 -2 -20 1 1 1
18 -1 -2 -20 1 1 1
19 0 -2 -20 1 1 1
20 1 -2 -20 1 1 1
21 2 -2 -20 1 1 1
22 3 -2 -20 1 1 1
23 -4 -1 -20 1 1 1
24 -3 -1 -20 1 1 1
25 -2 -1 -20 1 1 1
26 -1 -1 -20 1 1 1
27 0 -1 -20 1 1 1
28 1 -1 -20 1 1 1
29 2 -1 -20 1 1 1
30 3 -1 -20 1 1 1
31 -4 0 -20 1 1 1
32 -3 0 -20 1 1 1
33 -2 0 -20 1 1 1
34 -1 0 -20 1 1 1
35 0 0 -20 1 1 1
36 1 0 -20 1 1 1
37 2 0 -20 1 1 1
38 3 0 -20 1 1 1
39 -4 1 -20 1 1 1
40 -3 1 -20 1 1 1
41 -2 1 -20 1 1 1
42 -1 1 -20 1 1 1
43 0 1 -20 1 1 1
44 1 1 -20 1 1 1
45 2 1 -20 1 1 1
46 3 1 -20 1 1 1

```

Figure A - 3. Example of a correct shape.dat file.

First column is an index number, and simply lists the number of the dipole. Therefore, the last index number should match the number of rows that contain data points. The next three columns are the xyz coordinates for each dipole. No two dipoles can have the same xyz coordinates. Also, the xyz coordinates must be in whole numbers. The last three columns define the dielectric material that corresponds to that dipole. If there is

only one material in the system (i.e. a gold particle in air) then the last three columns should have 1's for all entries. If however, the system contains 2 materials (i.e. a gold particle on a silicon substrate) some of the rows should have all 1's in the last three columns and others should have 2's, where the 1's and 2's correspond to the different materials in the system. This is useful if the system contains particles of different materials, core-shell particles, alloy particles, or particle(s) sitting on a substrate. As indicated in parameter file description (section A.4), whichever material is represented by the 1's should be the first dielectric file listed in the parameter file, and the material represented by 2's should be listed second, and so forth. Also recall from the description of the polarization definitions in the parameter file (section A.4) that the light propagation direction is along the x direction and the light can be polarized in any direction in the yz plane.

Now that we have discussed the format and function of the shape.dat file, we will examine the various methods by which to generate the file. The first method is using a short set of code called the shape generator code (a copy should be available in our lab). We will discuss how to use the shape generator code to make a single solid particle, a single hollow particle, and then a pair of particles. We will then discuss other methods to generate the shape file.

### *A.5.1 Shape generator code and making a single solid particle*

The shape generator is a short code that generates shape files for a small selection of 3D shapes (cylinder, ellipsoid, prism, rectangle sphere). In each case there is a specific phrase to define the shape and then a set of numbers to define the dimensions of that shape. In the folder there are example files for each shape and their contents are listed below:

SPHERE

diameter, 1, 1

RCTNGL

X dimension

Y dimension

Z dimension

PRISM3

side length

1,1,1

ELLIPS

X dimension, Y dimension, Z dimension

CYLNDR

height

diameter

1

The folder also contains files named a, ct and inp. The file named inp is the input file, and that needs to contain the description of the desired shape, which should be based on what is shown in the example files and described above. Once the shape and dimensions have been defined the inp file, save it and double click on the "a" file to run the shape generator code. This will generate a file called target.out that will contain the xyz coordinates for that shape.

The target.out file can be opened in notepad to see the file, but to manipulate the file it is easiest to import it into Origin. Also, we need to rename/reformat the file type from target.out to shape.dat, and it is easiest to do this by importing and exporting in Origin. Once imported into Origin, there should be 7 columns. There are headers for the columns that correspond to the text lines in the shape file, but when imported in Origin they are rearranged. To check that the shape and dimensions are correct, select the second, third and fourth columns and set them as xyz xyz (Figure A - 4). The data can then be plotted as a 3D scatter plot (Figure A - 5). Origin will probably display the data in "speed mode", meaning it will not show all the data points. To change this go to the plot details, select layer 1, go to the size/speed tab and uncheck the boxes next to worksheet data and matrix data (Figure A - 6).

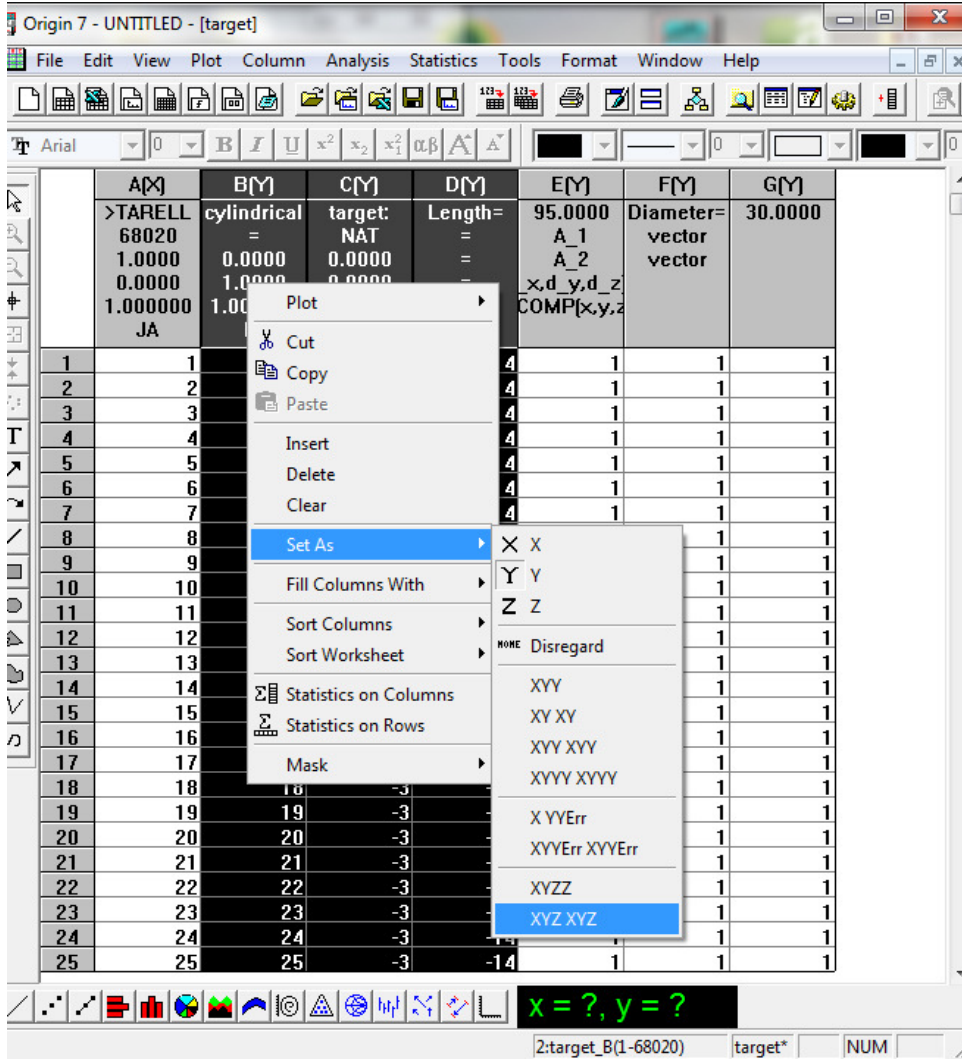
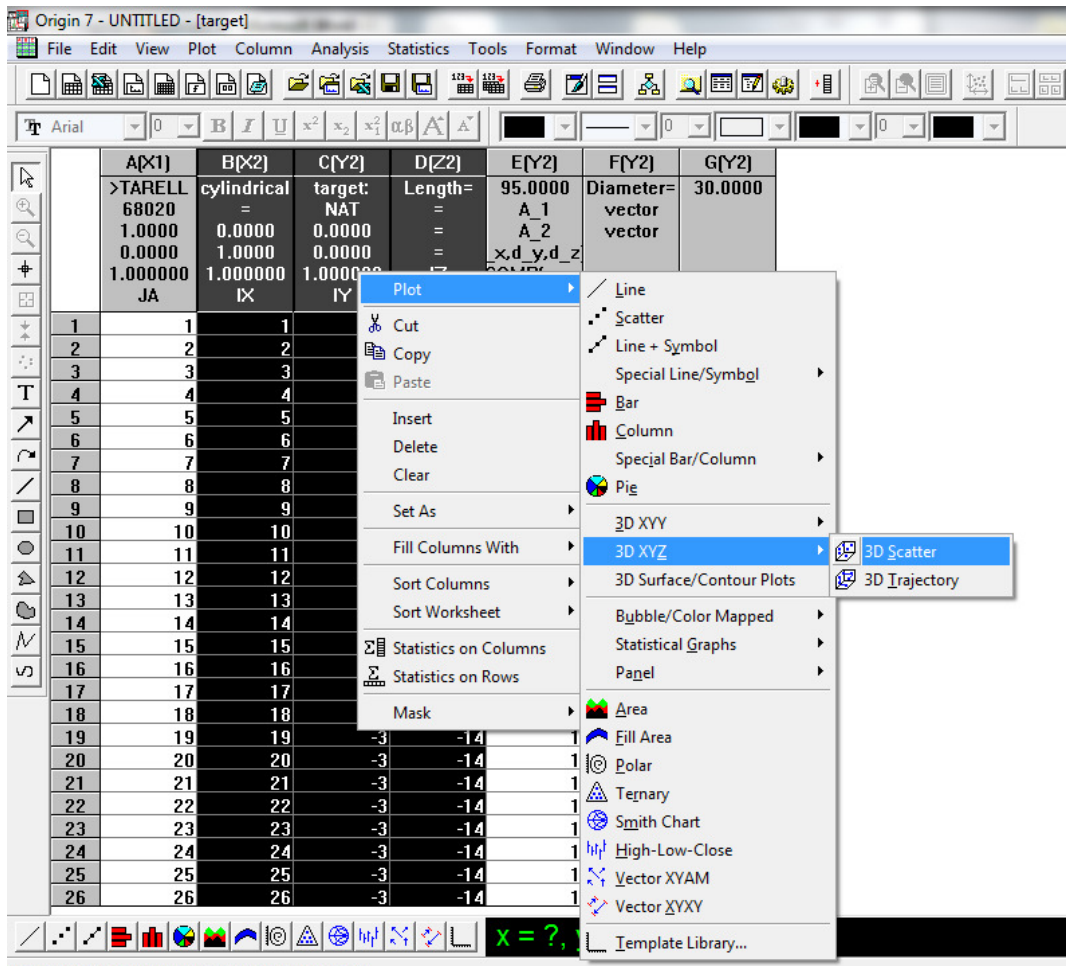


Figure A - 4. Setting the columns to xyz xyz.



Create a 3D scatter plot with the selected 7 columns.

Figure A - 5. Creating a 3D scatter plot.

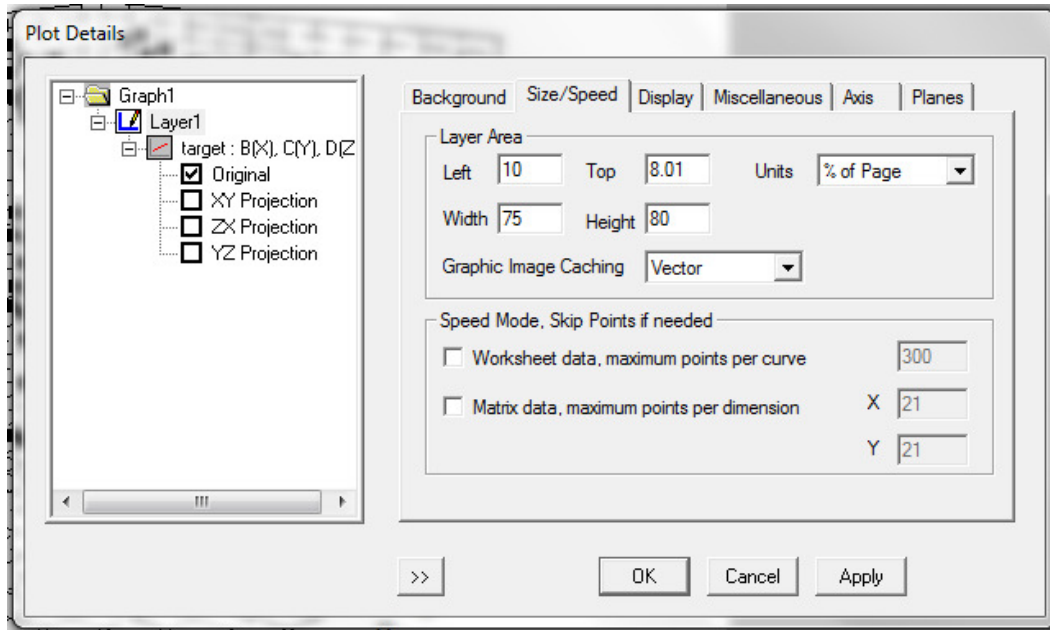


Figure A - 6. How to disable speed mode.

Once the target file contains the particle as desired, export the data (file --> export ASCII) to a file named shape.dat. A new window should open where it is possible to choose the export options. Check the middle box next to include columns labels, and have the other two boxes unchecked (Figure A - 7).

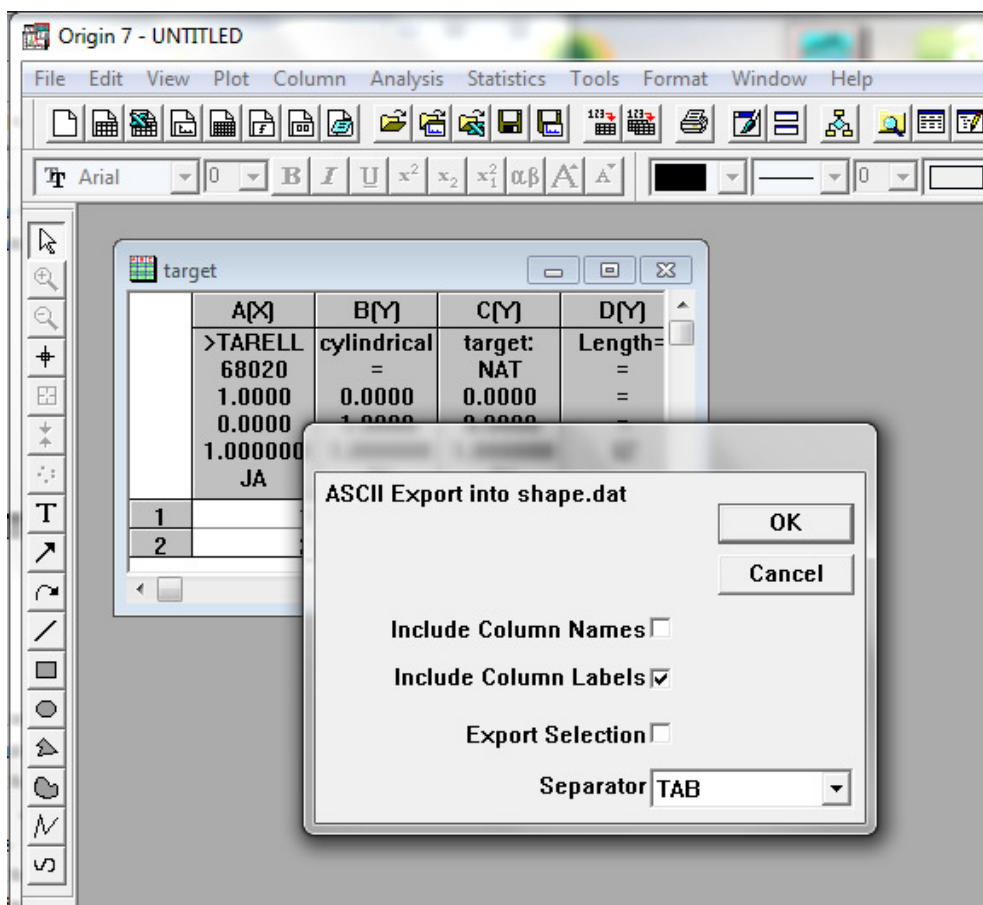


Figure A - 7. ASCII export options.

On the personal computer this file can be named anything, as long as the file type is a .dat. However, when running the calculation, it must be renamed to shape.dat or the calculation will not run.

Once the shape.dat file has been finalized, upload it to the computer cluster. The importing/exporting of the shape file in Origin rearranged some of the beginning text (Figure A - 8). Therefore, every time a shape.dat file is uploaded to the computer cluster



it needs to be opened (on the cluster, just double click and open the file with notepad or some other text editor) and make sure that the file looks like that seen in Figure A - 3.

```

shape - Notepad
File Edit Format View Help
>TARELL ellipsoidal grain; AX,AY,AZ= 40.0000 40.0000 40.0000
33552 = NAT = A_1 vector (d_x,d_y,d_z)/d
1.0000 0.0000 0.0000 = A_2 vector
0.0000 1.0000 0.0000 = lattice spacings
1.000000 1.000000 1.000000 IZ ICOMP(x,y,z)
JA IX IY
1 -3 -4 -20 1 1 1
2 -2 -4 -20 1 1 1
3 -1 -4 -20 1 1 1
4 0 -4 -20 1 1 1
5 1 -4 -20 1 1 1
6 2 -4 -20 1 1 1
7 -4 -3 -20 1 1 1
8 -3 -3 -20 1 1 1
9 -2 -3 -20 1 1 1
10 -1 -3 -20 1 1 1
11 0 -3 -20 1 1 1
12 1 -3 -20 1 1 1
13 2 -3 -20 1 1 1
14 3 -3 -20 1 1 1
15 -4 -2 -20 1 1 1
16 -3 -2 -20 1 1 1
17 -2 -2 -20 1 1 1
18 -1 -2 -20 1 1 1
19 0 -2 -20 1 1 1
20 1 -2 -20 1 1 1
21 2 -2 -20 1 1 1
22 3 -2 -20 1 1 1
23 -4 -1 -20 1 1 1
24 -3 -1 -20 1 1 1
25 -2 -1 -20 1 1 1
26 -1 -1 -20 1 1 1
27 0 -1 -20 1 1 1
28 1 -1 -20 1 1 1
29 2 -1 -20 1 1 1
30 3 -1 -20 1 1 1
31 -4 0 -20 1 1 1
32 -3 0 -20 1 1 1
33 -2 0 -20 1 1 1
34 -1 0 -20 1 1 1
35 0 0 -20 1 1 1
36 1 0 -20 1 1 1
37 2 0 -20 1 1 1
38 3 0 -20 1 1 1
39 -4 1 -20 1 1 1
40 -3 1 -20 1 1 1
41 -2 1 -20 1 1 1
42 -1 1 -20 1 1 1
43 0 1 -20 1 1 1
44 1 1 -20 1 1 1
45 2 1 -20 1 1 1
46 3 1 -20 1 1 1

```

Figure A - 8. Incorrect shape file headings after exporting from Origin.

### *A.5.2 Single hollow particle*

We will now discuss how to use the shape generator code to create a hollow or shell type particle. The shape generator code can only generate solid structures, therefore if we want to create a shell or hollow structure we will need to delete data points. The simplest method is to run the shape generator twice, once for the shape with dimensions for the outer part of shell and again with dimensions for the inner part of shell. Then, align both particles with the same origin and manually delete all the coordinates that appear in the smaller particle from the large particle. At the end of this procedure, the numbering of the first column will need to be adjusted as the index should always increase from 1 to N in increments of 1, where N is the number of rows or dipole in the system. In Origin, select the first column and select "fill column with row numbers"(Figure A - 9). This takes care of the first problem with the number of dipoles. But remember that in the final shape.dat file, the second line has the total number of dipoles in it (Figure A - 3). Therefore, when the shape file for the hollow particle is uploaded to super computer, make sure to open the shape file, adjust the beginning text and also make sure that the number of dipoles on line 2 matches the final index number in file.

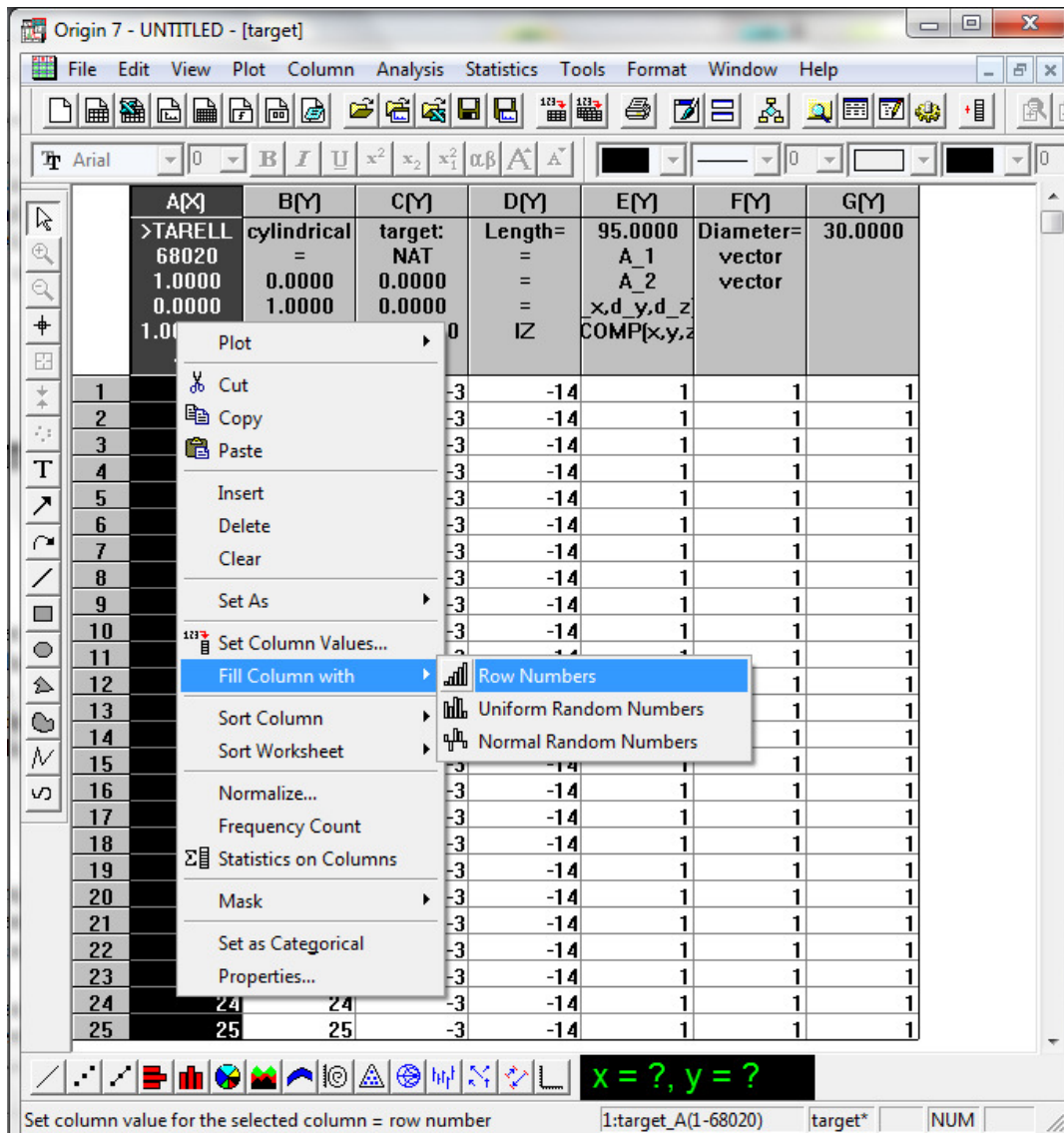


Figure A - 9. Renumbering the index column with row numbers.

### *A.5.3 Multiple particles*

Often we want to investigate not just a single particle, but a pair or several particles. In this case, it is necessary to manually repeat particles in the shape file and adjust their positions as desired. We will start by describing the procedure for a pair of particles.

In order to not confuse the various coordinate systems and orientations, it is simplest to always orient the pair so that the interparticle axis is the y-axis. Then it is easy to define the polarization along the interparticle axis  $[(0,0)(1,0)(0,0)]$  or perpendicular to it  $[(0,0)(0,0)(1,0)]$  in the parameter file (section A.4).

Here we must also reiterate the distinction between "dipole units" and "actual units". As discussed, the shape file only defines the shape of the particle, while the size is defined in the parameter file (section A.4). When defining the coordinates of a particle in the shape file it is necessary to remember which units to use. For example, we want to make a pair of spheres that are each 20 nm in diameter and separated by 10 nm. But, we have represented each 20 nm diameter sphere as a 40 dipole sphere in the shape file.

Therefore 1 nm is 2 dipole units. So the spheres need to be separated by 20 dipole units in the final shape file to achieve the desired 10 nm separation.

Continuing with this example, we will discuss the step to generate the final shape file for the pair of particles. First, generate single particle with the shape generator code. Import the target.out file into origin and make two copies of same file. We now need to adjust

the coordinates of the second particle to achieve the desired position. Continuing the example of the two spheres, initially the spheres will be located in the same position. We need to shift the second sphere along the y-axis by the appropriate amount. So we add 40 to the y column of the second sphere, to shift the second sphere by its diameter, so it now only just touches the first sphere. Then add the appropriate number of dipoles, i.e. 20, to the y column of the second sphere to achieve the desired separation.

Now that you have two data sets, one for each of the 2 particles at the desired coordinates, copy the data for the second particle into the first data sheet so that both particles are now in one data sheet. Select the first column and set it to fill with row numbers (Figure A - 9), because each dipole needs a unique index number. Export to the data to create the shape.dat file. Remember to reset the beginning text as well as the number of dipoles in the shape.dat file after it has been copied to the computer cluster.

The basic procedure described for creating a pair can also be repeated to create as many particles as are desired. The biggest things to remember when creating multiple particles is which direction to shift the particles to achieve the desired orientation with respect to the propagation and polarization of the light; and to remember the difference between dipole units and actual units to achieve the desired orientations and dimensions.

#### *A.5.4 ImageJ Method*

As discussed in Chapters 6 and 7 of this thesis, for some experimental samples (i.e. EBL fabricated samples) it may be desirable to directly convert images of the experimental particles into the shape files for the DDA calculations. This section will discuss how to achieve that using ImageJ (free image processing software available at <http://rsbweb.nih.gov/ij/>). However, this procedure will only involve particles that are in a certain sense 2D, with the same yz cross-section simply being repeated in the x-direction the appropriate number of times. This procedure also assumes the experimental particles have already been fabricated and SEM imaging of the sample has been completed.

Open the SEM file in ImageJ and adjust the threshold (brightness, contrast, etc.) to maximize the particle integrity (Image > adjust > threshold). Then convert the image to a binary image (process > binary > make binary). We need the particles to be black and the background to be white. If it is the other way around, simply invert the image (edit > invert). Delete everything except the particle(s) of interest. Then export the XY coordinates for the image (analyze > tools > save xy coordinates). This will save the xy coordinates of every black pixel in the image as a text file. This text file can then be imported into Origin for editing.

Once imported into Origin, it becomes clear that there are three columns of data. The third column should have the same value for all the data points, and it simply indicates

the color of the pixel in ImageJ. This data is not needed, so delete the third column. Plot the remaining xy coordinates as a scatter plot in Origin. It may be necessary to add or delete some of the points to make the particle's edges sharper. Once the editing has been completed for the single set of xy coordinates, we are ready to convert it into a three dimensional particle.

Add a column to the left of the data and rename the columns to x, y, z. Set the x column values to 1 for all the points in the y and z columns. Then copy and paste the data points in the yz columns to the bottom of the data set as many times as needed while incrementing the x column value to create the particle to the desired thickness. Once all of the xyz coordinates are set, it is easiest to open up another shape.dat file in Origin (that has the correct column headings, etc.) and simply paste the newly generated xyz coordinates into the appropriate part of that formatted file. Then, reset the numbering in the index column, delete or add any numbers for the dielectric columns, export the shape file, copy it to the computer cluster and adjust the beginning text as needed.

#### *A.5.5 Particle on a substrate*

As discussed in Chapters 6 and 7 of this thesis, sometimes particles are placed on a substrate that can affect the optical properties of the system. In such cases, we need to also include dipoles for the substrate as well. However, this is where we start to run up against the limits to how many dipoles the calculations can handle. In the experimental samples, the substrate is usually so much larger than the particle that it appears infinite.

However, we cannot have an infinite number of dipoles in our calculations. The upper limit to the number of dipoles the calculations can handle is around 300,000 dipoles. Therefore, by including the substrate we have to sacrifice many of our dipoles to represent the substrate. Choosing how big the substrate should be compared to the particle is then a balancing act of accurately representing the overall system while still having enough dipoles for the particle to get accurate results. It may be best to run a few test calculations to see how changing certain dimensions of the substrate affect the results in order to decide how many dipoles are really needed for the substrate.

The calculations of this type seem most sensitive to the thickness of the substrate along the propagation direction compared to any other dimension of the substrate. So I typically try to get that parameter as close as possible to the experimental sample. Again, some test calculations may be needed to test for each new system which parameters the calculations are most affected by.

Assuming the shape file for the particle has already been generated by one of the already mentioned techniques, we only need to add a large rectangular slab for the substrate. Use the shape generator code with the input file for a rectangle to create the rectangular slab for the substrate. Open the file in Origin along with that for the particle(s) to be placed on the substrate. Adjust the coordinates of the substrate so it is centered in the yz plane around the particle(s). Adjust the x coordinates of the substrate so that they are less than those of the particle (i.e. substrate is below the particle). Also, the substrate is typically a different material than the particle, so we need to adjust the last three columns of data for



the substrate file. The substrate needs to be the second dielectric material, so set the last three columns of data to 2's for all the dipoles in the substrate file. Then copy and paste the substrate data into the particle's shape file, renumber the index column (Figure A - 9) and export. As always, after copying to the super computer rearrange the comment lines and make sure the correct number of dipoles is specified at the top of the shape.dat file.

#### *A.5.6 From scratch*

It should be clear by now that it is also possible to make a shape file from scratch, just by defining the xyz coordinates of a system. For complicated particle types, this may actually be easiest. Simply generate the xyz coordinates to create the particle shape, then add the index column and the composition columns. Then copy this data into an existing shape.dat file to make sure the comments at the beginning of the shape file are appropriate. As always, after copying to the super computer rearrange the comment lines and make sure the correct number of dipoles is specified at the top of the shape.dat file.

### **A.6 Dielectric File**

The dielectric file (diel.tab) is a simple text file that contains the optical information for a particular material. This is then used to define the material being used in the calculations. These values can be found in many literature references.<sup>5,6</sup> The dielectric file can be

named anything, as long as it is a .tab file and the designation in the parameter file is the same name.

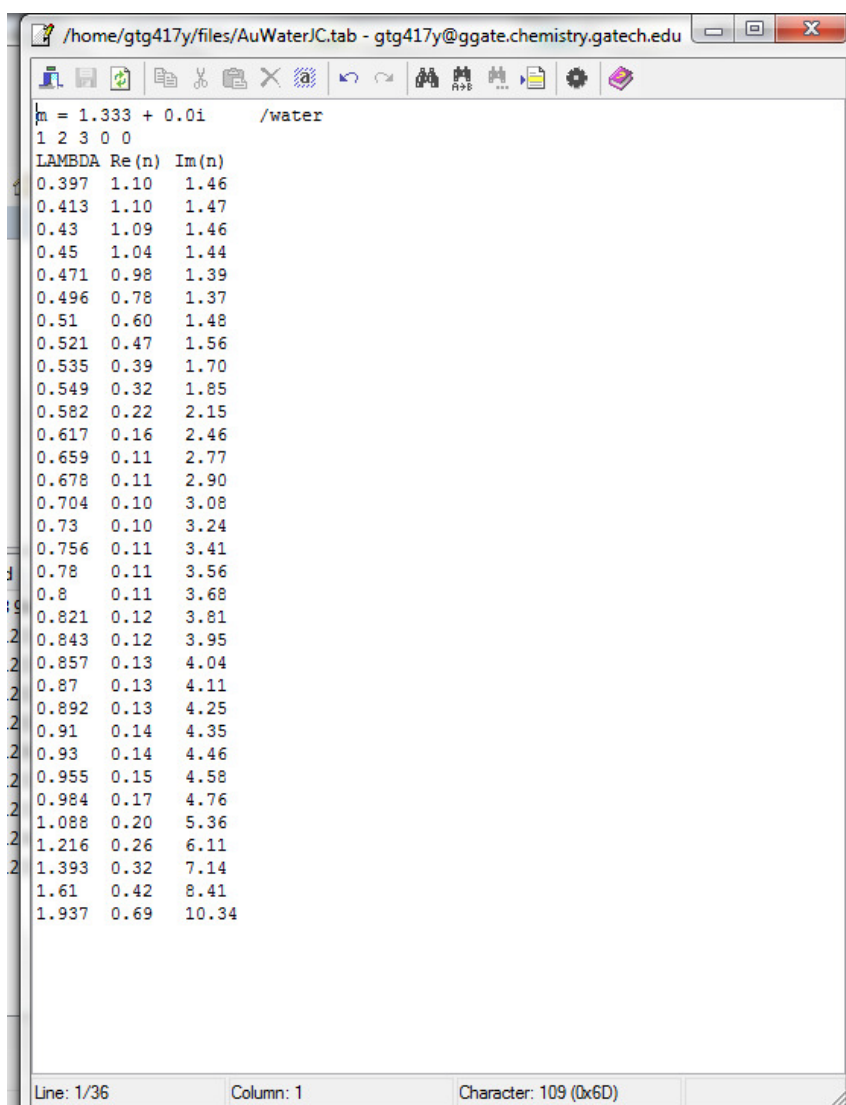
An example dielectric file for gold in air is shown in Figure A - 10. The first line is a comment on what material is being defined. The second and third lines must always be what is shown in this example. Then the first column is the wavelengths (in micrometers) at which the real (column 2) and imaginary (column 3) values for the dielectric function is defined to that material.

```
/home/gtg417y/files/dielAu.tab - gtg417y@ggate.chemistry.gatech.edu
m = 1.00 + 0.0i      /air
1 2 3 0 0
LAMBDA Re(n) Im(n)
0.397 1.470 1.950
0.413 1.460 1.960
0.430 1.450 1.950
0.450 1.380 1.920
0.471 1.310 1.850
0.496 1.040 1.830
0.510 0.800 1.970
0.521 0.620 2.080
0.535 0.520 2.270
0.549 0.430 2.460
0.582 0.290 2.860
0.617 0.210 3.280
0.659 0.140 3.690
0.678 0.140 3.860
0.704 0.130 4.100
0.730 0.130 4.320
0.756 0.140 4.540
0.780 0.150 4.740
0.800 0.150 4.910
0.821 0.160 5.080
0.843 0.160 5.260
0.857 0.170 5.380
0.870 0.170 5.480
0.892 0.170 5.660
0.910 0.180 5.800
0.930 0.190 5.940
0.955 0.200 6.100
0.984 0.220 6.350
1.088 0.270 7.150
1.216 0.350 8.145
1.393 0.430 9.519
1.610 0.560 11.21
1.937 0.920 13.78
Line: 1/36      Column: 1      Character: 109 (0x6D)
```

Figure A - 10. Dielectric file, diel.tab, for gold in air.

As discussed previously, if multiple materials are being modeled in the calculation, a dielectric file needs to be provided for each material. However, for particle(s) surrounded by a solution or other medium that is consistent and present in all directions we usually simply adjust the dielectric file for the particle material instead of sacrificing dipoles to model the surrounding medium. For this, simply divide the numbers from the

dielectric file for the particle material by the refractive index of the surrounding medium. So, for comparison the dielectric file for gold in air is shown in Figure A - 10 and the file for gold in water is shown in Figure A - 11, where all the values in Figure A - 10 were divided by the refractive index of water (1.333) to get the values in Figure A - 11.



```
m = 1.333 + 0.0i /water
1 2 3 0 0
LAMBDA Re(n) Im(n)
0.397 1.10 1.46
0.413 1.10 1.47
0.43 1.09 1.46
0.45 1.04 1.44
0.471 0.98 1.39
0.496 0.78 1.37
0.51 0.60 1.48
0.521 0.47 1.56
0.535 0.39 1.70
0.549 0.32 1.85
0.582 0.22 2.15
0.617 0.16 2.46
0.659 0.11 2.77
0.678 0.11 2.90
0.704 0.10 3.08
0.73 0.10 3.24
0.756 0.11 3.41
0.78 0.11 3.56
0.8 0.11 3.68
0.821 0.12 3.81
0.843 0.12 3.95
0.857 0.13 4.04
0.87 0.13 4.11
0.892 0.13 4.25
0.91 0.14 4.35
0.93 0.14 4.46
0.955 0.15 4.58
0.984 0.17 4.76
1.088 0.20 5.36
1.216 0.26 6.11
1.393 0.32 7.14
1.61 0.42 8.41
1.937 0.69 10.34
```

Line: 1/36 Column: 1 Character: 109 (1x6D)

Figure A - 11. Dielectric file, diel.tab, for gold in water.

However, if the particle(s) are sitting on a substrate, or in some other environment that is not consistent in all directions around the particle, the substrate will have to be modeled directly and a separate dielectric file will need to be provided.

### **A.7 a\_0.f and a.pbs**

The remaining two files are used only with the modified version of the ddscat code, which is for calculating the field plots and vectors plots. The a\_0.f file is very long, and contains many options for modifications. However, we only change two values in the file. The first value that we adjust is that shown on lines 14-16 that say "parameter (nxmin = -200, nxmax = 200)" and so on (Figure A - 12). These numbers control how many data points are in the plot, so they control how big the plot is (see section A.9).

The values shown in Figure A - 12 are usually large enough. But if the entire system is not contained on the final contour plot (see section A.9), these numbers may need to be increased. It is best to increment the minimum and maximum by equal amounts (i.e. if the minimum is changed to -300 the maximum should be 300), and all three lines (for x, y and z) should have the same numbers for their minimum and maximum values.

```

/home/gtg417y/files/efieldDDA/a_0.f - gtg417y@ggate.chemistry.gatech.edu
program sl_x_field
implicit none

c This program calculates the electric field and extinction, as well as
c generates plots of field intensity and polarization.

c declarations
integer i,j,k,l
integer nat0,nmax,iorth
integer nxmin,nxmax,nymin,nymax,nzmin,nzmax,itestx,itesty,itestz
integer ixmin,ixmax,iymin,iymax,izmin,izmax,iwrite,iskip
INTEGER nd
parameter(nmax=1500000,iskip=0)
parameter(nxmin=-200,nxmax=200)
parameter(nymin=-200,nymax=200)
parameter(nzmin=-200,nzmax=200)
PARAMETER(nd=1) !# of grad spacing
integer*2 ir0(nmax,3)
integer iocc(nxmin:nxmax,nymin:nymax,nzmin:nzmax)
real aeff,wave,refmed,pi,d,keff,const
real r,rx,ry,rz,r2,kr,qtot
real e2max,e2maxx,e2maxy,e2maxz
real akd(3)
real qlay(nxmin:nxmax,nymin:nymax,nzmin:nzmax)
complex eye,alpha
complex r3term,r5term,rdotp,rcoef,pcoef,eikr
complex exsum,eysum,ezsum,einx,einy,einz
complex e01(3),e02(3)
complex pol(3*nmax),alph(3*nmax),cxe(3*nmax),etmp(3*nmax)
complex px(nmax),py(nmax),pz(nmax)
complex ex,ey,ez
complex e2(nxmin:nxmax,nymin:nymax,nzmin:nzmax)
CHARACTER*4 filename

c ----- definitions and notes -----
c nmax = total # of dipoles
c iskip = 1 skips calculation of field outside of particle.
c      = 0 (anything other than 1) calculates field everywhere on grid
c nxmin,nxmax - grid parameters (similar for y and z)
c -----

c read input data generated by DDSCAT.f
read(11,*) wave,refmed,pi,d,keff,const

```

Figure A - 12. Changing the final plot/matrix size in the a\_0.f file.

The only other value in the a\_0.f file we ever change is that on line 142 of the file that says "DO i = #,#" (Figure A - 13). This line tells the calculation to calculate the field contour and vector plots for the yz slice at that #. As discussed for the shape.dat file, the particle is three-dimensional. However, for the contour and vector plots, the calculation can only do one two-dimensional slice at a time through the particle. The slice is always

in the yz plane. Here again, we also have a new set of coordinates to remember. These calculations start numbering the dipoles in the x direction from 1 to N, where N is the maximum dimension along the x axis. This is regardless of how the dipoles are numbered in the shape.dat file. So, if the particle is a 40 dipole sphere centered at (0,0,0), to calculate the fields through the middle slice of the particle line 142 would be set to "DO i = 20,20", because the 20th slice is the middle even though it occurs at 0 on the x-axis in the shape.dat file. These calculations can be run for any number slice, including those above and below the particle, however the vector plots are only generated for those slices that transect the particle.

```

/home/gtg417y/test/efield/389/slice00/a_0.f - gtg417y@ggate.chemistry.gatech.edu
end if
c
c You can zero out the field inside of particle for plotting purposes---
e2(ir0(i,1),ir0(i,2),ir0(i,3))=1.d-3
c -----
c
c qlay(ir0(i,1),ir0(i,2),ir0(i,3))=const*
> aimag(conjg(einx)*px(i)+conjg(einy)*py(i)+conjg(einz)*pz(i))
c > (real(einx)*aimag(px(i))-aimag(einx)*real(px(i))+
c > real(einy)*aimag(py(i))-aimag(einy)*real(py(i))+
c > real(einz)*aimag(pz(i))-aimag(einz)*real(pz(i)))
end do
c write(*,*)ixmin,ixmax
c write(*,*)iymin,iymax
c write(*,*)izmin,izmax
c STOP
c
c this is used to select the plane used during calculation + graphics
c
c DO i=0,0
c
c obtain the file names, s and g mean substrate and gold, respectively.
c the plan is at x=i, where the absolute value of i should be smaller
c than 100.
c
c IF(i.lt.100) THEN
c k=IABS(i)/10
c j=MOD(IABS(i),10)
c filename='a0'//CHAR(48+k)//CHAR(48+j)
c ELSE
c l=IABS(i)/100
c k=IABS(i-1*100)/10
c j=MOD(IABS(i),10)
c filename='a'//CHAR(48+l)//CHAR(48+k)//CHAR(48+j)
c ENDIF
c open output files
c open(unit=30,file='e2_0_'//filename//'.dat')
c open(unit=31,file='ext_0_'//filename//'.dat')
c open(unit=32,file='impol_0_'//filename//'.dat')
c open(unit=33,file='repol_0_'//filename//'.dat')
c
c
c calculate field intensity outside of particle

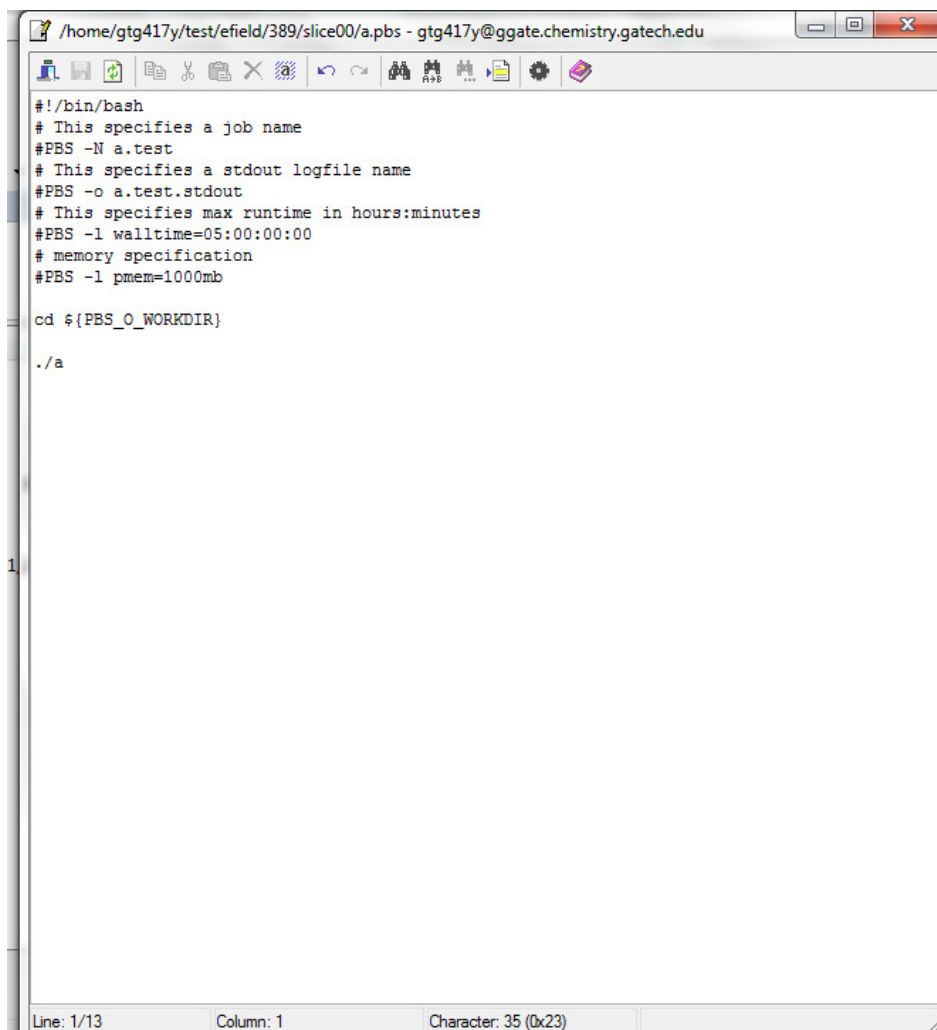
```

Figure A - 13. Choosing slice number in the a\_0.f file.

The final file to discuss is the a.pbs file. It is shown in Figure A - 14, and is very similar to the ddscat.pbs file, it just runs a different code. The field calculations usually take more memory than the spectral calculations, so the memory in the memory in the a.pbs



file usually needs to be around 1000 mb. Again, if the calculations don't run or quit unexpectedly try increasing the memory in the a.pbs file.



```
#!/bin/bash
# This specifies a job name
#PBS -N a.test
# This specifies a stdout logfile name
#PBS -o a.test.stdout
# This specifies max runtime in hours:minutes
#PBS -l walltime=05:00:00:00
# memory specification
#PBS -l pmem=1000mb

cd ${PBS_O_WORKDIR}

./a
```

Line: 1/13    Column: 1    Character: 35 (0x23)

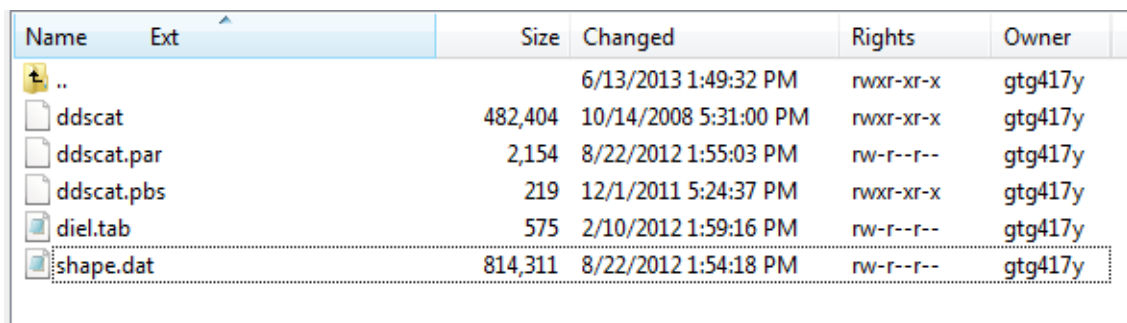
Figure A - 14. The a.pbs file.

## A.8. Spectra calculations

Now that all of the files have been thoroughly explained, we will discuss the actual process of submitting the calculations to run on the computer cluster and how to process the data that is generated.

### A.8.1 Running the spectral calculations

Create a folder on the computer cluster (remember there can be no spaces in the name) with a useful title. Place the `ddscat`, `ddscat.pbs`, `ddscat.par`, `diel.tab` and `shape.dat` files that have been prepared for that calculation in the folder (Figure A - 15). Make sure the permissions on the files are set correctly (see section A.2.1 and Figure A - 15).



Name	Ext	Size	Changed	Rights	Owner
..			6/13/2013 1:49:32 PM	rwxr-xr-x	gtg417y
ddscat		482,404	10/14/2008 5:31:00 PM	rwxr-xr-x	gtg417y
ddscat.par		2,154	8/22/2012 1:55:03 PM	rw-r--r--	gtg417y
ddscat.pbs		219	12/1/2011 5:24:37 PM	rwxr-xr-x	gtg417y
diel.tab		575	2/10/2012 1:59:16 PM	rw-r--r--	gtg417y
shape.dat		814,311	8/22/2012 1:54:18 PM	rw-r--r--	gtg417y

Figure A - 15. Folder containing the files needed for a spectral calculation.

To run the calculation, open the command terminal in the computer cluster by hitting control+t. Then in the command line type `qsub ddscat.pbs` (Figure A - 16) and hit enter or click execute. This submits the calculation to the cluster. To check on the status of calculations, enter the command `qstat` and then hit enter. This will give a list of all the calculations submitted for that account, their priority level and how long they have been running. To see all the files running on the cluster, enter the command `showq`. If for some reason a job needs to be stopped before it has finished running, enter the command `qdel` followed by the job id number, which can be found using the `qstat` command.

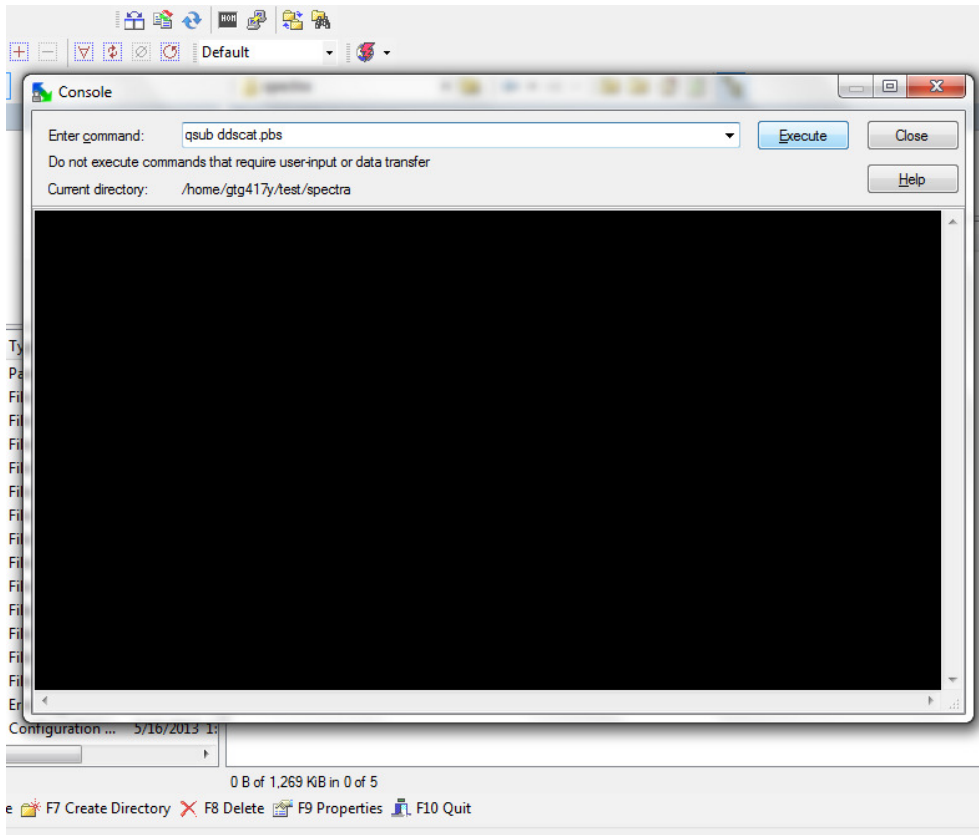


Figure A - 16. The command for submitting the `ddscat.pbs` calculation.

As the calculation is running, it will generate many files. One file is generated for each wavelength in the calculation, these are the w000r000.avg files seen in Figure A - 17. All these files are combined into one containing all the information for the spectra, and that is the qtable file. When the calculation has finished running, the qtable file should be copied off of the cluster onto a personal computer for processing. This file can be renamed to something more descriptive once it has been copied from the cluster if desired.

Name	Ext	Size	Changed	Rights	Owner
..			6/13/2013 1:49:32 PM	rwxr-xr-x	gtg417y
ddscat		482,404	10/14/2008 5:31:00 PM	rwxr-xr-x	gtg417y
ddscat.log_000		3,788,243	8/23/2012 11:27:50 AM	rw-r--r--	gtg417y
ddscat.par		2,154	8/22/2012 1:55:03 PM	rw-r--r--	gtg417y
ddscat.pbs		219	12/1/2011 5:24:37 PM	rwxr-xr-x	gtg417y
diel.tab		575	2/10/2012 1:59:16 PM	rw-r--r--	gtg417y
mtable		4,689	8/23/2012 11:27:50 AM	rw-r--r--	gtg417y
qtable		7,333	8/23/2012 11:27:50 AM	rw-r--r--	gtg417y
qtable2		2,976	8/23/2012 11:27:50 AM	rw-r--r--	gtg417y
shape.dat		814,311	8/22/2012 1:54:18 PM	rw-r--r--	gtg417y
w000r00ori.avg		3,875	8/22/2012 6:14:20 PM	rw-r--r--	gtg417y
w001r00ori.avg		3,875	8/22/2012 6:14:30 PM	rw-r--r--	gtg417y
w002r00ori.avg		3,875	8/22/2012 6:14:40 PM	rw-r--r--	gtg417y
w003r00ori.avg		3,875	8/22/2012 6:14:50 PM	rw-r--r--	gtg417y
w004r00ori.avg		3,875	8/22/2012 6:15:01 PM	rw-r--r--	gtg417y
w005r00ori.avg		3,875	8/22/2012 6:15:12 PM	rw-r--r--	gtg417y
w006r00ori.avg		3,875	8/22/2012 6:15:23 PM	rw-r--r--	gtg417y
w007r00ori.avg		3,875	8/22/2012 6:15:34 PM	rw-r--r--	gtg417y
w008r00ori.avg		3,875	8/22/2012 6:15:47 PM	rw-r--r--	gtg417y
w009r00ori.avg		3,875	8/22/2012 6:16:12 PM	rw-r--r--	gtg417y
w010r00ori.avg		3,875	8/22/2012 6:17:00 PM	rw-r--r--	gtg417y
w011r00ori.avg		3,875	8/22/2012 6:18:03 PM	rw-r--r--	gtg417y

Figure A - 17. Output from the spectra calculations.

### *A.8.2 Data processing*

To generate the spectra from the qtable file, import the qtable file in origin. There will be many columns, the ones containing the spectra data are the second through fifth columns. The second column contains the wavelengths in microns. The third, fourth and fifth columns contain the spectral data for the extinction, absorption and scattering from the particle, respectively. To plot the spectra, delete all the other columns, set the wavelength column to X and the others to Y then plot in the desired form (line, scatter, etc.). From the spectra, it is possible to see if/where there are any peaks. If there are peaks and better resolution data is needed, go back to the cluster and duplicate the 5 files into a new directory, change the wavelength bounds and steps in the parameter file and run the calculation again. This can be repeated as many times as needed to get the desired spectra resolution.

Origin 7 - UNTITLED - [qtable]

File Edit View Plot Column Analysis Statistics Tools Format Window Help

ODSCAT(X1) B(X2) C(Y2) D(Y2) E(Y2) F(Y2) G(Y2) H(Y2) I(Y2)

0.000 0.000 = beta\_min, beta\_max ; NBETA = 1  
 0.000 0.000 = theta\_min, theta\_max; NTHETA= 1  
 0.000 0.000 = phi\_min, phi\_max controlling # orientations of <cos^2>  
 0.5000 = ETASCA over incident wave Q\_ext 1 polarizing target Q\_sca g(1)=<cos>

Results and aeff averaged 1 wave

	ODSCAT(X1)	B(X2)	C(Y2)	D(Y2)	E(Y2)	F(Y2)	G(Y2)	H(Y2)	I(Y2)
1	0.053	0.3	0.66915	0.53733	0.13183	0.74192	0.62606	0.00118	408
2	0.053	0.35	0.49248	0.39307	0.09942	0.66883	0.55009	1.9488E-5	363
3	0.053	0.4	0.38919	0.31382	0.07538	0.56166	0.49405	3.3599E-4	323
4	0.053	0.45	0.34865	0.29017	0.05848	0.45928	0.45952	9.6539E-4	323
5	0.053	0.5	0.35686	0.30457	0.0523	0.37954	0.44013	0.00154	323
6	0.053	0.55	0.13996	0.09666	0.0433	0.31703	0.42889	0.00177	285
7	0.053	0.6	0.0589	0.02769	0.03121	0.25152	0.41635	0.00162	285
8	0.053	0.65	0.03302	0.01043	0.0226	0.20888	0.41209	0.0014	285
9	0.053	0.7	0.02389	0.00684	0.01706	0.17531	0.40961	0.00119	285
10	0.053	0.75	0.01867	0.00548	0.01319	0.14789	0.40763	0.001	248
11	0.053	0.8	0.01593	0.00555	0.01038	0.12419	0.40593	8.4493E-4	248
12	0.053	0.85	0.01348	0.00517	0.00831	0.10195	0.40433	7.1215E-4	248
13	0.053	0.9	0.01149	0.00472	0.00677	0.07853	0.40158	6.0145E-4	248
14	0.053	0.95	0.01038	0.00473	0.00566	0.08506	0.39621	5.082E-4	248
15	0.053	1	0.00875	0.00419	0.00457	0.10855	0.40178	4.2963E-4	248
16	0.053	1.05	0.00742	0.00365	0.00378	0.09165	0.40288	3.6688E-4	248
17	0.053	1.1	0.00625	0.00308	0.00316	0.07939	0.40295	3.1388E-4	248
18	0.053	1.15	0.00547	0.00281	0.00266	0.07039	0.40284	2.6951E-4	248
19	0.053	1.2	0.00498	0.00272	0.00226	0.06325	0.40272	2.3238E-4	248
20	0.053	1.25	0.00455	0.00262	0.00193	0.05728	0.40261	2.0142E-4	248
21									
22									
23									
24									
25									

x = ?, y = ?

Figure A - 18. The qtable file data.

### A.9 Field calculations

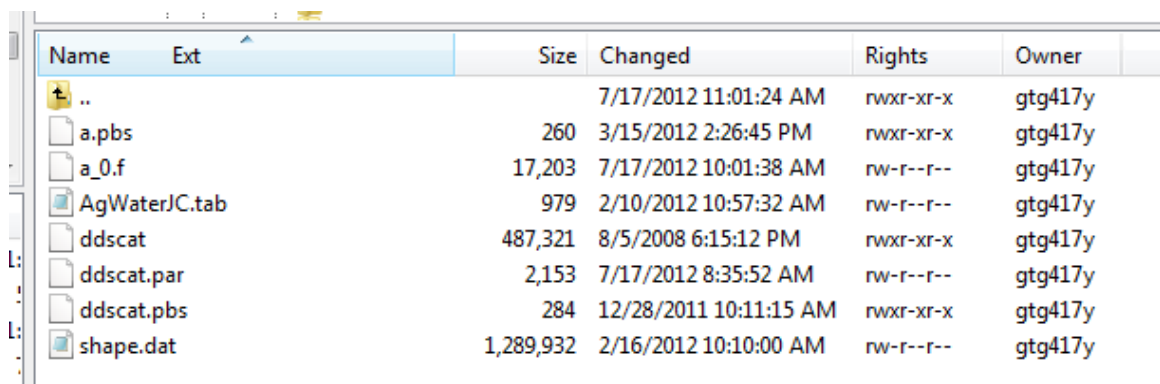
The field calculations can only be generated for a single wavelength at a time. Usually, we are interested in running the calculations for the plasmon resonance wavelength but

there is no way to know what wavelength that is without running the spectral calculations first. Once the wavelengths of interest are know, the field calculations can be run.

### *A.9.1 Running the field calculations*

Create a folder on the computer cluster (remember there can be no spaces in the name) with a useful title. Place the ddscat, ddscat.pbs, ddscat.par, diel.tab, shape.dat, a0.f and a.pbs files that have been prepared for that calculation in the folder (Figure A - 19).

These calculations can only be run for one slice at one wavelength at a time, if multiple calculations for multiple slices or at multiple wavelengths are needed, they will each need to have a separate folder.



Name	Ext	Size	Changed	Rights	Owner
..			7/17/2012 11:01:24 AM	rw-r--r--	gtg417y
a.pbs		260	3/15/2012 2:26:45 PM	rw-r--r--	gtg417y
a_0.f		17,203	7/17/2012 10:01:38 AM	rw-r--r--	gtg417y
AgWaterJC.tab		979	2/10/2012 10:57:32 AM	rw-r--r--	gtg417y
ddscat		487,321	8/5/2008 6:15:12 PM	rw-r--r--	gtg417y
ddscat.par		2,153	7/17/2012 8:35:52 AM	rw-r--r--	gtg417y
ddscat.pbs		284	12/28/2011 10:11:15 AM	rw-r--r--	gtg417y
shape.dat		1,289,932	2/16/2012 10:10:00 AM	rw-r--r--	gtg417y

Figure A - 19. Folder containing the files for a field calculation.

First, we need to run the ddscat calculation for the single wavelength of interest. Therefore, open the ddscat.par file and change the values on the wavelength line to the desired wavelength (Figure A - 20). Then open the terminal (control+t) and submit the ddscat calculation (qsub ddscat.pbs). As discussed previously, the two different version have the same name, but run different calculations and generate different output files. The modified version of the ddscat code for the field calculations generates the output files shown in Figure A - 21. We are not interested in any of these files, but they are required before running the next set of calculations to actually generate the field plots.



```

/home/gtg417y/test/efield/389/slice00/ddscat.par - gtg417y@ggate.chemistry.gatech.edu
|' ===== Parameter file ====='
|'**** PRELIMINARIES ****'
|'NOTORQ'= CMTORQ*6 (DOTORQ, NOTORQ) -- either do or skip torque calculations
|'PBCGST'= CMDSOL*6 (PBCGST, PETRKP) -- select solution method
|'GPFAFT'= CMETHD*6 (GPFAFT, FFTWJ, CONVEX)
|'LATTDR'= CALPHA*6 (LATTDR, SCLDR)
|'NOTBIN'= CBINFLAG (ALLBIN, ORIBIN, NOTBIN)
|'NOTCDF'= CNETFLAG (ALLCDF, ORICDF, NOTCDF)
|'FRMFIL'= CSHAPE*6 (FRMFIL, ELLIPS, CYLNDR, RCTINGL, HEXGON, TETRAH, UNICYL, UNIELL)
|'shape.dat' = shape parameters PAR1, PAR2, PAR3
|1      = NCOMP = number of dielectric materials
|'TABLES'= CDIEL*6 (TABLES, H2OICE, H2OLIQ; if TABLES, then filenames follow...)
|'AgWaterJC.tab' = name of file containing dielectric function
|'**** CONJUGATE GRADIENT DEFINITIONS ****'
|0      = INIT (TO BEGIN WITH |X0> = 0)
|1.00e-5 = TOL = MAX ALLOWED (NORM OF |G>=AC|E>-ACA|X>)/(NORM OF AC|E>)
|'**** Angular resolution for calculation of <cos>, etc. ****'
|0.5    = ETASCA (number of angles is proportional to [(3+x)/ETASCA]^2 )
|'**** Wavelengths ****'
|0.389 0.389 1 'LIN' = wavelengths (first,last,how many,how=LIN,INV,LOG)
|'**** Effective Radii **** '
|.05323 .05323 1 'LIN' = eff. radii (first, last, how many, how=LIN,INV,LOG)
|'**** Define Incident Polarizations ****'
|(0,0) (1.,0.) (0.,0.) = Polarization state e01 (k along x axis)
|1 = IORTH (=1 to do only pol. state e01; =2 to also do orth. pol. state)
|0 = IWRKSC (=0 to suppress, =1 to write ".sca" file for each target orient.
|'**** Prescribe Target Rotations ****'
|0. 0. 1 = BETAMI, BETAMX, NBETA (beta=rotation around a1)
|0. 0. 1 = THETMI, THETMX, NTHETA (theta=angle between a1 and k)
|0. 0. 1 = PHIMIN, PHIMAX, NPHI (phi=rotation angle of a1 around k)
|'**** Specify first IWAV, IRAD, IORI (normally 0 0 0) ****'
|0 0 0 = first IWAV, first IRAD, first IORI (0 0 0 to begin fresh)
|'**** Select Elements of S_ij Matrix to Print ****'
|6      = NSMELTS = number of elements of S_ij to print (not more than 9)
|11 12 21 22 31 41 = indices ij of elements to print
|'**** Specify Scattered Directions ****'
|0. 0. 180. 10 = phi, thetan_min, thetan_max, dtheta (in degrees) for plane A
|90. 0. 180. 10 = phi, ... for plane B

```

Line: 1/38      Column: 1      Character: 39 (lx27)

Figure A - 20. The ddscat.par file for a field calculation.

Name	Ext	Size	Changed	Rights	Owner
..			7/17/2012 11:01:24 AM	rw-r--r--	gtg417y
a.pbs		260	3/15/2012 2:26:45 PM	rw-r--r--	gtg417y
a_0.f		17,203	7/17/2012 10:01:38 AM	rw-r--r--	gtg417y
AgWaterJC.tab		979	2/10/2012 10:57:32 AM	rw-r--r--	gtg417y
ddscat		487,321	8/5/2008 6:15:12 PM	rw-r--r--	gtg417y
ddscat.log_000		28,369	7/17/2012 10:01:50 AM	rw-r--r--	gtg417y
ddscat.par		2,153	7/17/2012 8:35:52 AM	rw-r--r--	gtg417y
ddscat.pbs		284	12/28/2011 10:11:15 AM	rw-r--r--	gtg417y
fort.90		596,800	7/17/2012 10:01:50 AM	rw-r--r--	gtg417y
fort.91		40	7/17/2012 10:01:50 AM	rw-r--r--	gtg417y
fort.92		73	7/17/2012 10:01:50 AM	rw-r--r--	gtg417y
fort.93		10,288,933	7/17/2012 10:01:50 AM	rw-r--r--	gtg417y
fort.94		2,876,800	7/17/2012 10:01:50 AM	rw-r--r--	gtg417y
mtable		473	7/17/2012 10:01:50 AM	rw-r--r--	gtg417y
qtable		873	7/17/2012 10:01:50 AM	rw-r--r--	gtg417y
qtable2		664	7/17/2012 10:01:50 AM	rw-r--r--	gtg417y
shape.dat		1,289,932	2/16/2012 10:10:00 AM	rw-r--r--	gtg417y

Figure A - 21. Output for the modified ddscat code.

Once the ddscat calculation has finished running, modify the a\_0.f file to select the desired slice of the particle. Then open the command terminal and enter the command: `f77 a_0.f`. This will compile the a\_0.f file and create a new file called a.out. Rename the a.out file to just a. Then, open the command terminal again and enter the command `qsub a.pbs`. This will run the code to generate the field plots. The output files for this step can be seen in Figure A - 22. The files of interest are the e2\_0\_a000.dat and fort.32 files.

Copy both from the cluster onto a personal computer for processing.

Name	Ext	Size	Changed	Rights	Owner
..			7/17/2012 11:01:24 AM	rwxr-xr-x	gtg417y
a		33,768	7/17/2012 11:01:45 AM	rwxr-xr-x	gtg417y
a.pbs		260	3/15/2012 2:26:45 PM	rwxr-xr-x	gtg417y
a.test.stdout		298	7/17/2012 2:25:04 PM	rw-----	gtg417y
a_0.f		17,203	7/17/2012 10:01:38 AM	rw-r--r--	gtg417y
AgWaterJC.tab		979	2/10/2012 10:57:32 AM	rw-r--r--	gtg417y
ddscat		487,321	8/5/2008 6:15:12 PM	rwxr-xr-x	gtg417y
ddscat.log_000		28,369	7/17/2012 10:01:50 AM	rw-r--r--	gtg417y
ddscat.par		2,153	7/17/2012 8:35:52 AM	rw-r--r--	gtg417y
ddscat.pbs		284	12/28/2011 10:11:15 AM	rwxr-xr-x	gtg417y
ddscat.test.stdout		0	7/17/2012 9:55:42 AM	rw-----	gtg417y
e2_0_a000.dat		2,154,737	7/17/2012 2:25:04 PM	rw-r--r--	gtg417y
fort.31		804,252	7/17/2012 2:25:04 PM	rw-r--r--	gtg417y
fort.32		220	7/17/2012 2:25:04 PM	rw-r--r--	gtg417y
fort.33		220	7/17/2012 2:25:04 PM	rw-r--r--	gtg417y
fort.90		596,800	7/17/2012 10:01:50 AM	rw-r--r--	gtg417y
fort.91		40	7/17/2012 10:01:50 AM	rw-r--r--	gtg417y
fort.92		73	7/17/2012 10:01:50 AM	rw-r--r--	gtg417y
fort.93		10,288,933	7/17/2012 10:01:50 AM	rw-r--r--	gtg417y
fort.94		2,876,800	7/17/2012 10:01:50 AM	rw-r--r--	gtg417y
mtable		473	7/17/2012 10:01:50 AM	rw-r--r--	gtg417y
ntable		873	7/17/2012 10:01:50 AM	rw-r--r--	gtg417y

Figure A - 22. Output for the field calculation.

### A.9.2 Data processing

First, we will discuss the data processing for the e2\_0\_a000.dat file. Import this file into Origin. There will be 5 columns of data, but we are only interested in the first column. Before deleting the other columns, take note of the numbers in rows 3-6 of the third column. We will need those in a later step. Once those numbers have been noted, delete

all columns except the first column (Figure A - 23). The first couple rows of data, as well as the last, do not contain numbers but % symbols. Delete all these data points.

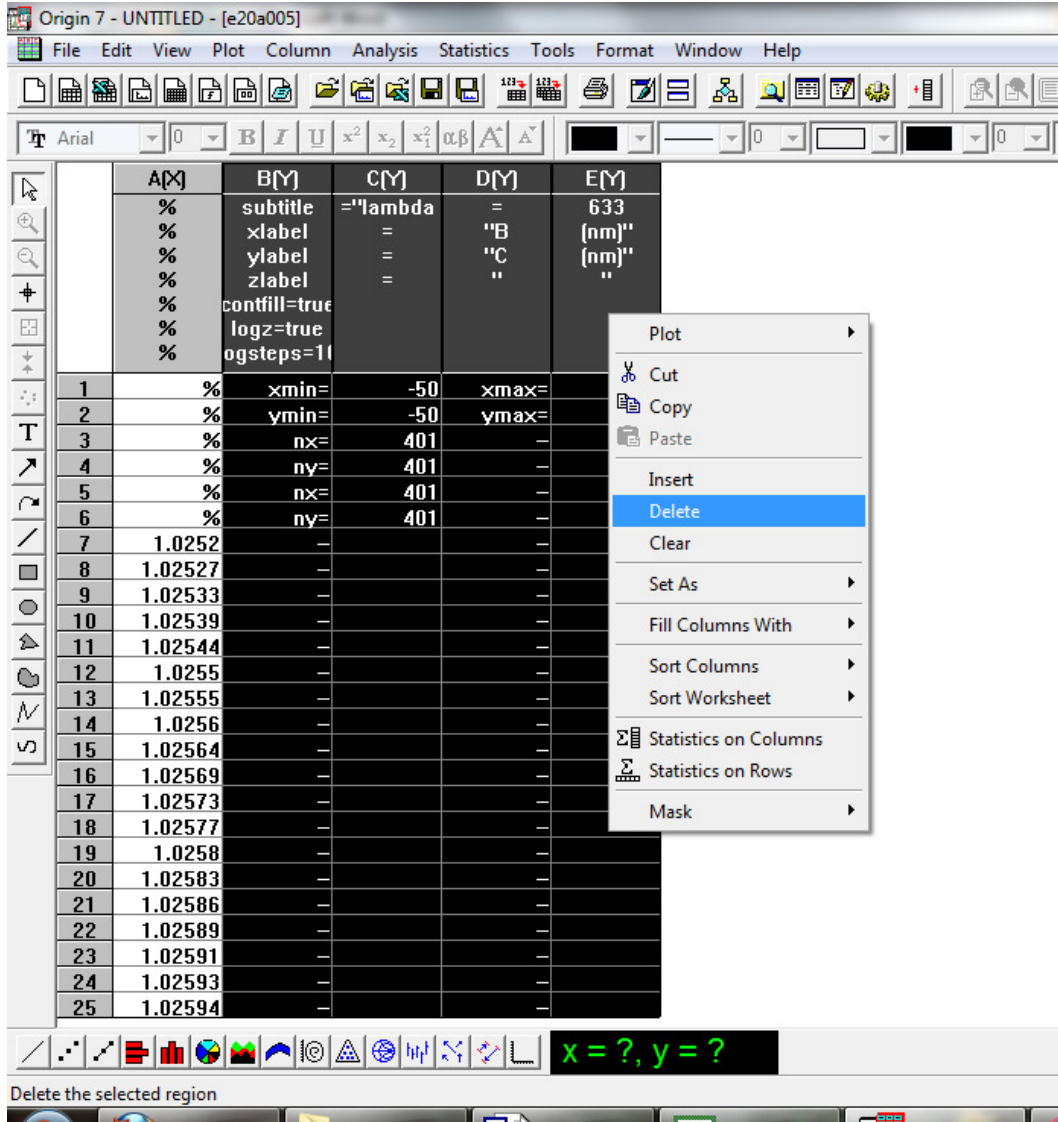


Figure A - 23. Delete the last four columns of the field data.

Now there should be a single column of data containing only numbers. Highlight the column of data and convert it into a matrix (edit --> convert to matrix --> direct; Figure A - 24). This will generate a matrix with a single column of data. To convert this into a square matrix, right click on the matrix and select set matrix dimensions (Figure A - 25). Set the number of columns and rows to the number that were noted from rows 3-6 of the third column of the original file (Figure A - 26). As a square matrix is desired, the number of rows and columns can also be calculated by taking the square root of the number of rows in the single column of data.

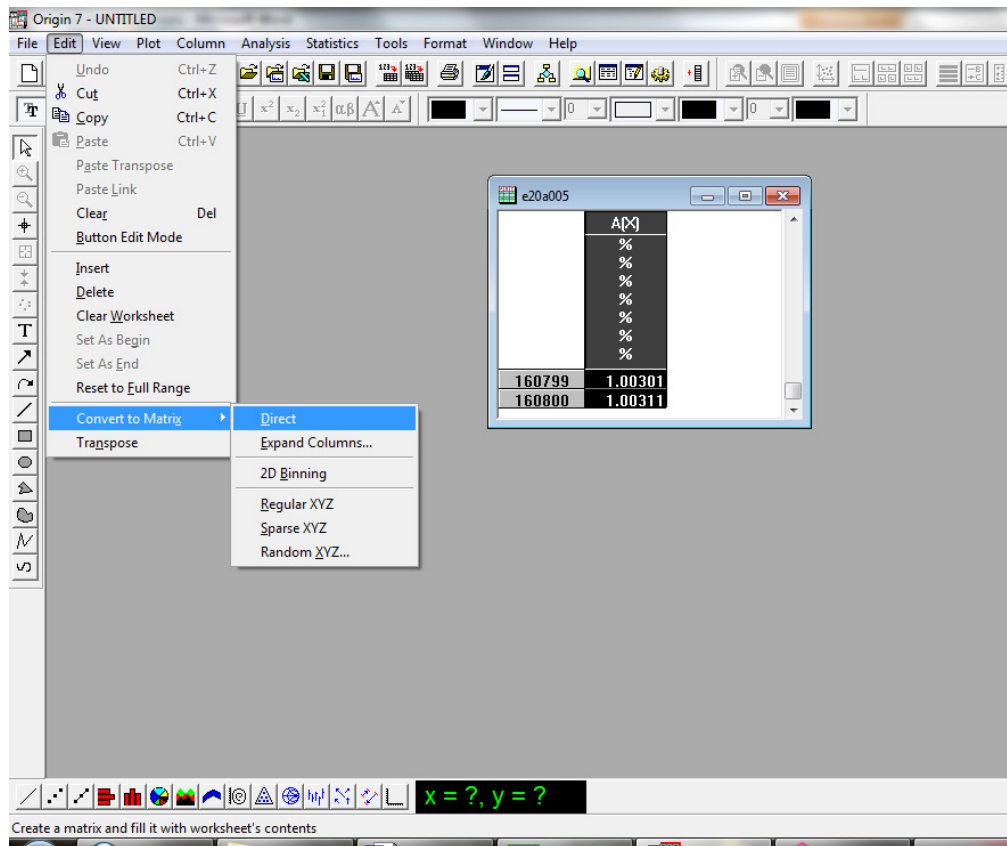


Figure A - 24. Convert the data to a matrix.



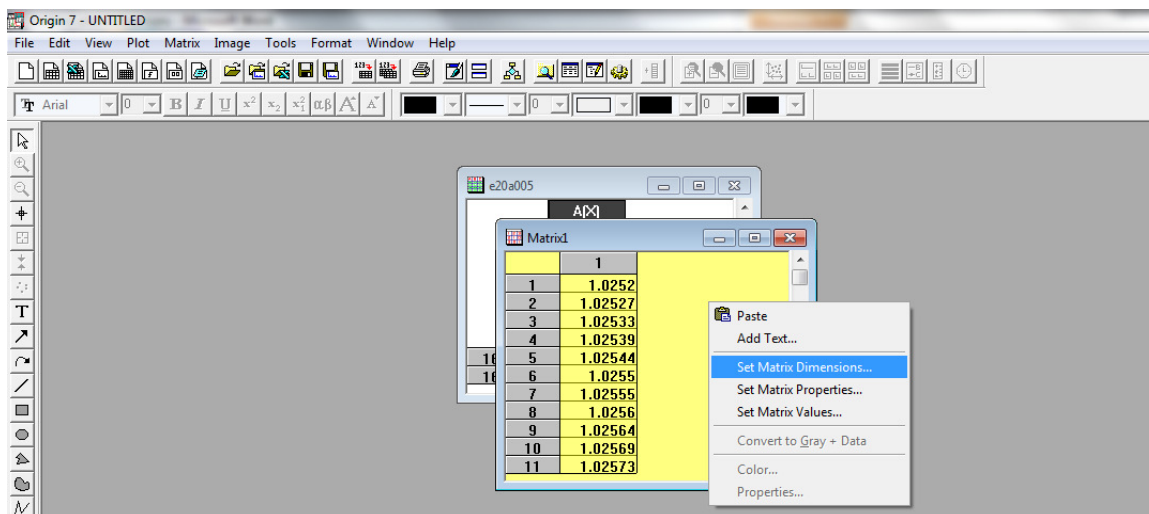


Figure A - 25. Choosing to set the matrix dimensions.

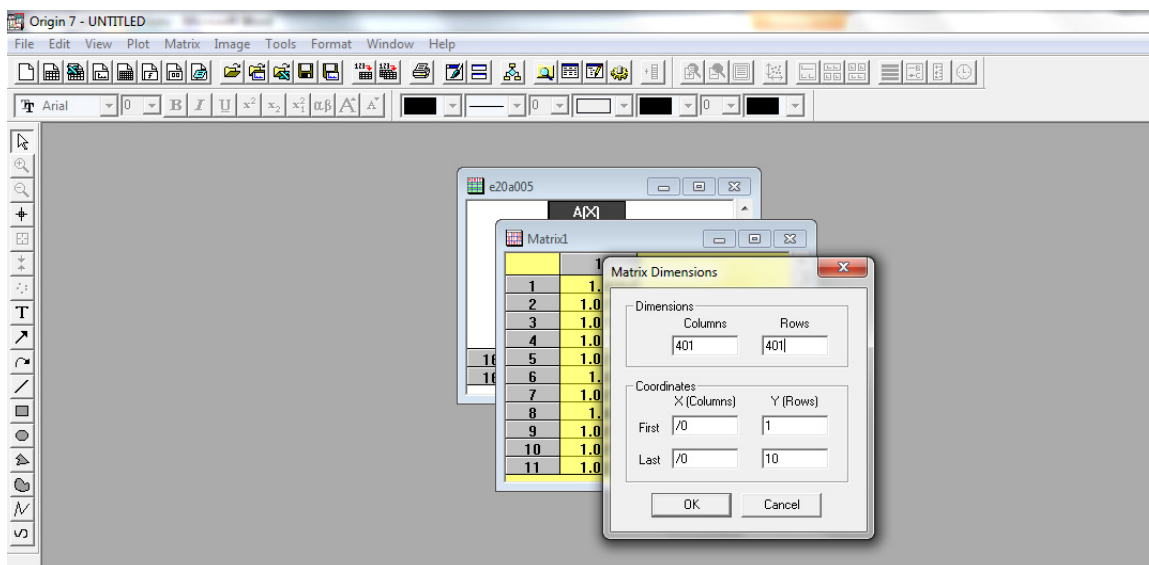


Figure A - 26. Setting the matrix dimensions.

Once the square matrix has been generated, the field contour plot can be generated (plot > contour plot > color fill; Figure A - 27). The initial plot will probably not look like much. We need to adjust several properties of the plot (right click on plot and select plot details; Figure A - 28). Select the matrix level and in the color map/contours tab click on the levels label. In the new window that pops up, click the "log scale" box at the bottom (Figure A - 29). This will require the minimum value to be set to something above zero, we typically pick 0.1 but as long as it's a small positive number it will work. The maximum value should already be filled in. The other change is to select the number of levels option, set that to 20 then click OK. The number of levels is again flexible, 20 just is what we typically choose. Next, click the fill tab and click the option "introduce other colors in mixing" with the first color being blue and the second color being red. Again, this choice is user preference and not concrete. One other option is to click the line label and choose to either show or hide all the contour lines. This choice is up to the user, sometimes it helps the readability of the plots and other times it does not. Finally, go to the layer 1 options, select the size/speed tab and uncheck the boxes next to maximum worksheet and matrix data.

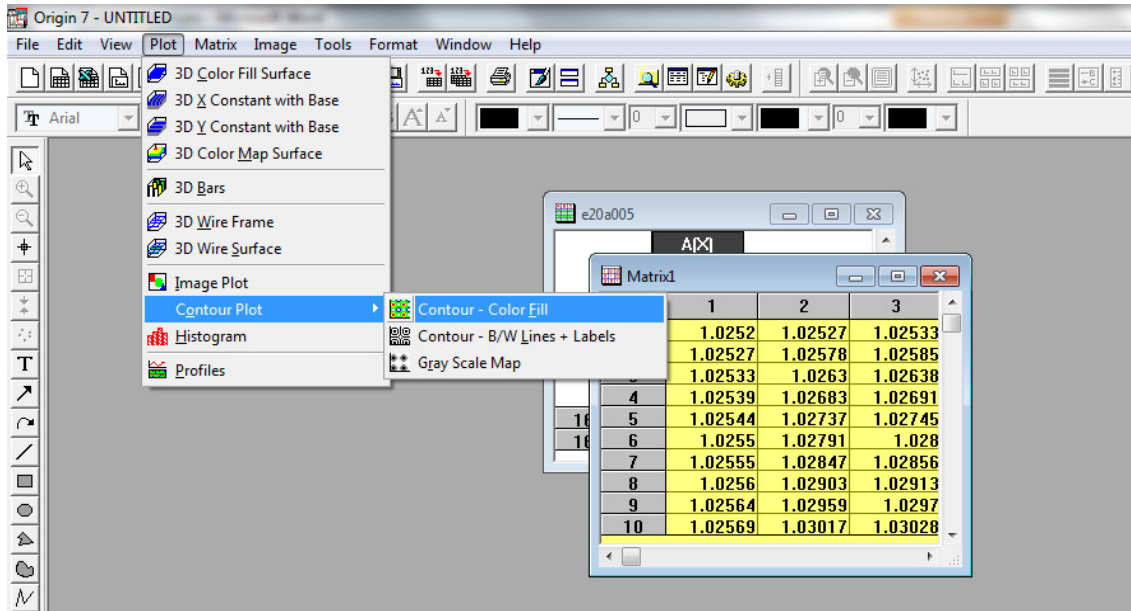


Figure A - 27. Generating a contour plot.

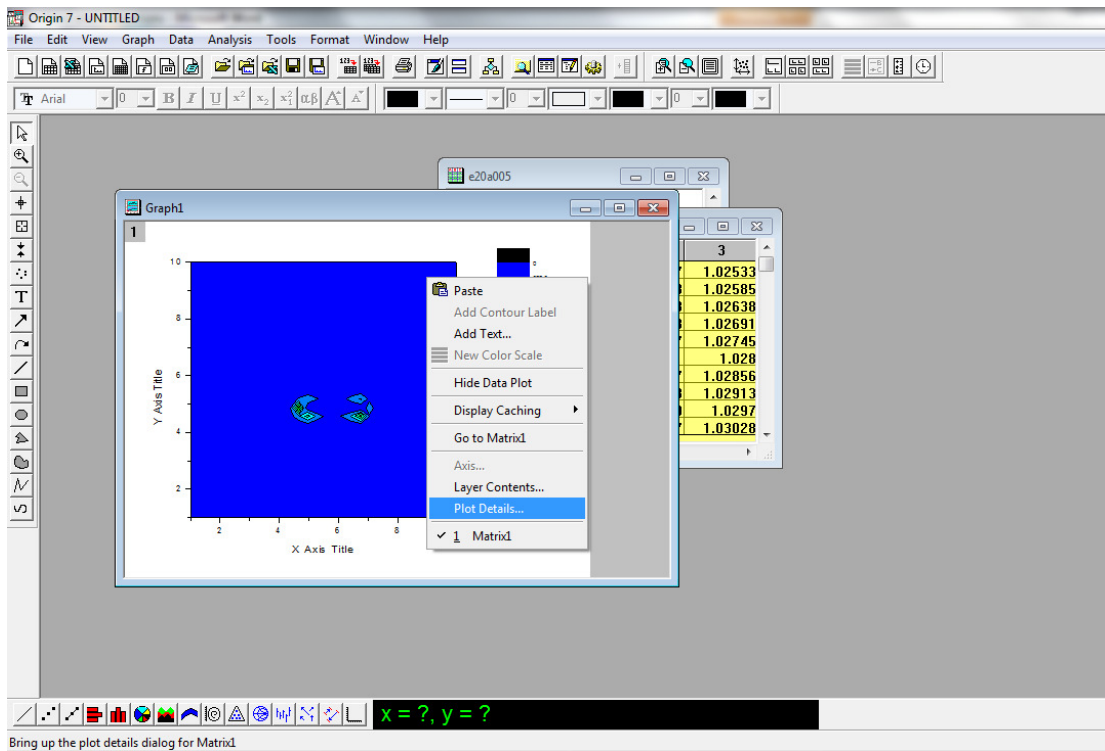


Figure A - 28. Editing the plot details.



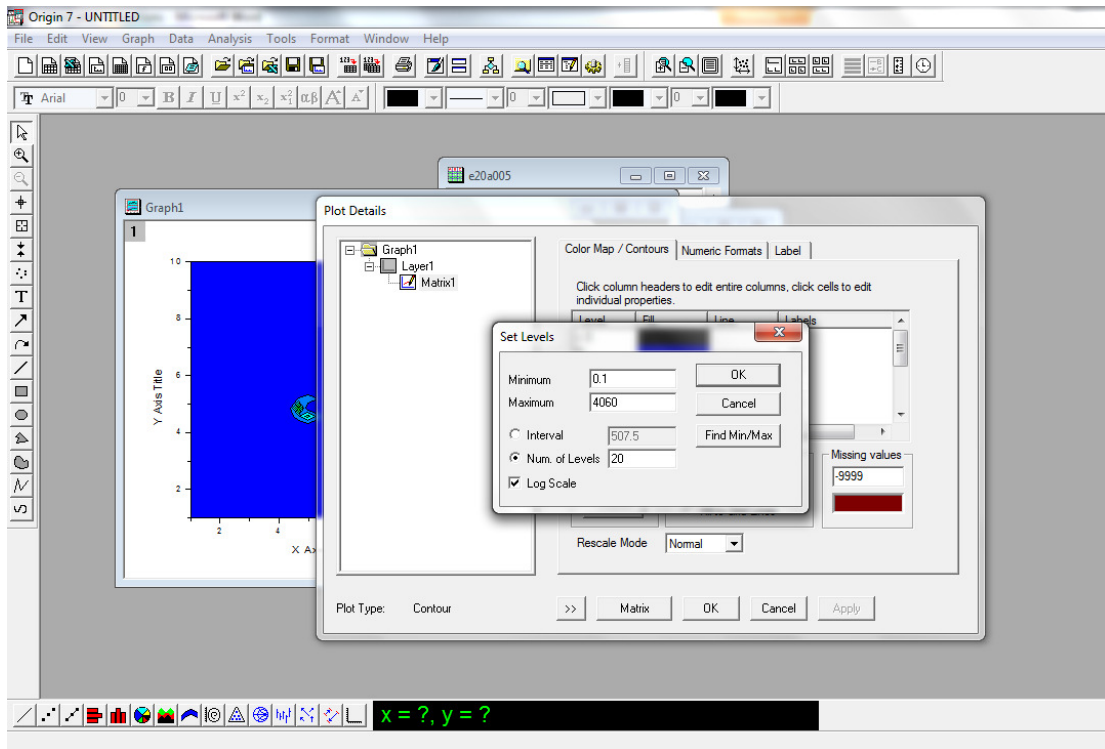


Figure A - 29. Changing the color map scale.

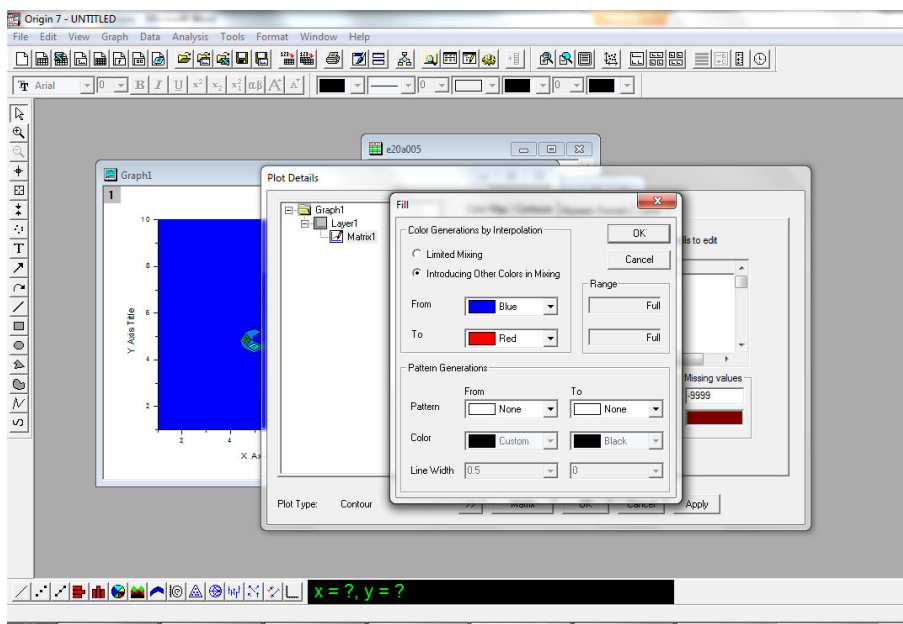


Figure A - 30. Changing the color fill.

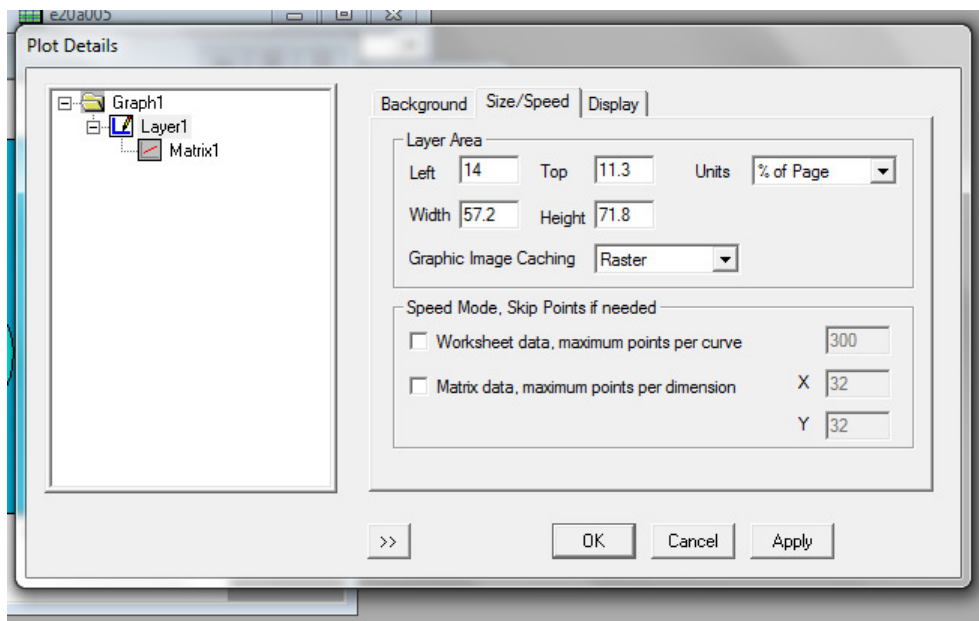


Figure A - 31. Exiting speed mode.

The next data we want to plot is that contained in the fort.32 file. Import the fort.32 file into Origin. There should be 6 columns of data. Delete the third and sixth columns of data (Figure A - 32). Now, insert two new, empty columns in between the second and third columns (Figure A - 33). Set the new third column (column C in Figure A - 33) to be the difference of the values in the first and fifth columns (Figure A - 34). Then set the fourth column to be the difference between the second and sixth columns (Figure A - 35). Now, select the first four columns and set them as xy xy (Figure A - 36). Finally, select the first four columns and create a Vector XYXY plot (Figure A - 37). This will generate a vector plot where each vector represents the orientation of each dipole in that slice of the particle.

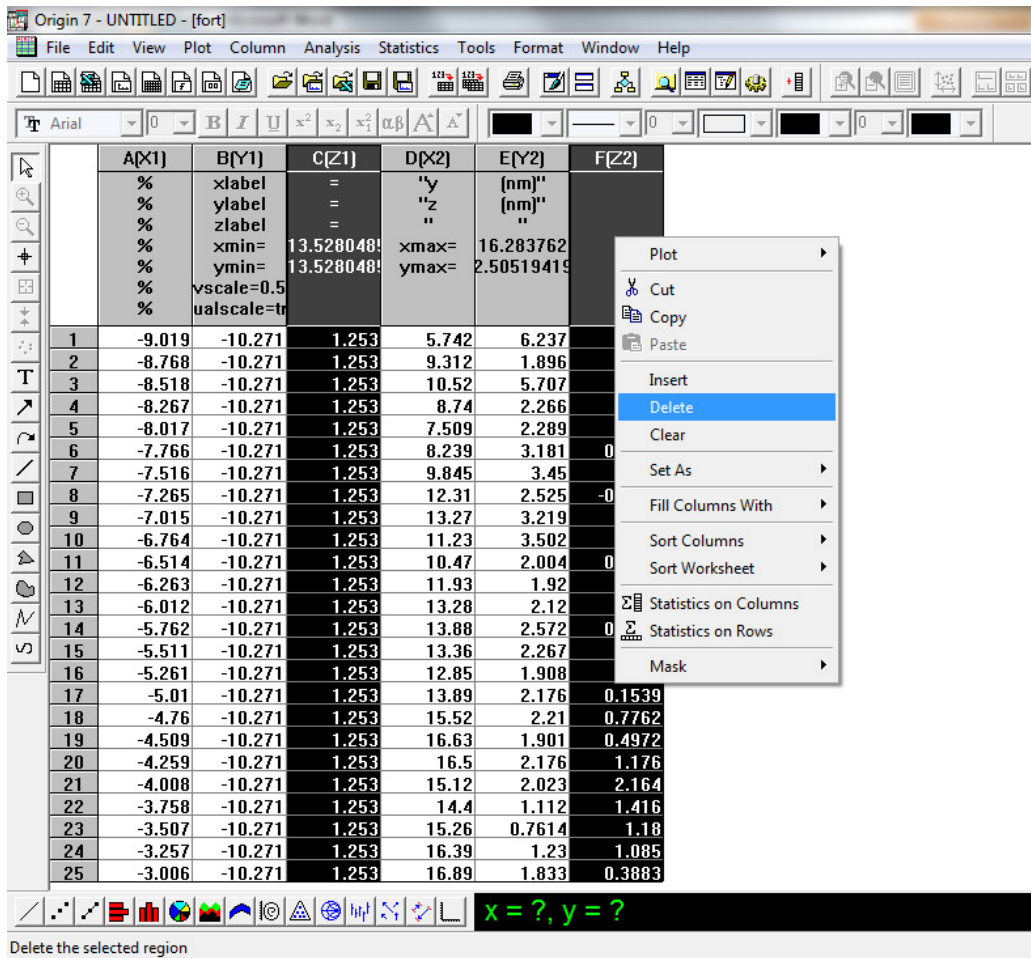


Figure A - 32. The fort.32 file data.

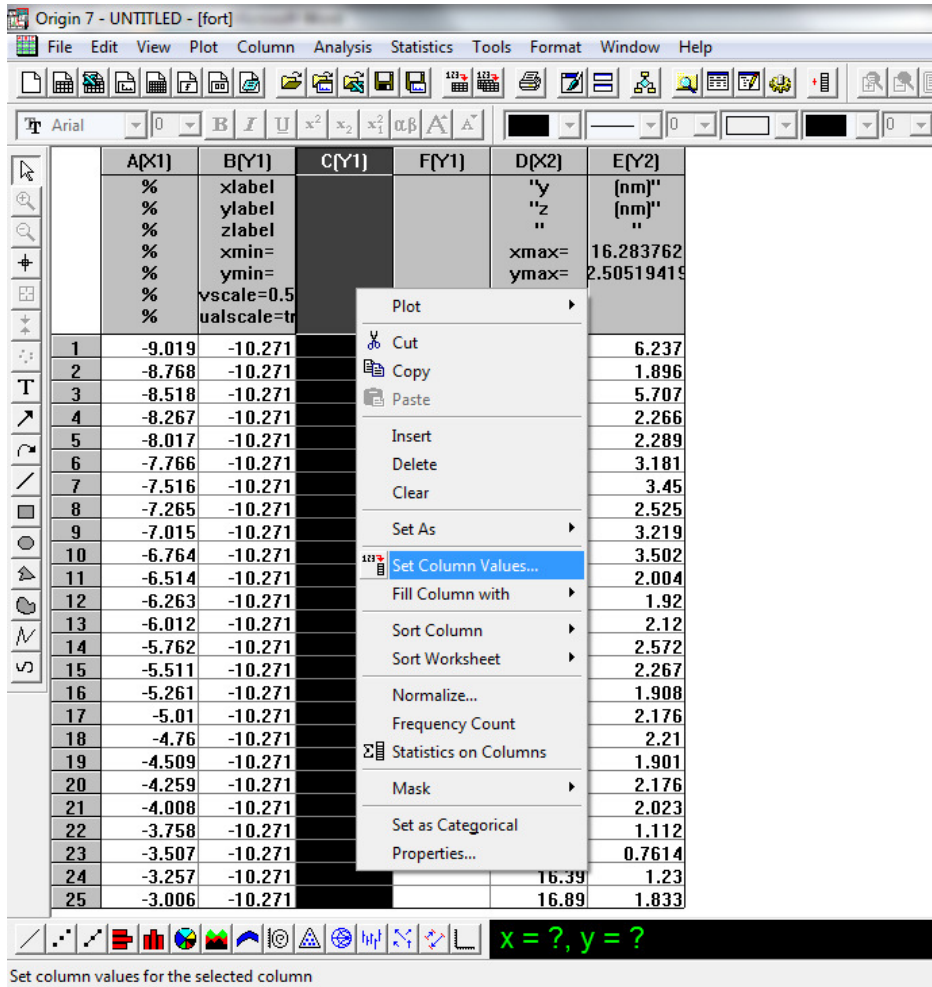


Figure A - 33. Inserting columns into the fort.32 data.

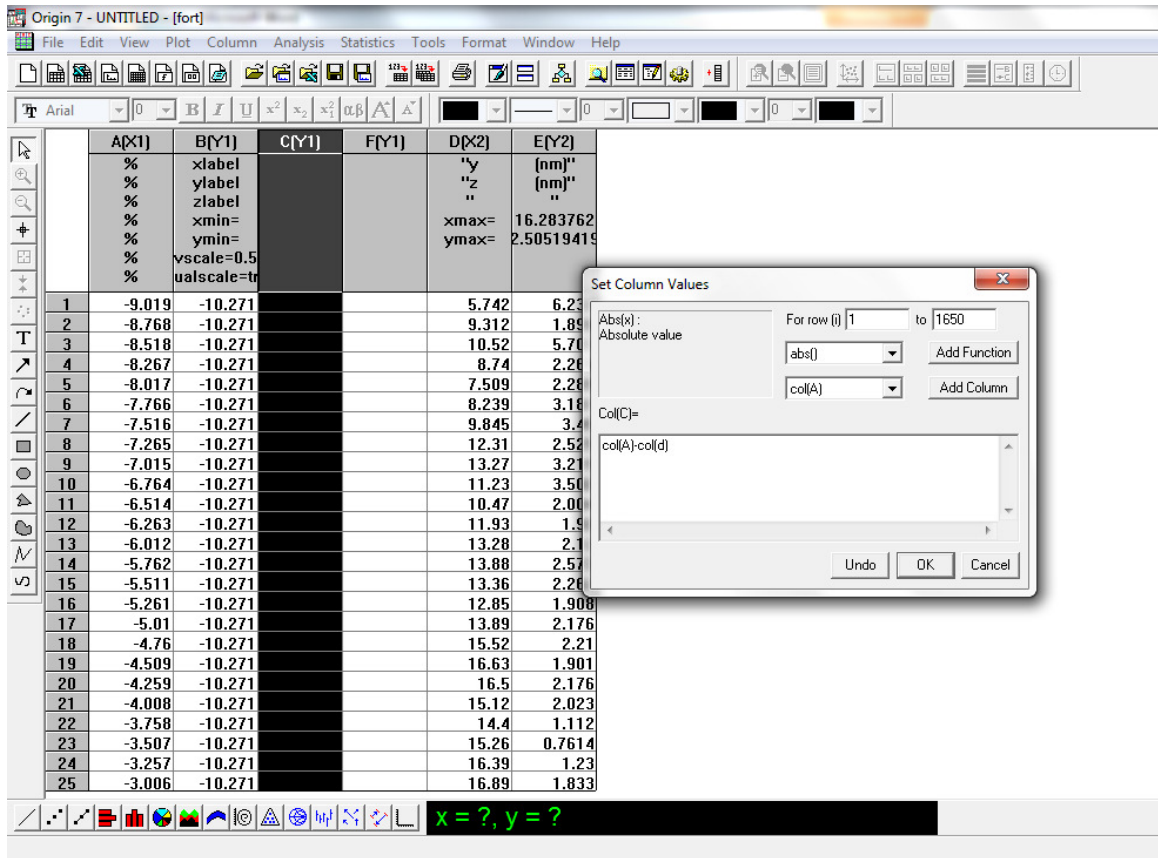


Figure A - 34. Setting the values for column c.

The screenshot shows the Origin 7 software interface. A data table is visible with the following columns and data:

	A[X1]	B[Y1]	C[Y1]	F[Y1]	D[X2]	E[Y2]
1	-9.019	-10.271	-14.761		5.742	6.23
2	-8.768	-10.271	-18.08		9.312	1.89
3	-8.518	-10.271	-19.038		10.52	5.70
4	-8.267	-10.271	-17.007		8.74	2.28
5	-8.017	-10.271	-15.526		7.509	2.28
6	-7.766	-10.271	-16.005		8.239	3.18
7	-7.516	-10.271	-17.361		9.845	3.4
8	-7.265	-10.271	-19.575		12.31	2.52
9	-7.015	-10.271	-20.285		13.27	3.21
10	-6.764	-10.271	-17.994		11.23	3.50
11	-6.514	-10.271	-16.984		10.47	2.00
12	-6.263	-10.271	-18.193		11.93	1.9
13	-6.012	-10.271	-19.292		13.28	2.1
14	-5.762	-10.271	-19.642		13.88	2.57
15	-5.511	-10.271	-18.871		13.36	2.26
16	-5.261	-10.271	-18.111		12.85	1.908
17	-5.01	-10.271	-18.9		13.89	2.176
18	-4.76	-10.271	-20.28		15.52	2.21
19	-4.509	-10.271	-21.139		16.63	1.901
20	-4.259	-10.271	-20.759		16.5	2.176
21	-4.008	-10.271	-19.128		15.12	2.023
22	-3.758	-10.271	-18.158		14.4	1.112
23	-3.507	-10.271	-18.767		15.26	0.7614
24	-3.257	-10.271	-19.647		16.39	1.23
25	-3.006	-10.271	-19.896		16.89	1.833

The 'Set Column Values' dialog box is open, showing the following settings:

- Abs(x): Absolute value
- For row (i): 1 to 1650
- col(F): col(b)-col(e)
- Buttons: Undo, OK, Cancel

Figure A - 35. Setting the values for column d.

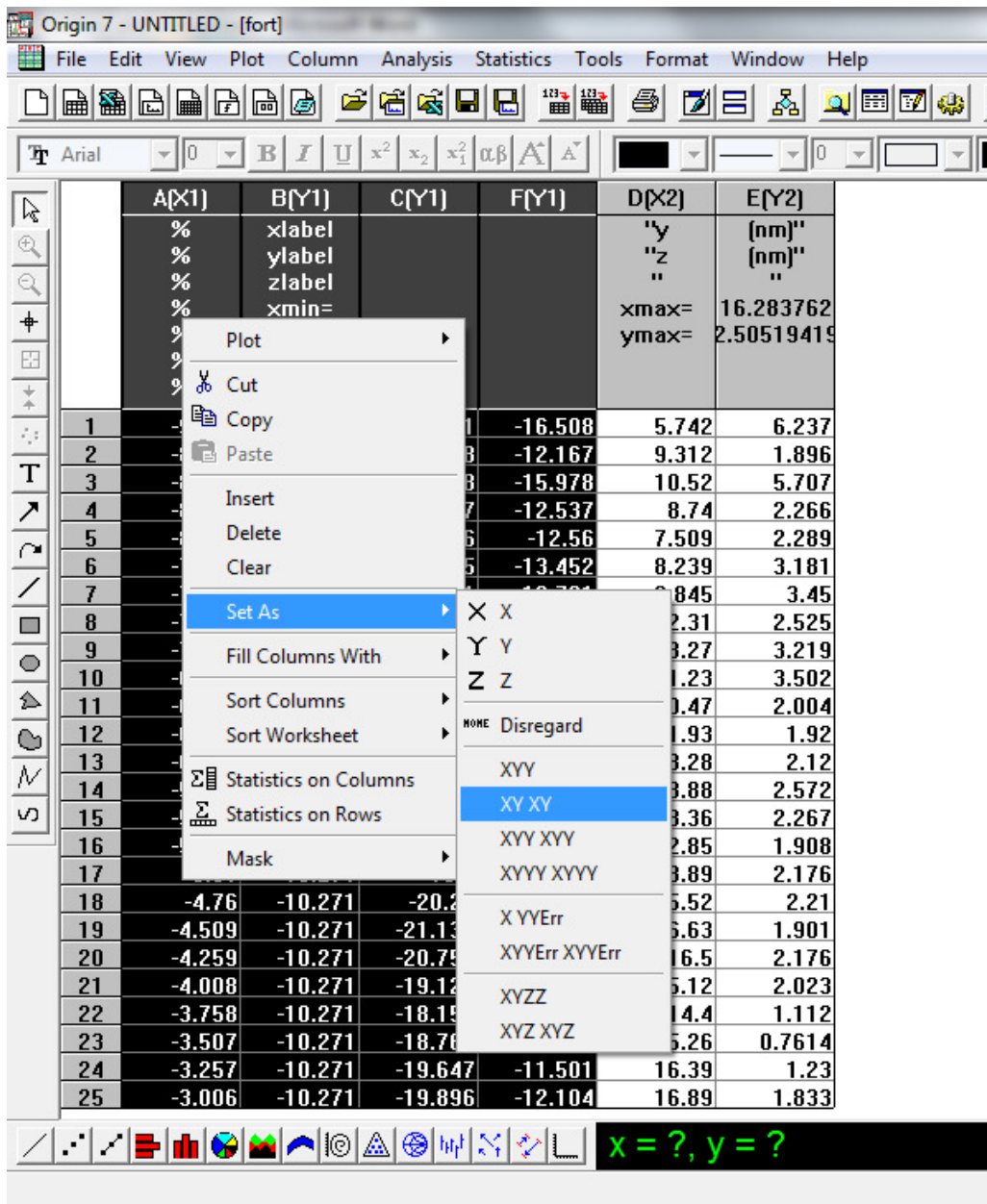


Figure A - 36. Setting the fort.32 columns to xy xy.



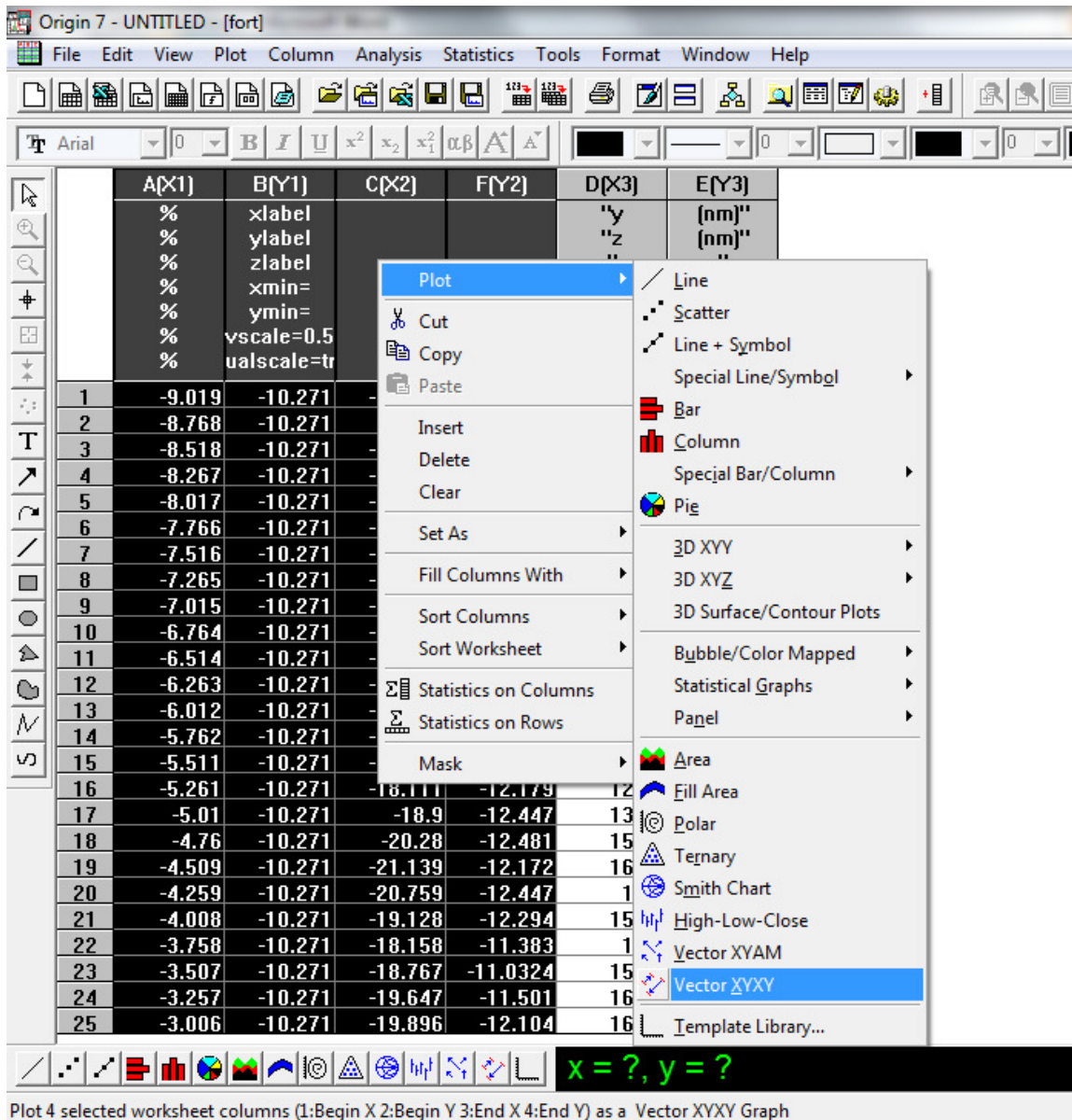


Figure A - 37. Creating the vector plot.



### A.9.3 Three dimensional composite plots

As mentioned, the field contour and vector plots can only be generated for one slice and at one wavelength at a time. But, as discussed in Chapters 5-7 of this thesis to get a better idea of the three dimensional nature of the plasmon mode it is necessary to repeat the field plots for several two dimensional slices and then create a composite plot. The example shown here will involve combining three slices into a composite plot. Import all three e2\*\*\*.dat files into the same Origin file and go through the same steps as was discussed in the previous section to turn the files into square matrices (Figure A - 38). But in this case the type of plots we will generate are different. Select the first matrix and create a 3D color map surface plot (Figure A - 39). As before the initial plot will not look like much because we need to make several changes to the plot details (Figure A - 40).

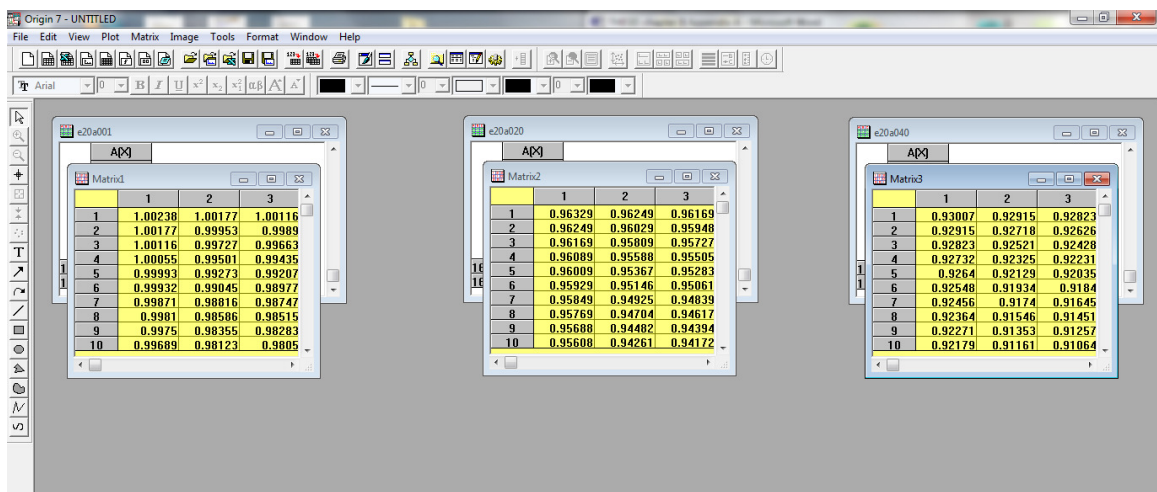


Figure A - 38. The three matrices.

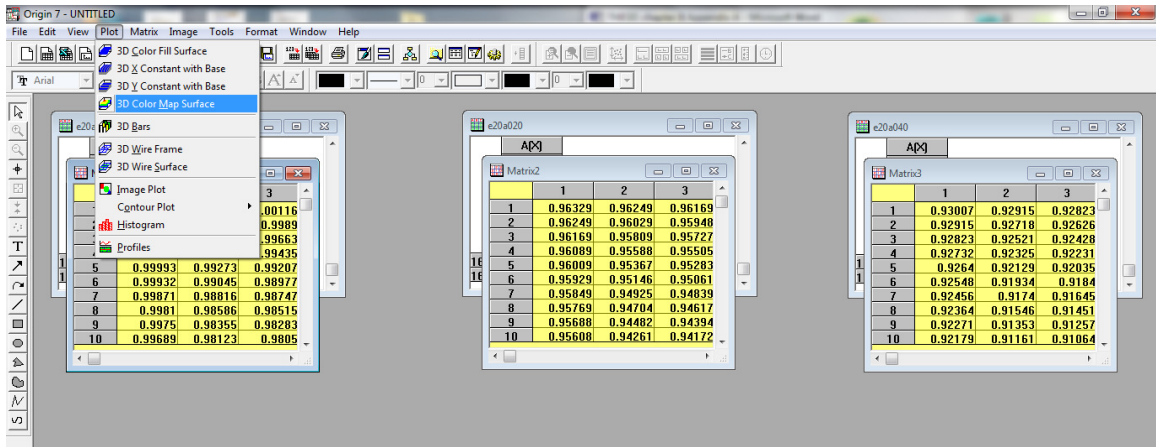


Figure A - 39. Creating the color map plot.

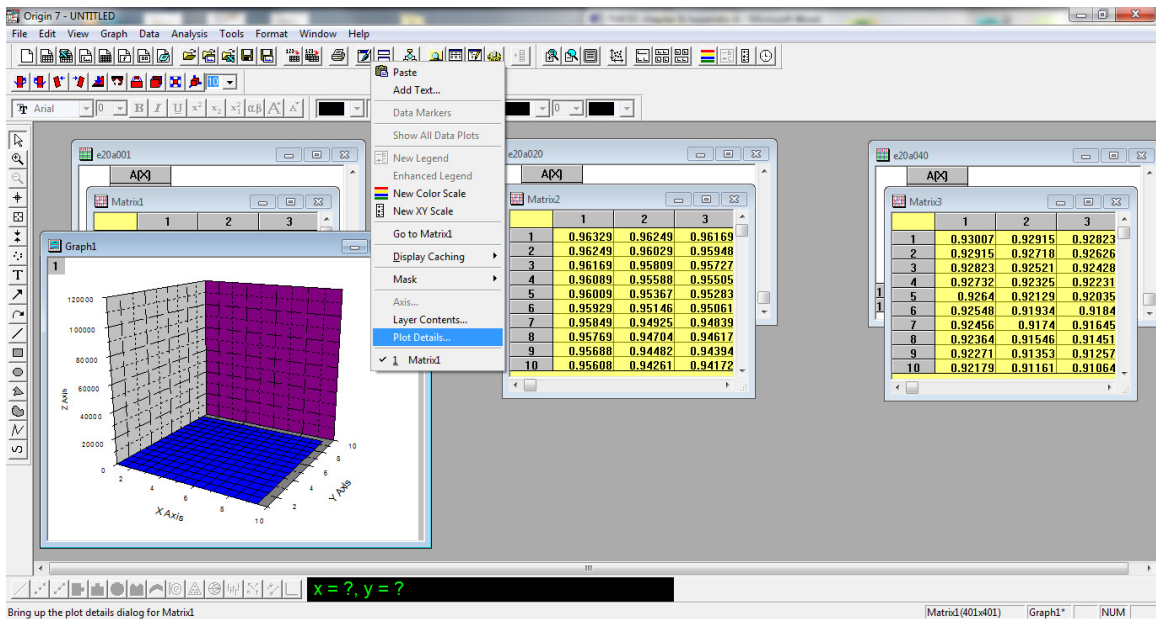


Figure A - 40. The initial 3D color map plot.

Select the matrix level and the color map tab. Click the level heading and change the scale so the minimum is a small positive number, select the number of levels option and set it to 20, and finally check the log scale box (Figure A - 41). Next go to the Grids tab and set the enable grids option to none and uncheck the box next to back color (Figure A - 42). Next go to the Surface/projections tab and check only the box for bottom contour color fill (Figure A - 43).

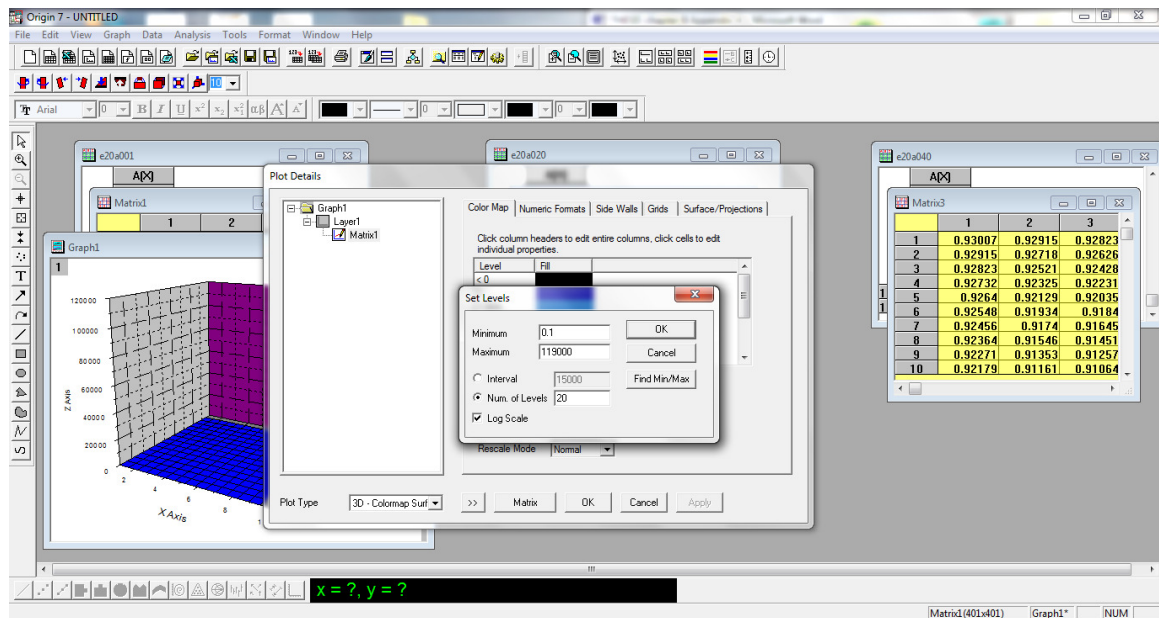


Figure A - 41. Setting the color map scale.

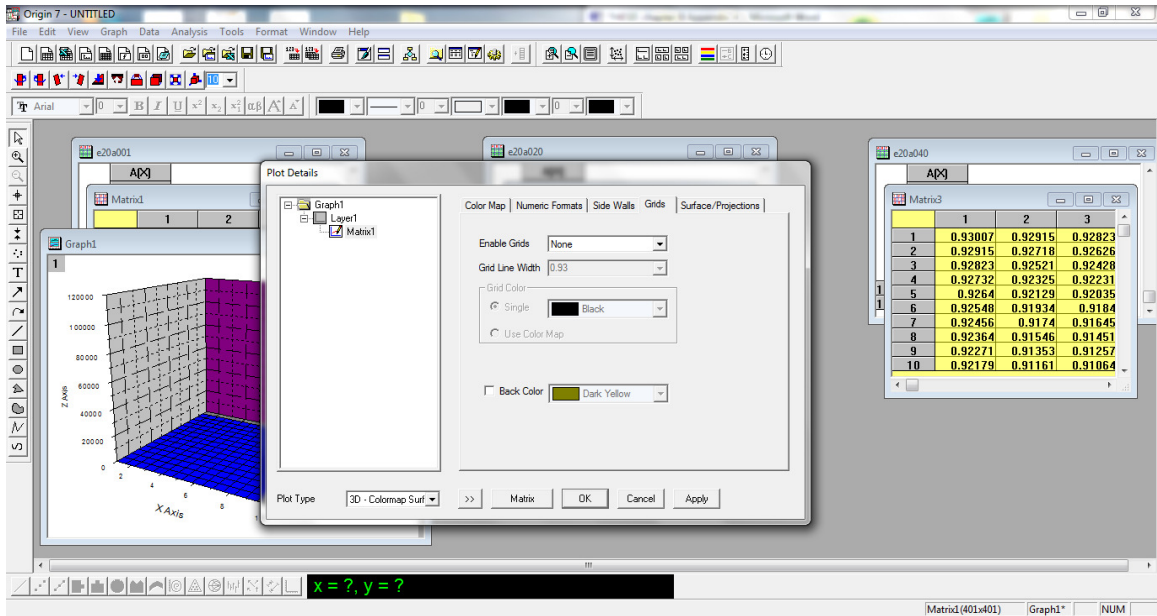


Figure A - 42. Changing the grids.

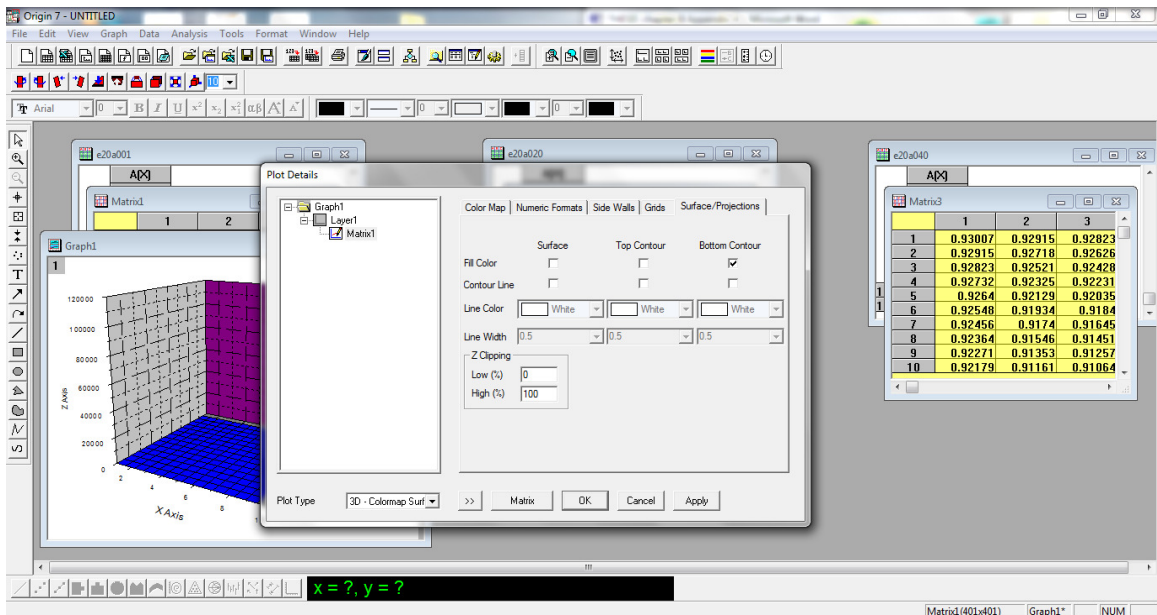


Figure A - 43. Selecting only bottom contour to color fill.

Next go to the size/speed tab in the layer 1 menu and uncheck the maximum data boxes (Figure A - 44). Next, go to the Miscellaneous tab and select orthographic projection (Figure A - 45). Go to the planes tab and set the color for each plane to "none". The plot should now be clearer, though it will probably be necessary to adjust the scales of the axes to zoom in on the particle. Repeat all of these steps for each of the matrices that will be used in the composite plot (three times for this example).

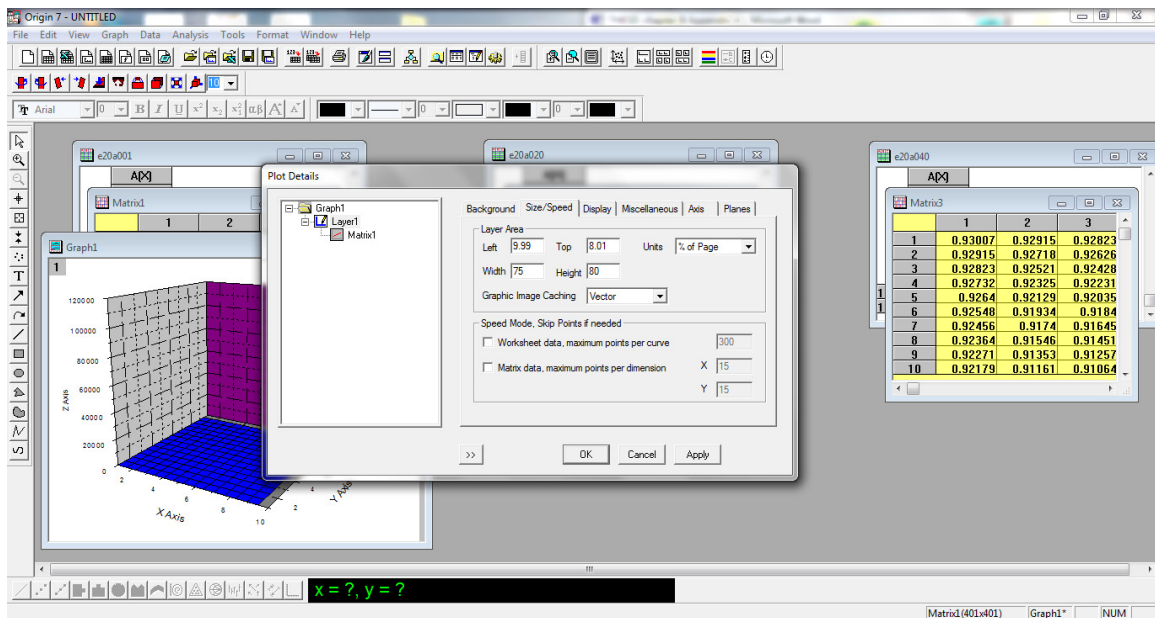


Figure A - 44. Deselecting speed mode.

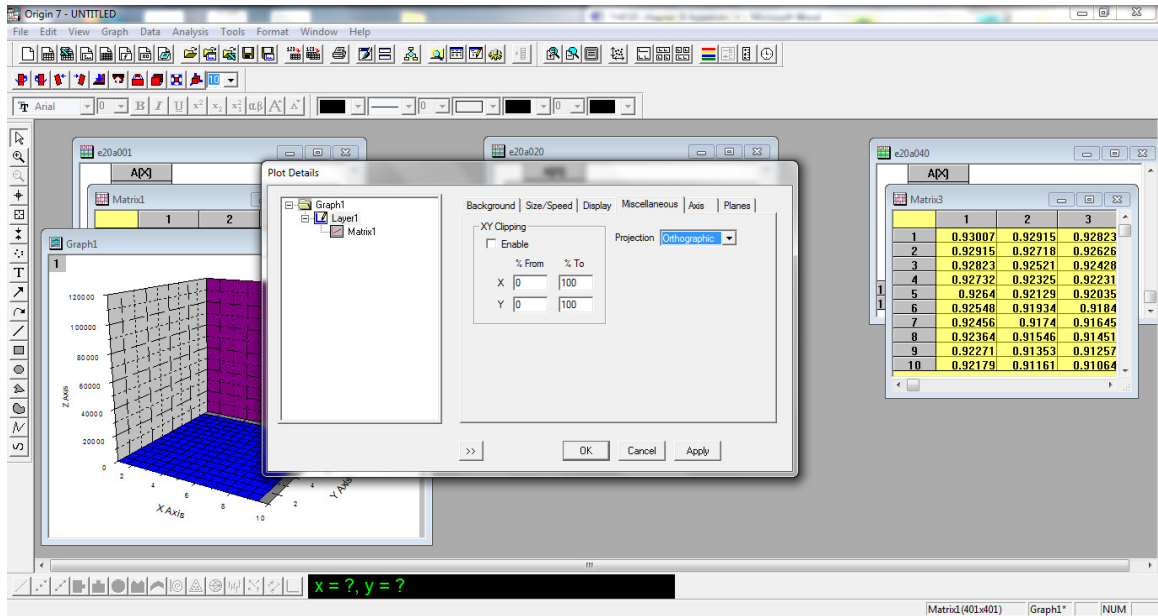


Figure A - 45. Setting the plot to orthographic display mode.

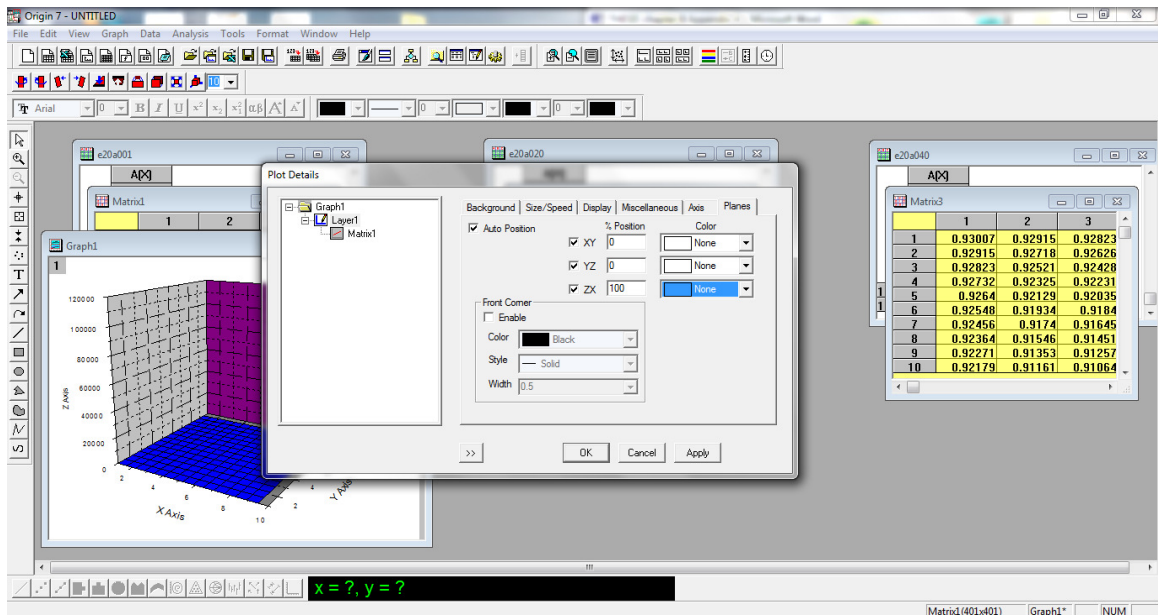


Figure A - 46. Setting the planes to not be colored.

Once plots have been generated for all of the slices that will be combined, it is necessary to go back through and make all of the plots have the same minimum and maximum settings in the color map. We only really want the plot for the bottom slice of the particle to be a three dimensional plot. So on all the other plots, go back into the plot details and in the layer 1 menu go to the display tab and uncheck the box for the z axis (Figure A - 47). Then go to the planes tab and uncheck the boxes next to the yz and xz planes (Figure A - 48). We also want to hide the major labels for the axes on all of the plots (Figure A - 49). Now that the individual plots are finalized, we want to merge them all into the same plot (Figure A - 51). We want to keep all the old graphs (Figure A - 52). Set the number of rows and columns to 1 (Figure A - 53). Then click Ok on the next window that pops up. This should create a new plot with three (or more) layers, one for each of the matrices (Figure A - 54). Click and drag the various layers to arrange them vertically along the z axis in the desired order (Figure A - 55).



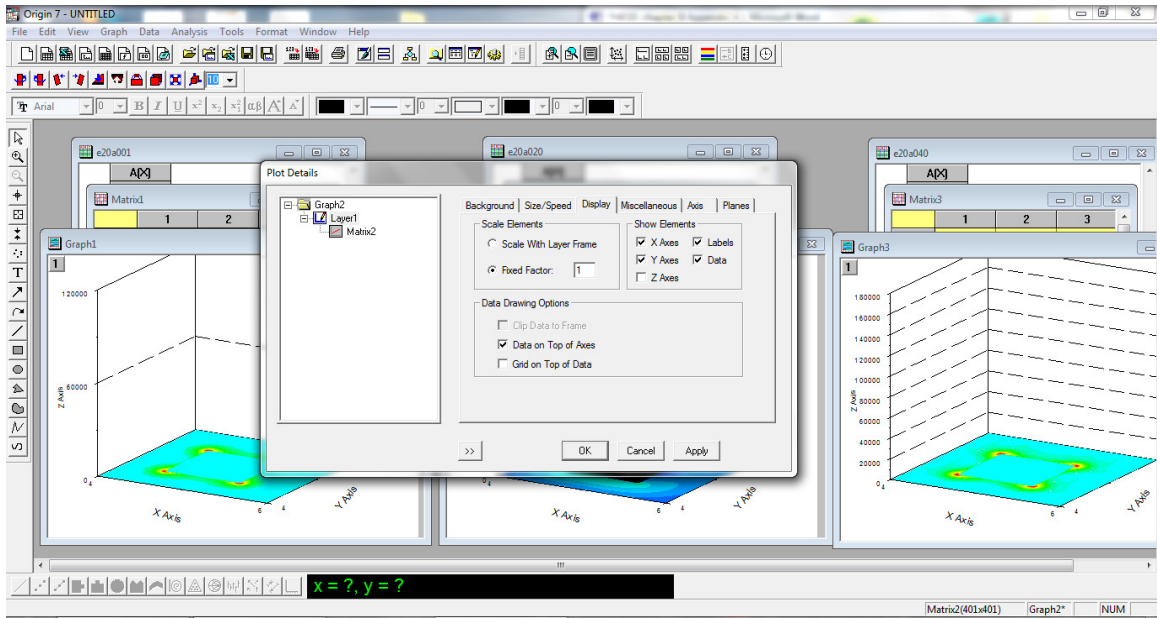


Figure A - 47. Hiding the z axis.

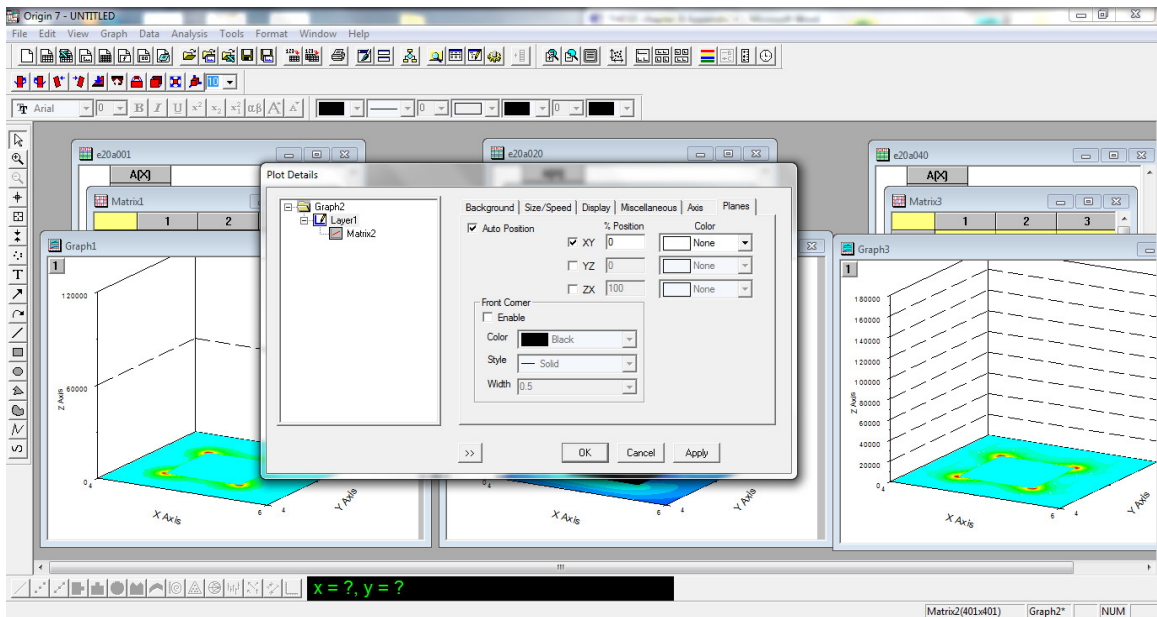


Figure A - 48. Hiding the yz and xz planes.



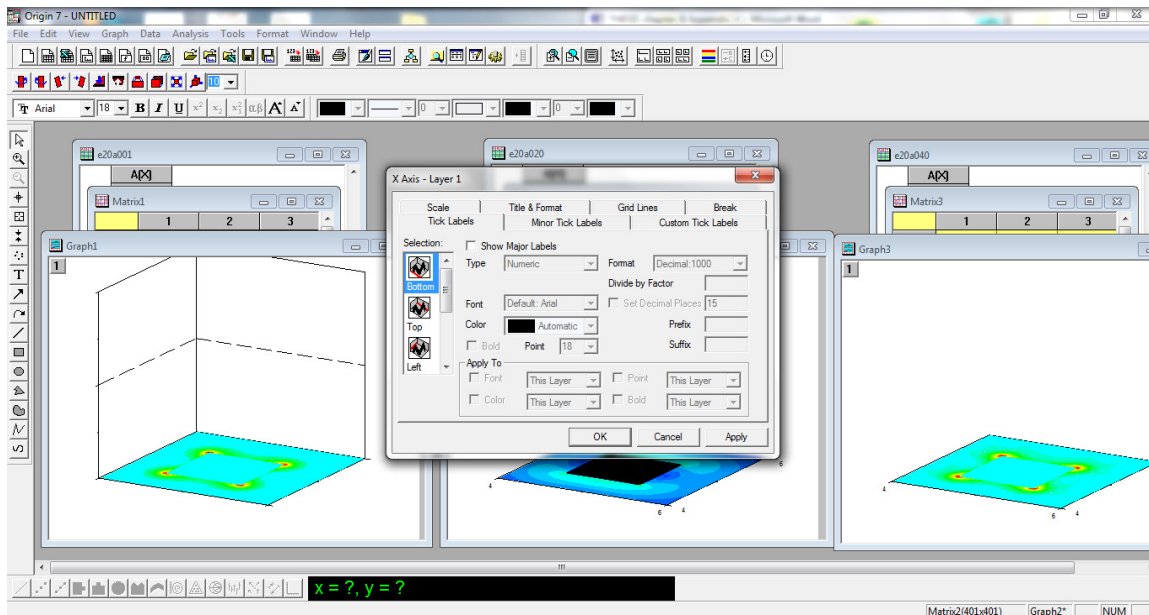


Figure A - 49. Hiding the major axis labels.

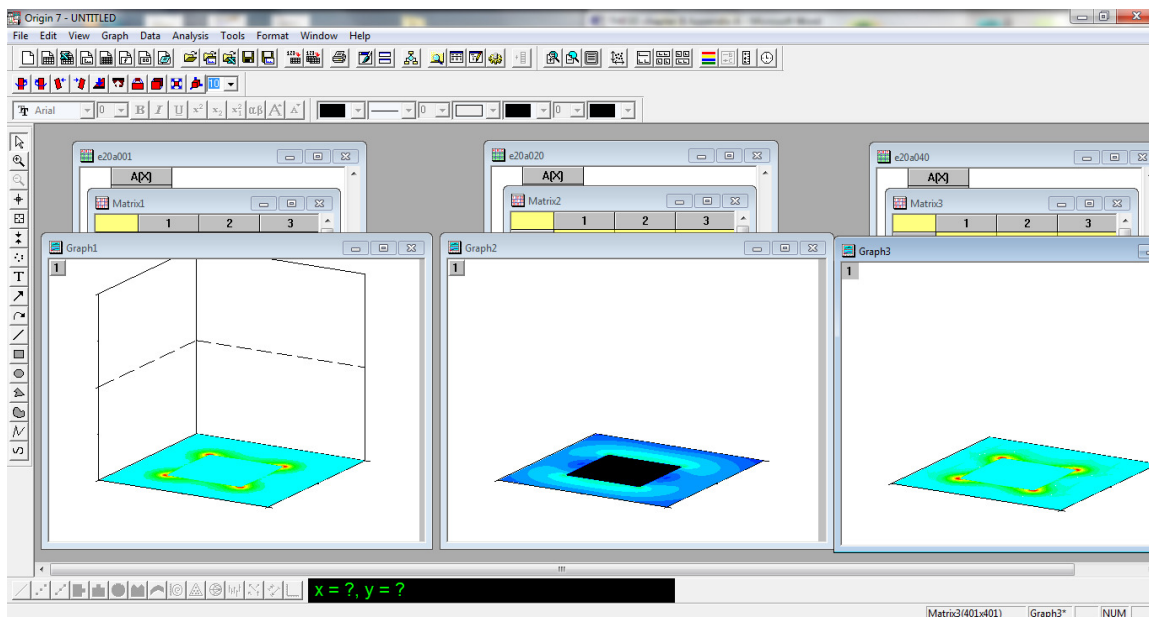


Figure A - 50. Final figures to combine into the 3D composite.

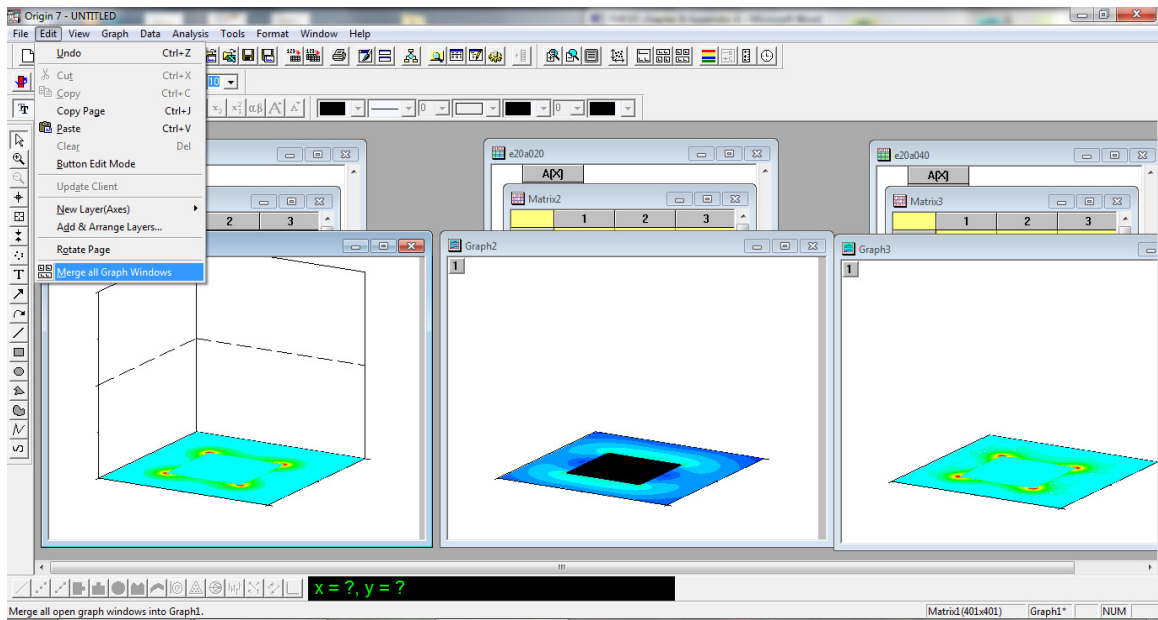


Figure A - 51. Merging the graphs.

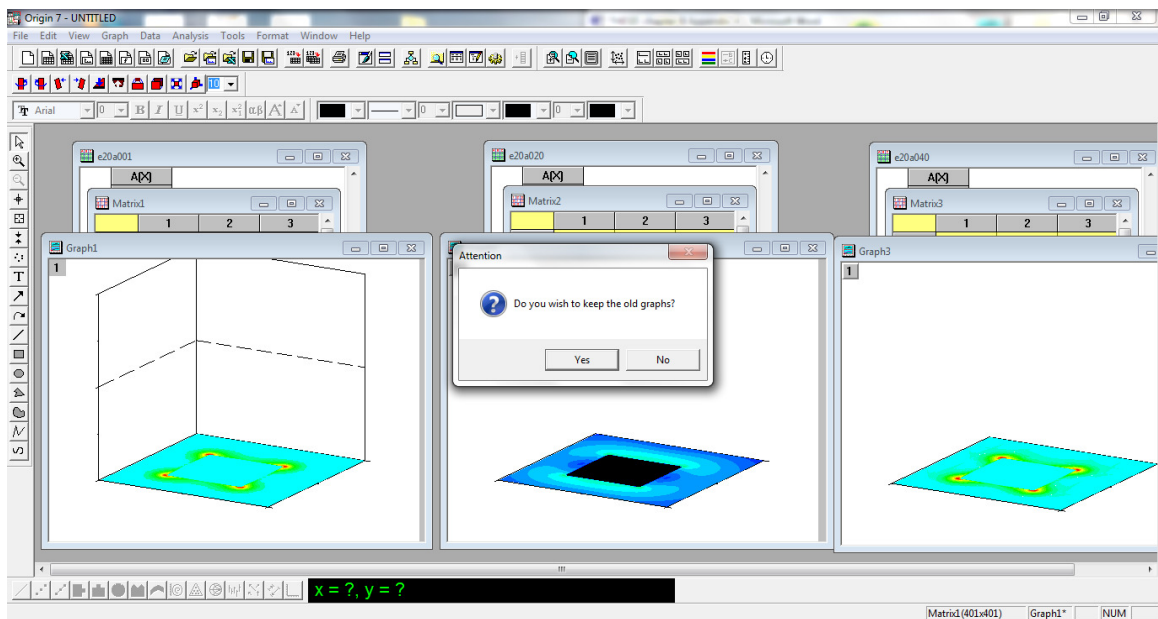


Figure A - 52. Keeping the old graphs.

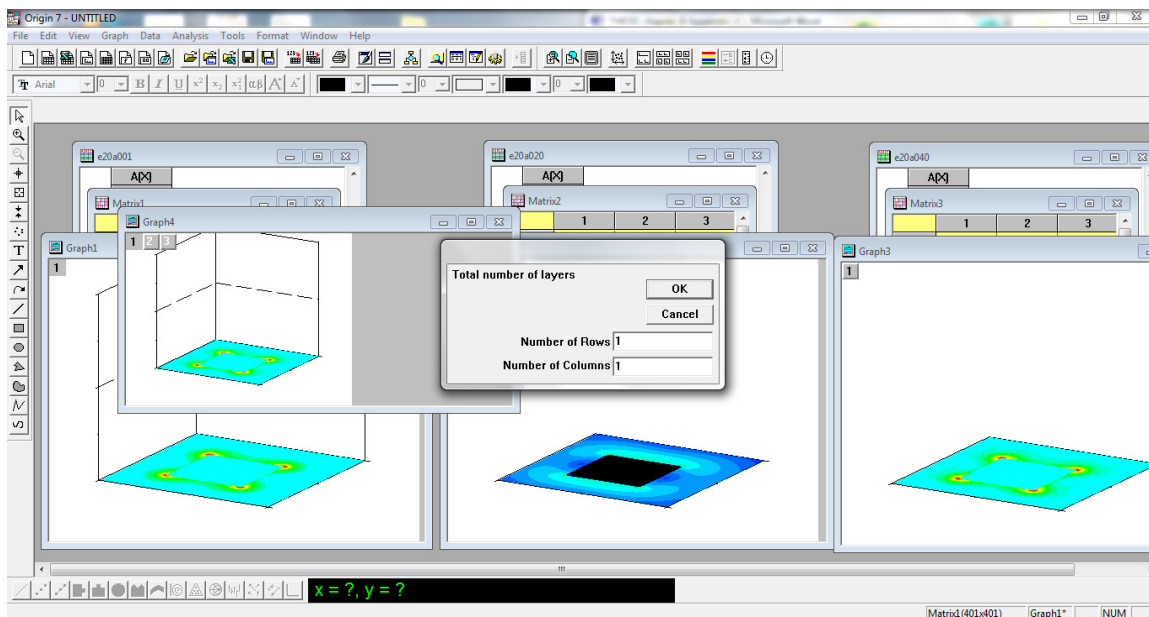


Figure A - 53. Setting the merged graph to be 1 row and column.

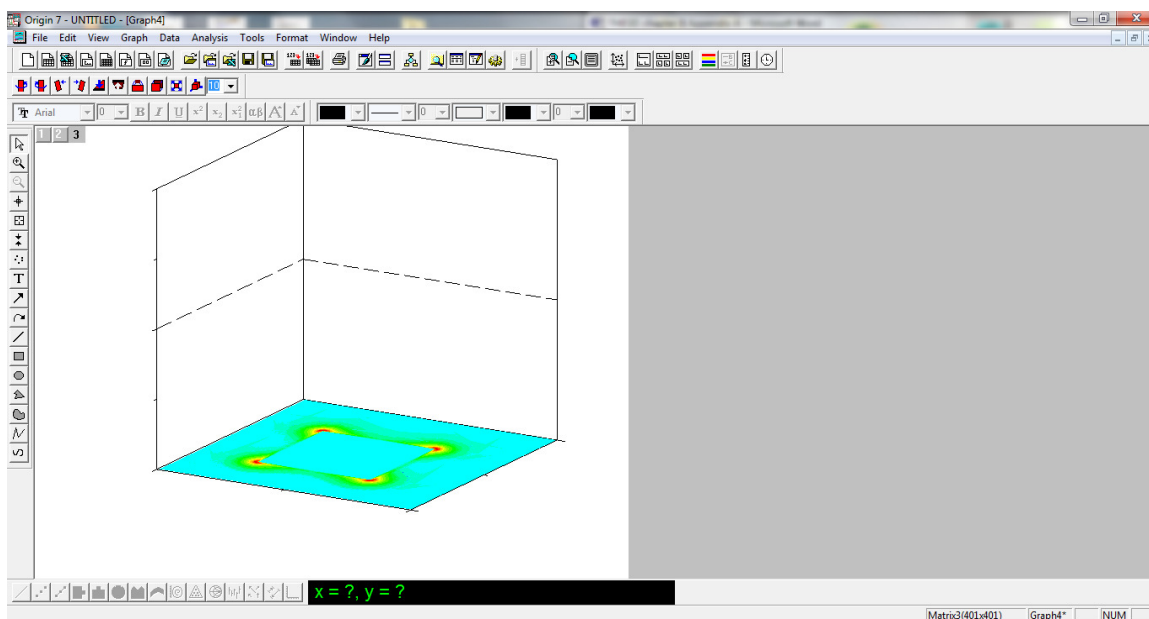


Figure A - 54. The initial merged plot.

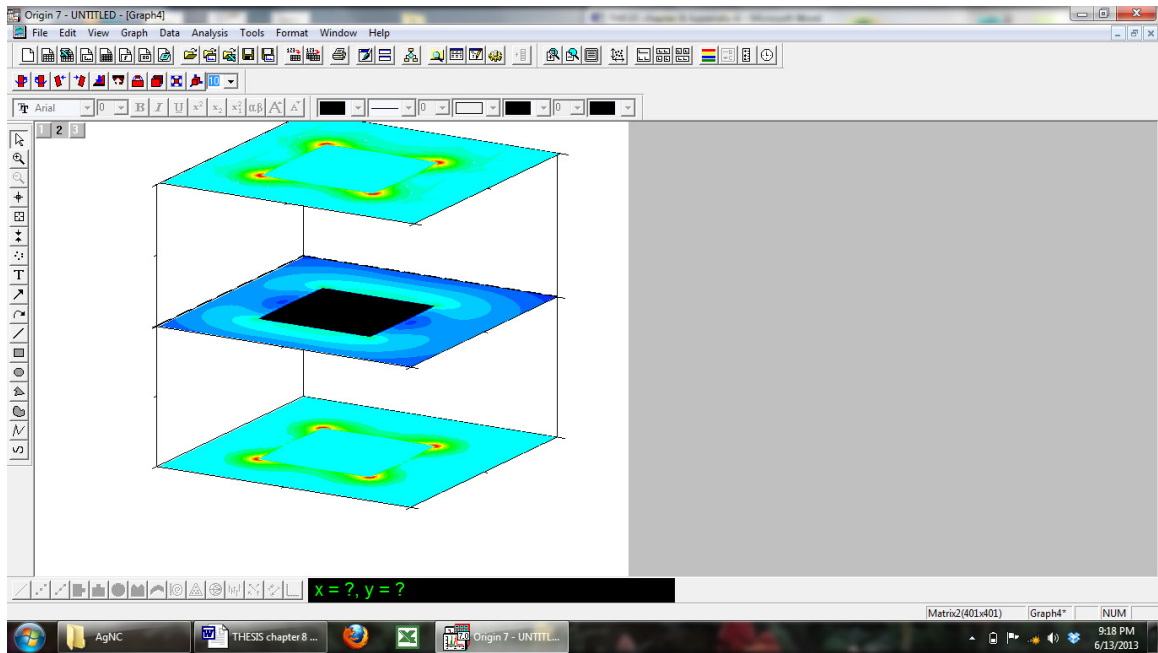


Figure A - 55. The final merged plot.

## **A. 10 Troubleshooting**

PROBLEM: Calculations didn't run.

SOLUTION: For a certain set of problems, the code should generate an error file that should be helpful in finding what or at least where the error is in your files.

However, this is not true for all problems. If there is no error file generated here are things to check:

- 1) Are the permissions on the files correct?
- 2) Are the files and folders named appropriately? Remember no spaces are allowed.
- 3) Try increasing the amount of memory allotted in the ddscat.pbs file

## A.11 References

- (1) Draine, B. T.; Flatau, P. J. Discrete-Dipole Approximation for scattering calculations. *J. Opt. Soc. Am. A-Opt. Image Sci. Vis.* **1994**, *11*, 1491-1499.
- (2) Goodman, J. J.; Draine, B. T.; Flatau, P. J. Application of Fast-Fourier-Transform techniques to the Discrete-Dipole Approximation. *Optics Letters* **1991**, *16*, 1198-1200.
- (3) Shuford, K. L.; Ratner, M. A.; Schatz, G. C. Multipolar excitation in triangular nanoprisms. *J. Chem. Phys.* **2005**, *123*.
- (4) Draine, B. T.; Flatau, P. J. User Guide for the Discrete Dipole Approximation Code DDSCAT 6.1. <http://arxiv.org/abs/astro-ph/0409262> **2004**.
- (5) Johnson, P. B.; Christy, R. W. Optical-constants of noble metals. *Physical Review B* **1972**, *6*, 4370-4379.
- (6) Palik, E. *Handbook of optical constants of solids*. Academic press: San Diego, 1985.

# RACHEL NEAR

## CIRRICULUM VITAE

### Education

- PhD** Georgia Institute of Technology **Expected 08/2013**  
Physical Chemistry  
GPA: 4.0/4.0
- BS** Georgia Institute of Technology **05/2008**  
Chemistry with Highest Honors; Physics with Highest Honors  
GPA: 3.93/4.0

### Summary

**Physical Chemistry Plasmonic Nanoparticles Optical Properties Spectroscopy**  
**Theoretical Modeling Electron Beam Lithography Colloidal Synthesis**

Eight years of experience designing plasmonic nanoparticles, investigating their optical properties, directing research projects and interfacing with collaborators in the industrial, engineering and biological disciplines. Proven track record of defining new research directions, building high-performance research teams, rapidly introducing innovative theoretical methods, improving connections between theory and experiment, and pioneering cross-discipline collaborations.

### Research Experience

- PhD Research, Georgia Institute of Technology, Atlanta, GA **2008-Present**
- Investigated the impact of physical geometry on the optical properties of nanoparticles
  - Designed AutoCAD files to create arrays of nanoparticles via Electron Beam Lithography with sub-nanometer resolution
  - Calculated relative plasmonic field strength to determine the ideal nanoparticle for photodynamic cancer therapy, yielding enhancement of a model drug by a factor of 200
  - Mastered colloidal synthesis of plasmonic metallic nanoparticles of a variety of shapes, sizes and compositions for Langmuir-Blodgett deposition to study interparticle effects
  - Developed expertise in spectroscopic and surface and transmission electron microscopic characterization of nanoparticles at sub-nanometer resolution
  - Developed expert skills at cross-cultural conflict resolution

Sole graduate researcher; BIONIC IRG 2-3 **2008-Present**

- Collaborated with Material Science Engineering and with the Air Force Research Lab
- Ascertaining the transient optical properties of adaptive organic and inorganic nanocomposites
- Engineered a microabsorption spectrometer set up during an Internship at the Air Force Research Lab in Dayton, OH
- Designed nanoparticle arrays to generate tunable responses based on light polarization

Undergraduate Research (PURA), Georgia Tech, **2007**

- Confirmed shape dependent catalysis kinetics of the ferrocyanide thiosulfate reduction reaction using Surface Enhanced Raman Spectroscopy
- Maximized catalytic activity of platinum nanoparticles by tailoring their shape during synthesis, achieving orders of magnitude enhancement in catalytic activity

Undergraduate Research (Dreyfus Fellow), Georgia Tech **2006**

- Developed a novel synthesis for gold nanoparticles with tunable optical properties

### **Leadership Experience**

- Trained and supervised incoming graduate students **2009 -present**
- Mentored over 20 students encouraging pursuit of careers in science and technology
  - Girls, Inc. **2011**
  - Independent tutor, Physical Chemistry (Quantum Mechanics) **2010-Present**
  - NNIN Youth Outreach Program **2010**
  - Incoming Graduate Students **2009-Present**
- Edited scientific journal articles and research proposals for both content and English grammar
  - Junior Editor, American Journal Experts **2011-Present**
  - Reviewer for President's Undergraduate Research Award **2010-Present**
- Collaborated with recruiters and facilitated networking
  - Georgia Tech Career Fair **2011**

### **Teaching Experience**

Trained and Supervised NNIN-REU Summer Intern **2010**

- Developed a research project focused on investigating the effects of development conditions on the shape and resolution of gold nanoparticles fabricated using electron beam lithography.

Teaching Assistant, Georgia Institute of Technology, Atlanta, GA. **2007-2009**

- Courses:
  - Quantitative Analysis **2009**
  - Advanced Chemistry Lab **2008**
  - Physical Chemistry II (Course Material: Quantum Mechanics) **2007**



- Assured safety of large groups of students by enforcing federal, state and institutional guidelines
- Prepared and administered lectures to more than 20 students a week
- Directed cumulative senior research projects
- Administered department-wide final presentations

### Awards and Scholarships

- Received over 15 academic awards and scholarships, including:
 

– Georgia Institute of Technology Presidential Fellowship	<b>2008-2012</b>
– President’s Undergraduate Research Award (PURA)	<b>2007</b>
– William M. Spicer Scholarship	<b>2007</b>
– Outstanding Undergraduate in Chemistry Award	<b>2006-2007</b>
– Joseph S. Fanning Memorial Scholarship	<b>2006-2007</b>
– Dreyfus Fellowship/Scholarship	<b>2006</b>
– Peter B. Sherry Memorial Scholarship	<b>2006</b>
– Laroche Corporate Scholarship	<b>2005-2006</b>
– Sidney Goldin Scholarship	<b>2005-2006</b>
– George Woodruff NM Scholarship; Newborn Scholarship	<b>2004-2006</b>
– Sibyl and Fred Lawton Harrison, Jr. Scholarship	<b>2004-2005</b>

### Publications

- Near R, El-Sayed MA. *Hollow Gold Nanorectangles: The Roles of Polarization, Shape and Substrate*. **J Chem Phys**, Accepted.
- Near R, Hayden S, El-Sayed MA. *Extinction vs Absorption: Which Is the Indicator of Plasmonic Field Strength for Silver Nanocubes?* **Journal of Physical Chemistry C**, **2012**, 116, 23019.
- Near R, Tabor C, Duan J, Pachter R, El-Sayed MA. *Pronounced Effects of Anisotropy on Plasmonic Properties of Nanorings Fabricated by Electron Beam Lithography*. **Nano Letters**, **2012**, 12, 2158.
- Mackey M, Near R, Austin L, Ali M, El-Sayed M. *Size-Dependent Gold Nanorod Plasmonic Photothermal Therapy: Theory and Experiment*. **JACS**, Submitted.
- Gupta MK, Konig T, Near R, Nepal D, Drummy LF, Biswas S, Naik S, Vaia RA, El-Sayed MA, Tsukruk VV. *Uniform Surface Assembly and Anisotropic Plasmonic Properties in Strongly Coupled Segmented Gold Nanorods*. **Small**, **2013**, ASAP.
- Hayden S, Austin L, Near R, Ozturk R, El-Sayed MA. *Plasmonic Enhancement of Photodynamic Cancer Therapy*. **J Photochem PhotoBio**, Accepted.
- Allam N, Yen CW, Near R, El-Sayed MA. *Bacteriorhodopsin/TiO(2) nanotube arrays hybrid system for enhanced photoelectrochemical water splitting*. **Energy & Environmental Science**, **2011**, 4, 2909.
- Dreaden E, Near R, Abdallah T, Talaat MH, El-Sayed MA. *Multimodal plasmon coupling in low symmetry gold nanoparticle pairs detected in surface-enhanced Raman scattering*. **Applied Physics Letters**, **2011**, 98, 183115.

## Presentations

- "Effects of Anisotropy on Plasmonic Properties of Nanorings Fabricated via EBL"  
**05/2013**  
**Poster**, 57th International EIPBN Conference, Nashville, TN
- "Pronounced Effects of Anisotropy on Plasmonic Properties of Nanorings"  
**04/2013**  
**Poster**, American Chemical Society National Meeting, New Orleans, LA
- "Extreme Sensitivity of Plasmonic Hollow Nanoparticles"  
**02/2013**  
**Poster**, Georgia Tech Research and Innovation Conference, Atlanta, GA
- "Plasmonic Coupling Phenomena in Organic/Inorganic Nanostructures"  
**09/2012**  
**Talk**, Annual BIONICS Meeting, Dayton, OH and Atlanta, GA
- "Pronounced Effects of Anisotropy on Plasmonic Properties of Nanorings"  
**02/2012**  
**Poster**, Georgia Tech Research and Innovation Conference, Atlanta, GA
- "Coupling Phenomena and Plasmonics in Organic/Inorganic Nanostructures"  
**09/2011**  
**Talk**, Annual BIONICS Meeting, Atlanta, GA
- "Coupling Phenomena in Arrays of Plasmonic Nanostructures"  
**07/2011**  
**Invited talk**, AFRL, Dayton, OH
- "Studying Coupling in Organic/Inorganic Nanostructures"  
**09/2010**  
**Talk**, Annual BIONICS Meeting, Atlanta, GA